

# **Measurements of Peroxy Radicals, Chemistry and Transport in the Atmosphere**

**Thesis submitted for the degree  
of Doctor of Philosophy  
at the University of Leicester**

**by**

**Alexander Edward Parker M.Chem. (Oxon)**

**Department of Chemistry**

**University of Leicester**

**September 2007**

UMI Number: U495429

All rights reserved

INFORMATION TO ALL USERS

The quality of this reproduction is dependent upon the quality of the copy submitted.

In the unlikely event that the author did not send a complete manuscript and there are missing pages, these will be noted. Also, if material had to be removed, a note will indicate the deletion.



UMI U495429

Published by ProQuest LLC 2013. Copyright in the Dissertation held by the Author.  
Microform Edition © ProQuest LLC.

All rights reserved. This work is protected against  
unauthorized copying under Title 17, United States Code.



ProQuest LLC  
789 East Eisenhower Parkway  
P.O. Box 1346  
Ann Arbor, MI 48106-1346

The work in this thesis was conducted at the Department of Chemistry of the University of Leicester in the Atmospheric Chemistry group between September 2003 and September 2007. The work is that of the author unless acknowledged in the thesis.

The thesis may be made available for consultation within the library of the University of Leicester.

Alexander Edward Parker

Leicester

24<sup>th</sup> September 2007

# Abstract

## Measurements of Peroxy Radicals, Chemistry and Transport in the Atmosphere

Alexander Edward Parker

This thesis explores the atmospheric chemistry of peroxy radicals ( $\text{HO}_2 + \Sigma_i \text{R}_i\text{O}_2$ ) via a series of new measurements. Peroxy radical measurement techniques are discussed, and the University of Leicester PERCA instrument is described in detail. Three field campaigns are described.

Peroxy radical concentrations during ITOP displayed an increase with altitude that is likely to have been impacted by the effects of long-range transport. Enhanced peroxy radical concentrations were observed within air-masses traversing the Atlantic indicating significant photochemical activity during transport. Net ozone production at clear sky limit is in general negative, and the summer mid-Atlantic troposphere is at limit net ozone destructive. There is evidence of positive ozone production within air masses undergoing long-range transport. Ozone production was  $\text{NO}_x$  limited throughout the airmasses measured during ITOP.

Two contrasting periods of meteorology were encountered at Jungfraujoch – days with and without heavy snowfall. Peroxy radicals were significantly suppressed during ‘snowy’ days, with neither increased  $\text{NO}_x$  nor reduced  $j(\text{O}^1\text{D})$  accounting for the difference. To reconcile the difference a pseudo first order loss rate of  $k_{\text{ex}} = 0.0063 \text{ s}^{-1}$  is required. Ozone production rates show that overall the Jungfraujoch was net neutral to marginally ozone destructive. Overall ozone production through the campaign was peroxy radical limited. The ozone compensation point for ‘snow free’ days was 28 pptv.

The formation of secondary organic aerosol was studied at a simulation chamber. High  $\text{NO}_x$ ,  $\text{O}_3$  and peroxy radical concentrations caused problems with peroxy radical measurements, but modelling studies showed that measurements under atmospheric conditions are only negligibly affected. Further experiments at low concentrations of  $\text{NO}_x$ ,  $\text{O}_3$  and peroxy radicals and constant HONO concentration showed peroxy radicals within the chamber began to build up prior to aerosol nucleation, indicating the potential role of organic hydroperoxides in the formation of secondary organic aerosol. Preliminary model results are also discussed.

# Acknowledgements

I would like to thank my supervisor Paul Monks for encouragement, support and foreign travel opportunities over the course of my Ph.D., and for being confident even when I wasn't. A huge thank you to the PSM and wider Mol. Props. groups for always being there for fun or to talk to – Mark, Zoë and Andrew for welcoming me and starting me off, Bob for the (sometimes dubious) pleasure of your jokes, Keggles for warring through hard times and higher mountains, Chris for good advice amongst the comic relief, Dan for finally taking over the reigns, and Kerry, Rebecca, Matt, Claire, Nika, Mindy, Kets, Karun, Gary, Niggle, Jonny, Andy, PMC, Corey, Steve and many others for Friday evenings in the SCR and making work and Leicester somewhere I wanted to be. All the friends I have made on ITOP, PSI, JFJ, AMMA and other field campaigns, thank you for making this such an interesting period of my life.

There was a house on Cromer Street... Gimpson, Gippo and James0r deserve massive praise for putting up with living with me for three solid years and me finally cutting the hair a week before leaving – thank you guys for all the good times, and best of luck for the future although none of you need it. Long live the Cromer Street posse!

Phil Acton, Gerry Butler, Keith Wilkinson, John Wheald, Carl Schieferstein, Roy Batchen, Si Choudhury and Julie Spence, thank you for never complaining no matter what the request and at how short notice – I still can't quite believe how much you put yourselves out to support our work.

Finally and most importantly my family, especially Mum and Dad, for never ending and unconditional support, and Grandpa for tireless reading, useful comments and constructive criticism (whilst still claiming to enjoy it!). Without you all I would never have done it.

I would like to thank NERC for the grant that enabled me to do this Ph.D.

# Contents

<b>Chapter 1 - Introduction .....</b>	<b>1</b>
1.1 The atmosphere.....	1
1.1.1 The structure of the atmosphere.....	2
1.2 Ozone in the Atmosphere .....	4
1.2.1 Tropospheric ozone.....	6
1.3 Tropospheric photochemistry .....	7
1.3.1 Photolysis rates .....	8
1.3.2 The OH radical.....	9
1.4 Peroxy radicals and tropospheric ozone production .....	10
1.4.1 Additional peroxy radical sources .....	12
1.4.2 Peroxy radical loss pathways .....	14
1.4.3 Control of ozone production .....	15
1.5 Long-range transport.....	17
1.5.1 Long-range transport processes .....	17
1.5.2 Impact of long-range transport .....	20
1.5.3 Eulerian and Lagrangian frameworks.....	25
1.6 Previous peroxy radical measurement campaigns .....	26
1.7 Summary.....	30
<b>Chapter 2 - Peroxy Radical Measurement Techniques.....</b>	<b>32</b>
2.1 The PERCA technique.....	32
2.1.1 PEROxy Radical Chemical Amplification – Laser Induced Fluorescence (PERCA-LIF) .....	34
2.2 Matrix Isolation Electron Spin Resonance (MI-ESR) .....	34
2.3 Fluorescence Assay by Gas Expansion (FAGE) .....	35
2.4 Peroxy radical Chemical Ionisation Mass Spectrometry (PerCIMS) .....	37
2.5 Proton Transfer Mass Spectrometry (PTr-MS) .....	38
2.6 The University of Leicester dual-channel PERCA.....	40
2.6.1 Instrument description .....	43
2.6.2 The inlet system.....	43

2.6.3	The calibration system.....	47
2.6.3.1	NO <sub>2</sub> sensitivity calibration.....	47
2.6.3.2	Chain length calibration.....	48
2.6.3.3	Measurement of $j(\text{CH}_3\text{I})$ .....	50
2.6.3.4	Inlet unit positioning.....	52
2.6.4	Deployment.....	53
2.6.5	Description of sub-systems.....	56
2.6.5.1	Detector systems.....	56
2.6.5.2	Linearisation unit.....	58
2.6.5.3	Uninterruptible Power Supply.....	58
2.6.5.4	Computer systems.....	59
2.6.5.5	DC supply box.....	60
2.6.5.6	Electrical distribution unit.....	60
2.6.5.7	Interconnection box.....	60
2.6.5.8	Isothermal unit.....	62
2.6.5.9	Gas supplies.....	62
2.6.5.10	The gas rack.....	63
2.6.1	Chain length optimization.....	65
2.6.2	Water vapour interference correction.....	66
2.7	Error analysis.....	67
2.7.1	Dual-channel PERCA instrument.....	69
2.8	Data work-up – from modulations to peroxy radicals.....	71
2.9	Summary.....	75

### **Chapter 3 - The Intercontinental Transport of Ozone and**

<b>Precursors (ITOP) Campaign.....</b>	<b>76</b>	
3.1	Overview.....	76
3.2	ITOP objectives.....	77
3.3	Instrumentation, forecasting and modelling.....	79
3.4	ITOP flight summaries.....	81
3.5	PERCA performance.....	83
3.5.1	Calibration.....	85
3.6	Results.....	87
3.6.1	Radicals and tracers.....	87
3.6.2	Overall photochemistry.....	108

3.6.3	Case studies.....	114
3.6.3.1	Low level (4.5km) Long-Range Transport.....	114
3.6.3.2	Multiple interceptions of American export.....	116
3.7	Conclusions.....	118

## **Chapter 4 - Composition Control in the European Free**

### **Troposphere.....120**

4.1	Overview.....	120
4.2	Objectives .....	120
4.3	Instrumentation .....	123
4.3.1	Peroxy radical measurements .....	123
4.3.2	Photolysis frequency measurements.....	124
4.3.2.1	Optical collection system.....	125
4.3.2.2	Photolysis frequencies derived .....	126
4.3.3	Other measurements .....	127
4.4	Results.....	129
4.4.1	Radicals and tracers observations .....	129
4.4.2	Back trajectories .....	136
4.4.3	Peroxy radical production and loss.....	139
4.4.3.1	Additional peroxy radical production sources.....	145
4.4.4	Seasonality.....	146
4.4.5	Ozone production and loss.....	148
4.4.5.1	Ozone compensation point.....	153
4.4.5.2	Comparison with previous results.....	154
4.5	Conclusions.....	154

## **Chapter 5 - The Role of Radicals in the Formation of Secondary**

### **Organic Aerosols.....157**

5.1	Aerosols in the atmosphere.....	157
5.1.1	Secondary Organic Aerosol (SOA) .....	159
5.1.2	Secondary organic aerosol formation mechanisms .....	159
5.2	The PSI atmospheric simulation chamber .....	163
5.3	Instrumentation .....	164
5.3.1	Peroxy radical measurements .....	164
5.3.2	HO <sub>2</sub> measurements .....	165

5.3.3	Additional gas phase instrumentation.....	166
5.3.4	Aerosol instrumentation.....	166
5.3.5	Experiments .....	167
5.4	Results.....	170
5.4.1	Veracity of peroxy radical measurements .....	177
5.4.2	Inlet chemistry modelling .....	177
5.4.3	Effect of wall loss rate .....	180
5.4.4	Impact on atmospheric measurements.....	181
5.5	HONO experiments .....	181
5.5.1	HONO and 1,3,5-trimethylbenzene system.....	183
5.5.1.1	Modelling.....	187
5.5.2	HONO and isoprene system .....	190
5.6	Conclusions.....	192
<b>Chapter 6 - Conclusions and Proposals for Future Work .....</b>		<b>194</b>
6.1	Peroxy radical measurements .....	194
6.2	Atmospheric field measurements.....	195
6.3	Aerosol chamber studies.....	196
<b>Appendix A - IGOR Data Workup Procedures .....</b>		<b>197</b>
A.1	Main.ipf.....	197
A.2	WAOWEX_Cals_ITOP.ipf .....	197
A.3	Work-up2.ipf.....	201
<b>Appendix B - Postgraduate Record .....</b>		<b>208</b>
B.1	Induction/Training Sessions Attended.....	208
B.2	Undergraduate Lecture Courses Attended.....	208
B.3	Departmental Seminars.....	209
B.4	Conferences/Meetings Attended.....	212
B.5	Presentations Given at Conferences .....	214
B.6	Departmental Presentations .....	215
B.7	Papers.....	216
B.8	Other .....	216
<b>References .....</b>		<b>218</b>

# Glossary and Definitions

<b>AMS</b>	<b>Aerosol Mass Spectrometry</b>
<b>BAe</b>	<b>British Aerospace</b>
<b>BOC</b>	<b>British Oxygen Company Ltd.</b>
<b>CCB</b>	<b>Cold Conveyor Belt</b>
<b>CIR-TOF-MS</b>	<b>Chemical Ionisation Reaction Time of Flight Mass Spectrometry</b>
<b>CL</b>	<b>Chain Length</b>
<b>CPC</b>	<b>Condensation Particle Counter</b>
<b>DLR</b>	<b>Deutsches Zentrum für Luft- und Raumfahrt</b>
<b>DMS</b>	<b>dimethylsulphide</b>
<b>DPC</b>	<b>Data Personal Computer</b>
<b>EDU</b>	<b>Electrical Distribution Unit</b>
<b>EMPA</b>	<b>Eidgenössische Materialprüfungs- und Forschungsanstalt</b>
<b>EPC</b>	<b>Ethernet Personal Computer</b>
<b>ETHZ</b>	<b>Eidgenössische Technische Hochschule Zürich</b>
<b>FAAM</b>	<b>Facility for Airborne Atmospheric Measurements</b>
<b>FAGE</b>	<b>Fluorescence Assay by Gas Expansion</b>
<b>FT</b>	<b>Free Troposphere</b>
<b>GC</b>	<b>Gas Chromatography</b>
<b>GPS</b>	<b>Global Positioning System</b>
<b>ICARTT</b>	<b>International Consortium for Atmospheric Research on Transport and Transformation</b>
<b>IGAC-ITCT</b>	<b>International Global Atmospheric Chemistry – Intercontinental Transport and Chemical Transformation</b>
<b>INS</b>	<b>Inertial Navigation System</b>
<b>ITOP</b>	<b>Intercontinental Transport of Ozone and Precursors</b>
<b>LIF</b>	<b>Laser Induced Fluorescence</b>
<b>LRT</b>	<b>Long Range Transport</b>
<b>Mbps</b>	<b>Megabits per second</b>
<b>MCM</b>	<b>Master Chemical Mechanism</b>

---

<b>MFC</b>	<b>Mass Flow Controller</b>
<b>MFM</b>	<b>Mass Flow Meter</b>
<b>MI-ESR</b>	<b>Matrix Isolation Electron Spin Resonance</b>
<b>NASA</b>	<b>National Aeronautics and Space Administration</b>
<b>NERC</b>	<b>Natural Environment Research Council</b>
<b>NIST</b>	<b>National Institute of Standards and Technology</b>
<b>NMHC</b>	<b>Non Methyl Hydrocarbon</b>
<b>NOAA</b>	<b>National Oceanic and Atmospheric Administration</b>
<b>ORAC</b>	<b>Organics by Real-time Airborne Chromatography</b>
<b>OVOC</b>	<b>Oxygenated Volatile Organic Compound</b>
<b>PAN</b>	<b>Peroxyacetylnitrate</b>
<b>PBL</b>	<b>Planetary Boundary Layer</b>
<b>PC</b>	<b>Personal Computer</b>
<b>PERCA</b>	<b>PERoxy Radical Chemical Amplifier</b>
<b>PerCIMS</b>	<b>PERoxy Radical Chemical Ionisation Mass Spectrometry</b>
<b>PICM</b>	<b>PERCA Inlet Control Module</b>
<b>PMT</b>	<b>Photo Multiplier Tube</b>
<b>PM<sub>x</sub></b>	<b>Particulate Matter with maximum diameter x <math>\mu\text{m}</math></b>
<b>POA</b>	<b>Primary Organic Aerosol</b>
<b>ppbv</b>	<b>parts per billion by volume</b>
<b>ppmv</b>	<b>parts per million by volume</b>
<b>pptv</b>	<b>parts per trillion by volume</b>
<b>PSAP</b>	<b>Particle Soot Absorption Photometer</b>
<b>PSI</b>	<b>Paul Scherrer Institut</b>
<b>PTR-MS</b>	<b>Proton Transfer Reaction – Mass Spectrometry</b>
<b>ROXMAS</b>	<b>RO<sub>x</sub> Mass Spectrometry</b>
<b>sccm</b>	<b>standard cubic centimetres per minute</b>
<b>slpm</b>	<b>standard litres per minute</b>
<b>SMPS</b>	<b>Scanning Mobility Particle Sizer</b>
<b>SOA</b>	<b>Secondary Organic Aerosol</b>
<b>TDLAS</b>	<b>Tuneable Diode Laser Absorption Spectrometry</b>
<b>TMB</b>	<b>1,3,5-trimethylbenzene</b>
<b>TUV</b>	<b>Tropospheric Ultra Violet radiation model</b>
<b>UEA</b>	<b>University of East Anglia</b>
<b>UKMO</b>	<b>United Kingdom Meteorological Office</b>

<b>UL</b>	<b>University of Leicester</b>
<b>UPS</b>	<b>Uninterruptible Power Supply</b>
<b>VOC</b>	<b>Volatile Organic Compound</b>
<b>VUV</b>	<b>Vacuum Ultra Violet</b>
<b>WCB</b>	<b>Warm Conveyor Belt</b>

# Chapter 1

## Introduction

The work contained within this thesis is primarily concerned with the role of peroxy radicals ( $\text{HO}_2 + \Sigma_i \text{R}_i \text{O}_2$ ) in the photochemistry of air-masses undergoing long-range transport leading to tropospheric ozone production remote from the source region. This chapter provides an introduction to the atmosphere and atmospheric chemistry, in addition to the processes through which long-range transport occurs.

### 1.1 The atmosphere

The Earth's atmosphere is a thin blanket of gas that extends above the surface of the planet for approximately 1000 km and has a mass of  $\sim 5.2 \times 10^{18}$  kg, approximately 90% of which is in the troposphere [Wayne, 2000]. The atmosphere has a dry composition of 78% nitrogen, 21% oxygen, and 1% argon, with the percentage composition of the major components remaining constant until approximately 80-90 km. The atmosphere is an essential requirement for life as we know it to exist.

In addition to the bulk constituents, many other species are present in the atmosphere at trace levels, including both gases and aerosols. These trace species constitute less than 1% of the atmosphere yet play a vitally important role in the chemistry of the atmosphere. The majority of trace gases are released from the Earth's surface, and are produced from a variety of sources including biogenic, anthropogenic, and chemical or geological processes, as well as *via* chemical production in the atmosphere. Trace species can include carbon species such as CO, CO<sub>2</sub>, CH<sub>4</sub> and other volatile organic compounds (VOCs); nitrogen containing species such as NO, NO<sub>2</sub>, NO<sub>3</sub>, N<sub>2</sub>O, peroxyacetylnitrate (PAN) and NH<sub>3</sub>; sulphur species such as SO<sub>2</sub>, dimethylsulphide (DMS) and H<sub>2</sub>S; and halogenated

compounds such as CFCs, HCFCs, HCl, HF, CH<sub>3</sub>Cl, CH<sub>3</sub>Br and CH<sub>3</sub>I. Also present are other trace gases such as water, ozone and various radical species, many of which are formed photochemically. Trace gas species are responsible for much of the varied chemistry that occurs within the atmosphere, e.g. ozone production within the troposphere, excess ozone depletion in the ozone layer in the stratosphere, and many other effects with wide ranging consequences on climate, chemistry, and health in human, animal and plant life.

It is the aim of the atmospheric chemist to attempt to understand the complex chemical reactor that is the atmosphere and to study the interplay between chemical and physical processes over the myriad of different timescales and conditions present.

### **1.1.1 The structure of the atmosphere**

The atmosphere can be divided into four distinct regions, on the basis of the vertical temperature-altitude profile as shown in Figure 1.1. A boundary occurs when the temperature gradient is zero, since little vertical mixing can take place.

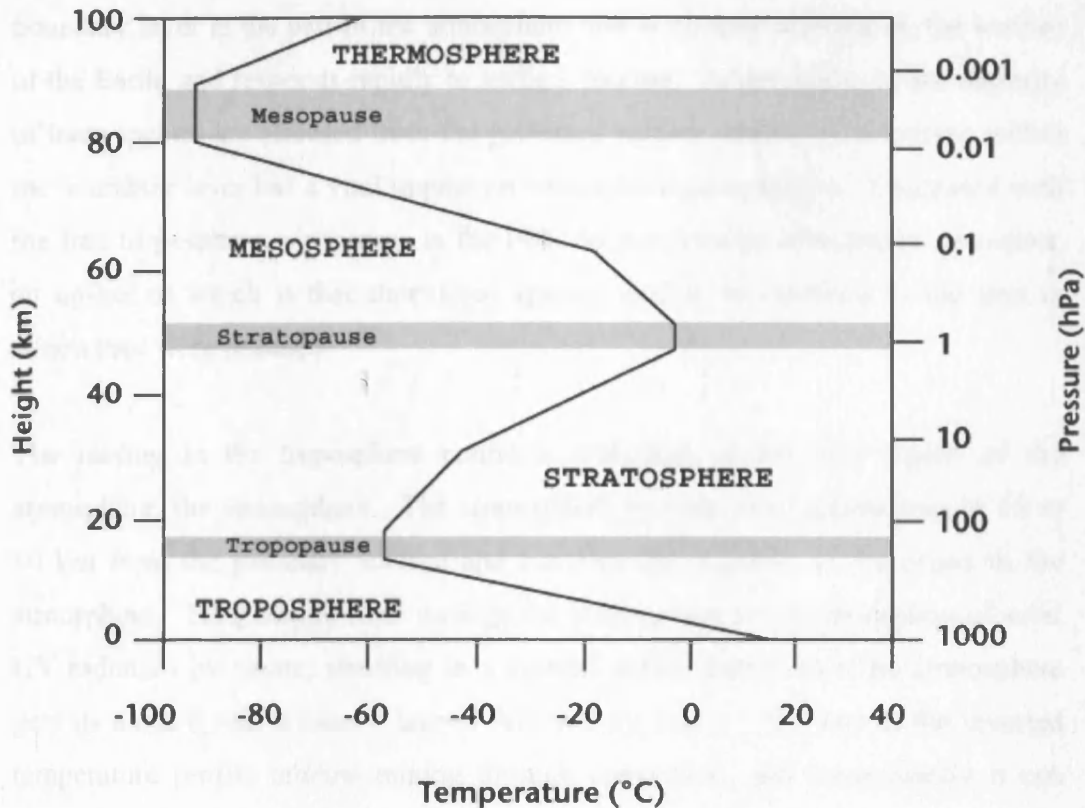


Figure 1.1 – Vertical temperature profile of the atmosphere

The lowest region in the atmosphere is called the troposphere, which extends from ground level to approximately 15 km. Temperature falls with altitude through the troposphere. Visible and near-UV solar radiation is absorbed by the Earth's surface and re-emitted as infra-red radiation that heats the atmosphere. Gas near the surface is warmed, rises due to convection, and as the air rises it adiabatically expands and cools. This temperature profile leads to strong vertical mixing in the troposphere (troposphere is named from the Greek *tropos* = turning and *sphaira* = ball), with species able to travel from the surface of the Earth to the top of the troposphere in a few days or less depending on weather conditions [Finlayson-Pitts and Pitts Jr., 2000].

The troposphere may itself be divided into two distinct regions, the planetary boundary layer (PBL) and the free troposphere (FT). The boundary layer is the area closest to the ground and extends to approximately 0.5 – 2 km during the day at mid-latitudes, but less at night – potentially only a few hundred metres. It is characterised by very turbulent mixing owing to radiative heating from the ground and increased deposition due to repeated contact of air masses with the ground. The

boundary layer is the part of the atmosphere that is directly affected by the surface of the Earth, and responds rapidly to surface forcing. Additionally, as the majority of trace species are released from the planetary surface, chemistry occurring within the boundary layer has a vital impact on atmospheric composition. Compared with the free troposphere, air masses in the PBL do not undergo as extensive transport, an upshot of which is that short-lived species tend to be confined to the area in which they were released.

The mixing in the troposphere contrasts with that of the next region of the atmosphere, the stratosphere. The stratosphere extends from approximately 15 to 50 km from the planetary surface and contains the majority of the ozone in the atmosphere. Temperature rises through the stratosphere due to absorption of solar UV radiation by ozone, resulting in a layered nature from which the stratosphere gets its name (Latin *stratus* = layer). Vertical mixing is very slow as the inverted temperature profile inhibits mixing through convection, and consequently it can take years for vertical transport through the stratosphere [Wayne, 2000].

The mesosphere occurs above the stratosphere at approximately 50 km and contains just 0.1% of the mass of the atmosphere. Through the mesosphere the temperature again starts to fall with altitude until the coolest part of the atmosphere at the junction between the mesosphere and thermosphere (the mesopause) at approximately 85 km, as a result of the concentration of ozone (and thus UV absorption) decreasing. At the mesopause temperature starts to rise again through the thermosphere due to absorption of solar radiation by nitrogen and oxygen.

## 1.2 Ozone in the Atmosphere

As mentioned in the previous section, the majority of ozone in the atmosphere (*ca.* 90%) is found in the stratosphere in a layer (the ‘ozone layer’) from approximately 20 – 30 km above the surface, as shown in Figure 1.2.

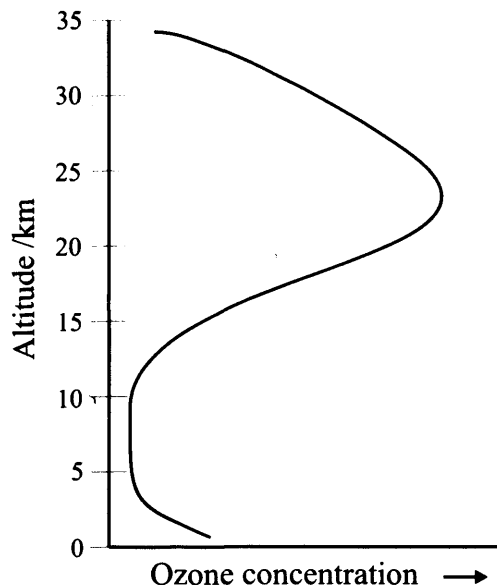


Figure 1.2 – Typical ozone profile through the atmosphere

The ozone layer helps protect life on the surface by absorbing damaging UV solar radiation. In the absence of external perturbation, a steady-state concentration of ozone in the ozone layer is maintained by the reactions known as the Chapman scheme:



where M is a third body (usually nitrogen or oxygen in the atmosphere). However, in recent years it has been reported that the ozone layer is being severely depleted over Antarctica [Farman, *et al.*, 1985] due to a large extent to man's activities and the widespread release of chlorofluorocarbons [Molina and Rowland, 1974] that can act as a halogen source under conditions present in the stratosphere and especially at the Antarctic. The halogen radical species released (e.g. chlorine and bromine atoms) can then destroy ozone *via* catalytic cycles.

## 1.2.1 Tropospheric ozone

Ozone is also present in the troposphere, where it is a major constituent of photochemical smog and in excessive concentrations can be harmful to human, animal and plant health. Tropospheric ozone can lead to irritation of the respiratory system, increased effects of asthma, reduce lung function and increased susceptibility to respiratory infections in humans and animals [Lippmann, 1993], as well as crop damage [Fiore, *et al.*, 1998]. For example, during the heatwave that occurred in Europe in August 2003, it has been estimated that between 423 and 769 excess deaths (21–38% of total excess deaths) were caused by elevated ambient ozone and PM<sub>10</sub> (particulate matter with a diameter of 10µm or less) concentrations in the UK alone [Stedman, 2004].

Ozone concentrations are generally higher in rural areas in comparison to urban areas, as species such as NO (that are generally present at higher concentrations in polluted urban centres) effectively scavenge ozone at high concentrations, thus reducing its concentration:



At rural sites the concentrations of these scavenging species tend to be lower, leading to higher ozone concentrations. Baseline ozone concentrations at Mace Head, Ireland, have been rising – in the years 1987–2003 the background ozone level in areas representative of Northern Hemisphere marine boundary layer has increased by about 24% [Simmonds, *et al.*, 2004].

Tropospheric ozone is generally produced close to the surface by the photochemical processing of trace gases, as detailed in sections 1.3 and 1.4. Ozone has a lifetime of several weeks in the troposphere [Liu, *et al.*, 1987], and thus can be transported great distances in that time. The transport of precursor species further means ozone formation may occur away from emission regions. The processes and consequences of transport are covered in section 1.5.

### 1.3 Tropospheric photochemistry

Photochemistry is the driving force of atmospheric chemistry, responsible for the initiation of much of the chemistry of the atmosphere and the loss of otherwise stable molecules. Owing to the strong absorption of light between 210-290 nm by ozone in the stratosphere and upper atmosphere, and at wavelengths shorter than 230 nm by oxygen, tropospheric photochemistry is limited to wavelengths longer than 290 nm, the atmospheric cut-off. The solar radiation reaching the Earth's surface is dependent on absorption and scattering by the species that make up the atmosphere. Some of the species responsible for the absorption of solar flux in the troposphere, and the corresponding wavelengths at which they absorb light are shown in Figure 1.3 [Kraus and Hofzumahaus, 1998].

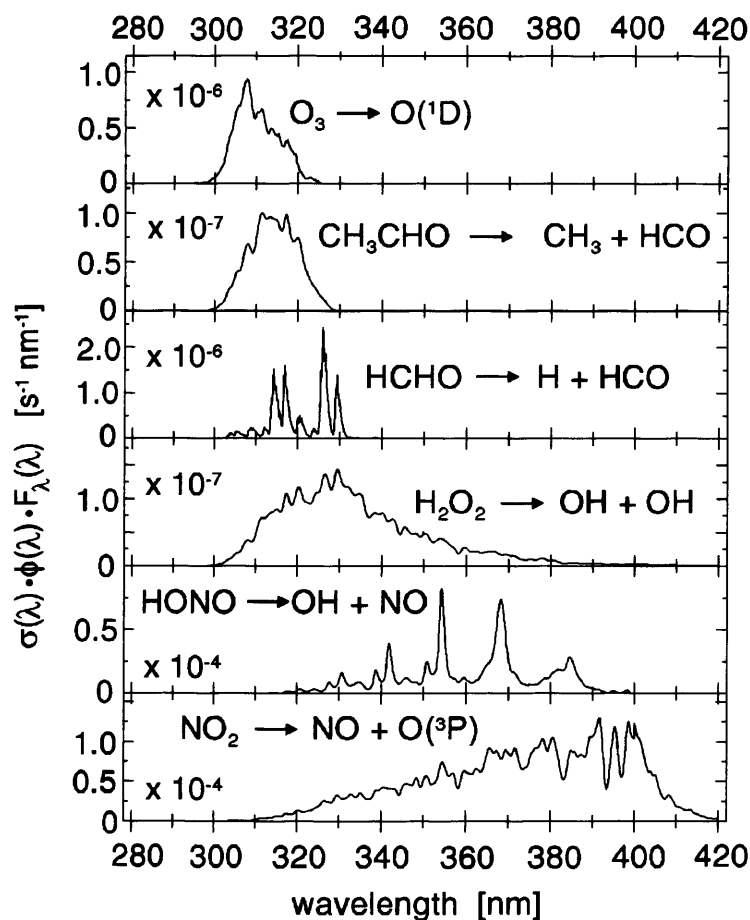


Figure 1.3 – Action spectrum showing photodissociation wavelengths for  $O_3$ ,  $CH_3CHO$ ,  $HCHO$ ,  $H_2O_2$ ,  $HONO$  and  $NO_2$  [Kraus and Hofzumahaus, 1998]

### 1.3.1 Photolysis rates

As photochemistry is an essential process in atmospheric chemistry, knowledge of the rate at which photochemistry occurs is very important. If a molecule absorbs light of sufficient energy, it may undergo photodissociation, which can be represented as a first order process:



The rate constant of this photodissociation, denoted  $j(AB)$ , is dependent on the actinic flux experienced by the molecule,  $F(\lambda)$ , the photodissociation quantum yield of the molecule,  $\phi$ , and the absorption cross-section of the molecule,  $\sigma$ .

$$j(AB) = \int_{\lambda_{\min}}^{\lambda_{\max}} F(\lambda)\phi(\lambda, T)\sigma(\lambda, T)d\lambda \quad (1.7)$$

The actinic flux is the spherical flux density available to the molecules which on absorption produces photodissociation in units of photons  $\text{cm}^{-2} \text{s}^{-1} \text{nm}^{-1}$ . The quantum yield is the number of molecules dissociated per photon of light absorbed, whilst the absorption cross-section is the quantity of light absorbed with respect to wavelength.

Therefore, if  $F(\lambda)$ , the actinic flux, is measured over the range of wavelengths relevant to a specific molecule and the absorption cross-section and quantum yield for the molecule of interest is known, it is possible to calculate the photolysis rate of the molecule. In practice, due to the atmospheric cut-off, the wavelength range for photodissociation is usually taken from a lower limit of 290 nm to a molecule specific upper wavelength. For example, the upper wavelength for photolysis of ozone to form  $\text{O}(^1\text{D})$  ( $j(\text{O}^1\text{D})$ ) is 340 nm and for the photolysis of  $\text{NO}_2$  ( $j(\text{NO}_2)$ ) is 420 nm. The photolysis of ozone to form  $\text{O}(^1\text{D})$  is one of the most important in atmospheric chemistry as shall be seen in the next section.

### 1.3.2 The OH radical

The OH radical is the primary daytime atmospheric oxidant. It is often referred to as the atmospheric cleanser, as along with ozone and the NO<sub>3</sub> radical (at night), the OH radical is primarily responsible for the oxidation of trace gas species in the atmosphere. The complementary nature of OH and NO<sub>3</sub> occurs as OH is generated photochemically during the day and is short lived with an atmospheric lifetime of the order of a second and therefore does not survive at night, whereas NO<sub>3</sub> is rapidly photolysed during the day and thus exists primarily at night. The OH radical is present in low concentrations in the atmosphere of the order of 10<sup>6</sup> molecules cm<sup>-3</sup>. NO<sub>3</sub> is less reactive than OH but is present in higher concentrations, of the order of 10<sup>9</sup> molecule cm<sup>-3</sup> [Wayne, 2000].

The primary production route of OH is *via* photolysis of ozone at wavelengths less than 340 nm to form an electronically excited O(<sup>1</sup>D) atom, the rate of which is denoted  $j(\text{O}^1\text{D})$ , followed by reaction with water vapour, *viz*



The reaction of O(<sup>1</sup>D) with water vapour competes with quenching of the excited oxygen atom to the ground state followed by reformation of ozone, thus



There are also a number of secondary OH production pathways, such as the photodissociation of acetone, formaldehyde, HONO and H<sub>2</sub>O<sub>2</sub>, and the reaction of HO<sub>2</sub> and NO. These production routes are known as secondary as the compounds responsible for OH production are often themselves a product of OH initiated oxidation.





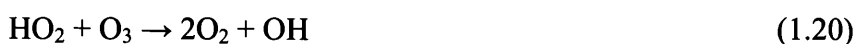
The formation of OH from HONO photolysis can be an important or even dominant early morning source of OH [Platt, *et al.*, 2002]. HONO builds up overnight in the presence of NO<sub>2</sub>, and is rapidly photolysed in the early morning. At high solar zenith angles (i.e. the sun is low in the sky), the path length through the atmosphere for solar radiation is longer and consequently more ozone molecules are present to absorb solar radiation. As the maximum photolysis wavelength of HONO is longer than that of ozone,  $j(\text{HONO})$  is less affected by high solar zenith angles than  $j(\text{O}^1\text{D})$ .

## 1.4 Peroxy radicals and tropospheric ozone production

The OH produced as described in the previous section can then oxidize CO, CH<sub>4</sub> and other organic compounds leading to production of peroxy radicals (HO<sub>2</sub> + Σ<sub>i</sub>R<sub>i</sub>O<sub>2</sub>), thus:



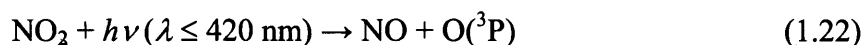
In a low NO<sub>x</sub> environment, such as the marine background troposphere, reaction with CO and CH<sub>4</sub> is the fate for the majority of OH molecules, and as such RO<sub>2</sub> is virtually all in the form of CH<sub>3</sub>O<sub>2</sub>. In a low NO<sub>x</sub> environment, peroxy radicals can contribute to ozone destruction, thus:



However, if there is NO present, it can be oxidised to NO<sub>2</sub> *via* reaction with peroxy radicals, thus



Whilst some tropospheric ozone owes its origins to stratospheric intrusion, or electrical production from lightning, the only known way of producing ozone in the troposphere is from  $\text{NO}_2$  photolysis:



$\text{NO}_2$  is emitted from sources such as fossil fuel burning, or can be produced chemically.  $\text{NO}$  can be converted into  $\text{NO}_2$  through reaction with ozone, but as this involves destruction of ozone, the result is zero net ozone production.



Consequently, as peroxy radicals enable the oxidation of  $\text{NO}$  to  $\text{NO}_2$  without the concomitant destruction of ozone, they also enable net ozone production. As a result peroxy radicals are important intermediates and chain carriers in the photochemical production of ozone. A simplified peroxy radical chain cycle showing ozone production is in Figure 1.4

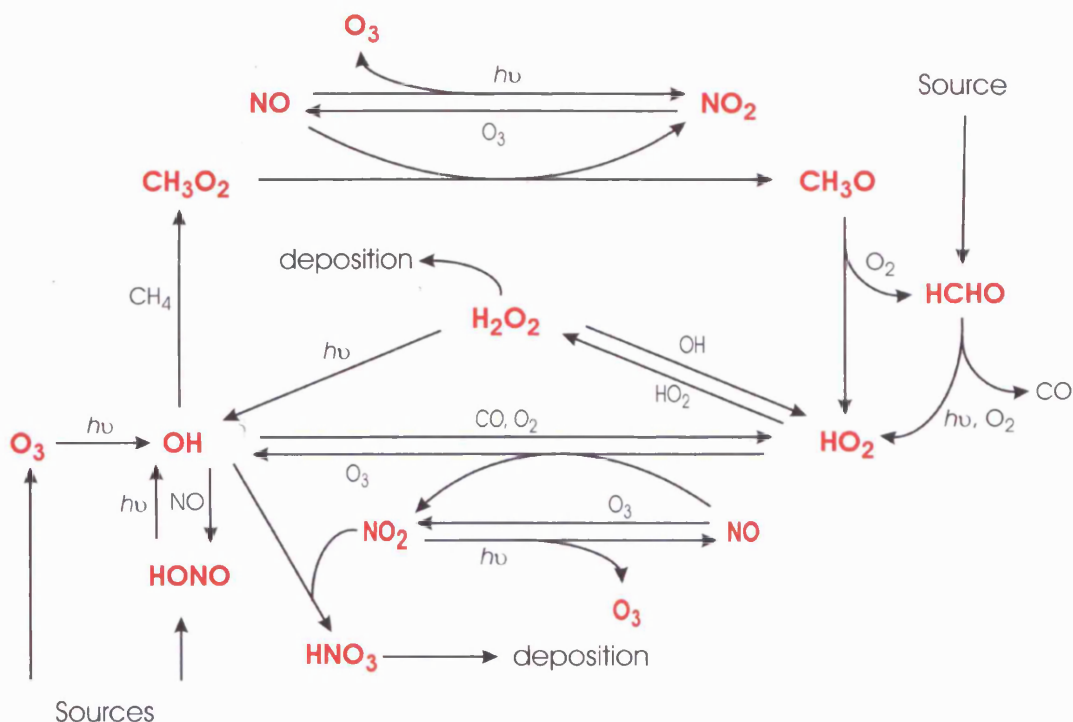


Figure 1.4 – Simplified HO<sub>x</sub> and RO<sub>x</sub> cycle showing ozone production

### 1.4.1 Additional peroxy radical sources

In addition to the reaction of OH with CO and CH<sub>4</sub> (and higher organic molecules) to form HO<sub>2</sub> and CH<sub>3</sub>O<sub>2</sub> (and other corresponding RO<sub>2</sub>) as shown in section 1.4, there are other peroxy radical production routes. Oxidation of organic compounds (especially alkenes and aldehydes) may also be initiated by reaction with NO<sub>3</sub> at night [Wayne, *et al.*, 1991]. NO<sub>3</sub> is not generally present during the day as it is rapidly photolysed, having a lifetime on the order of 5 seconds for clear sky noon-time conditions [Monks, 2005]. However, in very polluted atmospheres, daytime NO<sub>3</sub> can become important [Geyer, *et al.*, 2003], whilst the importance of production of peroxy radicals from NO<sub>3</sub>-alkene reactions has been studied in previous field work [Fleming, *et al.*, 2006b; Salisbury, *et al.*, 2001].

NO<sub>3</sub> is formed by the oxidation of NO<sub>2</sub> by O<sub>3</sub>,



and from the decomposition of  $\text{N}_2\text{O}_5$ , which is itself formed from the reaction of  $\text{NO}_2$  and  $\text{NO}_3$ :



The reaction of ozone with alkenes is another important route to peroxy radical production, especially at night [Fleming, *et al.*, 2006b; Heard, *et al.*, 2004; Salisbury, *et al.*, 2002]. Ozone undergoes an addition reaction across the double bond of an alkene to form a primary ozonide, which then quickly decomposes to form carbonyl compounds and Criegee intermediates. Criegee intermediates are produced in vibrationally excited states and as such can either undergo collisional deactivation or further dissociation to form OH,  $\text{HO}_2$  and  $\text{RO}_2$  radicals as shown below [Monks, 2005; Rickard, *et al.*, 1999; Salisbury, *et al.*, 2001].

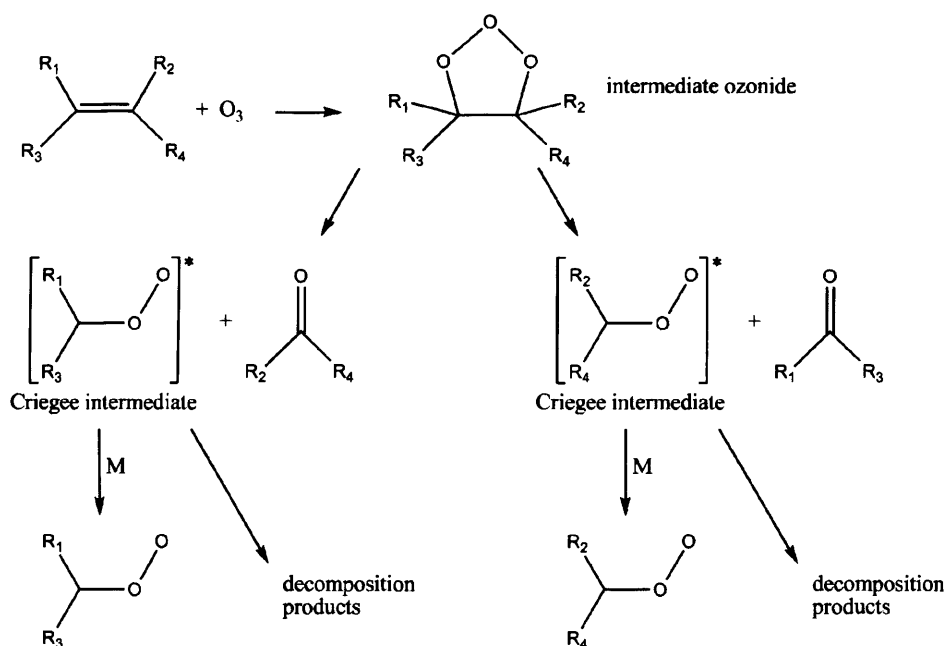
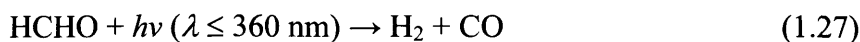
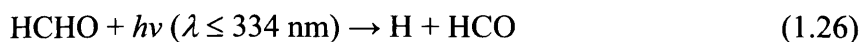


Figure 1.5 – Pathway for the ozonolysis of a generic alkene [Rickard, *et al.*, 1999].

The photolysis of other species is also relevant to peroxy radical production. Photolysis of formaldehyde as seen in Figure 1.4 can lead to production of two molecules of  $\text{HO}_2$  per molecule of  $\text{HCHO}$ , *viz*



### 1.4.2 Peroxy radical loss pathways

A major peroxy radical loss pathway is self-reaction and cross-reaction to form peroxides, thus



The peroxides formed by the above reactions can be lost altogether *via* deposition, but can also be photolysed to reform radicals, *viz*



The reaction of OH with NO<sub>2</sub> to form HNO<sub>3</sub> can also lead to significant losses of both HO<sub>x</sub> and NO<sub>x</sub> (NO + NO<sub>2</sub>) at high enough concentrations of NO<sub>2</sub>:



An additional potential peroxy radical loss route is through reaction with halogen species. In regions with enhanced concentrations of halogen species such as coastal marine sites, halogen species can have an impact on HO<sub>2</sub> and OH concentrations through the reaction of XO (X = Br, I) with HO<sub>2</sub> altering the HO<sub>2</sub>/OH partitioning.





At one such coastal marine site the reaction of IO with HO<sub>2</sub> was found to be responsible for up to 40% of the total HO<sub>2</sub> loss, and 15% of total midday OH production [Bloss, *et al.*, 2005].

### 1.4.3 Control of ozone production

As can be seen from the previous section, both NO<sub>x</sub> and Volatile Organic Compounds (VOCs) are integral to ozone production, and the balance between NO<sub>x</sub> and non-methane hydrocarbons (NMHC) is fundamental to the atmosphere's ability to produce or destroy ozone. The production or loss of ozone is a non-linear function, as demonstrated by Figure 1.6, an ozone isopleth diagram that shows the peak initial ozone production rate at different initial concentrations of NO<sub>x</sub> and VOCs.

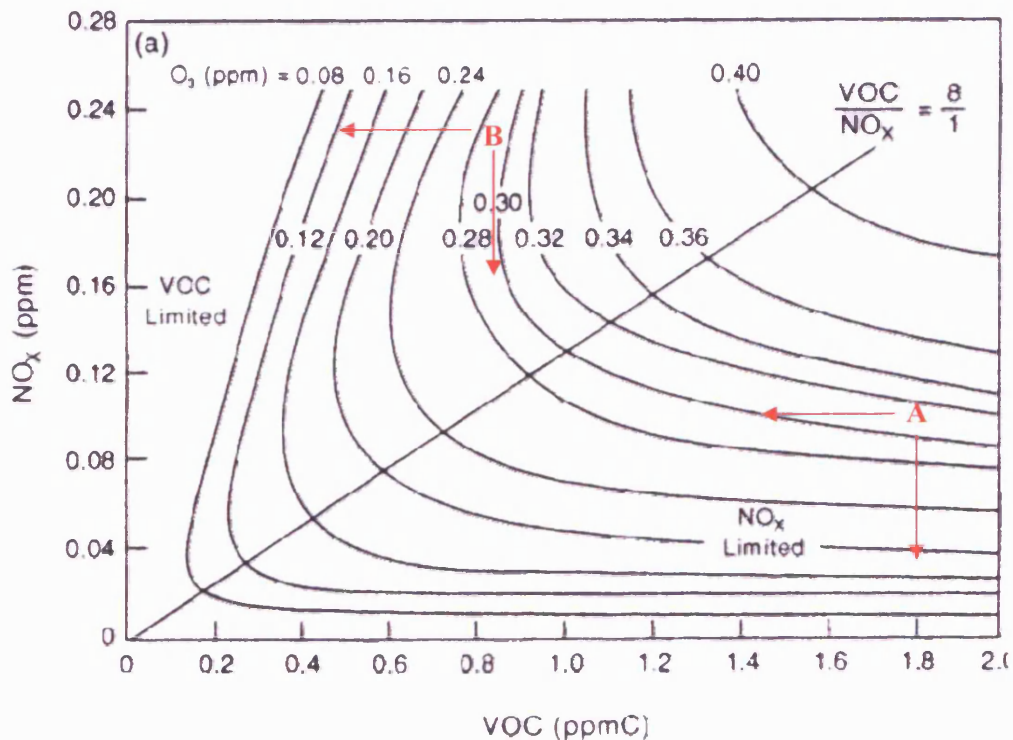


Figure 1.6 – Typical ozone isopleth [Finlayson-Pitts and Pitts, 1993]

It can be seen from Figure 1.6 that at a high VOC/NO<sub>x</sub> ratio (such as at point A), reducing the VOC concentration has very little effect on reducing ozone production, whereas reducing NO<sub>x</sub> concentration will rapidly reduce ozone production. The ozone production environment at point A is thus said to be NO<sub>x</sub> limited. However, the situation at point B is the opposite – reducing the VOC levels will rapidly reduce ozone production, whilst reducing NO<sub>x</sub> is ineffective and is therefore a VOC limited ozone production regime. Indeed, the ozone production rate may even initially rise on reducing NO<sub>x</sub> in a VOC limited regime, if the initial NO<sub>x</sub> concentration was high enough. At high concentrations of NO, ozone is removed through reaction with NO:



Ordinarily, the NO<sub>2</sub> produced in reaction 1.5 would be photolysed to produce NO and O(<sup>3</sup>P), with the O(<sup>3</sup>P) then combining with O<sub>2</sub> to reform ozone (reactions 1.22 and 1.11). However, at high levels of NO<sub>2</sub>, NO<sub>2</sub> competes with VOCs to react with OH to form nitric acid, HNO<sub>3</sub>. This has two effects, first NO<sub>2</sub> is removed without the concomitant production of ozone, and second the removal of OH disrupts the oxidation of further VOCs. Therefore, as NO<sub>x</sub> is initially lowered, these effects become less important and thus more ozone is produced. However, a further reduction in NO<sub>x</sub> results in less NO<sub>2</sub> available to be photolysed to produce ozone, and therefore the ozone production rate drops.

The point at which ozone production changes from a NO<sub>x</sub> limited regime to a VOC limited regime and *vice versa*, is often said to be approximately VOC/NO<sub>x</sub> = 8, although this can and does change depending on other conditions.

The ozone production regime one is operating in is important for pollution control strategies; the knowledge of whether a particular region is in a VOC or NO<sub>x</sub> limited ozone production regime is vital if effective pollution control mechanisms are to be put in place.

## 1.5 Long-range transport

In recent years it has been recognised that pollution is a global problem. Trace gases and aerosols can be transported over inter-continental distances [Derwent, *et al.*, 2004; Duncan and Bey, 2004; Stohl and Trickl, 1999; Wild and Akimoto, 2001]. Ozone can have a lifetime of weeks to several months in the troposphere [Liu, *et al.*, 1987], and can be transported great distances in that time. Furthermore, air masses undergoing long-range transport (LRT) consist of many ozone precursor species (such as nitrogen oxides and organic compounds) that can undergo photochemical processing as described in the previous sections of this chapter in order to produce ozone *in situ* at local sites. It is therefore not enough to put in place solely regional pollution controls, as the global transport of pollution and precursors means controls must be implemented on a worldwide scale. Transboundary transport of pollution requires a concerted global effort in order to begin to control it.

### 1.5.1 Long-range transport processes

There are three important processes related to long-range transport: frontal lifting, deep convection, and low-level transport. Frontal lifting and deep convection lift air masses into the upper troposphere where they can be transported great distances in the prevailing westerly jet streams, and subsequently descend many thousands of kilometres from the source region. This rapid vertical uplift contrasts with low-level transport, where the exported air-mass remains at lower altitudes during the transport event. Figure 1.7 summarizes these processes for transport across the Atlantic from the United States to Europe.

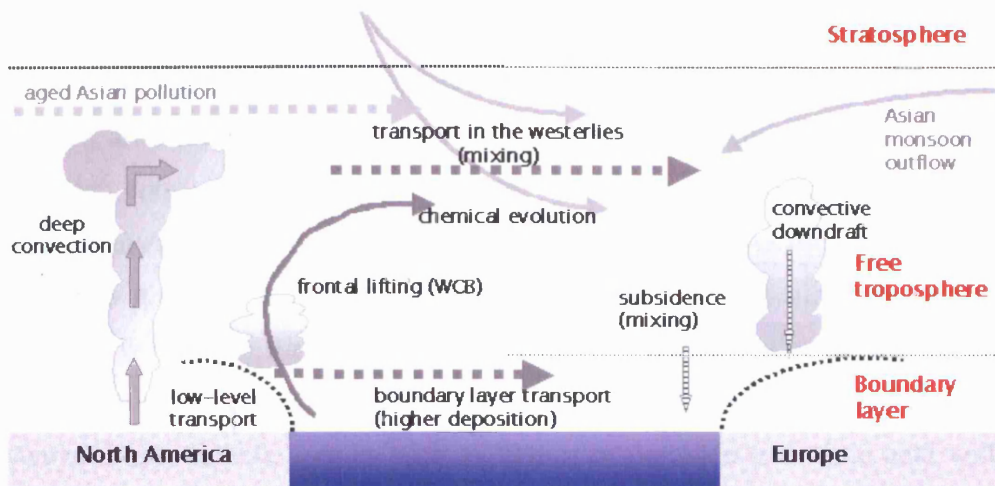


Figure 1.7 – Processes involved in long-range transport of pollution [Bey, 2004]

There are various air flows associated with frontal lifting, the most important of which is the warm conveyor belt [Cooper, *et al.*, 2007]. Warm conveyor belts form at cold or occluded frontal systems. A cold front is formed at the boundary between a warm air mass and a cold air mass, where the cold air is moving in to replace the warm air mass, as illustrated in Figure 1.8. The cold air pushes in and under the warm air mass, displacing it upwards and forming a warm conveyor belt. Warm conveyor belts can also be formed at occluded fronts, which are similar to cold fronts but occur when an existing cold front catches up with a warm front ahead of it. Frontal lifting is often associated with cyclones, with 90 – 100 % of warm conveyor belts in the northern hemisphere found within 1000 km of a cyclone centre, typically in a warm sector south of the cyclone centre [Eckhardt, *et al.*, 2004].

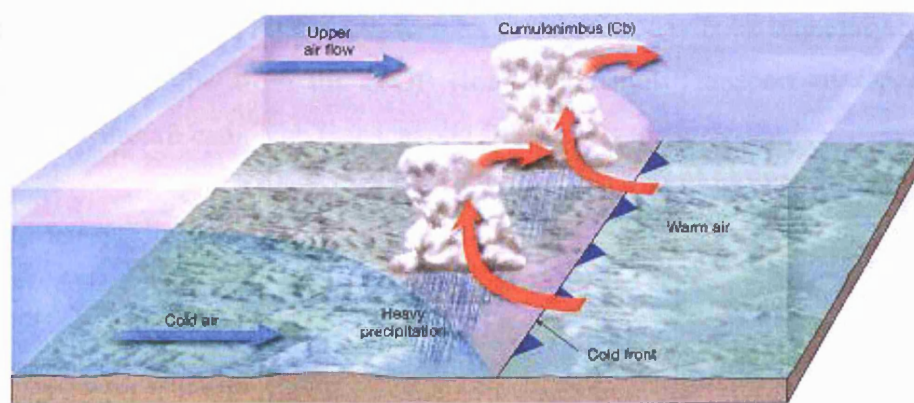
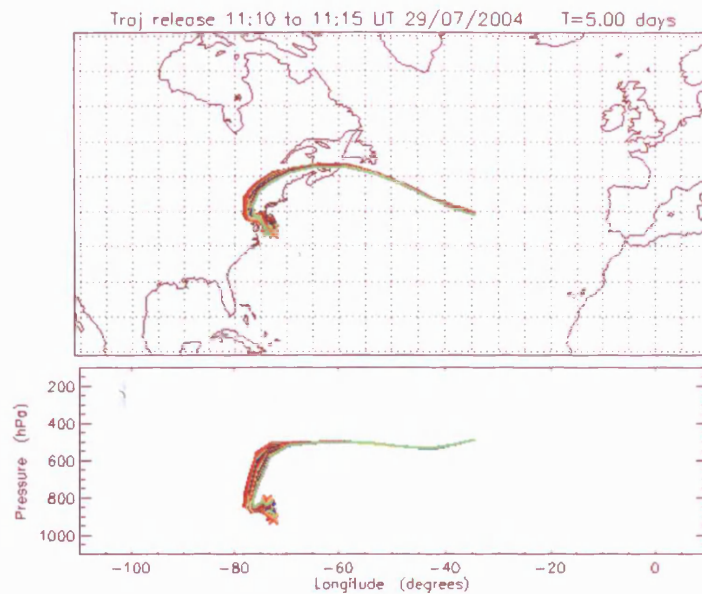


Figure 1.8 – Formation of a cold front [Short Sr., 2004]

Deep convection is the large scale convective uplift of air driven by surface heating by solar radiation. When the surface temperature is sufficiently warmer than the overhead air-mass an unstable atmosphere is formed, triggering deep convection. Both deep convection and warm conveyor belts often lead to cloud formation as they both involve the large scale uplift of warm moist air. As this warm moist air rises it undergoes adiabatic cooling and becomes saturated, at which point the water contained within the air can condense on cloud condensation nuclei, forming clouds. Owing to cloud formation, during uplift *via* deep convection and warm conveyor belts, soluble species such as hydrogen peroxide and nitric acid will be precipitated out, leaving only relatively non-soluble species such as NO<sub>x</sub> and hydrocarbons to undergo rapid vertical transport.

Once an air mass has been lifted into the upper troposphere, it can be rapidly transported great distances in the jet streams. Jet streams are winds that tend to occur between ten and fourteen kilometres above the Earth's surface, are a few hundred kilometres wide and a few kilometres thick, and can reach speeds of up to 480 km/h. Jet streams are formed by the temperature difference between two air masses, typically at northern hemisphere mid-latitudes between warm tropical air and cold polar air. The sudden change in temperature causes a large pressure difference, leading to air flows which travel along the boundary of the interface rather than across the interface owing to the Coriolis force. Jet streams are usually stronger in winter, as the temperature difference between the two air-masses tends to be greater.

An example of an air mass undergoing vertical uplifting prior to long-range transport can be seen in Figure 1.9, which shows a five day back trajectory of flight B036 on 29/07/2004 from the ITOP (Intercontinental Transport of Ozone and Precursors) aircraft campaign (see Chapter 3).



**Figure 1.9 – Five day back trajectory showing uplifting of air-mass prior to transport at high levels [Methven, 2004a].**

Air-masses can also undergo long-range transport at lower altitudes, although this transport is slower than high-level transport owing to lower wind speeds. As transport is slower, the increase in transport time for a given journey compared to high altitude transport results in increased photochemical processing and mixing of air-masses, in addition to the increased deposition (both wet and dry) experienced as a result of transport within the boundary layer or lowermost free troposphere.

## 1.5.2 Impact of long-range transport

Warm conveyor belts occur most often at mid-latitudes over the warm pools off the eastern seaboard of North America and Asia owing to the conditions experienced favouring cyclone formation [Stohl, 2001]. The eastern United States is the site of much industry, and therefore emissions, whilst Asian emissions are growing rapidly and are expected to grow further in the near future [van Aardenne, *et al.*, 1999]. The occurrence of warm conveyor belts over Europe is low, whilst most of those originating in the western Atlantic deposit their air mass over Europe [Stohl, 2001]. Seasonal and spatial distribution of WCB starting and ending points have been

calculated by [Stohl, 2001] for 1<sup>st</sup> April, 1997 to 3<sup>rd</sup> April, 1998 and are displayed in Figure 1.10 and Figure 1.11.

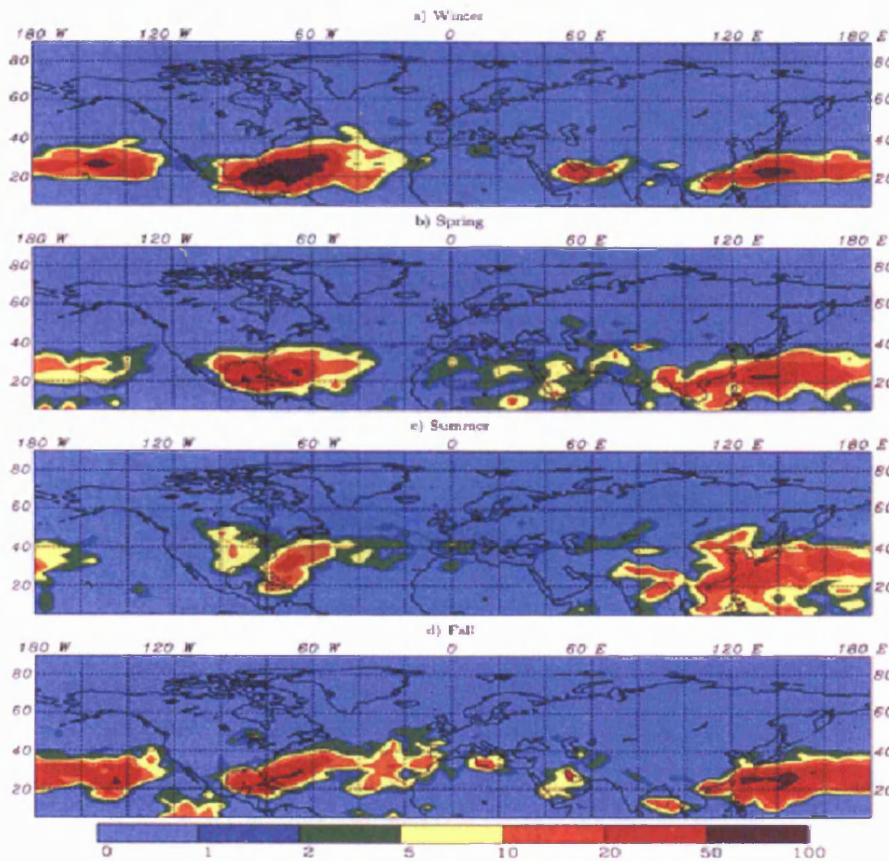


**Figure 1.10 – Seasonal and spatial distribution of WCB starting points (number per mil) starting from 500 m and 1500 m for 1<sup>st</sup> April, 1997 to 3<sup>rd</sup> April, 1998. In general, the frequency of WCBs is higher for 500 m starting point than 1500 m, but the geographical patterns are the same [Stohl, 2001].**

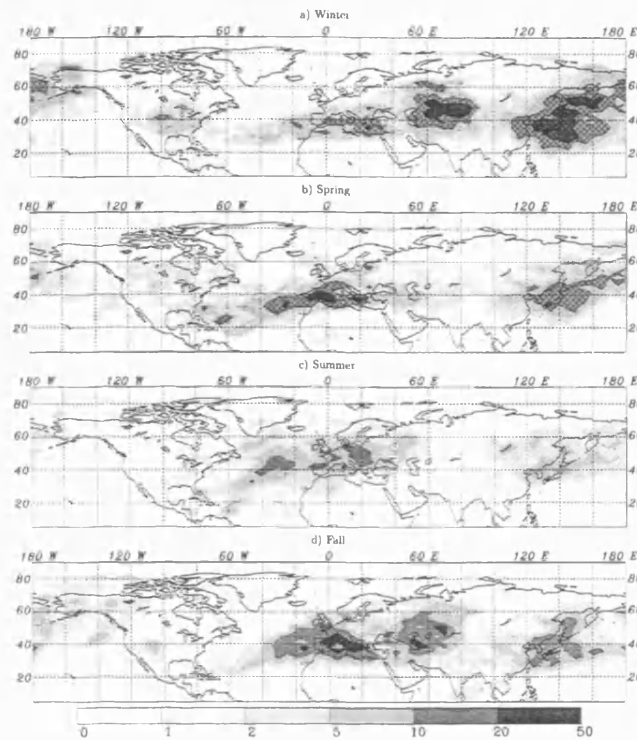


**Figure 1.11 – WCB end points (fraction per mil) between 8,500 m and 10,500 m for 1<sup>st</sup> April, 1997 to 3<sup>rd</sup> April, 1998 [Stohl, 2001].**

Deep convective uplifting can also be rapid [Prather and Jacob, 1997], and occurs worldwide [Auvray and Bey, 2005; Oshima, et al., 2004; Tulet, et al., 2002]. Large quantities of air can be uplifted in this way as demonstrated in Figure 1.12 which shows North American ozone convective flux ( $\text{kg s}^{-1}$ ) at 10 km from a GEOS-CHEM model for June and July 1997 [Auvray and Bey, 2005]. Deep convective events are most common in the summer time, and are particularly important over the south-eastern United States in summer as WCBs from midlatitude cyclones are less common at this time of year [Li, et al., 2005]. Furthermore, during summertime over land the distinction between warm conveyor belts and deep convection is difficult, as the warm conveyor belts of mid-latitude cyclones often have embedded deep convection [Cooper, et al., 2007].

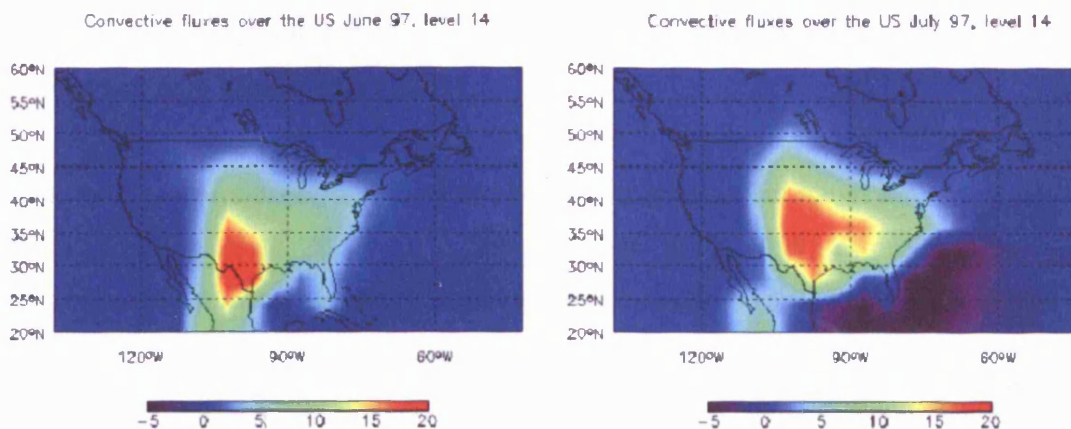


Figure 1.12 – North American ozone convective flux ( $\text{kg s}^{-1}$ ) [Auvray and Bey, 2005]

Whilst convective events can be an important mechanism of European emission transport (especially in June to August), European emissions have the strongest tendency to undergo low-level transport as the significantly lower frequency of cyclone formation (and therefore WCBs) over Europe and less vigorous convection inhibits transport by either warm conveyor belt or deep convection [Stohl, *et al.*, 2002]. Seasonal biomass burning emissions from south-east Asia undergo rapid convective vertical transport, but the major process driving the outflow of Asian pollution in spring is lifting *via* warm conveyor belts [Liu, *et al.*, 2006]. Nonetheless, deep convection is an important contributory factor for long-range transport [Auvray and Bey, 2005; Kiley and Fuelberg, 2006].

As a consequence of the longer transport time and greater deposition rate, the impact of low-level transport in terms of perturbing the air composition in regions remote from the source might be expected to be lower than for alternate transport pathways. However, recently [Liang, *et al.*, 2004] have suggested low-level outflow as an important export pathway in seasons other than spring for transpacific transport of Asian outflow whilst a model study by [Li, *et al.*, 2005] showed outflow in the boundary layer accounted for approximately 30% of the total North American CO outflow in the summers of 1998, 2000, 2001 and 2002. Low-level transport has also been shown to be responsible for most transport events of North American anthropogenic emissions to the central North Atlantic lower free troposphere during July 2003 [Owen, *et al.*, 2006], and significant enhancement of pollutants in the boundary layer and lower free troposphere were observed as a result of low-level

North American outflow during the ITOP campaign (the subject of Chapter 3) in the summer of 2004 [Lewis, *et al.*, 2007].

Long-range transport of pollution from North America to Europe at low-levels can occur [Methven, *et al.*, 2001] but is rare [Derwent, *et al.*, 1998], as ordinarily low-level transport events from North America travel south towards the Azores, whilst outflow in warm conveyor belts can result in a perturbation of background pollutant levels over mainland Europe such as ozone [Stohl and Trickl, 1999] and ozone and precursors [Stohl, *et al.*, 2003]. A series of aircraft measurements carried out in 1997 as part of the ACSOE (Atmospheric Chemistry Studies in an Oceanic Environment) project encountered many layers of polluted air between zero and eight kilometres over the North Atlantic which has been ascribed to North American outflow [Penkett, *et al.*, 2004]. Transport of boreal forest fire emissions from Canada resulting in enhanced carbon monoxide concentrations at Mace Head, Ireland in conjunction within aerosol and haze layers above Europe have been observed [Forster, *et al.*, 2001]; evidence of long-range transport of pollutants from North America to Mace Head, Ireland was also seen during an analysis of EASE '96 (East Atlantic Summer Experiment 1996) [Evans, *et al.*, 2000]. Other recent work has also shown significant chemical activity still present in air-masses that have reached Mace Head, Ireland having undergone long-range transport from North America [Heard, *et al.*, 2006]. Modelling work by [Derwent, *et al.*, 2004] has suggested that up to 20% of European surface ozone may be attributable to North American sources and work by [Auvray and Bey, 2005] has found that 11% of the summertime tropospheric ozone burden over Europe can be attributed to precursors emitted over North America. A study of transport of ozone from North America to Europe in the summer of 2000 found nine major incidents of long-range transport of ozone and related species, of which seven were associated with warm conveyor belts with the remaining two occurring at lower altitudes [Guerova, *et al.*, 2005].

It can thus be seen that the long-range transport of ozone and precursors is a very important subject in contemporary atmospheric science that requires further study on its impact on global pollution and impact on regulatory pollution controls.

### 1.5.3 Eulerian and Lagrangian frameworks

In order to study the transport of air-masses and the chemistry occurring within them, both field measurements and modelling studies are carried out. Models attempt to reproduce the chemistry and transport occurring within the atmosphere whilst field measurements constrain and test models.

Tropospheric chemistry models and experiments have traditionally used either a Eulerian or a Lagrangian approach; a Eulerian approach uses a fixed co-ordinate system through which air-masses pass relative to the observer, whilst a Lagrangian approach uses a moving co-ordinate system where the observer travels along with an air-mass. A Eulerian model divides the area of the Earth's surface of interest into a series of three dimensional cells, and then simulates advection, chemical processing, diffusion and deposition within each cell. Transport terms between cells are introduced based on meteorological parameters (e.g. modelled wind fields) in order to couple adjacent cells together. A full three dimensional Eulerian model on a small enough grid scale could ultimately completely simulate the transport of air-masses as well as all chemistry and other meteorological phenomena occurring within them, but currently the computational cost is too high. Consequently, chemical schemes contained within Eulerian models are often simplified, or models calculated only in one or two dimensions. A three dimensional model requires a set of kinetic equations to be solved for all hundreds of species and thousands of reactions contained within the model at each of many thousands of grid points, at each of which all meteorological processes must also be solved. However, with continually increasing computer power, it is becoming possible to solve ever more complex models.

Field measurements that are performed on a Eulerian basis are logistically fairly straightforward (compared to Lagrangian experiments). In an Eulerian framework observations are made from a fixed set of co-ordinates, whilst air-masses move relative to the observer. Many field campaigns have been carried out in this way, with measurements made from a specific location, with the aim of understanding local air chemistry at the measurement site.

In a Lagrangian model a cell is placed around the air-mass of interest rather than the position of interest, and allowed to move with the air-mass. Chemistry is simulated within the cell as it is allowed to move, and meteorological parameters (e.g. modelled wind fields) are used to model the motion of the cell. An advantage of the Lagrangian approach is that it is no longer necessary to have such complicated terms for input and output from the cell of interest, and thus it is computationally simpler. A Lagrangian approach allows the study of a constrained system and the photochemical processing occurring within that system. Often backward trajectories will be calculated to model the origin of air-masses that arrive at a site, and then chemistry models will be run along the trajectory to simulate the chemistry occurring during travel.

Performing Lagrangian experiments involves following a given air-mass and constantly monitoring the chemistry within it. As it is logistically virtually impossible to perform a 'full' Lagrangian experiment, instead pseudo-Lagrangian studies are performed where an air-mass is periodically measured during transport. Making multiple interceptions of one air-mass is logistically challenging, as it requires many measurement platforms (usually aircraft) with multiple crews (in order to fly back-to-back flights), in addition to the challenges in predicting the course of an air-mass as it is transported. However, studying the chemical processing occurring within an air-mass as it undergoes transport can be invaluable for learning about the processes that control the impact of pollution at a site remote from the source region.

## **1.6 Previous peroxy radical measurement campaigns**

Since peroxy radical measurements began to be performed in the mid 1980s / 1990s, there have been many field campaigns carried out around the world. These campaigns have utilised various measurement techniques, and have been performed from different platforms, such as the ground, aircraft or ships. The different measurement techniques are discussed in detail in Chapter 2.

Table 1.1 is a summary of some of these campaigns, from which it can be seen that the majority of measurements made have been from the ground and have used the PERCA and FAGE techniques. This is hardly surprising, as measurements on platforms other than ground based present many unique challenges that must be overcome, especially on aircraft platforms. Of the techniques utilised to date, MIESR is unwieldy, and CIMS is fairly new, and as such they have had less exposure.

Two of the field campaigns listed in Table 1.1 are the subject of this thesis – ITOP (Intercontinental Transport of Ozone and Precursors) in 2004, and the 2005 Jungfraujoch campaign. Other campaigns listed shall be discussed in the following chapters when relevant.

<b>Dates</b>	<b>Name</b>	<b>Location</b>	<b>Technique(s)*</b>	<b>Platform</b>	<b>Reference</b>
1990	-	Schauinsland	MIESR	Ground	[ <i>Mihelcic, et al., 1993</i> ]
1990	ROSE 1	Alabama	PERCA	Ground, Aircraft	[ <i>Frost, et al., 1998</i> ]
1991, 1992	MLOPEX 2	Mauna Loa, Hawaii	PERCA	Ground	[ <i>Cantrell, et al., 1997a</i> ; <i>Cantrell, et al., 1996c</i> ]
1993	FIELDVOC	Brittany, France	PERCA	Ground	[ <i>Cantrell, et al., 1996a</i> ]
1993	TOHPE	Idaho Hill, Colorado	PERCA, FAGE	Ground	[ <i>Cantrell, et al., 1997b</i> ]
1994, 1995	WAO-TIGER	Weybourne, Norfolk	PERCA	Ground	[ <i>Carpenter, et al., 1998</i> ; <i>Carslaw, et al., 1997</i> ; <i>Clemmitshaw, et al., 1997</i> ; <i>Penkett, et al., 1999</i> ]
1995	SOAPEX I	Cape Grimm, Tasmania	PERCA, FAGE	Ground	[ <i>Carpenter, et al., 1997</i> ; <i>Monks, et al., 1996</i> ; <i>Monks, et al., 1998</i> ; <i>Monks, et al., 2000</i> ; <i>Penkett, et al., 1997</i> ]

1995	ATAPEX	Mace Head, Ireland	PERCA	Ground	[ <i>Carpenter, et al., 1997</i> ]
1996	SUCCESS	Kansas, USA	FAGE, CIMS	Aircraft	[ <i>Brune, et al., 1998; Jaeglé, et al., 1998; Reiner, et al., 1997; Reiner, et al., 1999</i> ]
1996	ALBATROSS	Atlantic Ocean	PERCA	Ship	[ <i>Burkert, et al., 2001</i> ]
1996, 1997	ACSOE- EASE	Mace Head, Ireland	PERCA, FAGE	Ground	[ <i>Carslaw, et al., 2002; Carslaw, et al., 1999; Creasey, et al., 1997; Salisbury, et al., 2002; Salisbury, et al., 2001</i> ]
1996, 1998, 2001	FREETEX	Jungfrauoch, Switzerland	PERCA	Ground	[ <i>Zanis, et al., 2003; Zanis, et al., 2000a; Zanis, et al., 1999</i> ]
1997	SONEX	North Atlantic	FAGE	Aircraft	[ <i>Brune, et al., 1999; Faloona, et al., 2000; Jaeglé, et al., 2000; Jaeglé, et al., 1999</i> ]
1998	BERLIOZ	Berlin, Germany	PERCA, FAGE, MIESR	Ground	[ <i>Geyer, et al., 2003; Holland, et al., 2003; Mihelcic, et al., 2003; Volz-Thomas, et al., 2003</i> ]
1997, 1998	PROPHET	Michigan	PERCA	Ground	[ <i>Mihele and Hastie, 2003; Tan, et al., 2001b</i> ]
1999	SOAPEX II	Cape Grimm, Tasmania	PERCA, FAGE	Ground	[ <i>Haggerstone, et al., 2005b; Salisbury, 2001; Sommariva, et al., 2004</i> ]

1999	AEROSOLS 99	Atlantic and Southern Indian oceans	PERCA	Ship	[ <i>Andrés Hernández, et al., 2001</i> ]
1999	PEM-Tropics B	Pacific Ocean	FAGE	Aircraft	[ <i>Ravetta, et al., 2001; Tan, et al., 2001a</i> ]
1998, 1999	INDOEX	Indian Ocean	PERCA	Ship	[ <i>Burkert, et al., 2003</i> ]
2000	ISCAT	Antarctica	CIMS	Ground	[ <i>Mauldin III, et al., 2004</i> ]
2000	TOPSE	Colorado – Canada	CIMS	Aircraft	[ <i>Cantrell, et al., 2003a; Cantrell, et al., 2003c; Stroud, et al., 2004</i> ]
2000	HOPE	Hohenpeisse nberg, Germany	PERCA	Ground	[ <i>Handisides, et al., 2003</i> ]
2001	TRACE-P	Pacific	CIMS	Aircraft	[ <i>Cantrell, et al., 2003b</i> ]
		U.K.	PERCA	Aircraft	[ <i>Green, et al., 2003</i> ]
2002	-	Pennsylvania	LIF, CIMS	Ground	[ <i>Ren, et al., 2003</i> ]
2002	WAOWEX	Weybourne, Norfolk	PERCA	Ground	[ <i>Fleming, et al., 2006a</i> ]
2002	NAMBLEX	Mace Head, Ireland	PERCA, FAGE	Ground	[ <i>Bloss, et al., 2005; Fleming, et al., 2006b; Smith, et al., 2006</i> ]
2002	INSPECTRO	Weybourne, Norfolk	PERCA	Ground	[ <i>Fleming, et al., 2006a</i> ]
2003	TORCH I	Writtle, Essex	PERCA, FAGE	Ground	[ <i>Emmerson, et al., 2007; Lee, et al., 2006</i> ]
2004	TORCH II	Weybourne, Norfolk	PERCA, FAGE	Ground	Not yet published
2004	ITOP	Azores	PERCA, FAGE	Aircraft	This thesis, [ <i>Parker, et al., 2007</i> ]
2005	-	Jungfrauoch, Switzerland	PERCA	Ground	In this thesis
2005	CHABLIS	Halley, Antarctica	PERCA, FAGE	Ground	[ <i>Bloss, et al., 2007</i> ]

2006	MIRAGE	Veracruz, Mexico	CIMS	Aircraft	Not yet published
2006	TEXAQS	Gulf of Mexico	PERCA	Ship	Not yet published
2006	INTEX-B	Seattle, Washington	CIMS	Aircraft	Not yet published
2006	AMMA	Niamey, Niger	PERCA, FAGE	Aircraft	Not yet published
2007	OOMP	Chile – Reunion	PERCA, FAGE	Ship	Not yet published

**Table 1.1 – Summary of some previous field campaigns to have measured peroxy radicals. \*Measurement techniques are discussed in detail in Chapter 2.**

## 1.7 Summary

This chapter has provided an overview of the atmosphere and long-range transport, focussing on the importance of photochemistry and peroxy radicals in particular with respect to tropospheric ozone production. The impact of long-range transport on the global transport of pollution and precursors and consequently the effect on air quality in regions remote from a pollution source has been discussed, as well as different types of long-range transport and how they come about.

Chapter 2 focuses on the experimental aspect of measuring peroxy radicals with particular emphasis on the Peroxy Radical Chemical Amplification (PERCA) method that has been used to take all peroxy radical measurements presented in this thesis.

Chapter 3 is an in depth study on the peroxy radicals, ozone production and long-range transport encountered during the Intercontinental Transport of Ozone and Precursors (ITOP) field campaign that took place during July and August of 2003. Peroxy radicals were measured (in addition to other species) on board the UK Met Office/Natural Environment Research Council (UKMO/NERC) BAe 146-300 atmospheric research aircraft in order to study the chemical processing of air-masses as they underwent long-range transport across the Atlantic.

Chapter 4 is concerned with work carried out during August and September 2005 at the High Alpine Research Station on the Jungfraujoch in the Swiss Alps. This work aimed at investigating the role of *in-situ* photochemistry in controlling the composition of the summer European free troposphere and the effect of long-range transport on free tropospheric chemistry.

Chapter 5 describes work undertaken at the atmospheric simulation chamber at the Paul Scherrer Institut in Switzerland. Peroxy radical measurements were taken alongside a suite of other gas and aerosol phase measurements in order to study the formation of Secondary Organic Aerosol (SOA) from gas phase initiation.

Finally, Chapter 6 draws the thesis together, summarising the previous chapters and making suggestions for profitable areas of further research.

# Chapter 2

## Peroxy Radical Measurement Techniques

The work in this chapter describes the different methods for measuring peroxy radicals deployed today, with specific focus on the University of Leicester Peroxy Radical Chemical Amplifier (PERCA) instrument used to take all the peroxy radical measurements described in this thesis.

### 2.1 The PERCA technique

The Chemical Amplification technique was introduced by Cantrell in the early 1980's [Cantrell and Stedman, 1982; Cantrell, *et al.*, 1984] and has been widely deployed since then [Cantrell, *et al.*, 1993a; Green, *et al.*, 2006; Mihele and Hastie, 2003; Monks, *et al.*, 1998; Zanis, *et al.*, 2000a], although there is only one previous publication on aircraft measurements using the technique [Green, *et al.*, 2003]. Details of previous deployments are given in Table 1.1, which summarizes previous measurement campaigns during which peroxy radical measurements have been performed, including those performed with the PERCA technique.

In general, the PERCA technique utilises the HO<sub>2</sub> radical catalysed conversion of NO and CO into NO<sub>2</sub> and CO<sub>2</sub> respectively *via* addition of NO (3 ppmv) and CO (6% v/v) to the inlet region.



Organic peroxy radicals (RO<sub>2</sub>) are also detected by the PERCA technique as they are converted into HO<sub>2</sub> within the inlet region.



There is however a complication in the measurement of RO<sub>2</sub>, in that the efficiency of conversion of RO<sub>2</sub> into HO<sub>2</sub> is dependent on the structure and size of the organic group [Ashbourn, *et al.*, 1998; Clemitshaw, *et al.*, 1997]. Under the inlet conditions present in normal operating mode (3 ppmv NO), the chain propagation reactions ((2.5) and (2.6)) occur along with competing reactions of RO<sub>2</sub> and RO to form organic nitrates and nitrites:



Nonetheless, for structurally simple organic groups the conversion efficiency of RO<sub>2</sub> to HO<sub>2</sub> remains relatively high, e.g. 0.85 for CH<sub>3</sub>O<sub>2</sub> [Clemitshaw, *et al.*, 1997].

The yield of NO<sub>2</sub> and CO<sub>2</sub> produced from the inlet chemistry described above is equal to CL \* [HO<sub>2</sub> + Σ<sub>*i*</sub>R<sub>*i*</sub>O<sub>2</sub> + OH], where CL is the chain length, the number of HO<sub>2</sub>/OH conversion cycles that occur before termination. However, as the concentration of OH in the lower troposphere is much lower than that of HO<sub>2</sub> and RO<sub>2</sub> [Mather, *et al.*, 1997], the yield of NO<sub>2</sub> and CO<sub>2</sub> may be said to be given by CL \* [HO<sub>2</sub> + Σ<sub>*i*</sub>R<sub>*i*</sub>O<sub>2</sub>].

The NO<sub>2</sub> produced is subsequently detected *via* aqueous luminol II (5-amino-2,3-dihydro-1,4-phthalazinedione) solution chemiluminescence at λ = 424 nm with an improved LMA-3 detector as described by [Green, *et al.*, 2006]. Consequently the concentration of peroxy radicals measured is given by:

$$[\text{HO}_2 + \Sigma_i \text{R}_i \text{O}_2] = \Delta \text{NO}_2 / \text{CL} \quad (2.9)$$

The PERCA technique has been used to take all peroxy radical measurements reported in this thesis, and the University of Leicester PERCA instrument and operation shall be described in greater detail in section 2.6.

### **2.1.1 Peroxy Radical Chemical Amplification – Laser Induced Fluorescence (PERCA-LIF)**

A variation on the PERCA technique been recently developed by [*Sadanaga, et al., 2004*] in Japan that works on the same principle as the PERCA technique outlined above with the exception of the method of NO<sub>2</sub> detection. Instead of utilising luminol chemiluminescence to detect NO<sub>2</sub>, it is detected *via* laser induced fluorescence (LIF). This is intended to give greater sensitivity than the ‘traditional’ PERCA technique. However, whilst a detection limit on the order of 3 pptv has been quoted [*Sadanaga, et al., 2004*], no accuracies have been reported for this technique, and the use of cumbersome and expensive laser systems remove some of the advantages of PERCA, specifically that it is reliable, portable and moderately inexpensive. However, it is early days for PERCA-LIF, and it is possible that in the future it may become an important tool.

## **2.2 Matrix Isolation Electron Spin Resonance (MI-ESR)**

Matrix Isolation Electron Spin Resonance (MI-ESR) was pioneered by [*Mihelcic, et al., 1978*]. MI-ESR is a highly sensitive technique that uniquely allows some speciation of peroxy radicals. HO<sub>2</sub>, CH<sub>3</sub>C(O)O<sub>2</sub> and sum of alkyl peroxy radicals can be measured by isolating an air sample in a D<sub>2</sub>O matrix at 77K then running a series of electron spin resonance scans on the matrix which are then averaged to improve the signal-to-noise ratio. MI-ESR has a collection efficiency of (90 ± 10)% and a detection limit of about 20 pptv [*Mihelcic, et al., 1985*], and in principle

allows complete detection of all radicals trapped in the matrix. Another advantage of MI-ESR is the ability to simultaneously also measure  $\text{NO}_2$  and  $\text{NO}_3$  [Mihelcic, et al., 1993].

MI-ESR does have major drawbacks for the measurement of peroxy radicals in the atmosphere. The requirement for a long sampling time (20-30 minutes) in order to achieve adequate sensitivity means that the technique is unsuited to aircraft measurements or in regimes with a quickly changing background. The sampling is carried out at 77K and requires large amounts of liquid  $\text{N}_2$ . The sampled matrix is then required to be kept at 77K and under vacuum until it can be returned to the laboratory for scanning.

MI-ESR has been deployed on various field campaigns in past years, such as described in [Mihelcic, et al., 1993], and during the BERLIOZ (Berlin Ozone Experiment) campaign [Mihelcic, et al., 2003], where peroxy radical measurements were also made via PERCA [Volz-Thomas, et al., 2003] and Laser Induced Fluorescence (LIF) [Holland, et al., 2003].

### 2.3 Fluorescence Assay by Gas Expansion (FAGE)

The Fluorescence Assay by Gas Expansion (FAGE) technique measures OH and  $\text{HO}_2$ , but not currently  $\text{RO}_2$ , and was pioneered by Hard and O'Brien in the 1980's [Hard, et al., 1984]. Ambient air is expanded through a pinhole into a low-pressure expansion chamber where OH is measured by Laser Induced Fluorescence (LIF). The expansion chamber is held at approximately 1 mbar, and the OH is promoted from the ground electronic state,  $X^2\Pi$ , into the first excited electronic state,  $A^2\Sigma$ , by laser excitation at 308 nm. At reduced pressure, the fluorescence lifetime of OH is increased so that it becomes possible to detect the very small OH fluorescence signal (also at 308 nm) against the much more intense scattered exciting light by use of delayed-gated photon counting [Creasey, et al., 1998].

In order to measure HO<sub>2</sub>, ambient air is expanded into a low-pressure reaction chamber and reacted with excess NO to form OH (and NO<sub>2</sub>). The OH produced is subsequently measured as before. The conversion of RO<sub>2</sub> into HO<sub>2</sub> *via* reaction with NO and subsequently O<sub>2</sub> (as utilised by PERCA) does not significantly occur as the reaction of RO with O<sub>2</sub> to form HO<sub>2</sub> is too slow at the pressures present in the expansion chamber. FAGE has a typical detection limit for OH of 0.006 pptv and 0.004 – 0.04 pptv for HO<sub>2</sub> with a typical integration time of 30s and an accuracy of around ±30% [*Heard and Pilling, 2003*].

Development of the FAGE technique is currently underway in a number of groups worldwide to enable detection of RO<sub>2</sub> in addition to HO<sub>2</sub>. This requires the reaction cell to be held at a higher pressure than is used for HO<sub>2</sub> measurements, as the conversion of RO into HO<sub>2</sub> by reaction with oxygen does not occur fast enough at the lower pressures. However, there are problems involved with increasing the pressure of the reaction cell as it leads to large OH losses and therefore measurement difficulties. Nonetheless, the first reports of the measurement of RO<sub>2</sub> by the FAGE technique using a pre-reaction chamber to convert RO<sub>2</sub> into HO<sub>2</sub>, followed by further expansion into a secondary chamber at lower pressure, have recently been published [*Fuchs, 2006*]. The reported detection limit of 0.1 to 0.3 pptv for an integration time of 30 s and a signal-to-noise ratio of 2, are impressive and with further development FAGE could become an important RO<sub>2</sub> measurement technique.

The FAGE technique has been widely used in recent years for atmospheric field measurements, from both ground and airborne platforms [*Brune, et al., 1998; Brune, et al., 1999; Faloona, et al., 2000; Holland, et al., 2003; Ravetta, et al., 2001; Smith, et al., 2006; Tan, et al., 2001a*] (see also Table 1.1).

## 2.4 Peroxy radical Chemical Ionisation Mass Spectrometry (PerCIMS)

Peroxy Radical Chemical Ionisation Mass Spectrometry (PerCIMS) is very similar to Ion Molecule Reaction – Mass Spectrometry (IMR-MS) [Reiner, *et al.*, 1997] and ROXMAS (RO<sub>x</sub> Mass Spectrometry) [Hanke, *et al.*, 2002]. The technique involves chemical amplification and conversion of peroxy radicals to gaseous sulphuric acid according to the following scheme [Reiner, *et al.*, 1997].



Under atmospheric conditions, HSO<sub>3</sub> reacts rapidly with oxygen thus



and consequently HO<sub>2</sub> is reformed to continue the cycle. The SO<sub>3</sub> produced from reaction (2.12) forms H<sub>2</sub>SO<sub>4</sub> *via* reaction with water, thus



H<sub>2</sub>SO<sub>4</sub> is detected by CIMS as the stable anion HSO<sub>3</sub><sup>-</sup> following NO<sub>3</sub><sup>-</sup> induced hydrogen abstraction. As the background atmospheric concentration of H<sub>2</sub>SO<sub>4</sub> is low ( $\approx 10^7$  molecules cm<sup>-3</sup> [Eisele and Tanner, 1993]), only a short chain length is required to produce H<sub>2</sub>SO<sub>4</sub> concentrations exceeding those routinely present in the atmosphere. In practice, <sup>34</sup>SO<sub>2</sub> is used in order to produce a much larger concentration difference over that which is found naturally in the atmosphere.

Recent developments [Edwards, *et al.*, 2003; Hanke, *et al.*, 2002] have reported speciation of HO<sub>2</sub> and Σ<sub>i</sub>R<sub>i</sub>O<sub>2</sub> by varying the concentration of NO. If a much higher than standard concentration of NO is used then the conversion of RO (formed *via*

reaction of RO<sub>2</sub> with NO) to HO<sub>2</sub> *via* reaction with oxygen has to compete with the formation of RONO thus



Consequently the measurement efficiency of RO<sub>2</sub> becomes much smaller relative to HO<sub>2</sub> (approximately 10%, [Edwards, *et al.*, 2003]) and therefore to within a stated error, the response of the instrument can be said to be down to HO<sub>2</sub> only. By alternating between the standard HO<sub>x</sub>RO<sub>x</sub> mode and HO<sub>2</sub> mode it is possible to obtain separate HO<sub>2</sub> and Σ<sub>i</sub>R<sub>i</sub>O<sub>2</sub> measurements by difference between the measured quantities of HO<sub>2</sub> and HO<sub>2</sub> + Σ<sub>i</sub>R<sub>i</sub>O<sub>2</sub>. It is also possible to measure OH *via* the CIMS technique by utilising the above scheme but without the presence of NO [Clemishaw, 2004] and references therein. CIMS is estimated to have a detection limit of the order of < 0.4 pptv and an accuracy of 35 – 41%, with a precision of 10%.

In common to the PERCA and FAGE techniques, CIMS instruments have been deployed many times in recent years for atmospheric measurements [Cantrell, *et al.*, 2003a; Cantrell, *et al.*, 2003b; Cantrell, *et al.*, 2003c; Mauldin III, *et al.*, 2004; Stroud, *et al.*, 2004].

## 2.5 Proton Transfer Mass Spectrometry (PTr-MS)

Proton Transfer Mass Spectrometry (PTr-MS) is a recent development for measuring peroxy radicals, but is an established technique for measuring numerous organic compounds in the atmosphere [de Gouw and Warneke, 2007; Wyche, *et al.*, 2007a]. Briefly, protonated water clusters are produced in an ion source, frequently by using a radioactive alpha source (such as <sup>241</sup>Am) or an electric discharge in combination with water vapour. A proton is then transferred to the analyte molecule if it has a proton affinity higher than that of water:



Recently progress has been made on detecting peroxy radicals with this technique [Hanson, *et al.*, 2004]. Relatively low electric fields and high pressures have been used within the instrument compared to traditional PTR-MS, leading to the formation of large water clusters  $\text{H}^+(\text{H}_2\text{O})_n$  as opposed to the majority  $\text{H}_3\text{O}^+$  that would be formed at lower pressures and higher electric fields.

This technique can give good sensitivity ( $\sim 1$  pptv) and excellent speciation, but is not currently suitable for atmospheric detection of peroxy radicals as interference from other atmospheric species would likely overwhelm the signal obtained from peroxy radicals. The sensitivity also is affected by water vapour concentrations. However, it is possible that this technique may become more important in the future if more specific ionization can be carried out.

A summary of the major atmospheric peroxy radical measurement techniques is given in Table 2.1.

Technique	Errors	Detection Limit	Sampling Time	Pros	Cons
PERCA (sum of HO <sub>2</sub> + Σ <sub>i</sub> R <sub>i</sub> O <sub>2</sub> )	~ ± 40%	1 pptv	1 minute	Relatively inexpensive, portable, reliable, reasonable sensitivity	Indirect, sum of HO <sub>2</sub> + RO <sub>2</sub> measured
FAGE (OH, HO <sub>2</sub> )	~ ± 30%	0.006 pptv (OH) and 0.004 – 0.04 pptv (HO <sub>2</sub> )	30 seconds	Separate OH and HO <sub>2</sub> measurements, excellent sensitivity	Requires calibration, no RO <sub>2</sub> (yet), expensive, complicated
PerCIMS (HO <sub>2</sub> , Σ <sub>i</sub> R <sub>i</sub> O <sub>2</sub> )	~ ± 40%	< 0.4 pptv	15 seconds	Some separation of HO <sub>2</sub> and RO <sub>2</sub> , good sensitivity	Indirect
MIESR (HO <sub>2</sub> , CH <sub>3</sub> C(O)O <sub>2</sub> , Σ <sub>a</sub> R <sub>a</sub> O <sub>2</sub> )	~ ± 5%	20 pptv	20 – 30 minutes	Small errors, allows some speciation, direct technique	Long sampling time, poor sensitivity, lab analysis and cumbersome required.

Table 2.1 – Comparison of major atmospheric peroxy radical measurement techniques. <sup>a</sup>Alkyl peroxy radicals.

## 2.6 The University of Leicester dual-channel

### PERCA

The University of Leicester dual-channel PERCA makes use of the same chemistry outlined in section 2.1 in order to convert NO into NO<sub>2</sub> and CO into CO<sub>2</sub> *via* peroxy radical catalysed conversion, with subsequent NO<sub>2</sub> detection. However, in addition to the NO<sub>2</sub> detected as a result of conversion of NO to NO<sub>2</sub>, a significant NO<sub>2</sub> signal is also observed both directly from measurement of atmospheric NO<sub>2</sub> and the reaction of ozone and NO:



The total  $\text{NO}_2$  measured by the detector is therefore due to peroxy radical conversion, background  $\text{NO}_2$ , and  $\text{NO}_2$  from the oxidation of  $\text{NO}$  by ozone. Assuming a chain length of 100 (*i.e.* each radical molecule produces 100 molecules of  $\text{NO}_2$ ) and a radical concentration of 20 pptv, the radical chain cycle would produce 2 ppbv of  $\text{NO}_2$ . Under polluted atmospheric conditions, ambient ozone alone could contribute up to or over 100 ppbv of  $\text{NO}_2$ . Consequently, it is necessary to periodically measure only the background  $\text{NO}_2$  produced by means other than peroxy radical conversion.

In order to measure the background  $\text{NO}_2$  contribution, the measurements are modulated so that periods of amplification of the radical signal are alternated with periods where the radical signal is allowed to terminate in the inlets, and thus only ambient ozone and  $\text{NO}_2$  are measured. In amplification mode, the  $\text{NO}$  and  $\text{CO}$  reagent gases are injected into the inlet at the same position, close to where the ambient air is drawn in. In background or termination mode, measurement modulation is achieved by injecting  $\text{CO}$  downstream of the  $\text{NO}$  injection point in the inlet.  $\text{OH}$  produced as a result of reaction (2.1) cannot be recycled into  $\text{HO}_2$  as reactions (2.2) and (2.3) do not take place, and instead some  $\text{OH}$  reacts with  $\text{NO}$  in a chain termination step (reaction (2.11)), whilst  $\text{HO}_2$  is lost to the walls and through reaction with  $\text{NO}_2$ .



A flow of inert gas (nitrogen) is added in place of the  $\text{CO}$  so that in amplification mode  $\text{NO}$  and  $\text{CO}$  are injected upstream of  $\text{N}_2$ , and in background mode  $\text{NO}$  and  $\text{N}_2$  are injected upstream of  $\text{CO}$ . The  $\text{N}_2$  flow ensures that the properties of the sample gas flow remain unchanged in both operation modes. It also helps reduce pressure pulsing in the detected signal and allows the flows to settle again more quickly after switching.

The amplification and background cycles are summarised in Figure 2.1, whilst Figure 2.2 is an illustration showing injection of reagent gases into inlets in amplification and background modes [Jacob, 2005a]. Figure 2.3 shows examples of the  $\text{NO}_2$  modulations obtained during the work described in Chapter 3.

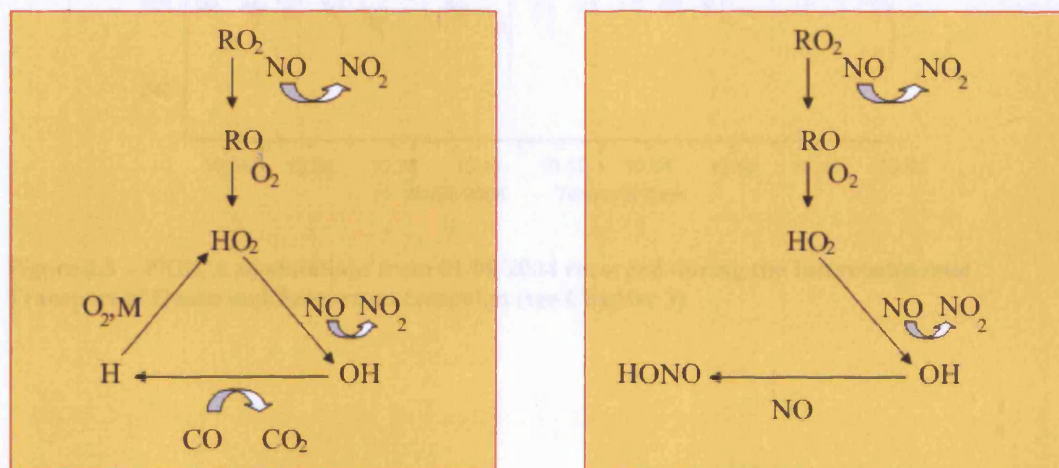


Figure 2.1 – Summary of amplification and background cycles for the PERCA technique

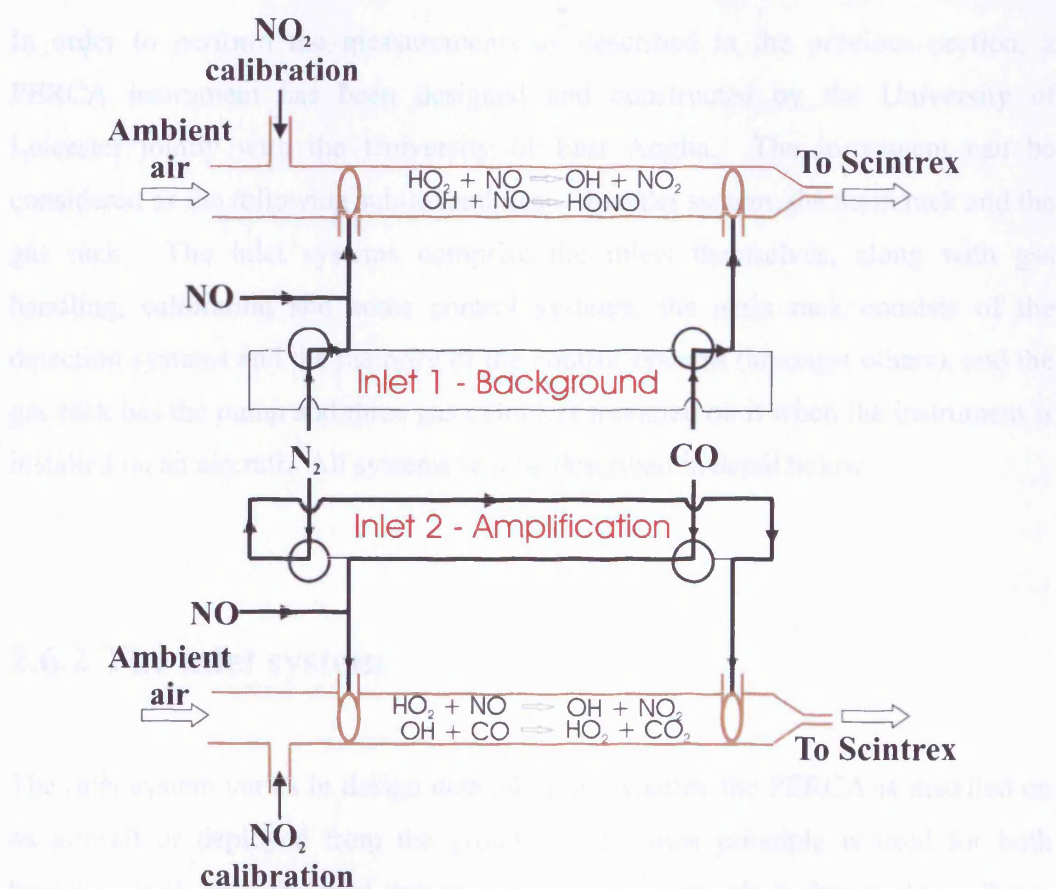


Figure 2.2 – Illustration showing injection of reagent gases into inlets in amplification and background modes [Jacob, 2005a]

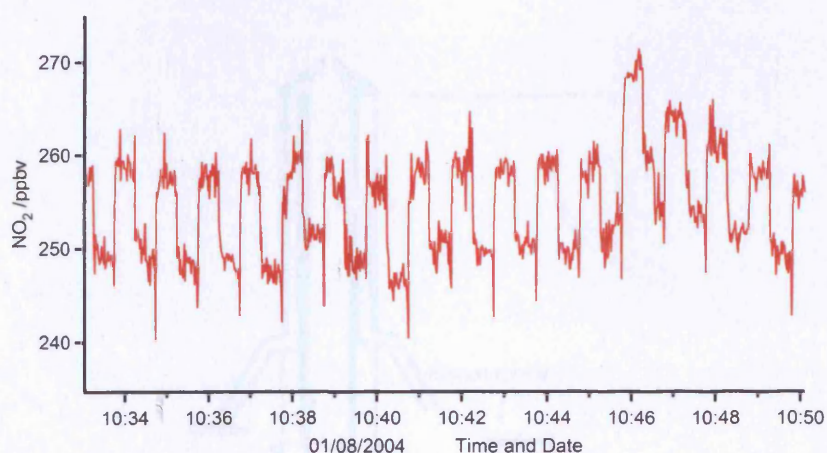


Figure 2.3 – PERCA modulations from 01/08/2004 recorded during the Intercontinental Transport of Ozone and Precursors campaign (see Chapter 3)

### 2.6.1 Instrument description

In order to perform the measurements as described in the previous section, a PERCA instrument has been designed and constructed by the University of Leicester jointly with the University of East Anglia. The instrument can be considered as the following sub-assemblies – the inlet system, the main rack and the gas rack. The inlet systems comprise the inlets themselves, along with gas handling, calibration and some control systems, the main rack consists of the detection systems and the majority of the control systems (amongst others), and the gas rack has the pump and three gas cylinders mounted on it when the instrument is installed on an aircraft. All systems will be described in detail below.

### 2.6.2 The inlet system

The inlet system varies in design depending on whether the PERCA is installed on an aircraft or deployed from the ground. The same principle is used for both however, with only the inlet design varying. Ambient air is drawn into a Pyrex inlet, an example of an aircraft inlet is shown in Figure 2.4.

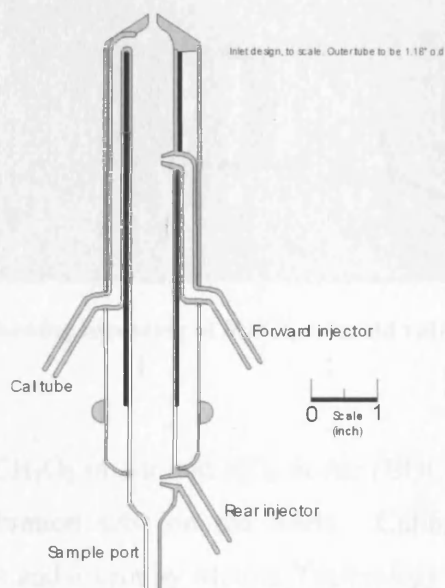


**Figure 2.4 – Pyrex inlet as used on the aircraft PERCA [Green, 2003]**

When the system is in amplification mode, NO and CO are injected *via* the forward injector, whilst N<sub>2</sub> is injected *via* the rear injector. Thus the amplification cycle outlined in Figure 2.1 occurs. When the system is in background mode, the CO and N<sub>2</sub> injection points are switched so that NO and N<sub>2</sub> are flowed into the forward injector and CO is injected *via* the rear injector. In this way the properties of the sample gas flow remain unchanged in the two different modes of operation.

Switching between the two modes is achieved with a Swagelok series 40 ball valve (SS-43YF2) that is turned by a Whitey 131 series pneumatic actuator (MS-131-31DA), fired by nitrogen (BOC, O<sub>2</sub> free) at 100 psi controlled with a Mac PME-501CAA solenoid. Gas flows are controlled with Mykrolis FC-260 mass flow controllers (MFCs) and supply 10 sccm NO in N<sub>2</sub> (600 ppmv NO in N<sub>2</sub>, Messer, certified  $\pm 2\%$ ), 100 sccm CO (Messer, 99.9%) and 100 sccm N<sub>2</sub> (BOC, zero grade). These units are mounted on the MFC tray, shown in Figure 2.5. This results in 3 ppmv NO and 6% v/v CO being injected into the inlet region.



Figure 2.5 – MFC tray showing mounting of MFCs, solenoid valve and pneumatic actuator

Calibration flows of  $\text{CH}_3\text{O}_2$  in Air and  $\text{NO}_2$  in Air (BOC, BTCA 178 grade) can be injected *via* the calibration tube on the inlets. Calibration flows are switched between the two inlets and a vent by Metron Technology 203-3414 series three-way valves and Parker series 9 three-way valves. The calibration system is described in detail later. Figure 2.6 shows a schematic diagram of the inlet system gas plumbing.

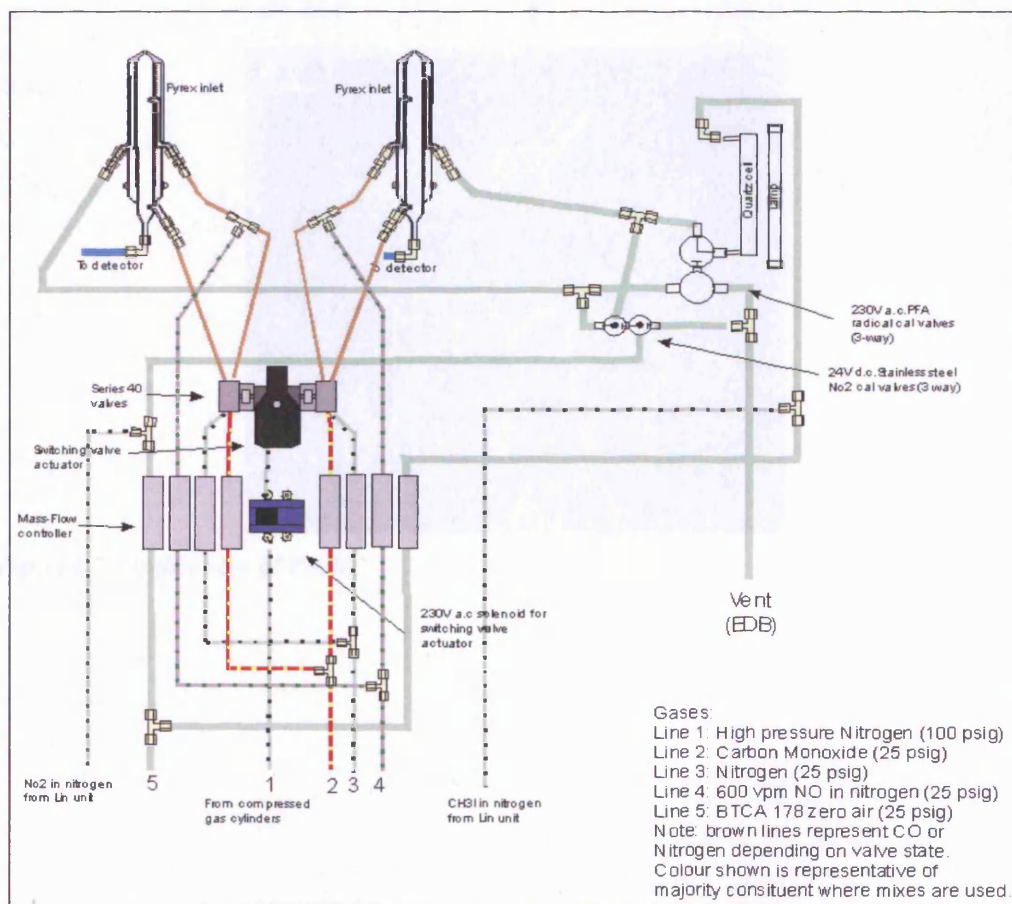


Figure 2.6 – Schematic of PERCA inlet plumbing

Each inlet has a length of cotton covered resistance wire ( $32.8 \Omega \text{ m}^{-1}$ ) wrapped around the inner tube to a total resistance of approximately  $700 \Omega$  (as denoted by the thick black line in Figure 2.4) to provide heating. The heaters are held in place using FC8 Autostic ceramic cement (Carlton Brown and Partners), and the temperature is monitored using a type-T thermocouple (Farnell). The temperature is usually held at  $30^\circ\text{C}$  with temperature controllers (Omega Newport i16 series) housed in the isothermal unit on the main rack, as the  $\text{HO}_2$  wall loss is much lower at  $30^\circ\text{C}$  than at lower temperatures.

The electrical switching for the inlet system is controlled by the PERCA Inlet Control Module (PICM). Control signals are received from various items on the PERCA rack that switch the solenoid, calibration valves, calibration lamp (all 5V TTL) and inlet heaters (11V d.c.) on and off. The PICM accepts 230V a.c. and 24V d.c. inputs from the rack along with the control signals, has six switched a.c. and four switched d.c. outputs, and is shown in Figure 2.7.

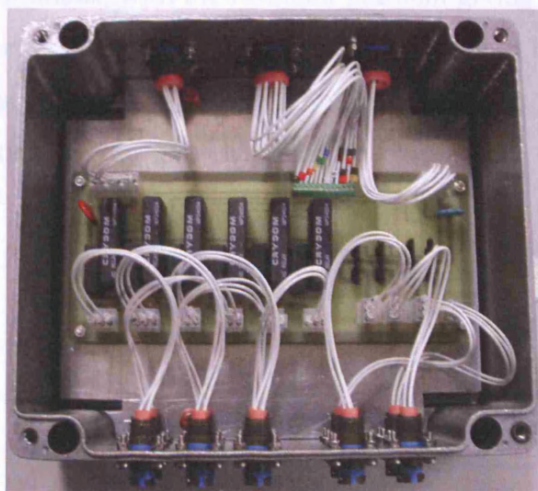


Figure 2.7 – Inside view of PICM

## 2.6.3 The calibration system

### 2.6.3.1 NO<sub>2</sub> sensitivity calibration

The response of the NO<sub>2</sub> detection system is linear once a certain concentration of NO<sub>2</sub> is exceeded (see section 2.6.5.2), and a calibration fit can be performed. NO<sub>2</sub> is produced from a wafer permeation device (Dynacal 30F3, approximate output 400 ng min<sup>-1</sup>, VICI Metronics) held at a constant temperature of 35 °C in the linearization unit on the main rack with a constant flow of 50 sccm of N<sub>2</sub> (zero grade, BOC) passing over it. The NO<sub>2</sub>/N<sub>2</sub> mixture is then mixed with varying amounts of zero air (BTCA 178 grade, BOC) to produce varying concentrations of NO<sub>2</sub> between approximately 35 and 85 ppbv.

NO<sub>2</sub> concentrations are calculated from the permeation rate and the volume of zero air the NO<sub>2</sub> is mixed with. The voltage response of the detector is then plotted against these concentrations, with the resultant gradient giving the sensitivity of the detector. The detector signal in volts can then be divided by this sensitivity to produce a concentration of NO<sub>2</sub>. Figure 2.8 shows a ground NO<sub>2</sub> calibration, and Figure 2.9 shows a typical NO<sub>2</sub> sensitivity plot.

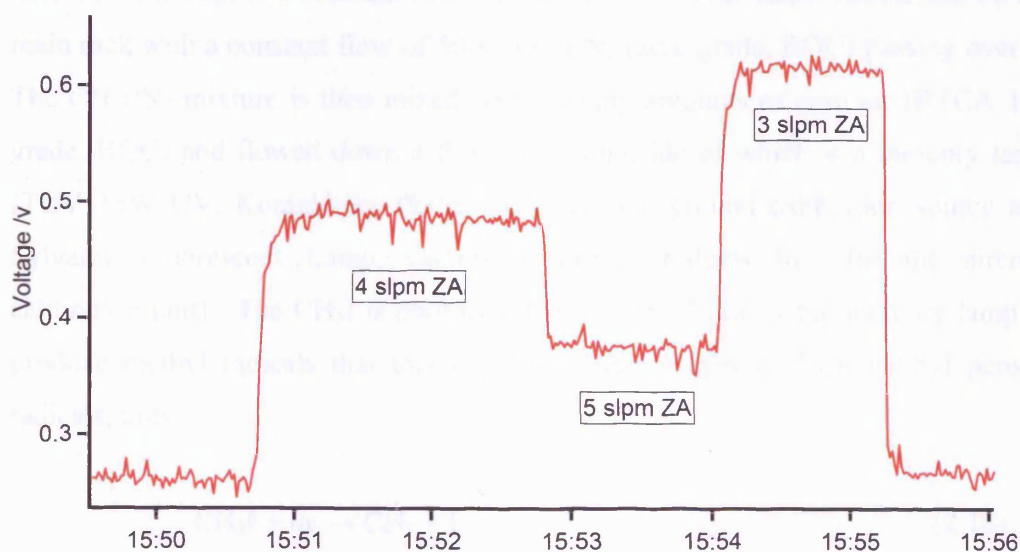


Figure 2.8 – Typical NO<sub>2</sub> sensitivity calibration.

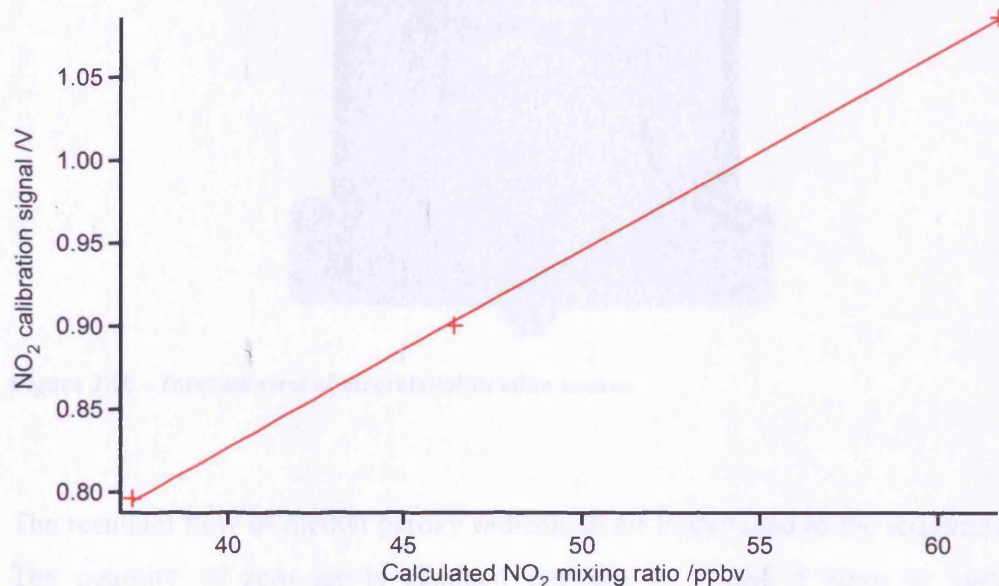


Figure 2.9 – Typical NO<sub>2</sub> detector sensitivity plot.

### 2.6.3.2 Chain length calibration

The calibration unit produces CH<sub>3</sub>O<sub>2</sub> to calibrate the chain length of the inlet and is based on the source described by [Clemishaw, *et al.*, 1997]. A CH<sub>3</sub>I wafer permeation device (Dynacal 4600 approximate output 260 ng min<sup>-1</sup>, VICI Metronics) is kept at a constant temperature of 35°C in the linearization unit on the main rack with a constant flow of 50 sccm of N<sub>2</sub> (zero grade, BOC) passing over it. The CH<sub>3</sub>I/N<sub>2</sub> mixture is then mixed with varying amounts of zero air (BTCA 178 grade, BOC) and flowed down a flow tube alongside of which is a mercury lamp (TUV 15W UV, Koninklijke Philips N.V. for the ground calibration source and Sylvania Fluorescent Lamp, Osram Sylvania Products Inc. for the aircraft calibration unit). The CH<sub>3</sub>I is photolysed at  $\lambda = 253.7$  nm by the mercury lamp to produce methyl radicals that then combine with oxygen to form methyl peroxy radicals, thus





Figure 2.10 – Internal view of aircraft calibration source

The resultant flow of methyl peroxy radicals in air is switched to the required inlet. The quantity of zero air is changed between 3, 4 and 5 slpm to vary the concentration of  $\text{CH}_3\text{O}_2$  being produced. There is an unknown species in the air that also photolyses to produce peroxy radicals, and thus at each flow rate of zero air, a corresponding period of calibrations is performed with no  $\text{CH}_3\text{I}$  present so that this ‘artefact’ can be removed.

The concentration of  $\text{CH}_3\text{O}_2$  is given by the following equation:

$$[\text{CH}_3\text{O}_2] = j(\text{CH}_3\text{I}) \cdot t_{\text{res}} \cdot [\text{CH}_3\text{I}] \quad (2.20)$$

where  $t_{\text{res}}$  is the residence time of the  $\text{CH}_3\text{I}$ /air mix in the flow tube. The chain length is calculated by subtracting the change in  $\text{NO}_2$  measured by the detector at each flow rate from zero air alone, from that produced from zero air and  $\text{CH}_3\text{I}$ , and dividing the subsequent  $\Delta\text{NO}_2$  by the calculated concentration of  $\text{CH}_3\text{O}_2$ :

$$\text{CL} = \frac{\Delta[\text{NO}_2]_{\text{CH}_3\text{I}+\text{artefact}} - \Delta[\text{NO}_2]_{\text{artefact}}}{[\text{CH}_3\text{O}_2]} \quad (2.21)$$

A typical calibration signal from the ground system is shown in Figure 2.11.

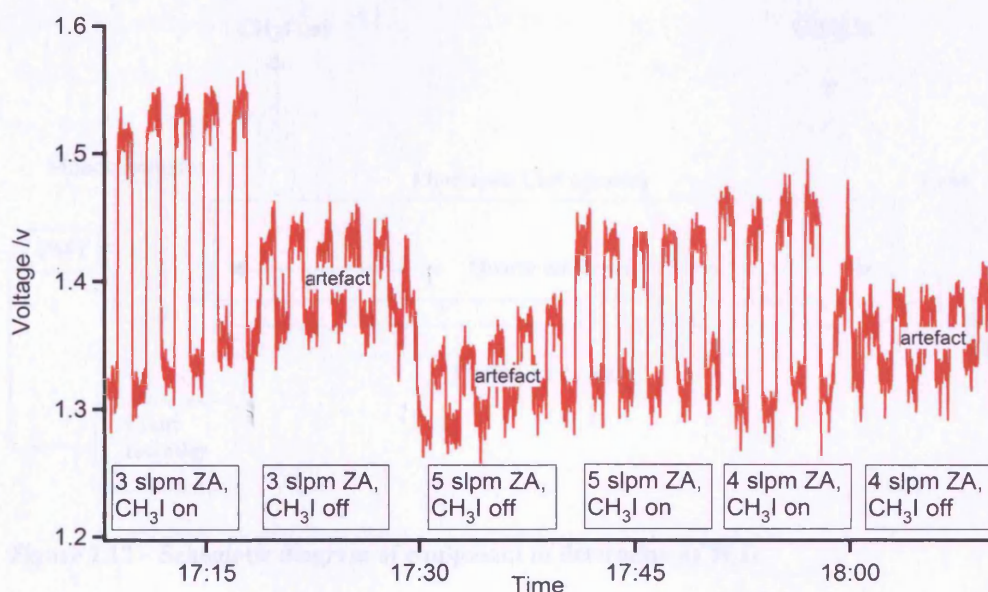


Figure 2.11 – Example of a chain length calibration using the ground calibration source

### 2.6.3.3 Measurement of $j(\text{CH}_3\text{I})$

In order to be able to calculate the concentration of methyl peroxy radicals produced by the calibration unit, it is necessary to determine  $j(\text{CH}_3\text{I})$  for the specific calibration source used. Following the method of [Carpenter, 1996], the apparatus was set up as shown in Figure 2.12. In each experiment,  $\text{CH}_3\text{I}$  vapour in varying flows of zero air was transferred to the photolysis cell from a capillary diffusion tube *via*  $\frac{1}{4}$ " o.d. PFA tubing in order to achieve varying  $\text{CH}_3\text{I}$  vapour pressures in the cell. The photolysis cell was then closed with Teflon taps (represented by encircled cross in Figure 2.12) and the reference lamp (Model L2196 deuterium lamp, Hamamatsu Photonics K.K.) was turned on, followed by the photolysis lamp. A 60 cm focal length lens (PLCX-25.4-257.5-UV, Elliot Scientific) was placed between the reference lamp and the photolysis cell in order to focus the light from the reference lamp through the cell. The attenuation of the reference lamp by the  $\text{CH}_3\text{I}$  vapour at  $\lambda = 265$  nm was monitored for several minutes using a Cornerstone  $\frac{1}{4}$ -m path-length monochromator (Oriol Instruments Ltd.) connected to a photomultiplier tube (PMT) (Model R4315, Hamamatsu Photonics K.K.) connected to a chart recorder. No photolysis of  $\text{CH}_3\text{I}$  by the reference lamp was observed.

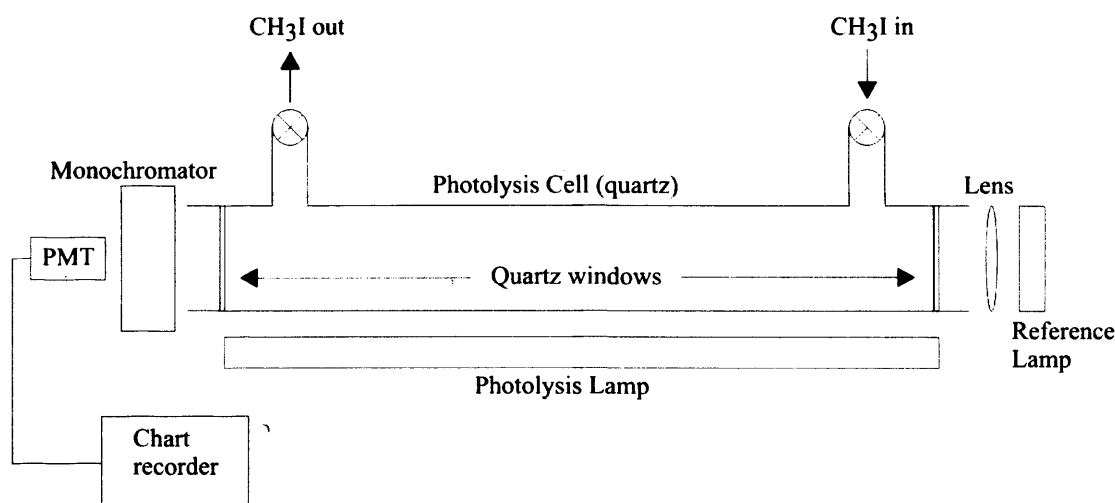


Figure 2.12 – Schematic diagram of equipment to determine  $j(\text{CH}_3\text{I})$

The Beer-Lambert law (equation (2.22)) can be used to calculate the initial concentration of  $\text{CH}_3\text{I}$  in the cell, where  $I_0$  is the incident intensity of the reference lamp with no  $\text{CH}_3\text{I}$  present,  $I$  is the intensity of the reference lamp with  $\text{CH}_3\text{I}$  present in the cell,  $c$  is the concentration of  $\text{CH}_3\text{I}$ ,  $l$  is the path length of the reference lamp light through the photolysis cell, and  $\sigma$  is the absorption coefficient for  $\text{CH}_3\text{I}$ .

$$I = I_0 e^{-cl\sigma} \quad (2.22)$$

Equation 2.22 can be rearranged to give equation 2.23, where OD is the optical density:

$$\ln\left(\frac{I_0}{I}\right) = \text{OD} = [\text{CH}_3\text{I}]l\sigma \quad (2.23)$$

Standard first order kinetics for the decay of  $\text{CH}_3\text{I}$  can be applied to obtain equation (2.24), where  $t$  is time and  $\text{OD}_0$  is optical density at time = 0:

$$\ln(\text{OD}) = -j(\text{CH}_3\text{I})t + \ln(\text{OD}_0) \quad (2.24)$$

Consequently, a plot of  $\ln(\text{OD})$  against time will result in a gradient of  $-j(\text{CH}_3\text{I})$ . An example of such a plot is in Figure 2.13, whilst the full range of measured values is given in Table 2.2.

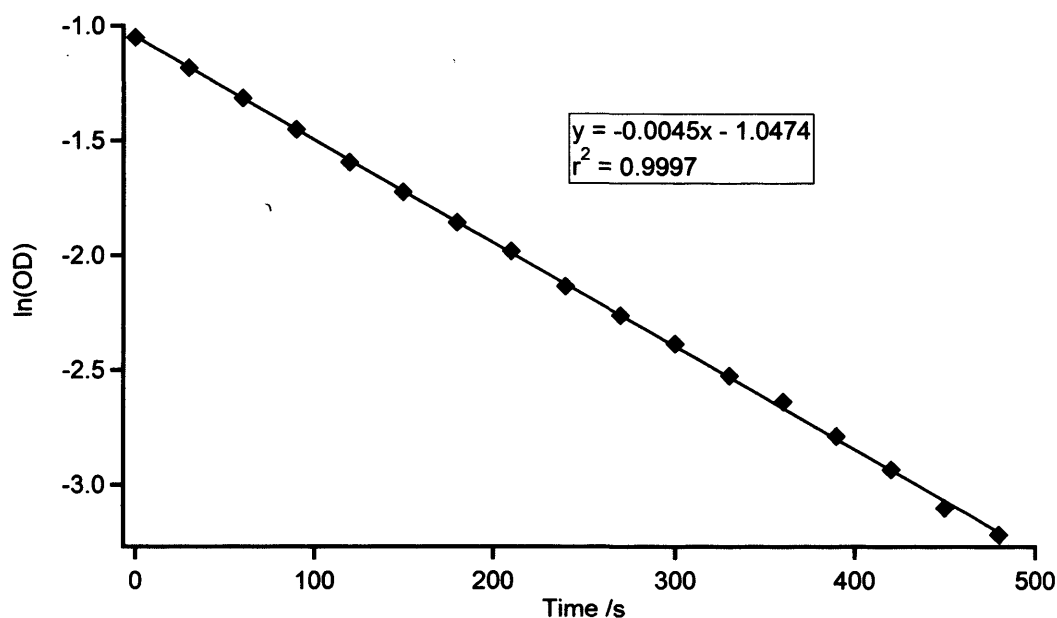


Figure 2.13 – Example of a  $j(\text{CH}_3\text{I})$  measurement.

$j(\text{CH}_3\text{I})$ measurements $/\times 10^{-3} \text{ s}^{-1}$						Mean (standard deviation)
6.0	5.8	5.3	4.7	4.5	5.7	5.5 (0.76)
4.3	5.5	6.3	6.4	6.4		

Table 2.2 – Results of  $j(\text{CH}_3\text{I})$  measurements

### 2.6.3.4 Inlet unit positioning

The four inlet units described (the inlets, the MFC tray, the calibration unit and the PICM) are mounted on the wall of the BAe-146. The inlets sample air through the aircraft skin *via* a blister on the side of the aircraft that allows sampling perpendicular to the outside ambient airflow.

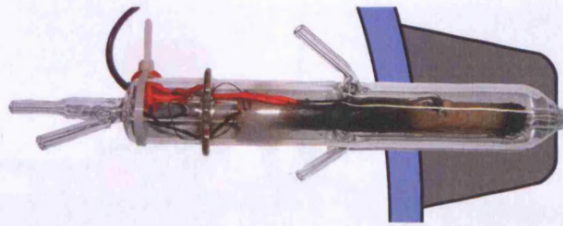


Figure 2.14 – Inlet mounted through fuselage of BAe-146

A schematic diagram of the four inlet units mounted on the wall of the aircraft is shown below.

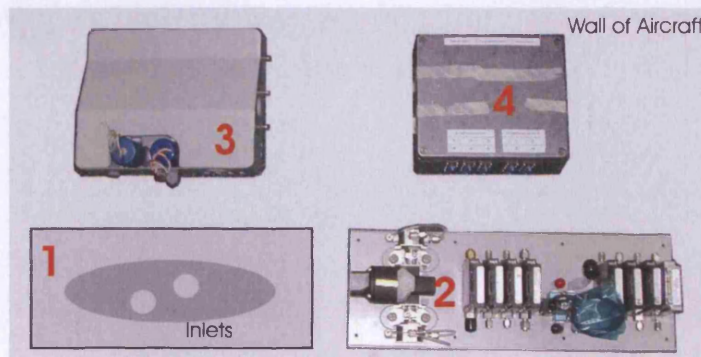


Figure 2.15 – Schematic diagram of the aircraft PERCA inlet systems layout where 1 – inlets, 2 – MFC tray, 3 – calibration unit and 4 – PICM

## 2.6.4 Deployment

The aircraft PERCA has two double-width half-height 19” rack units. One contains control and processing systems and is designated the Main Rack. The other holds gas cylinders and a vacuum pump and is designated the Gas Rack. The main rack is shown in Figure 2.16 along with a brief description of components in Table 2.3. The gas rack is shown in Figure 2.17 with Table 2.4 providing a brief description of components. The racks installed on the BAe-146 are shown in Figure 2.18, and a full description of components is given section 2.6.5.



Figure 2.16 – The main rack

Item	Name	Description
1	Detector systems	NO <sub>2</sub> detection and CO leak warning alarm
2	Linearization unit	Thermostated oven for permeation tubes
3	Uninterruptible power supply	Provides power smoothing and protection against power drop outs
4	Ethernet PC	PC providing connectivity to aircraft data systems
5	Data PC	PC to control instrument and log data
6	Keyboard/screen	Keyboard and screen to control items 4 and 5
7	DC Supplies	Provides various d.c. voltages to the instrument
8	Electrical Distribution Box	Distributes a.c. power to instrument components and contains exhaust gas scrubbing system
9	Interconnect Unit	Routes data lines between instrument components
10	Isothermal Unit	Sample flow control, inlet temperature control and luminol refrigerated storage

11	NO in N <sub>2</sub> cylinder	Reagent gas
12	CO containment box	Safe containment of CO cylinder

**Table 2.3 – Brief description of main aircraft rack items. A full description is given in the following section**



**Figure 2.17 – The gas rack**

Item	Name	Description
13	Vacuum pump	Vacuum pump used to provide sample flows and luminol waste extraction
14	Gas tray	Secure storage for the reagent and calibration gas cylinders (two N <sub>2</sub> and one zero air cylinders)

**Table 2.4 – Brief description of gas rack items. A full description is given in the following section**



Figure 2.18 – Main and gas racks installed on the BAe-146

## 2.6.5 Description of sub-systems

A brief description of the sub-systems contained on the racks was given in Table 2.3 and Table 2.4. The following section provides an in-depth description of the role of each sub-system.

### 2.6.5.1 Detector systems

Item 1 on the main rack is the NO<sub>2</sub> detector system and CO alarm. The NO<sub>2</sub> detectors are LMA-3 units (Unisearch Scintrex), modified such that two complete electronics and wick assemblies fit into the footprint of one original Scintrex. To achieve this space saving, the peristaltic pump and internal luminol reservoirs have been removed. Luminol is instead stored in a refrigerated unit in the Isothermal unit and is supplied to the detectors by over-pressuring the luminol container with

nitrogen (typically to 20 psi) to force the luminol out of the container along the supply tube. The liquid flow is regulated by the needle valves (Swagelok SS-SS2-A) located in the detector box. The flow rate of luminol to each detector is of the order of 0.5 ml per minute. Waste luminol from the detectors is removed under suction (provided by the vacuum pump) and regulated by needle valves in the detector box. It is stored in the waste reservoir in the isothermal unit.

The detectors consist of an acetal cell that houses a wick, down which luminol solution is run, and control electronics. Luminol chemiluminescence occurs at  $\lambda = 424$  nm in the presence of  $\text{NO}_2$  and  $\text{O}_2$  [Kelly, *et al.*, 1990], and a Photo Multiplier Tube (PMT) opposite the wick detects the emitted light. The reaction with luminol involves two  $\text{NO}_2$  molecules, and is consequently quadratic at low concentrations. At higher concentrations (above 2-3 ppbv of  $\text{NO}_2$ ) the rate limiting step changes to be that of  $\text{NO}_2$  solvation and thus the reaction becomes linear.

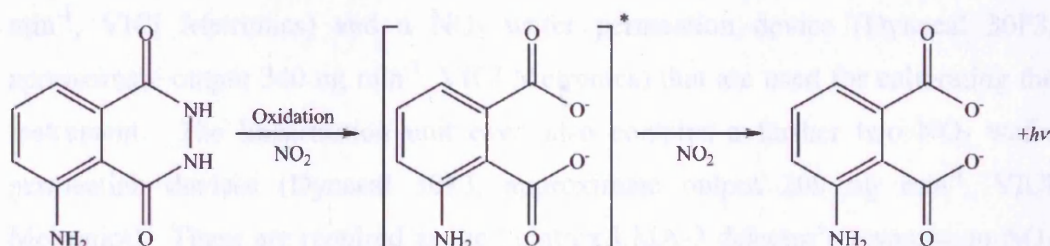


Figure 2.19 – Reaction of luminol with  $\text{NO}_2$  [Cantrell, *et al.*, 1993b]

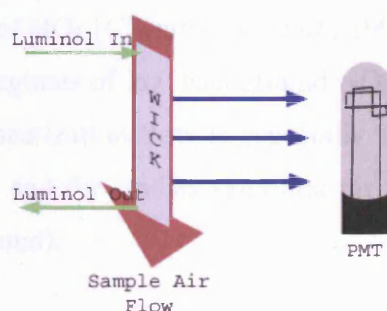


Figure 2.20 – Schematic diagram of Scintrex LMA-3 detector [Green, 2003]

An external readout and alarm system for a CO monitor (fitted to the CO containment box) is also fitted to the detector unit. It accepts an input from a Dräger Minipac CO monitor and displays the current CO concentration. Should the

monitor exceed a pre-set alarm condition, an audible alarm will be sounded and the flasher mounted on top of the rack will go off. This is especially important when the instrument is operated on board aircraft.

### 2.6.5.2 Linearisation unit

Underneath the detectors is the Linearisation Unit (unit 2 in Figure 2.16). This contains an oven consisting of an aluminium block fitted with two thermofoil heaters (Minco) and a type-T thermocouple (Farnell) linked to an Omega Newport i16 series temperature controller. The oven is capable of maintaining four wafer permeation devices at a constant temperature. A flow of 50 sccm N<sub>2</sub> is maintained over the permeation devices using needle valves (Swagelok SS-SS2). The oven contains a CH<sub>3</sub>I wafer permeation device (Dynacal 4600 approximate output 260 ng min<sup>-1</sup>, VICI Metronics) and a NO<sub>2</sub> wafer permeation device (Dynacal 30F3, approximate output 340 ng min<sup>-1</sup>, VICI Metronics) that are used for calibrating the instrument. The linearisation unit oven also contains a further two NO<sub>2</sub> wafer permeation devices (Dynacal 50F3, approximate output 200 ng min<sup>-1</sup>, VICI Metronics). These are required as the Scintrex LMA-3 detector's response to NO<sub>2</sub> is non-linear at low values of NO<sub>2</sub>. Whilst the detectors are only non-linear below a few ppbv of NO<sub>2</sub> in the absence of NO [Kelly, *et al.*, 1990], when the concentration of NO is of the order used in PERCA, the non-linear region extends up to approximately 20 ppbv of NO<sub>2</sub> [Clemishaw, *et al.*, 1997]. Consequently, when the PERCA is operated in regimes of low background NO<sub>2</sub> and O<sub>3</sub>, a linearisation flow must be added. The linearization flow is especially important during calibrations (when zero air is used) and for studies sampling air with low levels of pollution (such as remote background).

### 2.6.5.3 Uninterruptible Power Supply

Item 3 is an Uninterruptible Power Supply (UPS) (250VA, APC) that can supply about four minutes of power to the control PC in the event of a power failure. On

the previous UK aircraft, a Hercules C-130, this was especially important as the switch over between ground and aircraft power took enough time for electronic systems to be affected. However on the BAe-146, the switch over is on the order of 50 ms, and as such short enough to not affect the electronics. The UPS is however maintained as a safeguard.

#### 2.6.5.4 Computer systems

Mounted below the UPS is the first of two PCs, the Ethernet PC (EPC). The EPC has software installed to allow data manipulation and a CD-RW drive to allow data to be saved. It is a single board computer (Juki 760E, Wordsworth) mounted in a 19" rack mount case (RACK-2300B with PCI-2SD2 PCI backplate, ICP Electronics Inc). The EPC is connected to the Data PC (DPC) *via* a 100 Mbps ethernet link.

The Data PC (DPC) is a 1Ghz Pentium III single board computer (Rocky-3702EV, Wordsworth) mounted in a 19" rack mount case (Rack 360, Wordsworth). It contains three data acquisition boards, a 16 channel d/a analogue out board (CIO-DAC16, Talisman Electronics), a 64 channel a/d analogue input board with 21 bit digital I/O (PCI-DAS64, Talisman Electronics) and a 16 channel thermocouple input card (CIO-DAS-THERM, Talisman Electronics). This computer sets and records all flows, switches all valves and logs selected temperatures. All logging is done at 1 Hz. The control software is custom written in Microsoft Visual Basic 6 and interfaces with the data acquisition boards *via* Universal Library (Computer Boards).

The uppermost item on the other side of the main rack (item 6) is a combined 15.1" monitor/keyboard/mouse (LKM-926, Wordsworth) that is used to interface with both PCs installed on the rack.

### **2.6.5.5 DC supply box**

Item 7 is the DC Supply box. It contains d.c. power supplies to provide the +15 V, -15V and 5V (LPQ 253CEF, Astec); +24V (LPS 155C, Astec) and + 12V (UL electronics workshop) required in PERCA.

### **2.6.5.6 Electrical distribution unit**

Below the DC Supply Box is the Electrical Distribution Unit (EDU) and Scrubber. The EDU section of the unit is a distribution board that supplies 230V a.c. to all the other racking units and the inlets. It consists of eight 5A trip switches (3120 series, E-T-A Circuit Breakers Ltd).

The scrubber section has three traps to scrub the CO, NO and NO<sub>2</sub> from the exhaust gases of PERCA and one trap to scrub hydrocarbons and NO<sub>2</sub> from the calibration flow vent. The three exhaust traps contain molecular sieve (BDH 4A, Molecular Products) to dry the gas flow (as moisture degrades the second trap), Hopcalite (Molecular Products) to oxidise the CO to CO<sub>2</sub> and the NO to NO<sub>2</sub>, and the third trap contains Sofnofil (Molecular Products) to absorb the NO<sub>2</sub>.

The calibration flow trap contains both Sofnofil to absorb the NO<sub>2</sub> and activated charcoal to absorb hydrocarbons. There are two ball valves (Swagelok SS-43YTF2) mounted on the front to allow the scrubbers to be bypassed when in flight so as to reduce restriction of the sample flow of the instrument.

### **2.6.5.7 Interconnection box**

Item 9 is the Interconnection Box (ICB). The ICB maps the large number of analogue and digital inputs and outputs from all around the instrument to the data

acquisition cards in the PC. Figure 2.21 is a schematic diagram of electrical wiring in the PERCA, with inlet wiring enlarged.

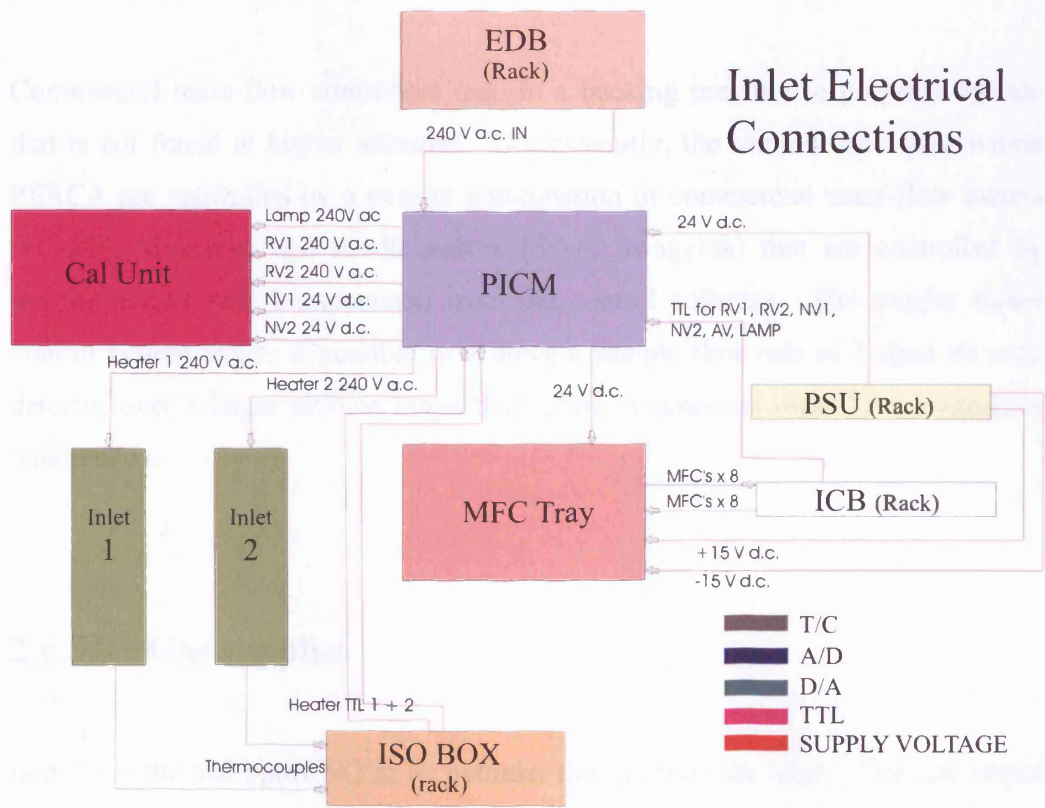
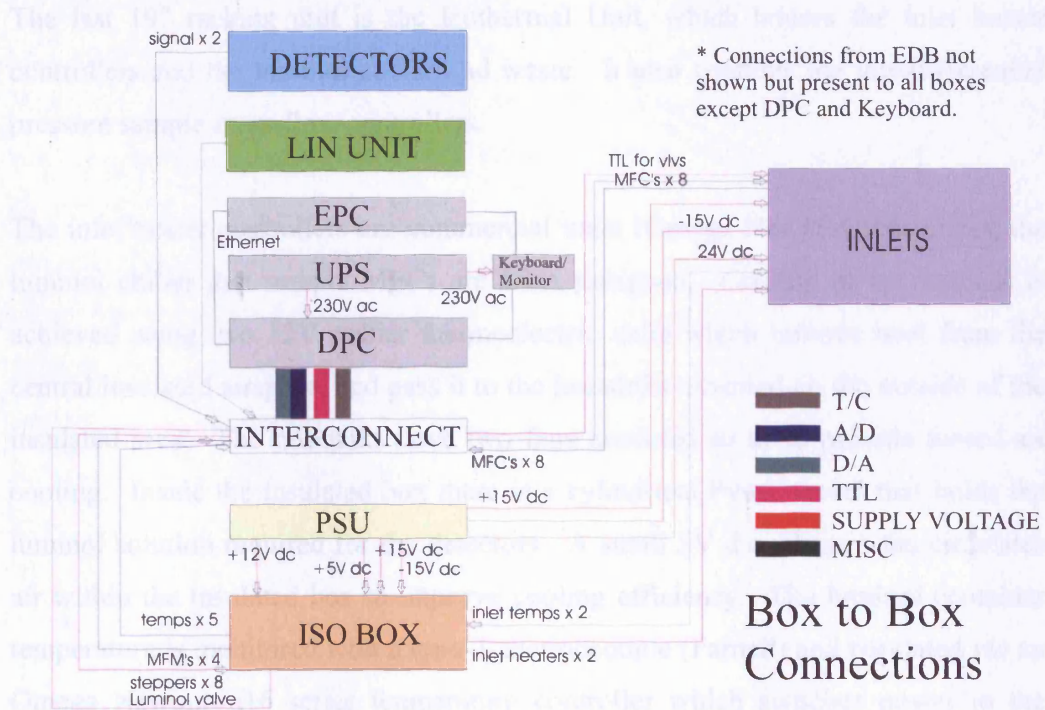


Figure 2.21 – Schematic of PERCA electrical wiring with inlet wiring enlarged

### 2.6.5.8 Isothermal unit

The last 19" racking unit is the Isothermal Unit, which houses the inlet heater controllers and the luminol cooler and waste. It also contains the low-differential pressure sample mass-flow controllers.

The inlet heater controllers are commercial units (Omega Newport i16 series), the luminol chiller and sample MFCs are UEA designed. Cooling of the luminol is achieved using two 12V peltier thermoelectric units which remove heat from the central insulated airspace, and pass it to the heatsinks mounted on the outside of the insulated area. The heatsinks have two fans mounted so as to provide forced-air cooling. Inside the insulated box there is a cylindrical Pyrex vessel that holds the luminol solution required for the detectors. A small 5V d.c. electric fan circulates air within the insulated box to improve cooling efficiency. The luminol container temperature is monitored with a type-T thermocouple (Farnell) and regulated *via* an Omega Newport i16 series temperature controller which switches power to the peltier units.

Commercial mass-flow controllers require a backing pressure to properly operate that is not found at higher altitudes. Consequently, the sample flow rates within PERCA are controlled by a custom combination of commercial mass-flow meters (FC-360, Mykrolis) and needle valves (SS-4, Swagelok) that are controlled by stepper motors (RS Components) from the control software. The stepper motor control system makes it possible to achieve a sample flow rate of 2 slpm on each detector over a larger altitude range than using commercial mass flow controllers would allow.

### 2.6.5.9 Gas supplies

Item 11 is the 600 ppmv NO in N<sub>2</sub> cylinder that supplies the inlets. The gas output goes through a FeSO<sub>4</sub>·7H<sub>2</sub>O trap to reduce any NO<sub>2</sub> to NO, and then on to the inlet MFCs.

Also mounted on the bottom of the main rack is the CO Containment Box. PERCA requires a cylinder of pure CO, and a leak onboard aircraft would be dangerous. Consequently the CO cylinder is isolated inside an airtight box. All high-pressure CO lines are housed in this container, together with a CO monitor (Dräger Minipac). A feed-through allows the cylinder to be turned on and off, and takes the monitor reading from the box and to a secondary display (mounted with the detectors, see section 2.6.5). In the event of a leak an audible and visual alarm is triggered (at a CO mixing ratio of 35 ppmv). The box has a vent line (connected using Swagelok quickconnect coupling) that is connected directly to the aircraft exhaust line, so if the cylinder should leak the CO will be dumped outside the aircraft. The final connector on the box is a swagelok 1/8" bulkhead to allow the low-pressure CO through to the inlet MFCs. The CO is run through a hydrocarbon trap (activated charcoal, Fisher Scientific) before leaving the box.

### 2.6.5.10 The gas rack

The gas rack has the vacuum pump and the remaining gas cylinders mounted on it. The pump is a Leybold Sogevac SV16 oil filled rotary vane vacuum pump. It is capable of an ultimate pressure of lower than 1.5 mbar, and a pumping rate of up to  $14.5 \text{ m}^3 \text{ h}^{-1}$ . It has an integrated oil return line and so no oil loss through the exhaust can occur. It is used to pull the sample flows from the inlets through the detectors, flow regulators and scrubber, and to remove waste luminol from the detectors by reducing the pressure of the luminol waste chamber.

The middle tray on the rack has mounts for three BOC AH size (5 litre) gas cylinders. These are used to hold the zero air, oxygen free nitrogen and zero grade nitrogen necessary to run the instrument.

A simplified block diagram of the PERCA plumbing connections between these units is shown in Figure 2.22.

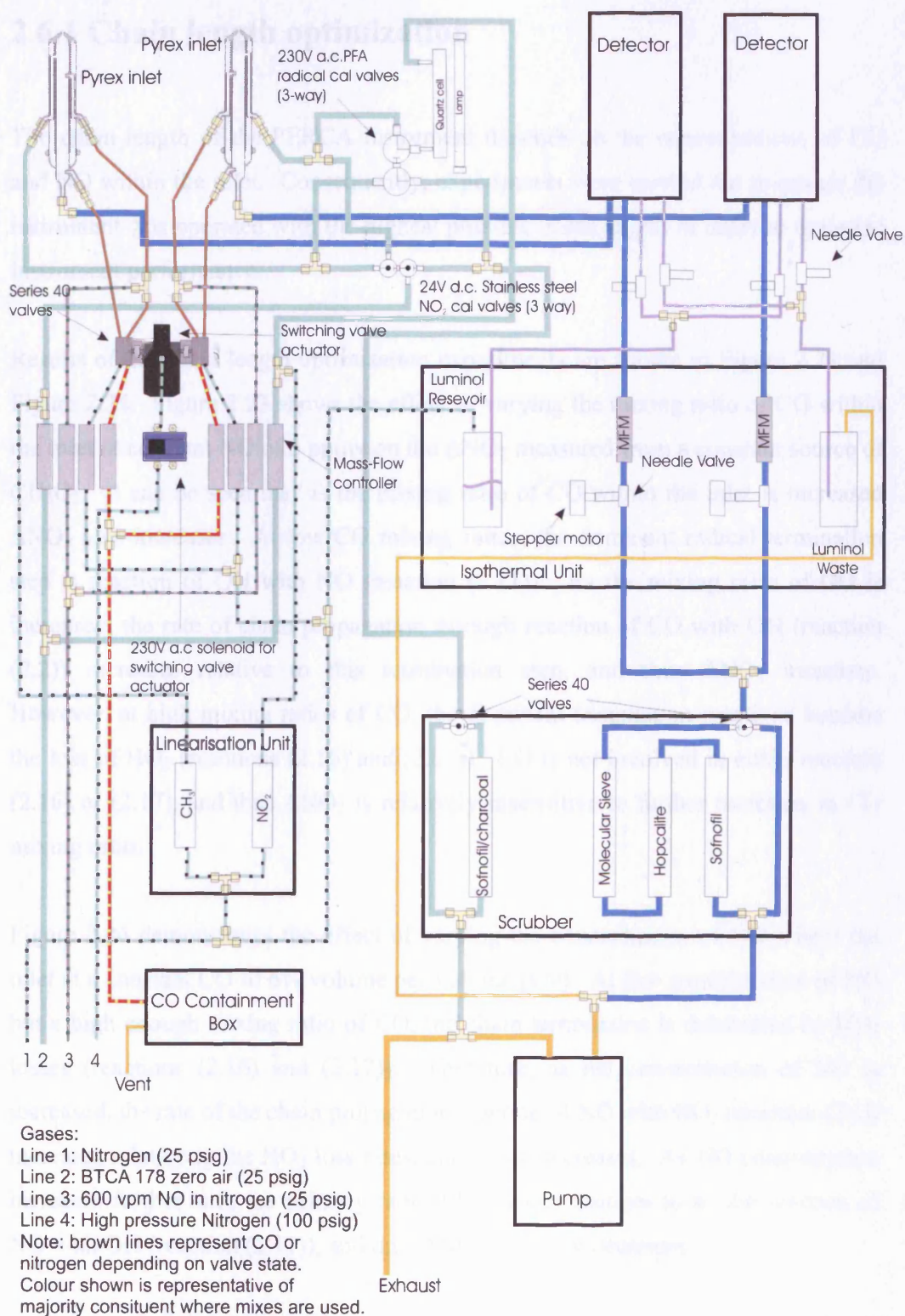


Figure 2.22 – Block diagram of PERCA plumbing with linearization NO<sub>2</sub> flows omitted for clarity

### 2.6.1 Chain length optimization

The chain length of the PERCA instrument depends on the concentrations of CO and NO within the inlet. Consequently, experiments were carried out to ensure the instrument was operated with the highest possible chain length in order to optimize instrument performance.

Results of the chain length optimization experiments are shown in Figure 2.23 and Figure 2.24. Figure 2.23 shows the effect of varying the mixing ratio of CO within the inlet at constant NO of 3 ppmv on the  $\Delta\text{NO}_2$  measured from a constant source of  $\text{CH}_3\text{O}_2$ . It can be seen that as the mixing ratio of CO within the inlet is increased  $\Delta\text{NO}_2$  also increases. At low CO mixing ratios, the dominant radical termination step is reaction of OH with NO (reaction (2.11)). As the mixing ratio of CO is increased, the rate of chain propagation through reaction of CO with OH (reaction (2.2)) increases relative to this termination step, and thus  $\Delta\text{NO}_2$  increases. However, at high mixing ratios of CO, the dominant termination reactions become the loss of  $\text{HO}_2$  (reactions (2.16) and (2.17)). CO is not involved in either reaction (2.16) or (2.17), and thus  $\Delta\text{NO}_2$  is relatively insensitive to further increases in CO mixing ratio.

Figure 2.24 demonstrates the effect of varying the concentration of NO within the inlet at a constant CO of 6% volume per volume (v/v). At low concentration of NO but a high enough mixing ratio of CO, the chain termination is dominated by  $\text{HO}_2$  losses (reactions (2.16) and (2.17)). Therefore, as the concentration of NO is increased, the rate of the chain propagation reaction of NO with  $\text{HO}_2$  (reaction (2.1)) increases relative to the  $\text{HO}_2$  loss rates, and  $\Delta\text{NO}_2$  increases. As NO concentration increases further still, the primary radical loss route changes to be the reaction of NO with OH (reaction (2.11)), and thus  $\Delta\text{NO}_2$  begins to decrease.

Figure 2.23 and Figure 2.24 show that the peak  $\Delta\text{NO}_2$  (and therefore chain length) occurs at approximately 6% v/v CO and 2.5–3 ppmv NO. Consequently the instrument was run at these concentrations for the work reported in this thesis.

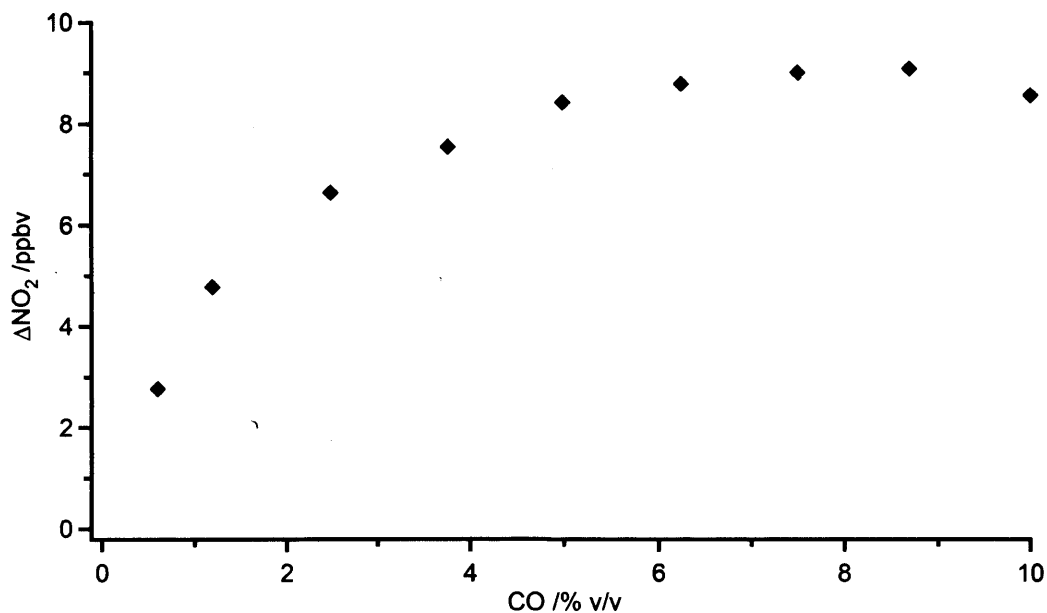


Figure 2.23 – Dependence of chain length on CO mixing ratio.

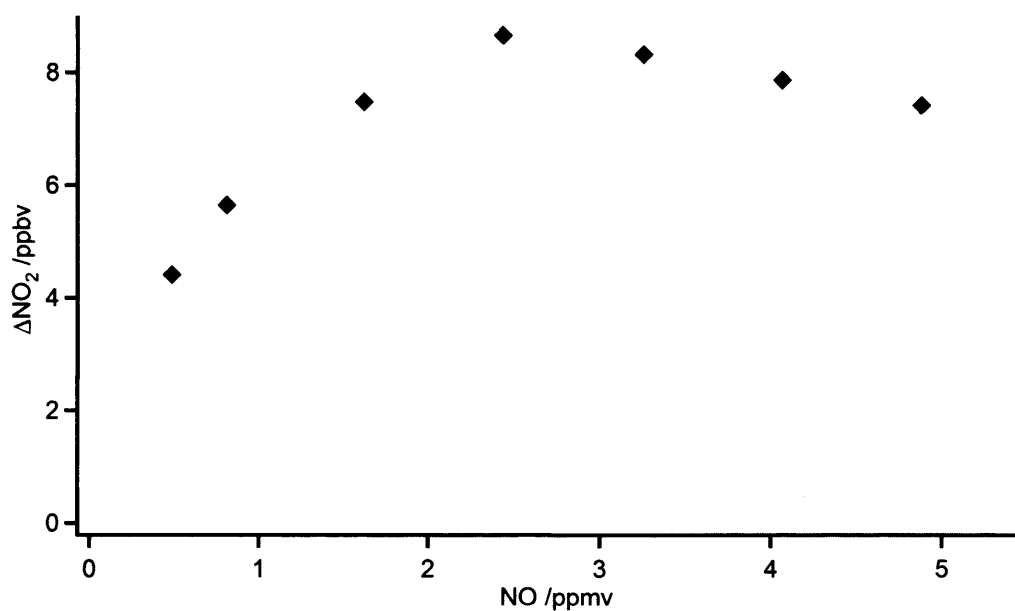


Figure 2.24 – Dependence of chain length on NO concentration.

## 2.6.2 Water vapour interference correction

The sensitivity of the PERCA instrument to humidity is well known [Mihele and Hastie, 1998; Mihele, et al., 1999]. The chain length (the number of  $\text{NO}_2$  molecules produced from each initial molecule of  $\text{HO}_2$  or  $\text{RO}_2$ ) is dependent on concentration

of water vapour, with the chain length dropping by up to a factor of 2 at  $8 \text{ g kg}^{-1}$  specific humidity compared to dry air [Mihele and Hastie, 1998; Mihele, et al., 1999; Salisbury, 2001]. As calibrations are carried out in dry air, the chain length when measuring ambient air can be substantially lower than during calibration. Work carried out by [Salisbury, 2001] demonstrated that the chain length reduction in the presence of water was not a result of wall losses of  $\text{CH}_3\text{O}_2$ , but a result of a change in  $\text{HO}_2$  chemistry in the inlet. Following a series of experiments, it was speculated by [Salisbury, 2001] that the reduction in chain length from increased humidity experienced by the PERCA was a result of  $\text{HO}_2$  wall losses within the inlet increasing with humidity.

However, further work by [Reichert, et al., 2003] suggest an additional three mechanisms for the humidity dependence of chain length:



Consequently an experimentally determined humidity correction given in equation (2.28) where CF is the correction factor,  $T_{\text{inlet}}$  is the inlet temperature in K and SH is the ambient specific humidity in  $\text{kg kg}^{-1}$  has been applied to all peroxy radical data recorded in this thesis as per Salisbury et al. [Salisbury, et al., 2002].

$$\text{CF} = 100 / ((0.17 * T_{\text{inlet}} - 57.08) * \text{SH} + 99.96) \quad (2.28)$$

## 2.7 Error analysis

There are three major sources of error inherent in the PERCA technique: the chain length determination, the detection of  $\text{NO}_2$ , and the necessity of a water correction to be performed.

The chain length determination is affected by the measurement of  $j(\text{CH}_3\text{I})$  for the calibration source, the accuracy of mass flow controllers, the measurement of the volume of the photolysis cell, and the  $\text{CH}_3\text{I}$  source permeation rate. The  $\text{NO}_2$  detection on the other hand is affected by the thermal stability of luminol. The factors affecting accuracy are listed in Table 2.5, with an analysis of each component following. Overall error  $\sigma$  has been calculated from:

$$\sigma = \sqrt{(\sigma_{j(\text{CH}_3\text{I})})^2 + (\sigma_{\text{MFC}})^2 + (\sigma_{\text{cellvolume}})^2 + (\sigma_{\text{CH}_3\text{Ipermeationrate}})^2 + (\sigma_{\text{NO}_2\text{detection}})^2 + (\sigma_{\text{humidity}})^2} \quad (2.29)$$

Affected component	Source	Estimated uncertainty /%
Chain length	$j(\text{CH}_3\text{I})$ measurement	14
	MFC accuracy ( $\text{CH}_3\text{I}$ and zero air)	5
	Photolysis cell volume	5
	$\text{CH}_3\text{I}$ permeation rate	1
$\text{NO}_2$ detection	Background variability + luminol thermal stability	20
Humidity correction	Experimental results	25
Overall		36%

Table 2.5 – Contributions to PERCA measurement error

The calculation above leads to the conclusion that for a single-inlet PERCA, the error is 36%.

The error in measuring  $j(\text{CH}_3\text{I})$  was calculated from the standard error in measurement. The MFC flow rates were calibrated with a primary flow calibrator (Gillian Gilibrator 2, Sensidyne Inc.) and found to be highly reproducible, and thus the errors reported in Table 2.5 may be exaggerated. The humidity correction was calculated by [Salisbury, *et al.*, 2001], and the accuracy of this correction was found to be 20 – 25%. In order to perform the error analysis above, it has been assumed that the error for the humidity correction is 25% for all values of specific humidity and thus a linear propagation of errors is valid. The error in  $\text{NO}_2$  detection is a lot more difficult to quantify, and the error of 20% reported here is after the estimation of [Carpenter, 1996].

As the permeation tubes are losing mass at a rate of *circa* 300 ng min<sup>-1</sup>, a high precision scale is required in order to accurately weigh them. This is hard to achieve due to the accuracy of available mass balances, but was offset by performing multiple measurements on each occasion, and repeating the measurements over a number of months. Thus the errors for measurement of permeation rate were reduced to acceptable levels.

The precision of the PERCA has been calculated from the standard deviations of CH<sub>3</sub>I calibrations. During a calibration, a known amount of CH<sub>3</sub>O<sub>2</sub> is added to the inlet, and the variation in signal calculated. A typical calibration yields a precision of approximately 5%. [Green, *et al.*, 2006] reported PERCA 4 to have a precision of 1 pptv (on a minute-averaged timescale) and an accuracy of 25%. Previous error calculations carried out by [Salisbury, 2001] lead to a non-humidity corrected single-channel error of 35%. The originally quoted single-channel non-humidity corrected PERCA data was quoted at 30% [Clemishaw, *et al.*, 1997].

### 2.7.1 Dual-channel PERCA instrument

In an environment with rapidly changing ozone or NO<sub>2</sub> concentrations such as aircraft measurements, if the ambient ozone changes between two concurrent background cycles, it can mask the NO<sub>2</sub> signal due to peroxy radicals such that determination of the peroxy radical derived signal becomes less accurate, or even nonsense. If during the transition from an amplified to a background period of measurement an air-mass is encountered where ozone increases by (for example) 40 ppbv, the NO<sub>2</sub> signal resulting from the increased ozone will be much larger than any from peroxy radicals. Thus a negative ΔNO<sub>2</sub> and therefore negative peroxy radical concentrations will result. Cantrell *et al.* [Cantrell, *et al.*, 1996b] thus developed the principle of a dual-channel PERCA whereby both background and amplified signal are measured simultaneously. In a single-channel instrument, the background and amplified signal is measured consecutively as the inlet is modulated, whereas a dual-channel instrument comprises of two separate inlet and detection systems that are run out of phase, allowing simultaneous measurements of both the amplified and background signals. This simultaneous measurement of

amplified and background signals gives the dual-channel instrument the ability to reduce both instrumental noise from atmospheric variability, and erroneous measurements in environments with variable background ozone and NO<sub>2</sub> concentrations. Dual-channel data also has a higher temporal resolution than single-channel data, which requires the averaging of two background and one amplification period to obtain data. Dual-channel measurements allow data to be taken on a minimum of a one second timescale as owing to the two channels being modulated out of phase both the background and the amplified signal are constantly measured.

However, as dual-channel data uses two detectors, errors from NO<sub>2</sub> detection included in the error analysis in section 2.7 must be included twice (once for each detector), leading to an overall error of 41%. Including the entire NO<sub>2</sub> detection error twice may lead to an overestimation of the total error, as some terms in the NO<sub>2</sub> detection error such as luminol stability apply equally to both detectors, and therefore should not be included twice. Due to the difficulty in disentangling the various terms involved in the estimation of NO<sub>2</sub> detection error, herein 41% has been stated as an upper limit. It can therefore be seen that the use of dual-channel data increases systematic error as each detector is now contributing to the error. The advantage that dual-channel data brings is in a reduction in error for NO<sub>2</sub> background variability and the ability to work under rapidly varying background conditions.

The precision of PERCA is improved in dual-channel data compared to single-channel, especially in situations where background signal (i.e. ozone or NO<sub>2</sub>) are variable. Figure 2.25 shows a typical dual-channel compared to single-channel plot, in which it can be seen that a number of large spikes have been eliminated and overall variability reduced.

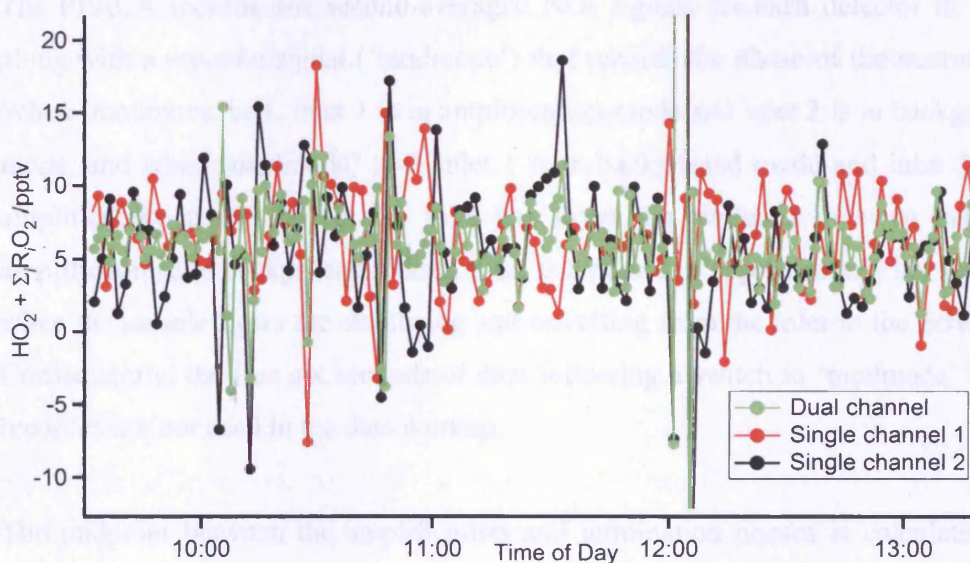


Figure 2.25 – Data demonstrating reduction in variability in dual-channel compared to single-channel data

## 2.8 Data work-up – from modulations to peroxy radicals

In order to obtain peroxy radical concentrations from the PERCA, it is necessary to convert from the measured  $\text{NO}_2$  signal into peroxy radicals. In a single-channel instrument the inlet is switched between amplification and termination mode every 30 seconds. The average of an amplification phase was taken, and the average of the two termination phases surrounding it was subtracted from the amplification period.

In the dual-channel instrument a more complicated method must be used. As the inlets are run out of phase, an amplified signal and a background signal are constantly being measured, and the peroxy radical concentration is calculated by subtracting the termination channel from the background channel. A series of specially written functions have been written in Wavemetrics<sup>®</sup> IGOR Pro v6 software to perform the data work-up. The main functions are reproduced in Appendix A.

The PERCA records one second-averaged  $\text{NO}_2$  signals for each detector in volts, along with a separate signal ('modmode') that records the phase of the instrument. When 'modmode' is 1, inlet 1 is in amplification mode and inlet 2 is in background mode, and when 'modmode' is 0, inlet 1 is in background mode and inlet 2 is in amplification mode. When the inlet gas flows are switched to swap between amplification and background modes, there is a period of approximately six seconds when the sample flows are stabilising and travelling from the inlet to the detectors. Consequently, the first six seconds of data following a switch in 'modmode' being recorded are not used in the data workup.

The midpoint between the amplification and termination phases is calculated for each channel by interpolating between one minute averaged amplification and termination phases for each channel, as shown in Figure 2.26.

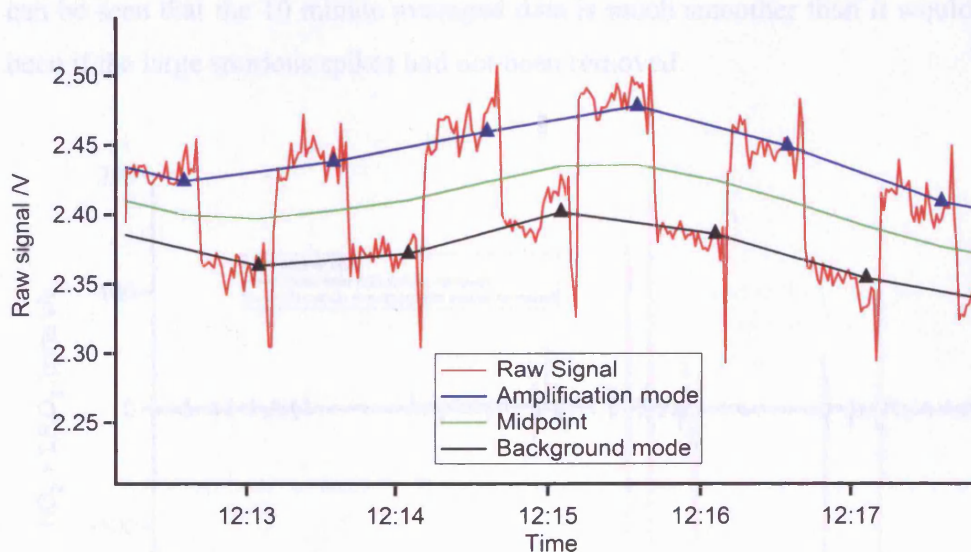


**Figure 2.26 – Interpolated one minute averages for background and amplification phases and calculated midpoint for an inlet**

The difference between the raw signal and interpolated midpoint is then calculated by subtracting the midpoint from the raw signal, resulting in a positive signal during amplification and a negative signal during termination. The resulting signal in volts is then converted into a  $\text{NO}_2$  mixing ratio in ppbv, and one minute average values are calculated for each termination and amplification phase. The termination minute average from one channel is then subtracted from the amplification minute

average for the corresponding time for the other channel, resulting in a  $\Delta\text{NO}_2$  from peroxy radical amplification. The resulting  $\Delta\text{NO}_2$  is then converted into a peroxy radical mixing ratio by division by the chain length calculated for the inlet that was in amplification at the time the  $\Delta\text{NO}_2$  was measured.

The resulting data then has a further filter applied to the data. There can be occasional very large spikes in the data caused by instrumental noise that should not be considered as part of a data analysis. These spikes are usually caused by a fluctuation in luminol flow to one of the two detectors or some other detection glitch. In order to remove these, a system has been developed [Fleming, 2005] whereby any minute data that deviates from an hourly interpolated mean by more than  $\sqrt{2}$  times the standard deviation of the entire day's minute data is removed. Figure 2.27 shows an example of original minute data, minute data with spikes removed as described, and 10 minute averaged data after spikes were removed. It can be seen that the 10 minute averaged data is much smoother than it would have been if the large spurious spikes had not been removed.

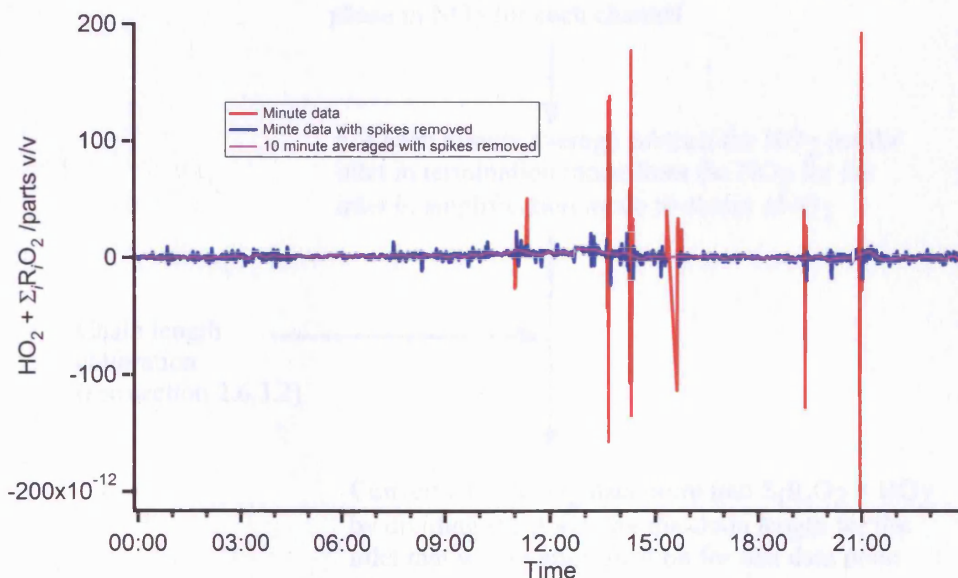


**Figure 2.27 – Minute and 10 minute averaged peroxy radical data with instrument spikes removed.**

A flow diagram covering the data work-up steps is shown in Figure 2.28.

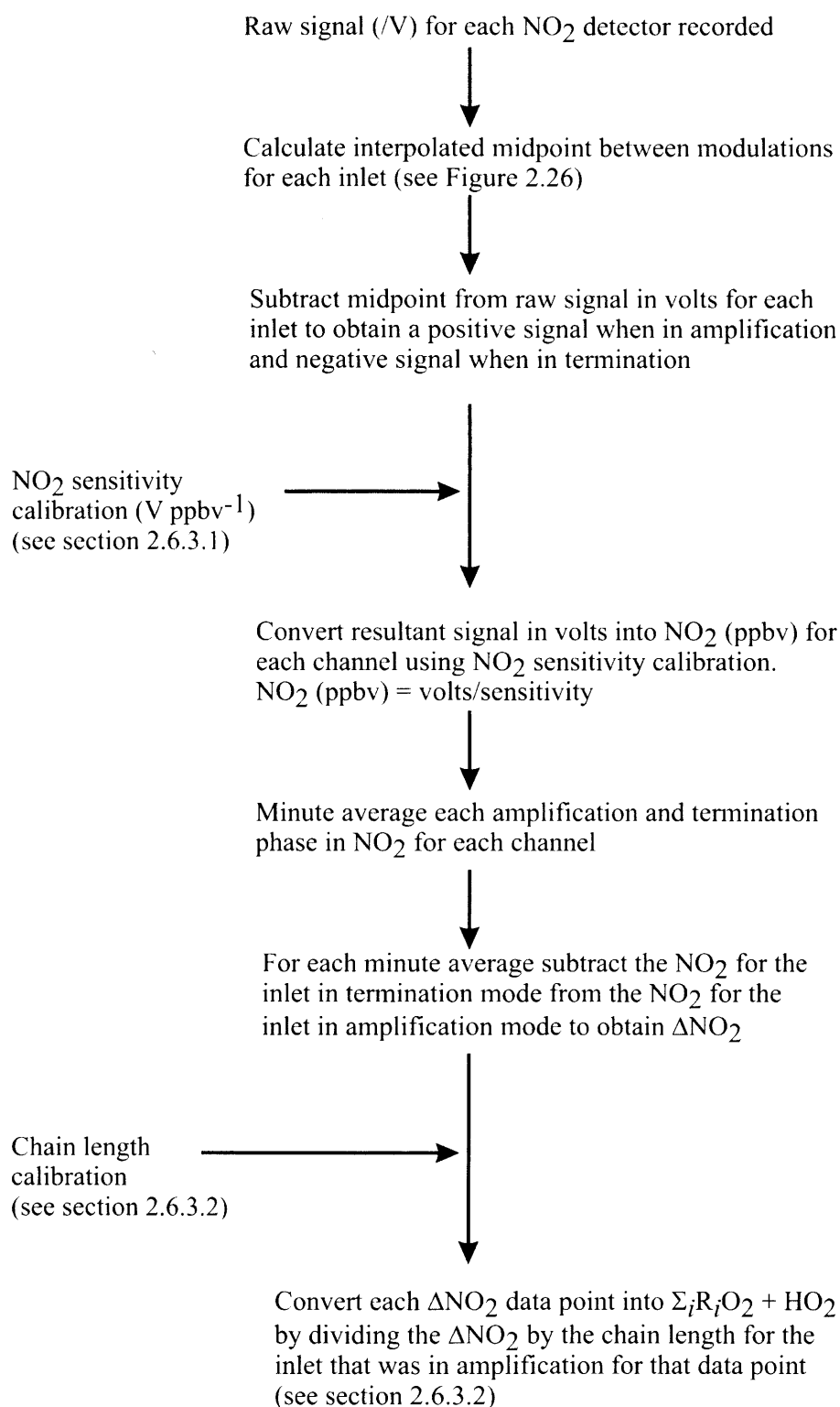


**Figure 2.28 – Flow diagram showing main data work-up steps for converting raw signals in volts into HO<sub>2</sub> + Σ<sub>i</sub>R<sub>i</sub>O<sub>2</sub> in pptv**

## 2.9 Summary

This chapter has provided an overview of techniques for measuring peroxy radicals, with particular emphasis on the PERCA technique that has been used to make the peroxy radical measurements discussed in this thesis. The instrument used in this thesis has been described, along with experiments carried out to optimize instrument performance, including the method of calibration has been described. The necessity of a humidity correction to the PERCA data has been discussed, as have the advantages of a dual-channel PERCA instrument compared to a single-channel PERCA. An error analysis has been performed, and the technique for working up the data from raw signals into peroxy radical concentrations has been described.

## Chapter 3

# The Intercontinental Transport of Ozone and Precursors (ITOP) Campaign

### 3.1 Overview

The Intercontinental Transport of Ozone and Precursors (ITOP) campaign took place during July and August 2004, based at Horta Airport, Faial, Açores (38° 31' 12'' N, 028° 42' 59'' W). ITOP was an aircraft campaign with several instruments from different institutions deployed on the Natural Environment Research Council/UK Met Office (NERC/UKMO) BAe 146-300 atmospheric research aircraft, operated by the Facility for Airborne Atmospheric Measurements (FAAM). The BAe 146-300 was originally constructed as a 146-100 in 1981, since when it was extended to a 146-300 in 1987 and re-registered as G-LUXE. The aircraft has a range of approximately 1,800 nautical miles, a ceiling of 35,000 feet and maximum flight duration of approximately five and a half hours. It carries 3 crew and up to 18 scientists along with instruments. Figure 3.1 shows G-LUXE during flight.



Figure 3.1 – G-LUXE in flight [McIntosh, 2004]

## 3.2 ITOP objectives

Whilst there has been increasing recognition of the importance of the long-range transport of pollutants in recent years (see Chapter 1), the fate of polluted air masses exported from the eastern seaboard of North America remains uncertain – transport to Europe is one possibility, as is transport to the Arctic or the Tropics. It is therefore of vital importance to European pollution budgets to properly quantify the extent and magnitude of trans-Atlantic transport.

To this end, ITOP was part of a larger international experiment, ICARTT (International Consortium for Atmospheric Research on Transport and Transformation) involving aircraft from NASA (National Aeronautics and Space Administration) and NOAA (National Oceanic and Atmospheric Administration) from the USA, FAAM from the UK, and DLR (Deutsches Zentrum für Luft- und Raumfahrt) from Germany, amongst others. An overview of the ICARTT campaign is given in [Fehsenfeld, *et al.*, 2006].

The NASA INTEX-NA (INtercontinental Chemical Transport EXperiment – North America) and NOAA AESOP (Airborne Experiment to Study Ozone and Particles)

experiments were conducted close to the east coast of the United States in order to study North American outflow. DLR performed flights over Europe to try to intercept previously sampled air that had been transported from North America. ITOP in the mid-Atlantic co-ordinated with NOAA, NASA and DLR to attempt to perform a pseudo Lagrangian study of North American outflow where an air mass is intercepted multiple times to study the photochemical processing occurring during transport. The ideal aim was to perform a three point Lagrangian, whereby air sampled over North America was further sampled over the mid-Atlantic and then over Europe. Other more likely scenarios are two point Lagrangians, where air is intercepted by two of the aircraft, e.g. air is sampled over the USA and the mid-Atlantic, but then turns away to the Tropics or the Arctic rather than going on to Europe [Methven, *et al.*, 2006].

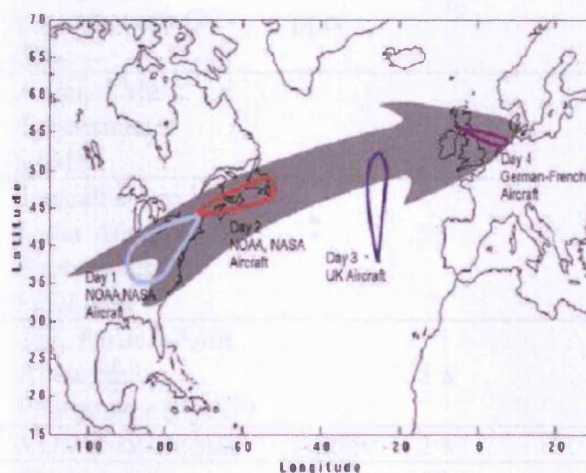


**Figure 3.2 – Lagrangian opportunities for transport from North America to Europe [NOAA, 2004].**

ITOP then had two main objectives; to study the local chemistry occurring within air undergoing long-range transport, focussing on the chemistry of radicals, nitrogen oxides and volatile organic compounds, and to determine to what extent the transport of ozone and precursors affects local air quality remote from the source region. The work presented in this chapter focuses on the first of those aims, detailing the measurements of the sum of peroxy radicals ( $\text{HO}_2 + \Sigma_i \text{R}_i\text{O}_2$ ) using the PEROxy Radical Chemical Amplification (PERCA) technique. The data have been analysed to investigate the oxidant production in air masses undergoing long-range transport.

### 3.3 Instrumentation, forecasting and modelling

G-LUXE was comprehensively outfitted with chemistry instrumentation for ITOP to allow a complete chemical profile to be obtained. Table 3.1 shows the instrumentation fitted.

Instrument	Technique	DL <sup>1</sup>	Frequency	Institute
>100 VOCs inc. NMHCs, alcohols, ketones, aldehydes, ethers	Canister samples then ground analysis with dual channel GC	0.1-5 pptv	3 m	York/Leeds
>40 halocarbons	Canister samples then ground analysis with GC- MS	Sub pptv	3 m	UEA
Aerosol size + composition	Aerosol Mass Spectrometer (AMS)		1 s	UMIST
CH <sub>4</sub> and CO <sub>2</sub>	Tunable Diode Laser Absorption Spectrometry (TDLAS)			FAAM/ Cambridge
CN / Black carbon	TSI, Particle Soot Absorption Photometer (PSAP)		1 s	FAAM
CO	VUV fluorescence	1 ppbv	1 s	FAAM
HCHO	Fluorometric	50 pptv	10 s	UEA
HNO <sub>3</sub>	Gold converter + chemiluminescence	100 pptv	1 s	UEA
<i>j</i> (NO <sub>2</sub> )	Photometer		1 s	Leicester
<i>j</i> (O <sup>1</sup> D)	Fixed band radiometry		1 s	Leicester
NO	Chemiluminescence	10 pptv	1 s	UEA
NO <sub>2</sub>	Photolysis and chemiluminescence	20 pptv	1 s	UEA
NO <sub>y</sub>	Gold converter + chemiluminescence	20 pptv	1 s	UEA
OH and HO <sub>2</sub>	FAGE	0.04 pptv 0.1 pptv	10 s	Leeds
Oxygenates	PTR-MS	10 pptv	10 s	UEA
Ozone	Photometric monitor	1 ppbv	60 s	FAAM

Peroxy radicals (HO <sub>2</sub> + ΣR <sub>i</sub> O <sub>2</sub> )	PERCA chemical amplifier	1 pptv	1 m	Leicester
PAN	Gas chromatography (GC)	20 pptv	5 m	FAAM/Leeds
Position, winds, u, v, w	INS, GPS, wind vanes			FAAM
Real-time VOCs	ORAC in-flight GC	5 pptv	4 m	Leeds
Semivolatile VOCs	Canister samples then ground analysis with dual channel GC	0.1-5 pptv	3 m	York/Leeds
Speciated peroxides (organic + inorganic)	Fluorometric	5 pptv	10 s	UEA
Temperature, T	Rosemount PRT	0.1°	1 s	FAAM
Water Vapour	Lyman-α fluorescence and dewpoint	±1°	1 s	FAAM/ Cambridge

**Table 3.1 – Instruments aboard G-LUXE during ITOP. <sup>1</sup> Detection Limit**

The ability to measure species from an airborne platform is of limited use however if flights are carried out blindly; it is essential that some form of targeting of polluted air masses is done. To this end, an integral part of ITOP was forward trajectory forecasting [Methven, *et al.*, 2006]. Following a flight by NOAA or NASA (or input from satellite data), flight tracks and concentrations of relatively unreactive tracer species (such as CO and O<sub>3</sub>) were rapidly communicated to the ITOP forecasters who were then able to predict with remarkable accuracy where any polluted air masses encountered by the American aircraft would have been transported to. It was then possible to re-intercept the air mass further downstream.

In the long run, it would be ideal to be able to accurately model the transport and transformation of air masses. Before this is possible, models must be able to reproduce existing data; thus data collected during ITOP will be used to evaluate model results. One model used during ITOP is the p-TOMCAT chemical transport model developed at the University of Cambridge and capable of near-real-time chemical analyses (as described in [Savage, *et al.*, 2004]).

### 3.4 ITOP flight summaries

Twelve flights were carried out during ITOP, including the transit flights. In the ICARTT Lagrangian period as a whole there were more than forty flights from the BAE-146, NASA DC-8, NOAA P3 and DLR Falcon.

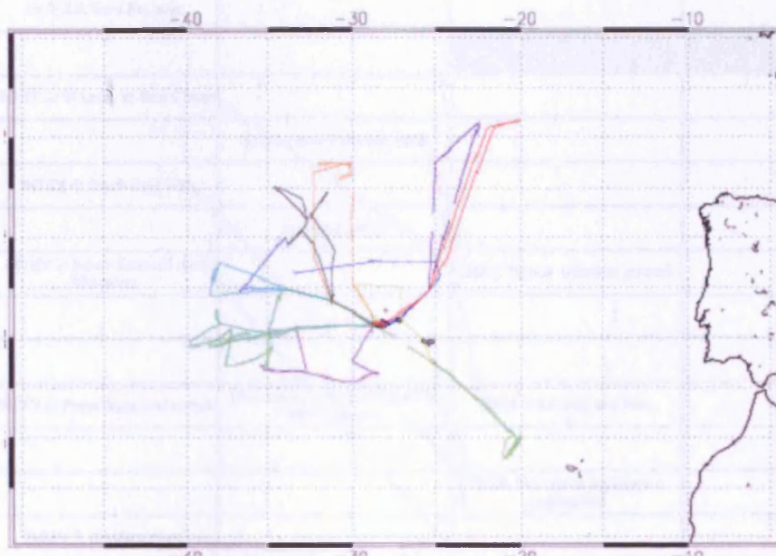


Figure 3.3 – ITOP flight tracks (not including transit flights) [Methven, 2004c]

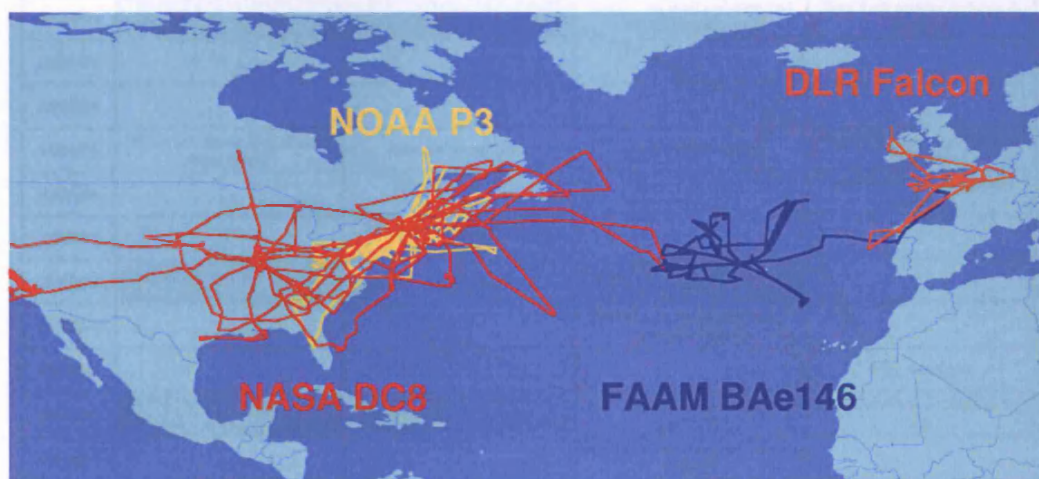


Figure 3.4 – ICARTT flight tracks [Evans, 2004]

Figure 3.5 shows the flights carried out by ICARTT participants during the Lagrangian period (06/07/2004-03/08/2004) along with possible and probable Lagrangian opportunities.

ICARTT Lagrangian Opportunities

	DC8 (NASA)	P3 (NOAA)	BAe-146 (UK)	Falcon (DLR)
05/07/04		Transit		
06/07/04	INTEX 2: from St Louis			
07/07/04			B027: Comparison	Comparison
08/07/04	INTEX 3: St Louis to East Coast			
09/07/04		Boston and Canadian fires		
10/07/04	INTEX 4: South East US			
11/07/04		Boston at night		
12/07/04	INTEX 5: South East US and Mid-West		B028: Transit (Alaskan plume)	
13/07/04				
14/07/04				
15/07/04	INTEX 6: Penn State and transit	New York plume (1) and meet with balloons	B029: Low level and fires	
16/07/04				
17/07/04			B030: First good lagrangian opportunity	
18/07/04	INTEX 7: Newfoundland			
19/07/04			B031: New York plume (2)	
20/07/04	INTEX 8: South East US	New York City (1)	B032: Alaskan fires	
21/07/04		New York City (2)		
22/07/04	INTEX 9: Comparison and East Coast	New York City (3) and comparison	B033: Low level pollution and ENVISAT underpass	New York plume (3) (West of Portugal)
23/07/04				
24/07/04				
25/07/04	INTEX 10: South East US and East Coast	Montour power plant	B034: Out of Africa	New York City (4) (West of Ireland)
26/07/04				New York City (5) (English Channel)
27/07/04		Warm conveyor belt (1) and thunderstorm		
28/07/04	INTEX 11: Comparison and upper level warm conveyor belt (1)	Warm conveyor belt (2) and fire	B035: Comparison	
29/07/04			B036: Upper level warm conveyor belt (2)	
30/07/04				Ship emissions
31/07/04	INTEX 12: Comparison and Bermuda High	Comparison and New York City at night	B037: Low level warm conveyor belt (1)	Upper level warm conveyor belt (3)
01/08/04			B038: Low level warm conveyor belt (2)	
02/08/04				
03/08/04			B039: Transit and comparison	Comparison

Key: → Probable lagrangian success → Possible lagrangian success Aircraft intercomparisons are highlighted in blue

Figure 3.5 – Summary of ICARTT flights with possible and probable Lagrangian opportunities marked [Methven, 2004b]

### 3.5 PERCA performance

Overall, the PERCA performed well during ITOP, with data coverage for nearly every flight. The majority of problems were due to the sample flows falling. Each channel of the PERCA pulls 2 slpm through the inlets, on to the detectors and then the pump. The pump installed on the aircraft was not able to pull the required flow as the altitude of the aircraft increased owing to the reduced backing (atmospheric) pressure at those altitudes. This has caused difficulties in extracting data for some of the higher altitude runs.

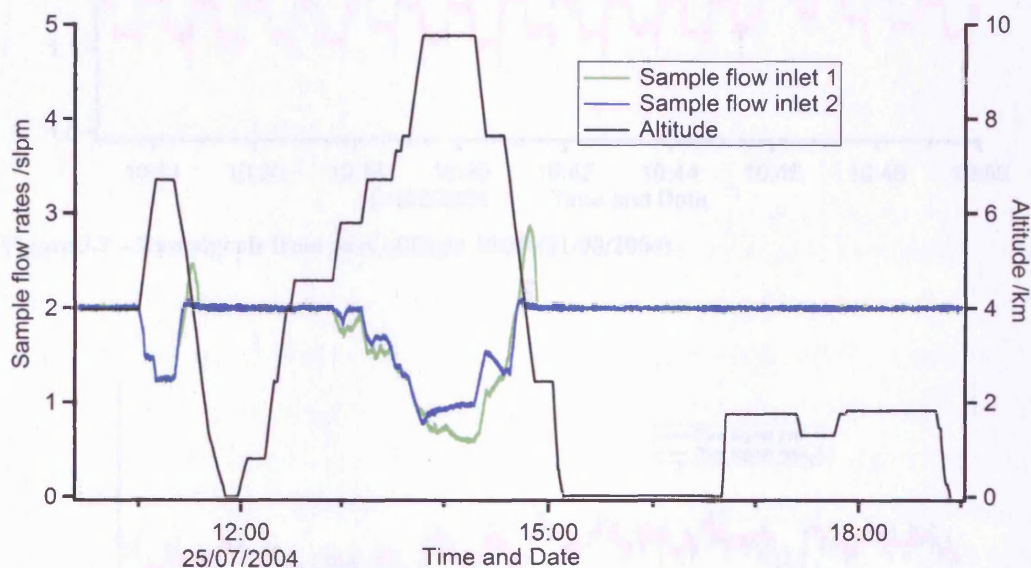


Figure 3.6 – Graph showing drop of sample flow rates with altitude from flight B034

As detailed in Chapter 2, the raw data that are obtained from the PERCA is a voltage from each detector, which is directly proportional to  $\text{NO}_2$  whilst in the linear region of the detectors. Upon calibration these are converted into a peroxy radical signal. The first indication that peroxy radicals are present however, is modulation of the raw signals. The modulation occurs due to the switching between background and amplification modes, as detailed in Chapter 2. Figure 3.7 shows raw signals from ITOP, Figure 3.8 shows raw signals from relatively clean Atlantic air during the NAMBLEX (North Atlantic Marine Boundary Layer EXperiment) campaign that was situated at the Mace Head Observatory on the west coast of

Ireland [Fleming, 2005], and Figure 3.9 are raw signals recorded at Cape Grim, Tasmania showing (b) very clean Southern Hemisphere background and (c) semi-polluted air [Monks, 2007].

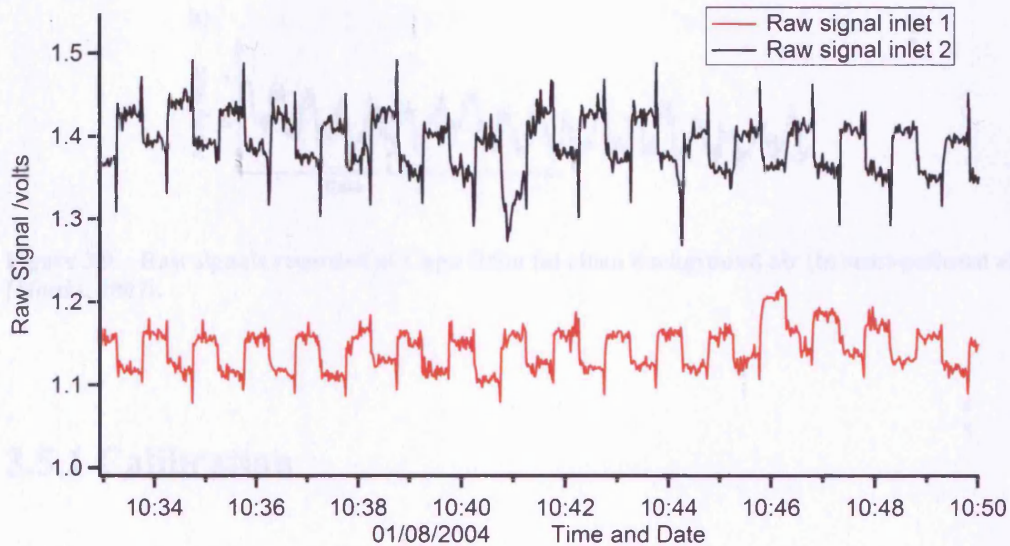


Figure 3.7 – Raw signals from part of flight B038 (01/08/2004)

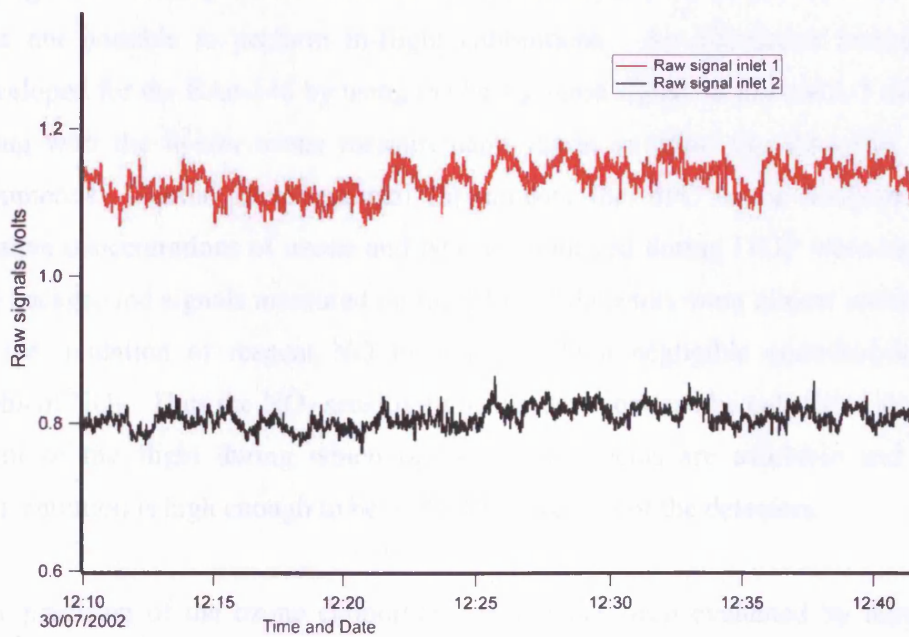


Figure 3.8 – Raw signals from NAMBLEX [Fleming, 2005]

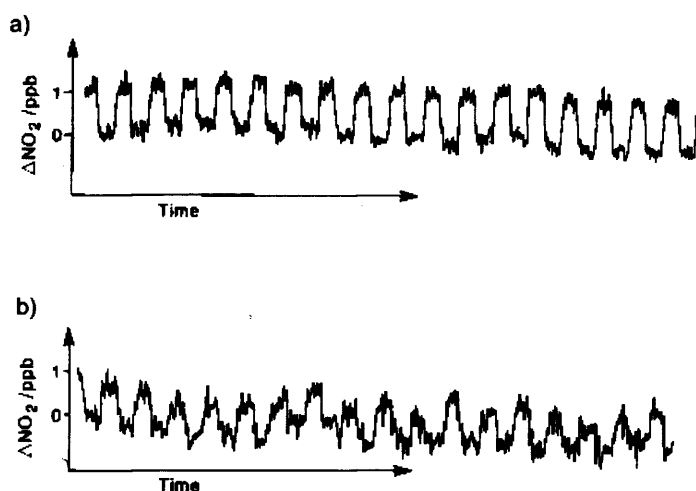


Figure 3.9 – Raw signals recorded at Cape Grim (a) clean background air (b) semi-polluted air [Monks, 2007].

### 3.5.1 Calibration

Ordinarily the LMA-3  $\text{NO}_2$  detectors are calibrated by mixing the output from a VICI Metronics  $\text{NO}_2$  wafer permeation device with varying flows of zero air, but owing to technical problems with the calibration system on-board the BAe-146, it was not possible to perform in-flight calibrations. An alternative method was developed for the BAe-146 by using the background signal on the LMA-3 detectors along with the *in-situ* ozone measurements made on-board the BAe-146 with a commercial Thermo Environmental Instruments Inc. 49C ozone analyser. The relative concentrations of ozone and  $\text{NO}_2$  encountered during ITOP were such that the background signals measured on the LMA-3 detectors were almost entirely due to the oxidation of reagent NO by ozone with a negligible contribution from ambient  $\text{NO}_2$ . Thus the  $\text{NO}_2$  sensitivity of the detectors can be calculated for every point of the flight during which ozone measurements are available and ozone concentration is high enough to be in the linear region of the detectors.

The precision of the ozone calibration method has been evaluated by taking the standard deviation of the ratio of ozone concentration divided by the background signal as a percentage of the mean of the same for a series of straight and level runs within a flight. The precision was determined to be around 6%.

A graph of a period of constant altitude from flight B037 on 31/07/2004 is shown in Figure 3.10. The background and ozone signals are well correlated, with the period shown having an  $r^2$  of 0.98.

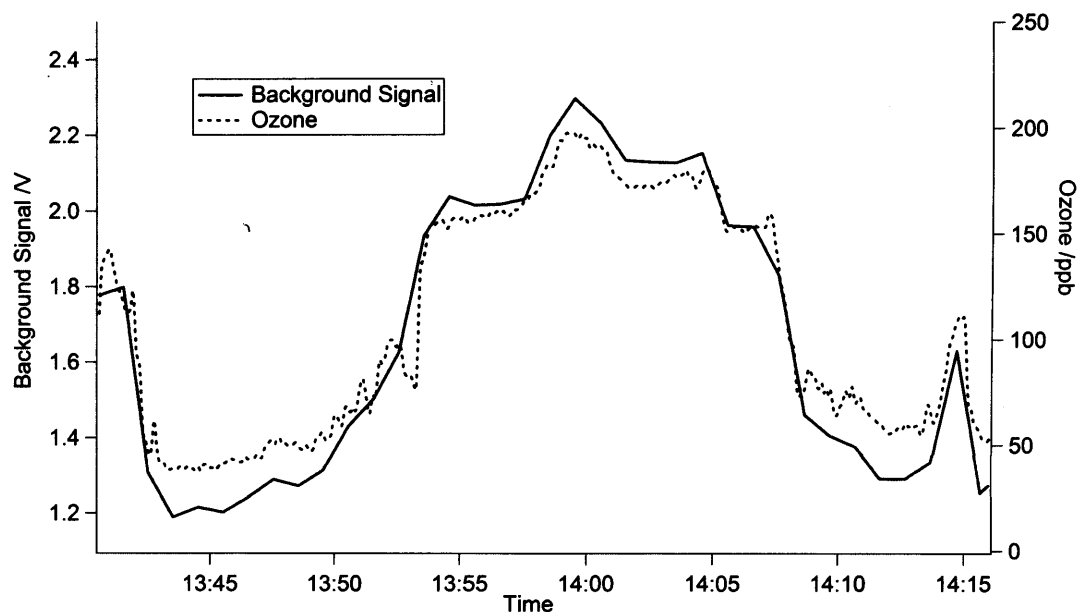


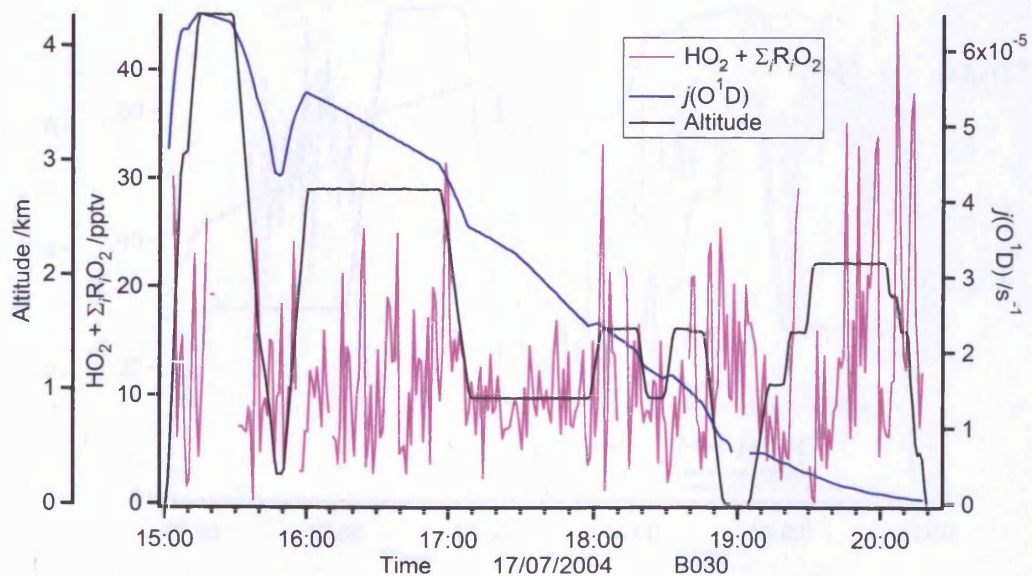
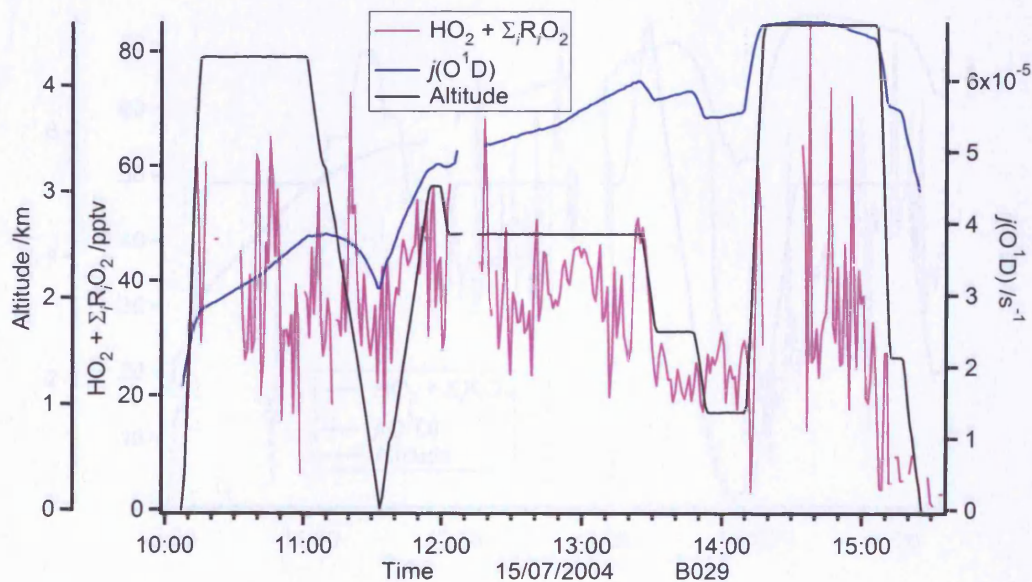
**Figure 3.10 – Example of background signal from a  $\text{NO}_2$  detector tracking ozone concentrations during flight B037 on 31/07/2004**

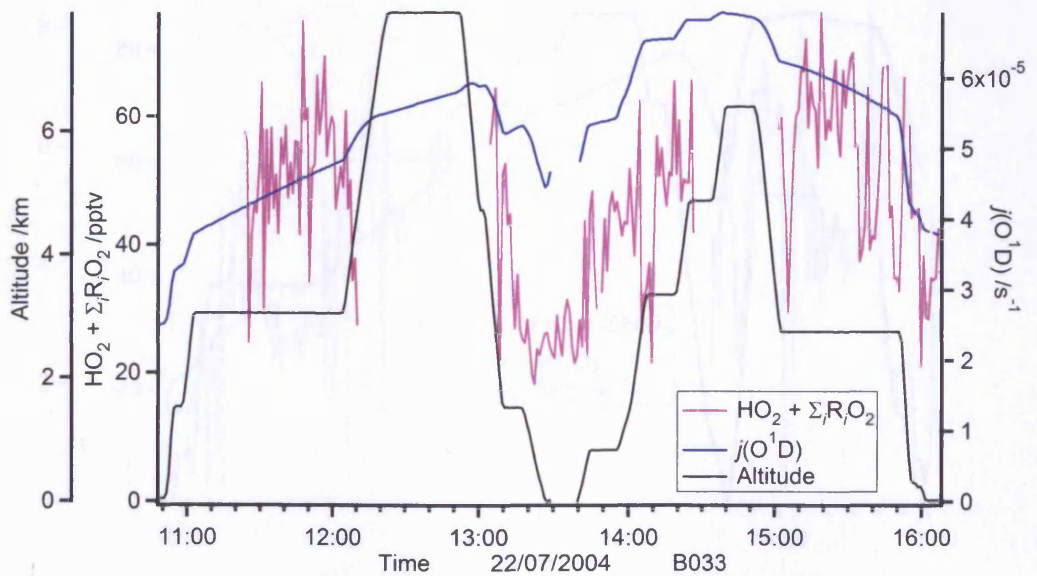
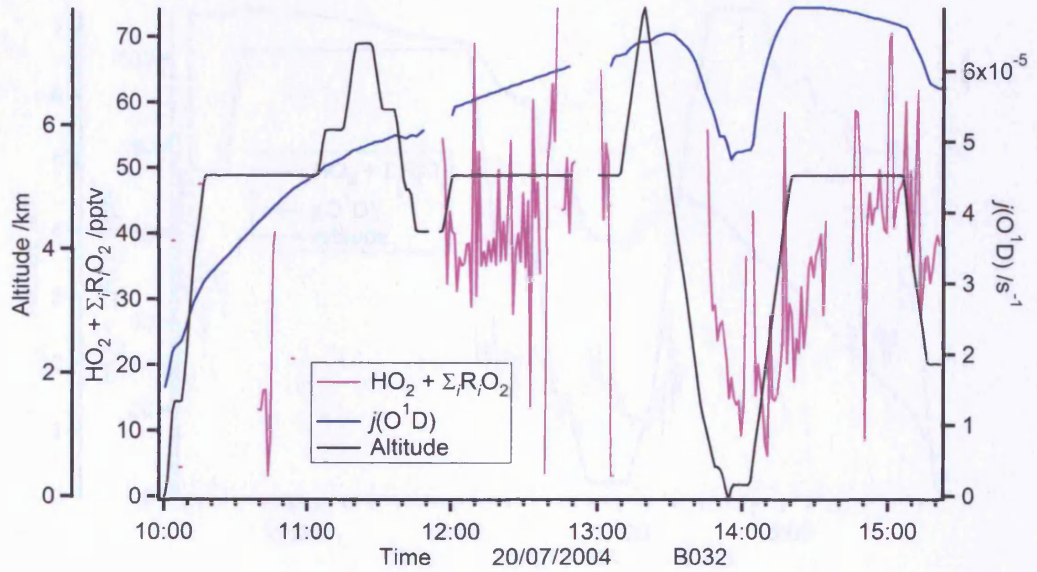
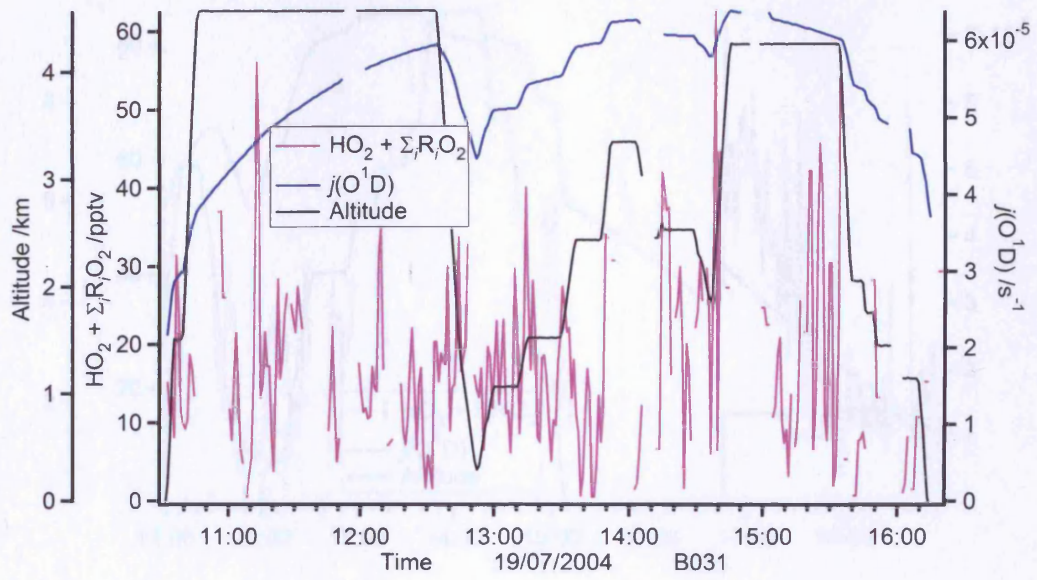
It was also not possible to perform in-flight chain length calibrations, and consequently calibrations were performed on the ground only. It would be ideal to perform chain length calibrations at different altitudes, as the chain chemistry reactions in the inlets have temperature and pressure dependent rate constants. However, a series of in-flight calibrations were performed by [Green, *et al.*, 2003], where no clear chain length dependence on altitude was seen. All reported chain lengths were within the error reported in section 2.7 for chain length calculation from the chain length calibrations carried out on the ground. As such, although in-flight chain length calibrations would be ideal, to a reasonable approximation using ground calibrations is acceptable.

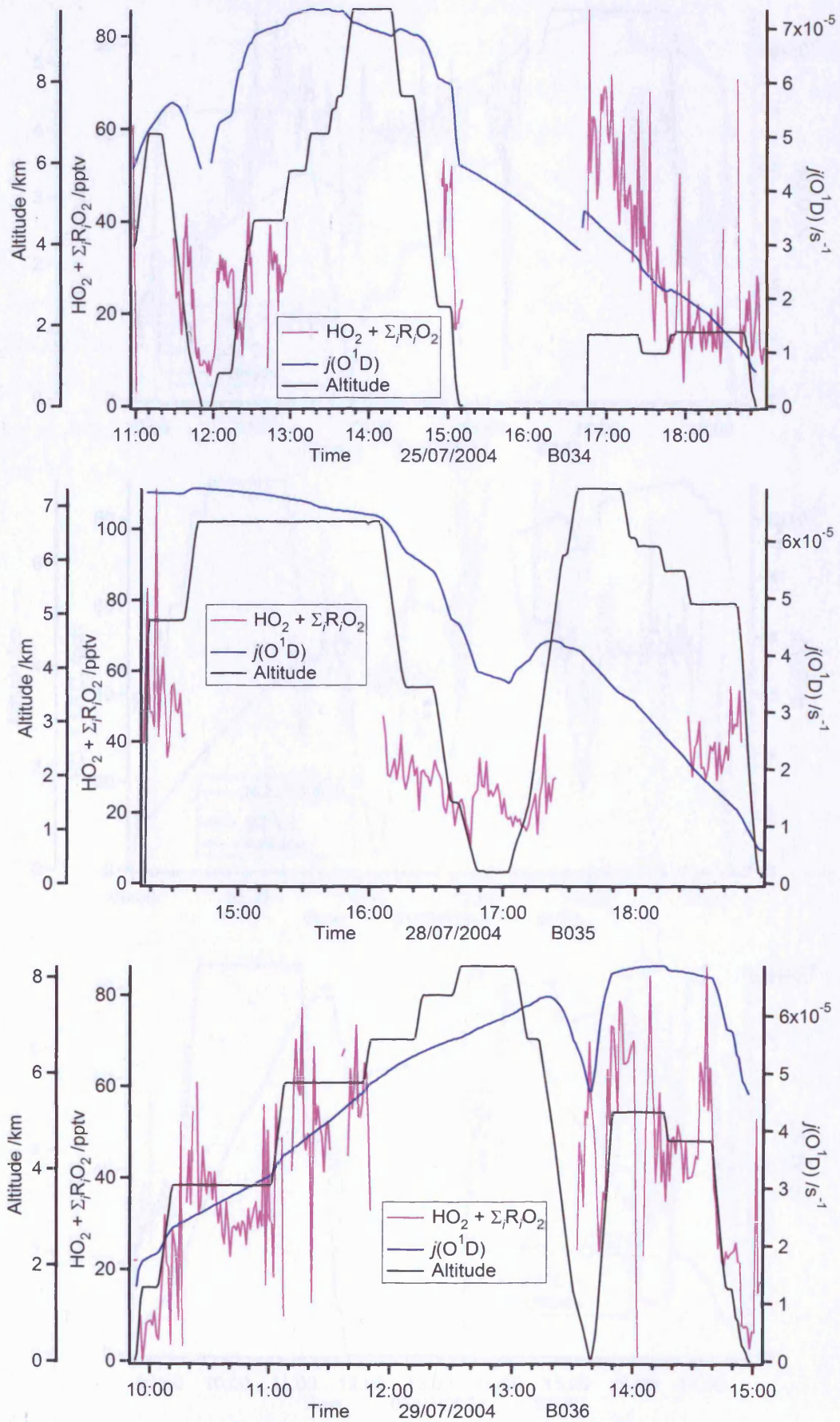
## 3.6 Results

### 3.6.1 Radicals and tracers

Of the twelve ITOP flights, the PERCA was operated on all but the initial transit flight. There were gaps in the data during a flight, usually as a result of sample flow problems as outlined in section 3.5, but nonetheless, a significant data set was recorded. The peroxy radical temporal profile for each flight along with modelled  $j(\text{O}^1\text{D})$  (see later in this section) and altitude is shown in Figure 3.11.





Figure 3.11 - Temporal profiles of  $\text{HO}_2 + \Sigma R_i \text{O}_2$  and  $j(\text{O}^1\text{D})$  for balloon flights B034, B035 and B036.

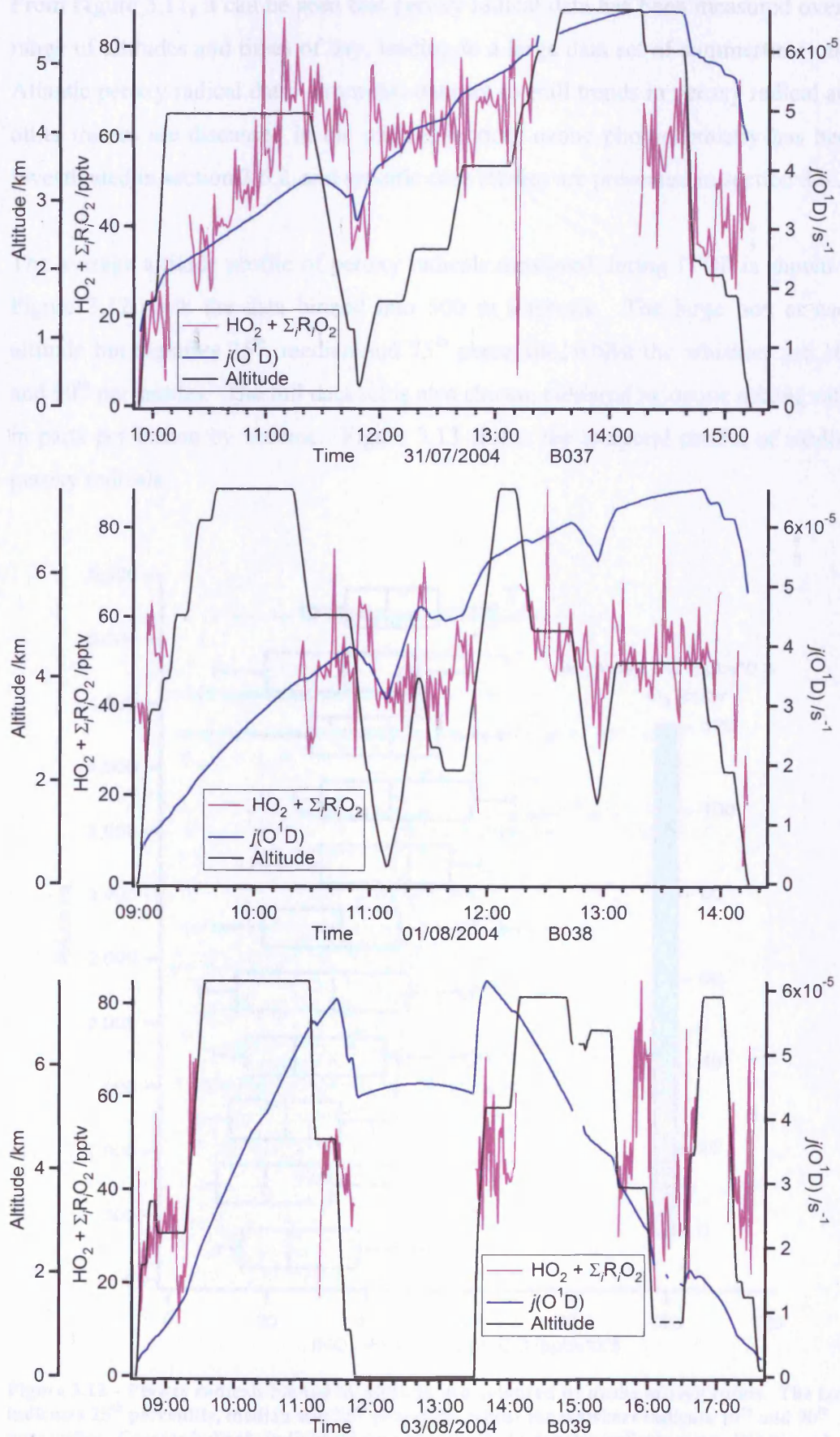


Figure 3.11 – Temporal profiles of peroxy radicals,  $j(O^1D)$  and altitude for flights B029 – B039

From Figure 3.11, it can be seen that peroxy radical data has been measured over a range of altitudes and times of day, leading to a large data set of summertime mid-Atlantic peroxy radical data. From this data set overall trends in peroxy radical and other tracers are discussed in the current section, ozone photochemistry has been investigated in section 3.6.2, and specific case studies are presented in section 3.6.3.

The average altitude profile of peroxy radicals measured during ITOP is shown in Figure 3.12, with the data binned into 500 m intervals. The large box at each altitude bin signifies 25<sup>th</sup>, median and 75<sup>th</sup> percentile, whilst the whiskers are 10<sup>th</sup> and 90<sup>th</sup> percentiles. The full data set is also shown, coloured by ozone mixing ratio in parts per billion by volume. Figure 3.13 shows the temporal profile of median peroxy radicals.

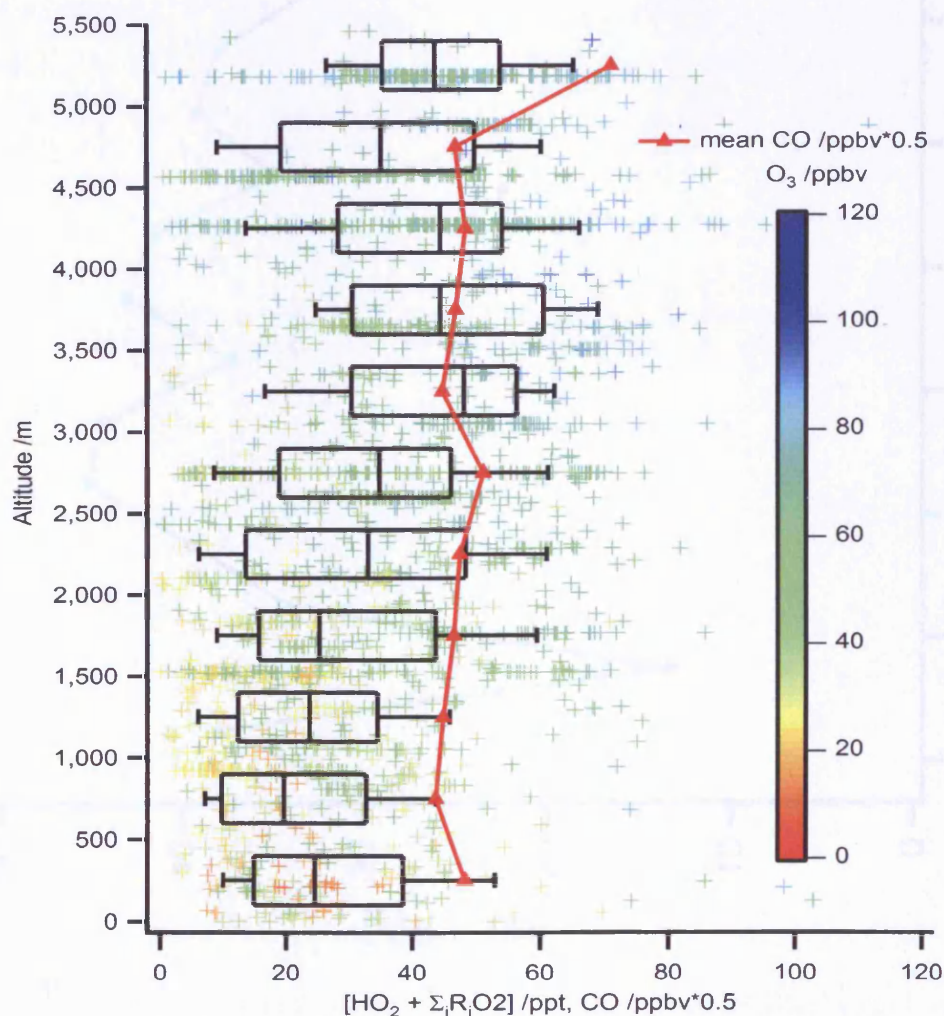


Figure 3.12 – Peroxy radicals binned by altitude and coloured by ozone mixing ratios. The box indicates 25<sup>th</sup> percentile, median and 75<sup>th</sup> percentile whilst the whiskers indicate 10<sup>th</sup> and 90<sup>th</sup> percentiles. Crosses indicate individual data points. Red triangles indicate mean CO binned by altitude.

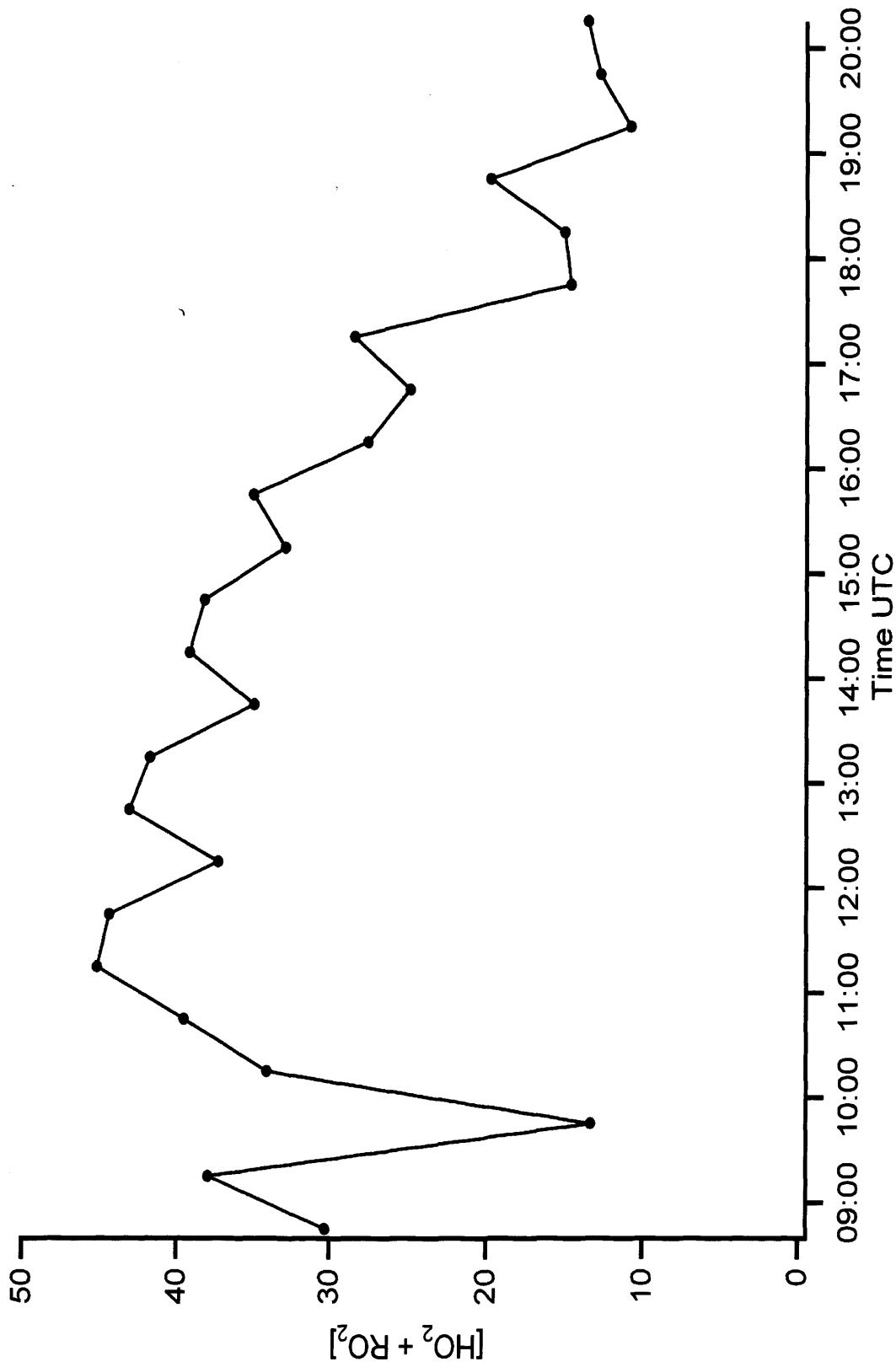


Figure 3.13 – Median Peroxy radicals binned by time UTC.

Figure 3.14 and Figure 3.15 show the campaign data set for NO and O<sub>3</sub> respectively, binned by altitude. Details of other measurements made during ITOP can be found in the ITOP overview paper [Lewis, *et al.*, 2006]. It should be noted that grouping the data by altitude in this way results in data from different latitudes, longitudes and times of day being grouped together, and thus one bin may be influenced heavily by a single air mass as will be discussed later.

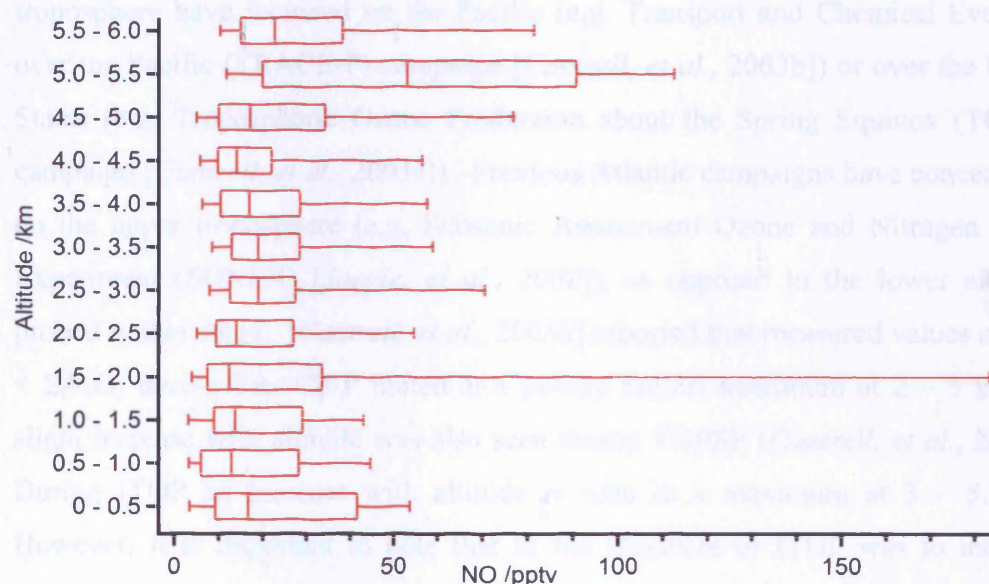


Figure 3.14 – Campaign data set for NO binned by altitude. The box indicates 25<sup>th</sup> percentile, median and 75<sup>th</sup> percentile whilst the whiskers indicate 10<sup>th</sup> and 90<sup>th</sup> percentiles.

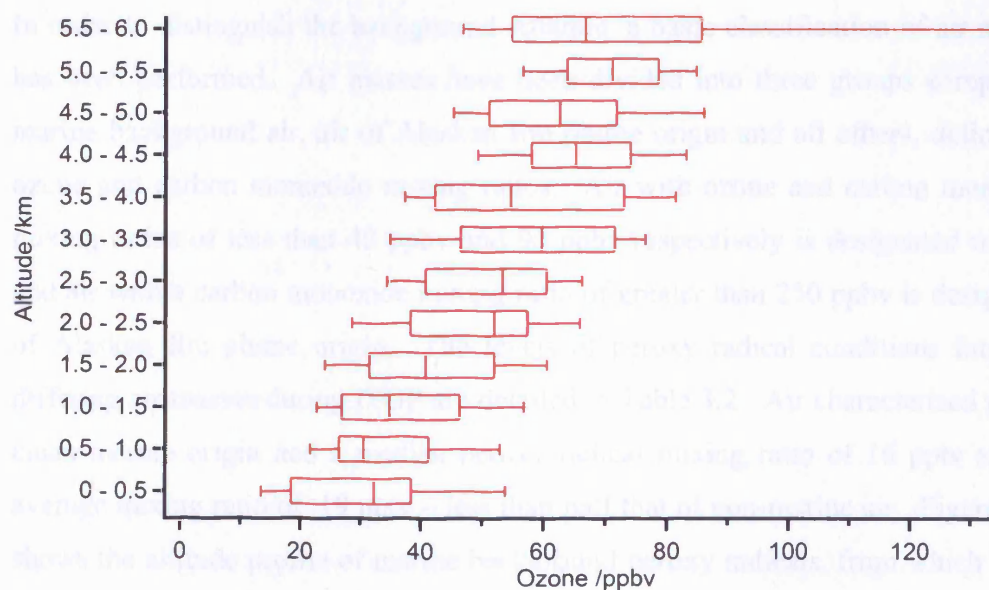


Figure 3.15 – Campaign data set for O<sub>3</sub> binned by altitude. The box indicates 25<sup>th</sup> percentile, median and 75<sup>th</sup> percentile whilst the whiskers indicate 10<sup>th</sup> and 90<sup>th</sup> percentiles.

The overall peroxy radical distribution increases with altitude from an average of 28 pptv at 0 – 0.5 km to 44 pptv at 5 – 5.5 km. There are very few points over 5.5 km owing to the inability of the installed pumping system to maintain a constant flow through the inlets at the lower ambient pressures found at higher altitudes and thus points over 5.5 km are not considered.

Previous aircraft campaigns that have measured peroxy radicals in the lower/mid troposphere have focussed on the Pacific (e.g. Transport and Chemical Evolution over the Pacific (TRACE-P) campaign [Cantrell, *et al.*, 2003b]) or over the United States (e.g. Tropospheric Ozone Production about the Spring Equinox (TOPSE) campaign [Cantrell, *et al.*, 2003a]). Previous Atlantic campaigns have concentrated on the upper troposphere (e.g. Subsonic Assessment Ozone and Nitrogen Oxide Experiment (SONEX) [Jaegle, *et al.*, 2000]), as opposed to the lower altitudes probed in this study. [Cantrell, *et al.*, 2003b] reported that measured values of  $\text{HO}_2 + \Sigma_i \text{R}_i\text{O}_2$  during TRACE-P hinted at a peroxy radical maximum at 2 – 5 km. A slight increase with altitude was also seen during TOPSE [Cantrell, *et al.*, 2003a]. During ITOP an increase with altitude is seen to a maximum at 3 – 5.5 km. However, it is important to note that as the objective of ITOP was to intercept polluted air masses and most of these interceptions happened out of the planetary boundary layer, the profile presented here for all flights is not necessarily that of the background mid-Atlantic.

In order to distinguish the background Atlantic, a basic classification of air masses has been performed. Air masses have been divided into three groups comprising marine background air, air of Alaskan fire plume origin and all others, defined by ozone and carbon monoxide mixing ratios. Air with ozone and carbon monoxide mixing ratios of less than 40 ppbv and 90 ppbv respectively is designated marine, and air with a carbon monoxide mixing ratio of greater than 250 ppbv is designated of Alaskan fire plume origin. The levels of peroxy radical conditions found in differing air masses during ITOP are detailed in Table 3.2. Air characterised with a clean marine origin had a median peroxy radical mixing ratio of 16 pptv and an average mixing ratio of 19 pptv – less than half that of non-marine air. Figure 3.16 shows the altitude profile of marine background peroxy radicals, from which it can be seen that there is no discernable altitude trend.

	$[\text{HO}_2 + \text{RO}_2] / \text{pptv}$		
	Marine Air ( $\text{O}_3 < 40$ ppbv, $\text{CO} < 90$ ppbv)	Alaskan Fire Plume ( $\text{CO} > 250$ ppbv)	All Others
<b>Mean</b>	19	36	41
<b>Standard Deviation</b>	13	18	19
<b>Median</b>	16	37	42
<b>10<sup>th</sup> Percentile</b>	5	12	15
<b>90<sup>th</sup> Percentile</b>	38	59	65

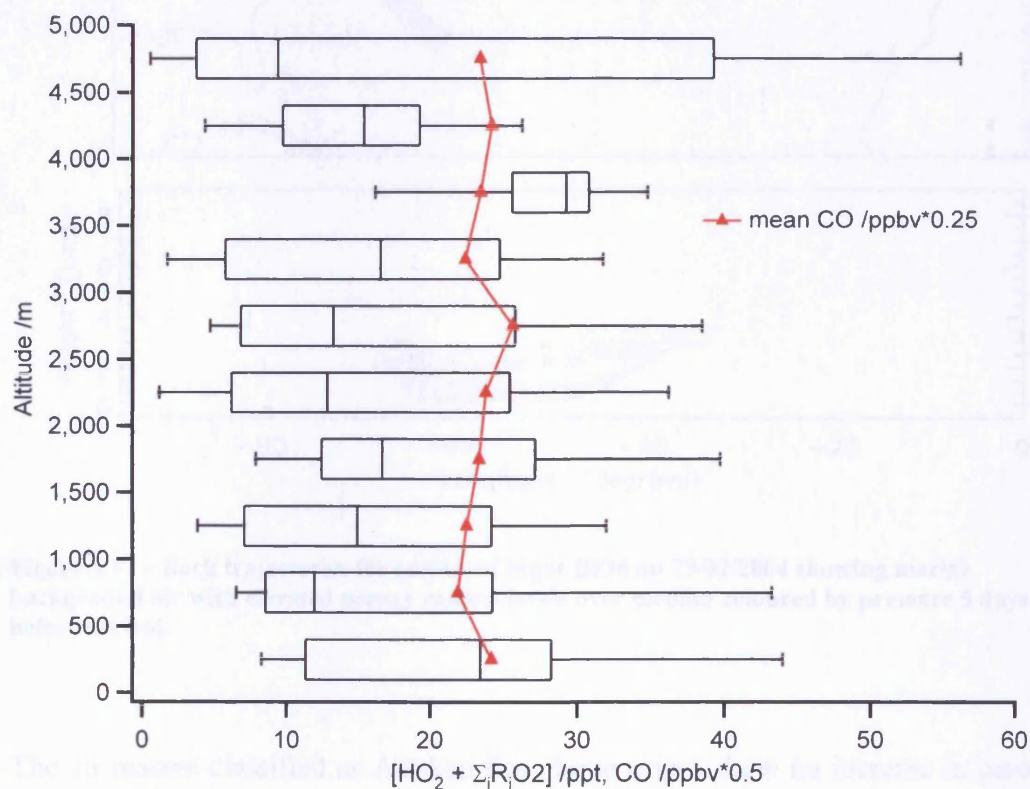
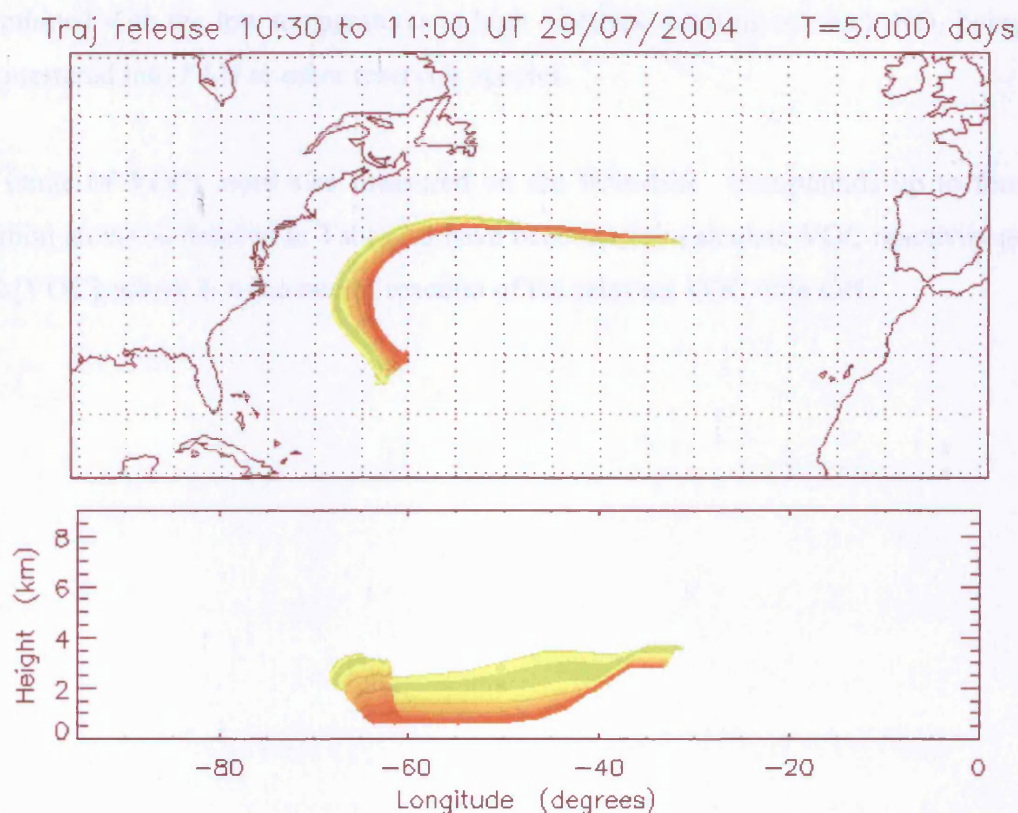
Table 3.2 – Mean  $[\text{HO}_2 + \Sigma_i \text{R}_i \text{O}_2]$  binned into differing air masses.

Figure 3.16 - Altitude profile of peroxy radicals in air designated of marine origin ( $\text{O}_3 < 40$  ppbv,  $\text{CO} < 90$  ppbv). The box indicates 25<sup>th</sup> percentile, median and 75<sup>th</sup> percentile whilst the whiskers indicate 10<sup>th</sup> and 90<sup>th</sup> percentiles. Red triangles indicate mean CO binned by altitude.

An apparent anomaly in the altitude profile of peroxy radicals in marine air shows a distinct peak at 3.5 – 4 km. The air sampled at this altitude was almost exclusively from flight B036 on 29/07/2004. Flexpart [Stohl, *et al.*, 2005] emission tracers for the section of interest of flight B036 show very low concentrations of aged

American emissions, and back trajectories [Methven, *et al.*, 2006] show air of Atlantic background as shown in Figure 3.17.



**Figure 3.17 – Back trajectories for section of flight B036 on 29/07/2004 showing marine background air with elevated peroxy radical levels over median coloured by pressure 5 days before arrival.**

The air masses classified as Alaskan fire plume origin show no increase in peroxy radicals over standard air masses but a minor decrease in both mean and median of 41 pptv to 36 pptv and 42 pptv to 37 pptv respectively. There are only 35 data points available for Alaskan fire plume air masses as the majority of the air masses associated with Alaskan fire plumes encountered were at high altitude where the PERCA had difficulty sampling as noted previously and it is therefore difficult to draw concrete conclusions. However, the fact that peroxy radicals were not elevated in Alaskan fire plume air-masses over the levels found in other non-marine air-masses whilst the median concentrations of other species were greatly enhanced, e.g. median NO concentrations were enhanced by over a factor of 5, and median PAN (peroxy acetyl nitrate) concentrations were enhanced by more than a factor of

8, is of interest. Furthermore, within the Alaskan fire plume, airmasses with extremely high CO concentrations of up to 600 ppbv were observed with no associated enhancement of ozone. The non-enhancement of peroxy radicals within Alaskan fire plume air-masses is likely a result of the lack of enhanced ozone, combined with the low temperatures at high altitudes resulting in much NO<sub>2</sub> being sequestered into PAN or other reservoir species.

A range of VOCs were also measured on the BAe-146. Compounds up to four carbon atoms as detailed in Table 3.3 have been used to calculate VOC reactivity as  $\sum_i k_i [\text{VOC}]_i$  where  $k_i$  is the rate of reaction of the relevant VOC with OH.

Compound	Measurement Technique	Institution	Reaction rate reference
carbon monoxide	Aero-Laser GmbH AL5002 Fast Carbon Monoxide (CO) Monitor <sup>1</sup> .	FAAM	[Atkinson, et al., 2004]
methane <sup>2</sup>	n/a	n/a	[Atkinson, et al., 2006]
ethane	Dual-channel GC-FID of WAS	York	[Atkinson, et al., 2006]
ethene	Dual-channel GC-FID of WAS	York	[Atkinson, et al., 2005]
propane	Dual-channel GC-FID of WAS	York	[Atkinson, et al., 2006]
propene	Dual-channel GC-FID of WAS	York	[Atkinson, et al., 2006]
iso-butane	Dual-channel GC-FID of WAS	York	[Atkinson, 2003]
n-butane	Dual-channel GC-FID of WAS	York	[Atkinson, et al., 2006]
acetylene	Dual-channel GC-FID of WAS	York	[Atkinson, et al., 1992]
trans-2-butene	Dual-channel GC-FID of WAS	York	[Atkinson, 1986]
1-butene	Dual-channel GC-FID of WAS	York	[Atkinson, 1986]
iso-butene	Dual-channel GC-FID of WAS	York	[Atkinson, 1986]
cis-2-butene	Dual-channel GC-FID of WAS	York	[Atkinson, 1986]
1,2-butadiene	Dual-channel GC-FID of WAS	York	[Atkinson, 1986] <sup>3</sup>
1,3-butadiene	Dual-channel GC-FID of WAS	York	[Atkinson, 1986]
propyne	Dual-channel GC-FID of WAS	York	[Boodaghians, et al., 1987]
isoprene	Dual-channel GC-FID of WAS	York	[Atkinson, 1986]
acetaldehyde	Dual-channel GC-FID of WAS	York	[Atkinson, et al., 2006]
methanol	Dual-channel GC-FID of WAS	York	[Atkinson, et al., 2006]
acetone	Dual-channel GC-FID of WAS	York	[Atkinson, et al., 2006]
formaldehyde	Hantschz fluorescence	UEA	[Atkinson, et al., 2006]

Table 3.3 – VOCs and measurement techniques used to calculate VOC reactivity. <sup>1</sup>[Gerbig, et al., 1999], <sup>2</sup>methane was set to a constant 1750 ppbv [Dlugokencky, et al., 2003], <sup>3</sup>rate for OH + 1,3-butadiene used.

Methane was not measured on board the BAe-146 and has been set to a constant 1750 ppbv [Dlugokencky, *et al.*, 2003]. CO and methane make a significant contribution as is expected, however the additional importance of non-methane hydrocarbons can be seen from Figure 3.18.

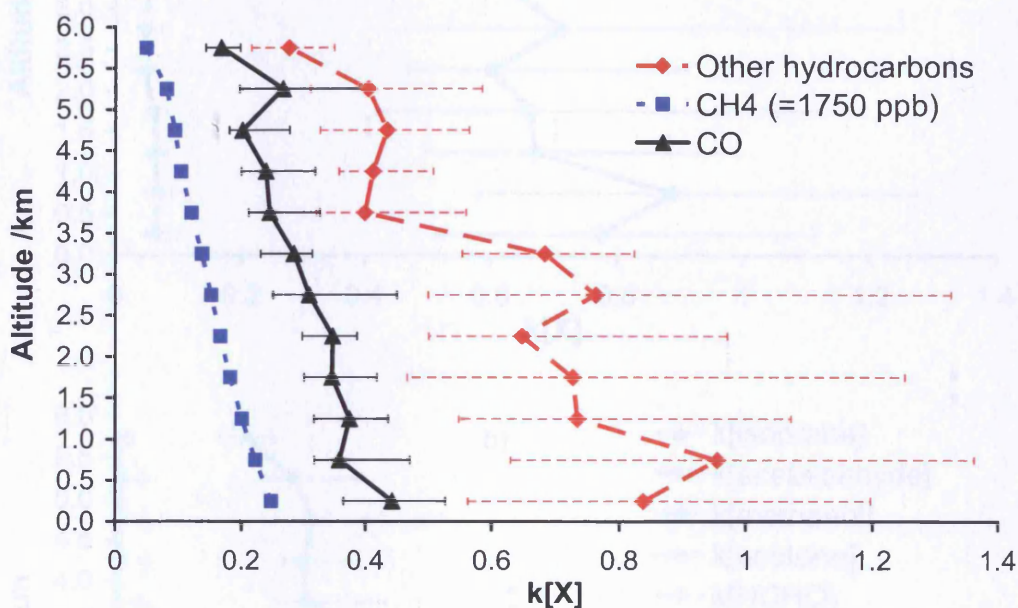


**Figure 3.18** – Relative contributions of methane, carbon monoxide, and other non-methane hydrocarbons to OH reactivity. Points represent median values and error bars 25<sup>th</sup> and 75<sup>th</sup> percentiles. [X] is in molecules cm<sup>-3</sup>.

The decrease in OH reactivity attributed to methane with altitude even though the concentration of methane is set to 1750 ppbv is owing to the temperature dependence of the OH + CH<sub>4</sub> rate constant. The combined non-methane hydrocarbons contribute more to OH reactivity than methane and carbon monoxide combined, and are especially important under 3.5 km. From the measured non-methane hydrocarbons, it is the oxygenated VOCs that contribute the most to OH loss as indicated in Figure 3.19, with the most significant of those being formaldehyde and acetaldehyde. Indeed, acetaldehyde alone is responsible for almost as much OH reactivity as carbon monoxide and methane together.

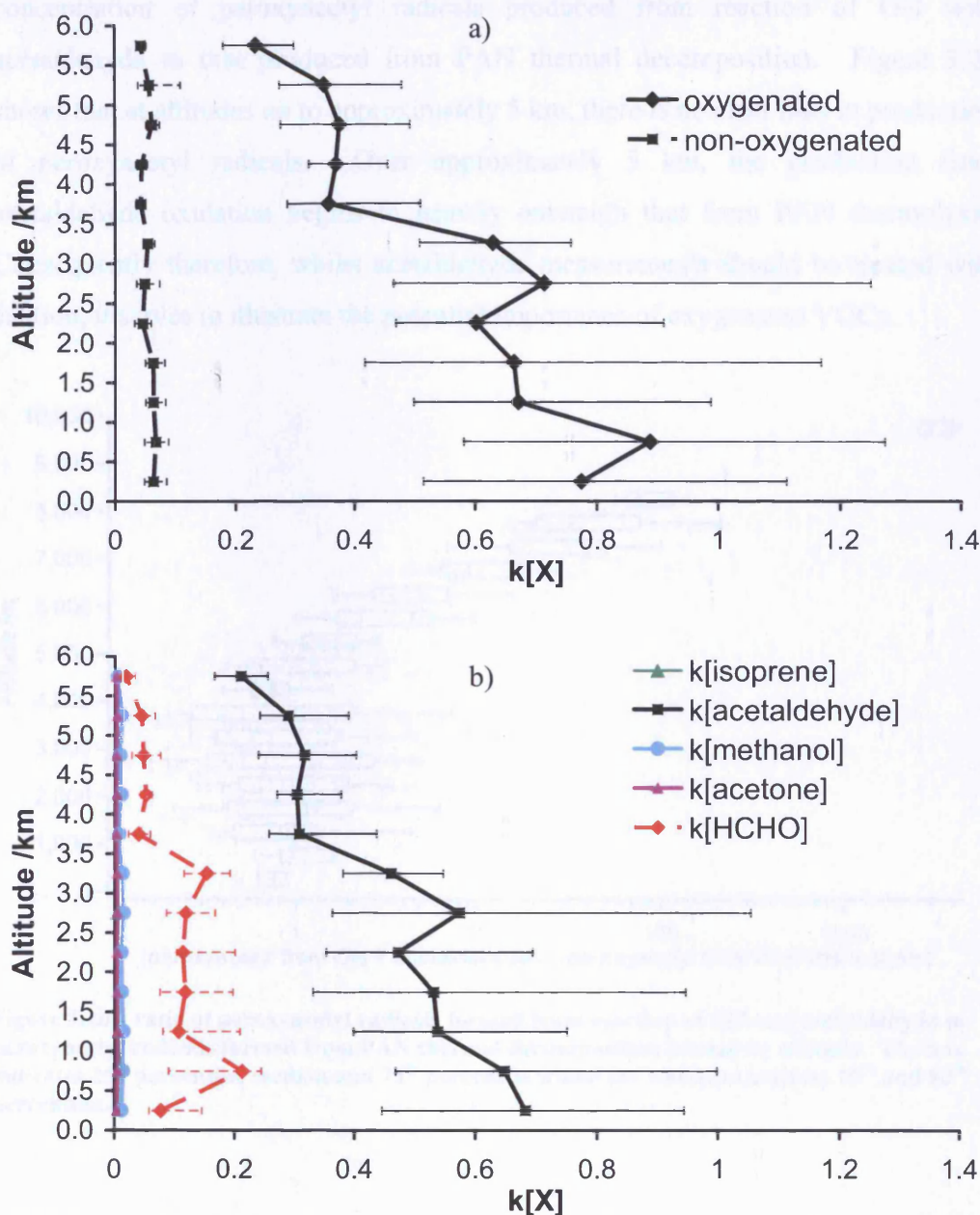


Figure 3.19 – a) Relative contributions of oxygenated and non-oxygenated  $C_2-C_4$  non-methane hydrocarbons to OH reactivity and b) contribution of various oxygenates to OH reactivity. Points represent median values and error bars 25<sup>th</sup> and 75<sup>th</sup> percentiles.  $[X]$  is in molecules  $cm^{-3}$

However, recent studies have demonstrated that acetaldehyde artefacts may be present in measured data leading to erroneously high concentrations of acetaldehyde being reported [Apel, et al., 2003; Northway, et al., 2004]. It is worth noting that the artefact reported [Apel, et al., 2003; Northway, et al., 2004] is correlated with ozone, but acetaldehyde data measured during ITOP does not correlate with ozone. Furthermore, the veracity of the acetaldehyde data can be checked by comparing the

concentration of peroxyacetyl radicals produced from reaction of OH with acetaldehyde to that produced from PAN thermal decomposition. Figure 3.20 shows that at altitudes up to approximately 5 km, there is no clear bias in production of peroxyacetyl radicals. Over approximately 5 km, the production from acetaldehyde oxidation begins to heavily outweigh that from PAN thermolysis. Consequently therefore, whilst acetaldehyde measurements should be treated with caution, it serves to illustrate the potential importance of oxygenated VOCs.

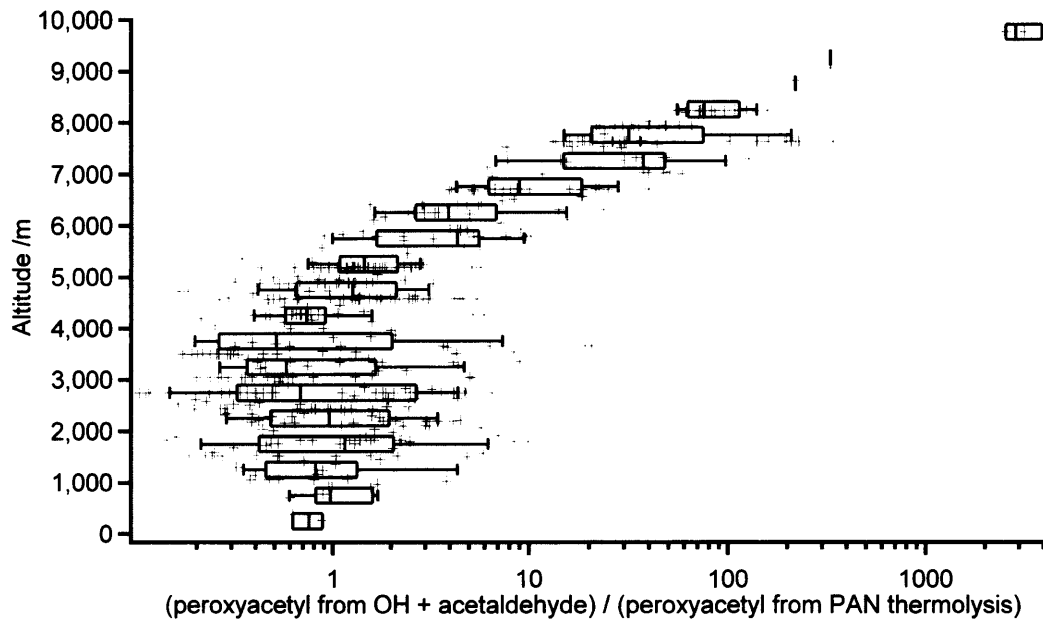


Figure 3.20 – ratio of peroxyacetyl radicals formed from reaction of OH and acetaldehyde to peroxyacetyl radicals formed from PAN thermal decomposition binned by altitude. The box indicates 25<sup>th</sup> percentile, median and 75<sup>th</sup> percentile whilst the whiskers indicate 10<sup>th</sup> and 90<sup>th</sup> percentiles.

A steady state analysis of the production and loss of peroxy radicals during ITOP has been carried out based on the method described by Mihele and Hastie [Mihele and Hastie, 2003]. In this analysis it is assumed that peroxy radicals are in steady state, thus

$$\frac{d[\text{HO}_2 + \sum_i \text{R}_i \text{O}_2]}{dt} = P_{[\text{HO}_2 + \sum_i \text{R}_i \text{O}_2]} - L_{\text{SR}} - L_{\text{NO}_x} = 0 \quad (\text{A})$$

where  $P_{[\text{HO}_2 + \sum_i \text{R}_i \text{O}_2]}$  is the rate of production of radicals,  $L_{\text{SR}}$  is the rate of loss of peroxy radicals owing to self-reaction, and  $L_{\text{NO}_x}$  is the rate of loss of peroxy radicals owing to reaction with  $\text{NO}_x$ . Assuming the major radical source is ozone photolysis

and introducing  $\gamma$  as an additional fractional radical production, the radical production term becomes:

$$P_{[\text{HO}_2 + \Sigma_i \text{R}_i \text{O}_2]} = 2f \cdot j(\text{O}^1\text{D}) \cdot [\text{O}_3] \cdot (1 + \gamma) \quad (\text{B})$$

where  $f$  is a measure of the proportion of  $\text{O}^1\text{D}$  produced that consequently reacts with water vapour and is given by equation C,

$$f = \frac{k_{3.1}[\text{H}_2\text{O}]}{k_{3.1}[\text{H}_2\text{O}] + k_{3.2}[\text{M}]} \quad (\text{C})$$

where  $k_{3.1}$  and  $k_{3.2}$  are the reaction rates for reaction 3.1 and reaction 3.2 respectively.



It may appear that there is an assumption in equation (B) that all OH formed by the photolysis of ozone to form  $\text{O}^1\text{D}$  and subsequent reaction of this  $\text{O}^1\text{D}$  with water vapour, will then react with VOCs to form peroxy radicals, with potential loss of OH by reaction with  $\text{NO}_2$  being ignored. However, OH loss by reaction with  $\text{NO}_2$  is accounted for in the peroxy radical loss due to reaction with  $\text{NO}_x$  term ( $L_{\text{NO}_x}$ ) in reaction (A).

Combining self-reaction rates of  $\text{HO}_2$  and  $\Sigma_i \text{R}_i \text{O}_2$  into a single rate constant  $k_{\text{self}}$ , setting  $\beta = L_{\text{NO}_x}/L_{\text{SR}}$  so as to describe the dominant loss mechanism and introducing parameter  $\alpha$  to describe the partitioning between  $\text{HO}_2$  and  $\text{RO}_2$ , thus:

$$\alpha = \frac{[\text{HO}_2]}{[\text{HO}_2 + \Sigma_i \text{R}_i \text{O}_2]} \quad (\text{D})$$

gives the radical loss terms as:

$$L_{[\text{HO}_2 + \Sigma_i \text{R}_i \text{O}_2]} = 2 \cdot k_{\text{self}} \cdot \alpha (1 + \beta) \cdot [\text{HO}_2 + \Sigma_i \text{R}_i \text{O}_2]^2 \quad (\text{E})$$

where the loss owing to self-reaction is given by the following equations,



which leads to the following self-reaction loss rate,

$$L_{\text{SR}} = 2k_{3.3}[\text{HO}_2][\text{HO}_2] + 2k_{3.4}[\text{HO}_2][\text{RO}_2] + 2k_{3.5}[\text{RO}_2][\text{RO}_2] \quad (\text{F})$$

Assuming that  $k_{3.3} \approx k_{3.4}$ , and that  $k_{3.5}$  is slow enough that reaction (3.5) can be discarded, Equation (F) reduces to that found in *Mihele and Hastie* [*Mihele and Hastie, 2003*]:

$$L_{\text{SR}} = 2.k_{\text{self}}.\alpha.[\text{HO}_2 + \sum_i \text{R}_i \text{O}_2]^2 \quad (\text{G})$$

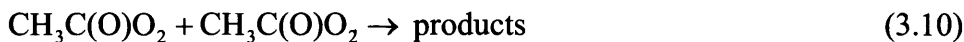
However, the assumption in the derivation of the self-reaction loss rate that  $k_{3.3} \approx k_{3.4}$  only holds if  $\text{RO}_2$  is solely in the form of  $\text{CH}_3\text{O}_2$ , neglecting the contribution of other species. The OH reactivity calculations earlier in this chapter have demonstrated that this assumption does not hold for the conditions encountered during ITOP where non-methane hydrocarbons and especially acetaldehyde are very important in terms of OH reactivity.

If the acetylperoxy radical is introduced along with the ratio of  $\delta = [\text{CH}_3\text{C}(\text{O})\text{O}_2] / ([\text{CH}_3\text{O}_2] + [\text{CH}_3\text{C}(\text{O})\text{O}_2])$ , then the self-reaction loss rate reduces thus:

$$L_{\text{SR}} = 2 \cdot \left( \frac{k_{3.3}\alpha^2 + k_{3.6}\alpha(1-\alpha)(1-\delta) + k_{3.7}(1-\alpha)^2(1-\delta)^2 + k_{3.8}\alpha(1-\alpha)\delta + k_{3.9}(1-\alpha)^2\delta(1-\delta) + k_{3.10}(1-\alpha)^2\delta^2}{k_{3.3}\alpha^2 + k_{3.6}\alpha(1-\alpha)(1-\delta) + k_{3.7}(1-\alpha)^2(1-\delta)^2 + k_{3.8}\alpha(1-\alpha)\delta + k_{3.9}(1-\alpha)^2\delta(1-\delta) + k_{3.10}(1-\alpha)^2\delta^2} \right) [\text{HO}_2 + \sum_i \text{R}_i \text{O}_2]^2 \quad (\text{H})$$

where





and where the rate constants at 1 atmosphere pressure and 298 K are given in Table 3.4.

Reaction	Rate constant <sup>a</sup> /molecule cm <sup>-3</sup> s <sup>-1</sup>	Reference
HO <sub>2</sub> + HO <sub>2</sub>	2.6 × 10 <sup>-12</sup> <sup>b</sup>	[Atkinson, et al., 2006]
HO <sub>2</sub> + CH <sub>3</sub> O <sub>2</sub>	5.2 × 10 <sup>-12</sup>	[Atkinson, et al., 2006]
CH <sub>3</sub> O <sub>2</sub> + CH <sub>3</sub> O <sub>2</sub>	3.5 × 10 <sup>-13</sup>	[Atkinson, et al., 2006]
HO <sub>2</sub> + CH <sub>3</sub> C(O)O <sub>2</sub>	1.4 × 10 <sup>-11</sup>	[Atkinson, et al., 2006]
CH <sub>3</sub> O <sub>2</sub> + CH <sub>3</sub> C(O)O <sub>2</sub>	1.1 × 10 <sup>-11</sup>	[Atkinson, et al., 2006]
CH <sub>3</sub> C(O)O <sub>2</sub> + CH <sub>3</sub> C(O)O <sub>2</sub>	1.6 × 10 <sup>-11</sup>	[Atkinson, et al., 2006]

Table 3.4 – Rate constants for reaction (3.3) and reactions (3.6) – (3.10). <sup>a</sup>At 298K and 1 atmosphere, <sup>b</sup>H<sub>2</sub>O concentration = 2.47 × 10<sup>17</sup> molecule cm<sup>-3</sup>.

It can be seen from Table 3.4 that acetylperoxy is a fast-reacting peroxy radical compared to methyl peroxy. If  $\delta$  is set to 0.5, that is half of the RO<sub>2</sub> present is in the form of acetylperoxy (the remaining half being CH<sub>3</sub>O<sub>2</sub>), then at 298K, the combined peroxy radical self-reaction rate is approximately double the self-reaction rate when  $\delta$  is zero. Further to this, the rate constant for the reaction of acetylperoxy with NO is approximately 2.6 times faster than that for methylperoxy with NO at 298K. Consequently, the loss rate of peroxy radicals through reaction with NO<sub>x</sub> will also be greater than if all the RO<sub>2</sub> were CH<sub>3</sub>O<sub>2</sub>. The importance of this relative to  $\beta$  and  $\gamma$  shall be shown in the following section.

Assuming that all RO<sub>2</sub> is in the form of CH<sub>3</sub>O<sub>2</sub>, the peroxy radical steady state can thus be re-written as

$$\frac{d[\text{HO}_2 + \sum_i \text{R}_i \text{O}_2]}{dt} = 2f \cdot j(\text{O}^1\text{D}) \cdot [\text{O}_3] \cdot (1 + \gamma) - 2k_{\text{self}} \cdot \alpha (1 + \beta) \cdot [\text{HO}_2 + \sum_i \text{R}_i \text{O}_2]^2 = 0 \quad (\text{I})$$

The term  $j(\text{O}^1\text{D})$  is the photolysis rate of ozone to produce excited oxygen atoms (reaction (3.11)), and here is modelled data from the Tropospheric Ultraviolet and Visible radiation model (TUV) version 4 [Madronich and Flocke, 1998]. Filter radiometers [Junkerman, et al., 1989; Phillips, 2002; Volz-Thomas, et al., 1996] to measure  $j(\text{O}^1\text{D})$  and  $j(\text{NO}_2)$  (the photolysis rate of reaction (3.14)) were fitted to the aircraft during ITOP, but unfortunately owing to technical problems with the data logging the data produced were unusable. Consequently, all photolysis frequencies should be considered clear sky maxima.



Equation (H) can be rearranged to give the following expression for peroxy radical concentrations,

$$[\text{HO}_2 + \sum_i \text{R}_i \text{O}_2] \approx \sqrt{\frac{2f \cdot j(\text{O}^1\text{D}) \cdot [\text{O}_3] \cdot (1 + \gamma)}{2 \cdot k_{\text{self}} \cdot \alpha \cdot (1 + \beta)}} = \sqrt{\frac{f \cdot j(\text{O}^1\text{D}) \cdot [\text{O}_3]}{k_{\text{self}}}} \sqrt{\frac{1}{\alpha}} \sqrt{\frac{1}{1 + \beta}} \sqrt{1 + \gamma} \quad (\text{J})$$

$\beta$  is a measure of the dominant loss process for peroxy radicals. If  $\beta$  is less than one, then the dominant loss process is radical self-reaction rather than loss through reaction with  $\text{NO}_x$ . Figure 3.21 is a time series of  $\beta$  for flights B031 to B034 and B036 to B039. B029 and B030 are omitted owing to a lack of NO data, and B035 because of a lack of PAN data.

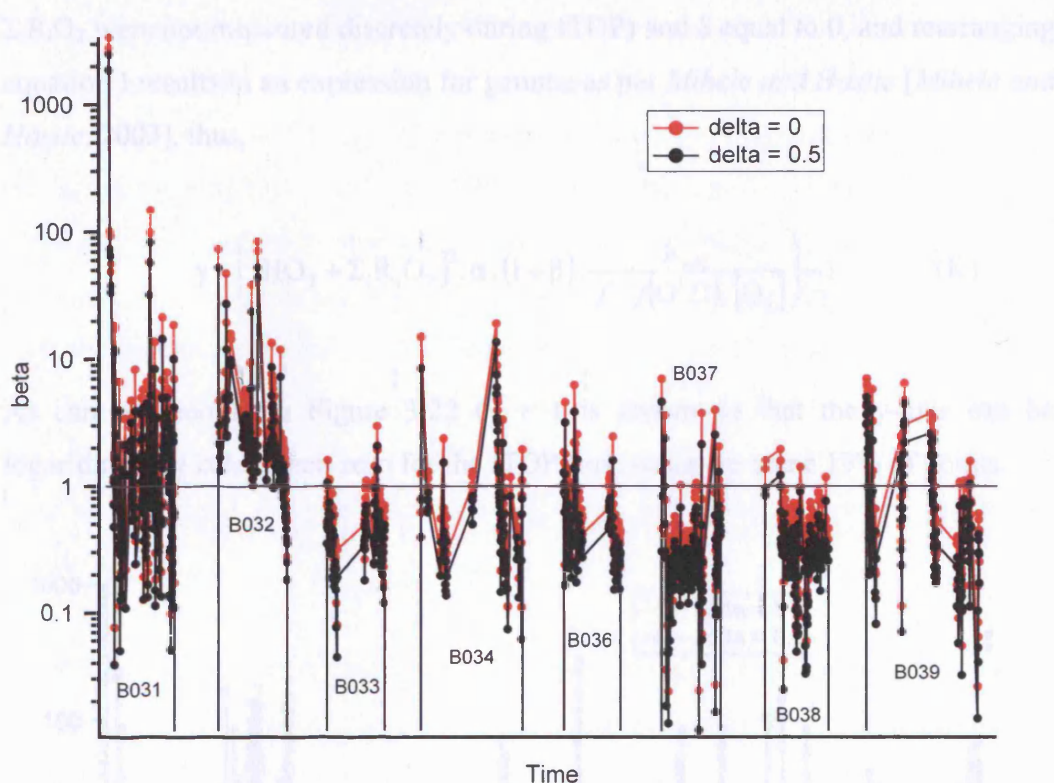


Figure 3.21 – Time series showing  $\beta$  values with  $\delta = 0$  and  $\delta = 0.5$  for flights B031 to B034 and B036 to B039.

For the time series as a whole,  $\beta$  is greater than one for just over 35% of points, demonstrating that even in the low  $\text{NO}_x$  conditions encountered during ITOP the loss of peroxy radicals owing to reaction with  $\text{NO}_x$  is important. If acetylperoxy is considered in addition to methylperoxy with  $\delta = 0.5$ , then  $\beta$  is greater than one for just over 26% of points whilst the median value for  $\beta$  drops from 0.62 to 0.40, showing that whilst the peroxy radical self-reaction accounts for more peroxy radical loss, reaction with  $\text{NO}_x$  remains at an appreciable level. The continued relevance of reaction with  $\text{NO}_x$  is as the combined rate constant for  $[\text{HO}_2 + \Sigma_i \text{R}_i\text{O}_2] + \text{NO}$  is of a similar value to that for the peroxy radical self-reaction rate constant. Thus only low concentrations of  $\text{NO}_x$  are needed for peroxy radical losses due to reaction with  $\text{NO}_x$  to become significant.

$\gamma$  is a measure of additional peroxy radical production from sources other than ozone photolysis. Therefore a  $\gamma$  of zero indicates no excess production, whilst a  $\gamma$  of less than zero indicates that a higher concentration of peroxy radicals is calculated from ozone photolysis than is actually observed. Setting  $\alpha$  equal to 0.5 (as  $\text{HO}_2$  and

$\Sigma_i R_i O_2$  were not measured discretely during ITOP) and  $\delta$  equal to 0, and rearranging equation J results in an expression for gamma as per *Mihele and Hastie* [*Mihele and Hastie, 2003*], thus,

$$\gamma = \left( \left[ \text{HO}_2 + \Sigma_i R_i O_2 \right]^2 \cdot \alpha \cdot (1 + \beta) \cdot \frac{k_{\text{self}}}{f \cdot j(\text{O}^1\text{D}) \cdot [\text{O}_3]} \right)^{-1} \quad (\text{K})$$

As can be seen from Figure 3.22 ( $\gamma + 1$  is shown so that the y-axis can be logarithmic),  $\gamma$  is less than zero for the ITOP time series for some 19% of points.

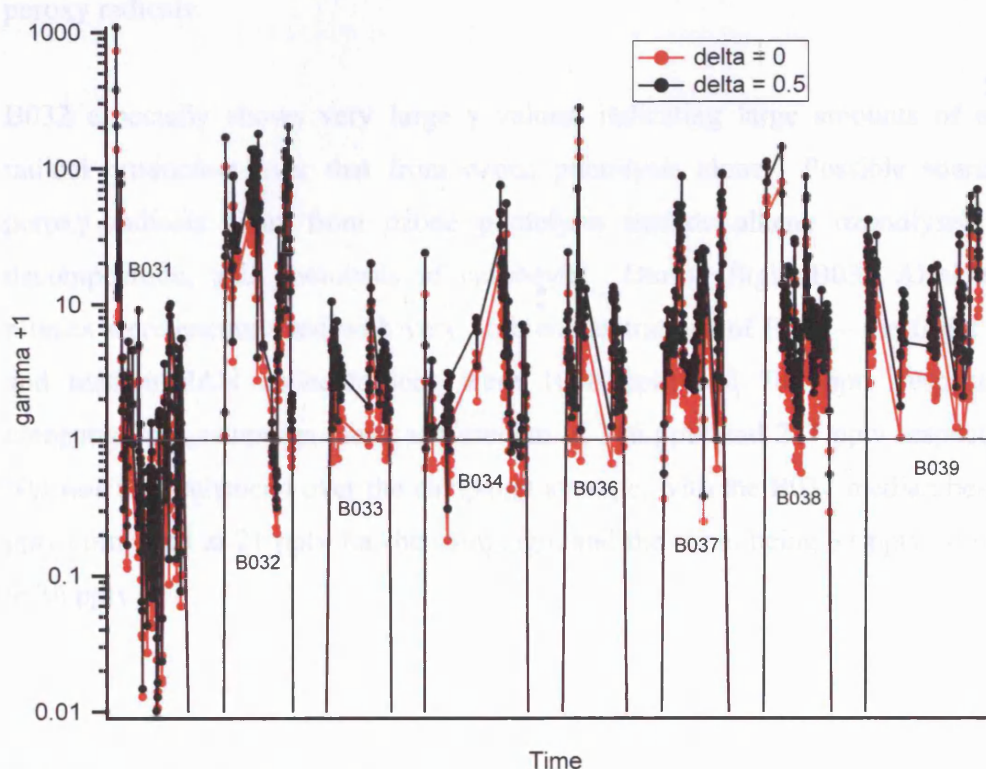


Figure 3.22 – Time series showing  $\gamma + 1$  values with  $\delta = 0$  and  $\delta = 0.5$  for flights B031 to B034 and B036 to B039.

This low  $\gamma$  could be due to either an overestimation of peroxy radical production from ozone photolysis or due to underestimation of peroxy radical losses. There is scope for overestimation of peroxy radical production in this work due to  $j(\text{O}^1\text{D})$  being from TUV modelled values rather than measured and thus a clear sky limit. Furthermore,  $\gamma$  is negative more often at lower altitudes, which would correspond to higher cloud cover at lower altitudes and thus a greater  $j(\text{O}^1\text{D})$  overestimation from

TUV. There is also scope for an underestimation of peroxy radical losses both from self-reactions and reactions with  $\text{NO}_x$  owing to the assumption that all  $\text{RO}_2$  is present in the form of  $\text{CH}_3\text{O}_2$ . If  $\delta$  is set to 0.5 such that half of the peroxy radicals present are  $\text{CH}_3\text{C}(\text{O})\text{O}_2$  and half  $\text{CH}_3\text{O}_2$  and equation (K) is rewritten to take account of the expanded peroxy radical loss rates with the addition of acetylperoxy reactions, then  $\gamma$  is increased by a large amount over that given by equation (K), with the median value for  $\gamma$  more than doubling. It should be noted that owing to the possible unreliability of acetaldehyde data, the use herein of acetylperoxy radicals as forming half the concentration of  $\Sigma_i\text{R}_i\text{O}_2$  (with the remaining half being  $\text{CH}_3\text{O}_2$ ) is a useful proxy for demonstrating the potential importance of fast reacting peroxy radicals.

B032 especially shows very large  $\gamma$  values, indicating large amounts of excess radical production over that from ozone photolysis alone. Possible sources of peroxy radicals apart from ozone photolysis include alkene ozonolysis, PAN decomposition, and photolysis of carbonyls. During flight B032 Alaskan fire plumes were encountered with very high concentrations of PAN – the flight mean and median PAN concentrations were 1018 pptv and 785 pptv respectively, compared to a campaign mean and median of 316 pptv and 217 pptv respectively. NO was also enhanced over the campaign average, with the B032 median being 89 pptv compared to 21 pptv for the campaign, and the mean being 88 pptv compared to 36 pptv.

### 3.6.2 Overall photochemistry

The net photochemical ozone production or loss gives a measure of instantaneous *in-situ* ozone production or loss within an air-mass and has been calculated in this work from measured peroxy radicals, thus,

$$N(\text{O}_3) = k_c \cdot [\text{HO}_2 + \text{RO}_2] \cdot [\text{NO}] - \{f \cdot j(\text{O}^1\text{D}) + k_{3,12}[\text{OH}] + k_{3,13}[\text{HO}_2]\}[\text{O}_3] \quad (\text{L})$$

with  $k_c$  representing the combined rate constant for oxidation of NO to NO<sub>2</sub> by ΣR<sub>i</sub>O<sub>2</sub> and HO<sub>2</sub> and  $k_{3.12}$  and  $k_{3.13}$  the reaction rates for reactions (3.12) and (3.13) respectively.



The first term in equation (L) is the ozone production term and is the only known way of producing ozone in the troposphere in excess of the photostationary steady state between ozone and NO<sub>x</sub>. NO<sub>2</sub> produced from the oxidation of NO by peroxy radicals is photolysed to produce oxygen atoms that then form ozone, *viz*,



The other terms of equation (L) represent the loss processes of ozone in the troposphere, specifically the photolysis of ozone to form excited ozone atoms multiplied by  $f$ , the proportion of O(<sup>1</sup>D) that then react with water vapour, the reaction of ozone with OH (reaction (3.12)), and the reaction of ozone with HO<sub>2</sub> (reaction (3.13)). As stated previously, photolysis rates used in this chapter are modelled values, and thus ozone loss rates should be considered clear sky maxima.

The net ozone production or loss rate calculated by equation (L) contains a number of assumptions such as neglecting cloud processes, dry deposition, and reactions with alkenes and halogens. Nevertheless, equation (L) remains a good approximation for the free troposphere.

OH and HO<sub>2</sub> were not measured discretely during ITOP, and so assumptions have to be made about their concentrations. In this chapter  $\alpha$  has been taken as 0.5 and the concentration of OH radicals has been taken at  $1 \times 10^6$  molecules cm<sup>-3</sup>. A sensitivity analysis with OH concentrations of  $1 \times 10^6$  molecules cm<sup>-3</sup> and  $5 \times 10^6$  molecules cm<sup>-3</sup> corresponding to a reasonable minimum and 90<sup>th</sup> percentile value respectively as derived from OH data recorded between ground level and 7 km on the NASA DC-8 during INTEX-NA demonstrated that the ozone loss term is

relatively insensitive to OH concentration as increasing the OH concentration from  $1 \times 10^6$  molecules  $\text{cm}^{-3}$  to  $5 \times 10^6$  molecules  $\text{cm}^{-3}$  results in an increase of average  $L^{\text{CS}}(\text{O}_3)$  of  $0.04$  ppbv  $\text{hr}^{-1}$  from  $0.51$  ppbv  $\text{hr}^{-1}$  to  $0.55$  ppbv  $\text{hr}^{-1}$ .

Photochemical activity as characterised by enhanced peroxy radicals was observed within long-range transport air-masses with young east-coast North American air masses, biomass burning, and aged Asian emission signatures. Enhanced peroxy radicals (and photochemical ozone production) were also seen within low-level transported air masses, a larger than normal number of which occurred during the summer of 2004. A specific example of a low-level export event is presented later in this chapter.

A time series of  $P(\text{O}_3)$ ,  $L^{\text{CS}}(\text{O}_3)$  and  $N(\text{O}_3)$  for all flights is shown in Figure 3.23. Figure 3.24, Figure 3.25 and Figure 3.26 show binned altitude profiles for  $P(\text{O}_3)$ ,  $L^{\text{CS}}(\text{O}_3)$  and  $N(\text{O}_3)$  respectively, whilst Figure 3.27 shows median  $P(\text{O}_3)$ ,  $L^{\text{CS}}(\text{O}_3)$  and  $N(\text{O}_3)$  split into 30 minute time bins. Table 3.5 shows net ozone production in different air masses defined as for peroxy radicals previously.

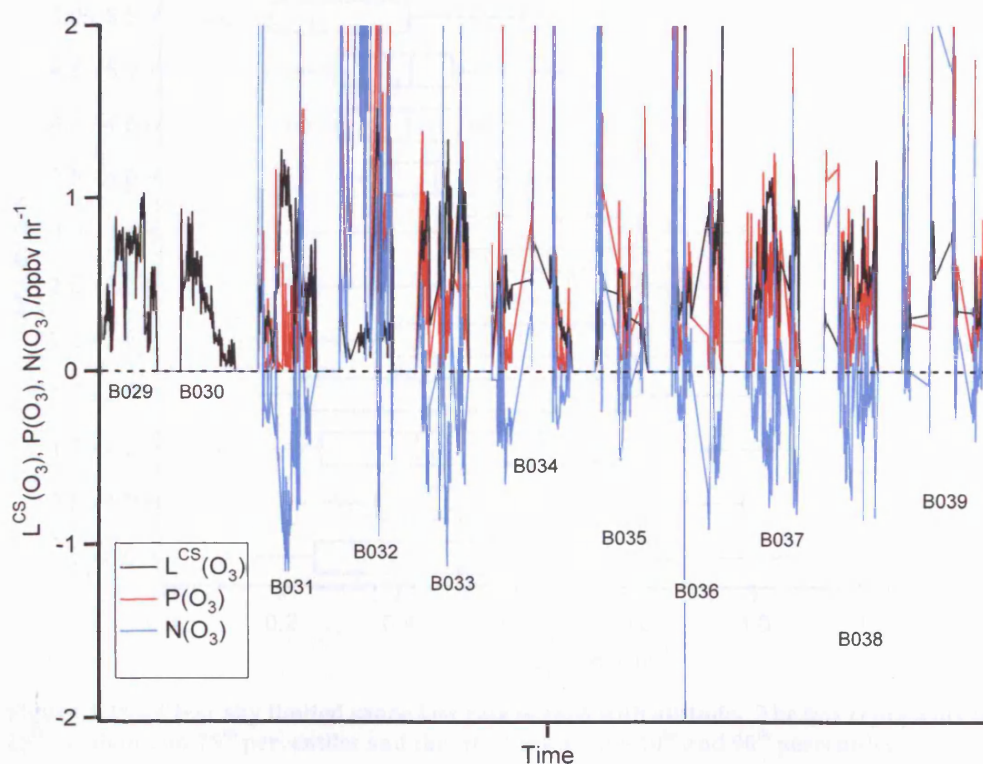


Figure 3.23 – Timeseries showing  $P(\text{O}_3)$ ,  $L^{\text{CS}}(\text{O}_3)$  and  $N(\text{O}_3)$  for all flights.

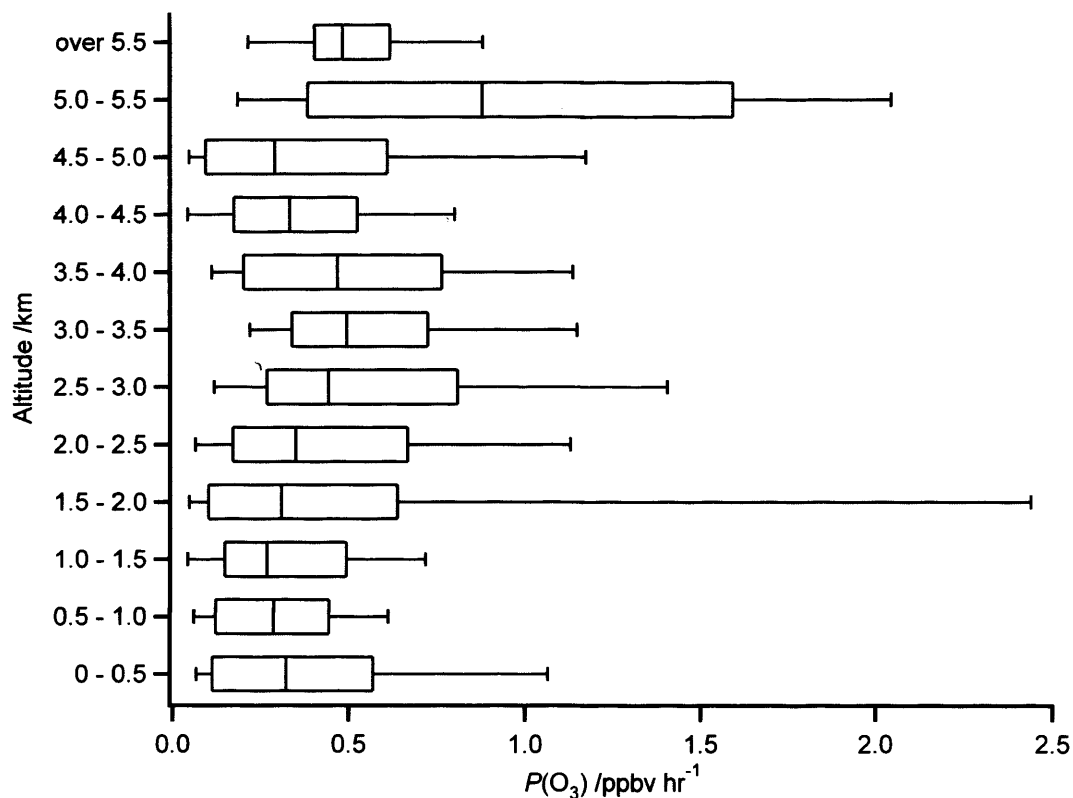


Figure 3.24 – Ozone production rate binned with altitude. The box represents the 25<sup>th</sup>, median and 75<sup>th</sup> percentiles and the whiskers denote 10<sup>th</sup> and 90<sup>th</sup> percentiles.

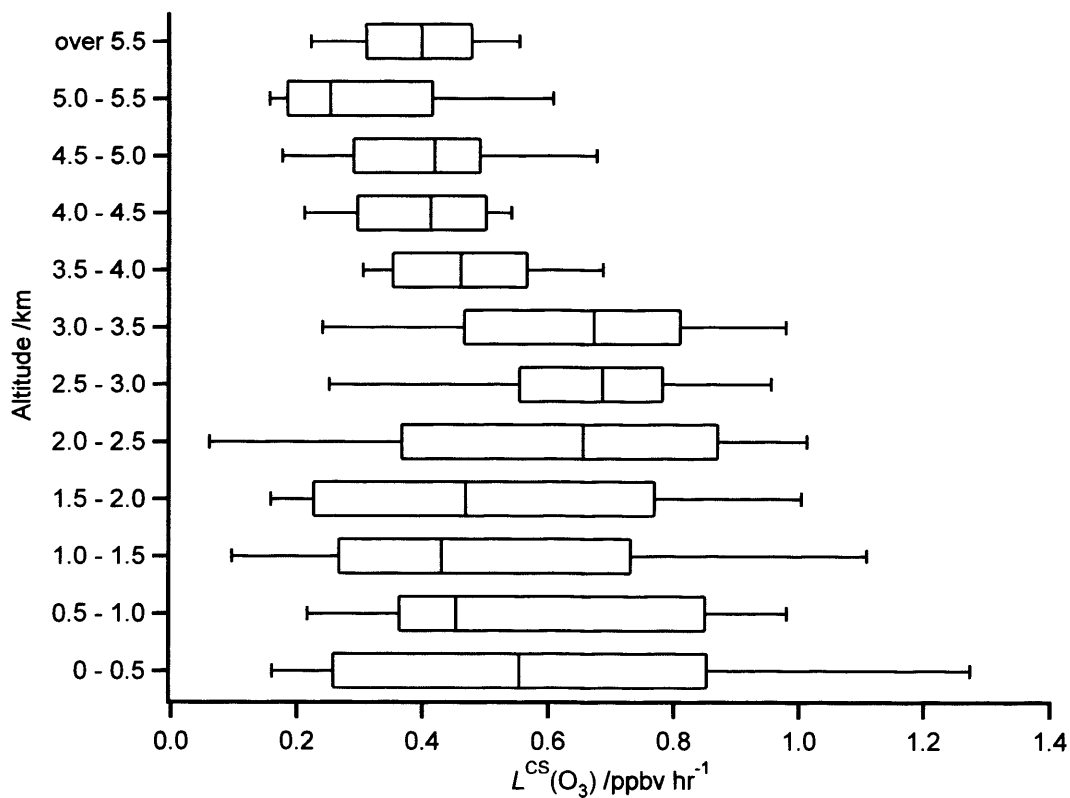


Figure 3.25 – Clear sky limited ozone loss rate binned with altitude. The box represents the 25<sup>th</sup>, median and 75<sup>th</sup> percentiles and the whiskers denote 10<sup>th</sup> and 90<sup>th</sup> percentiles.

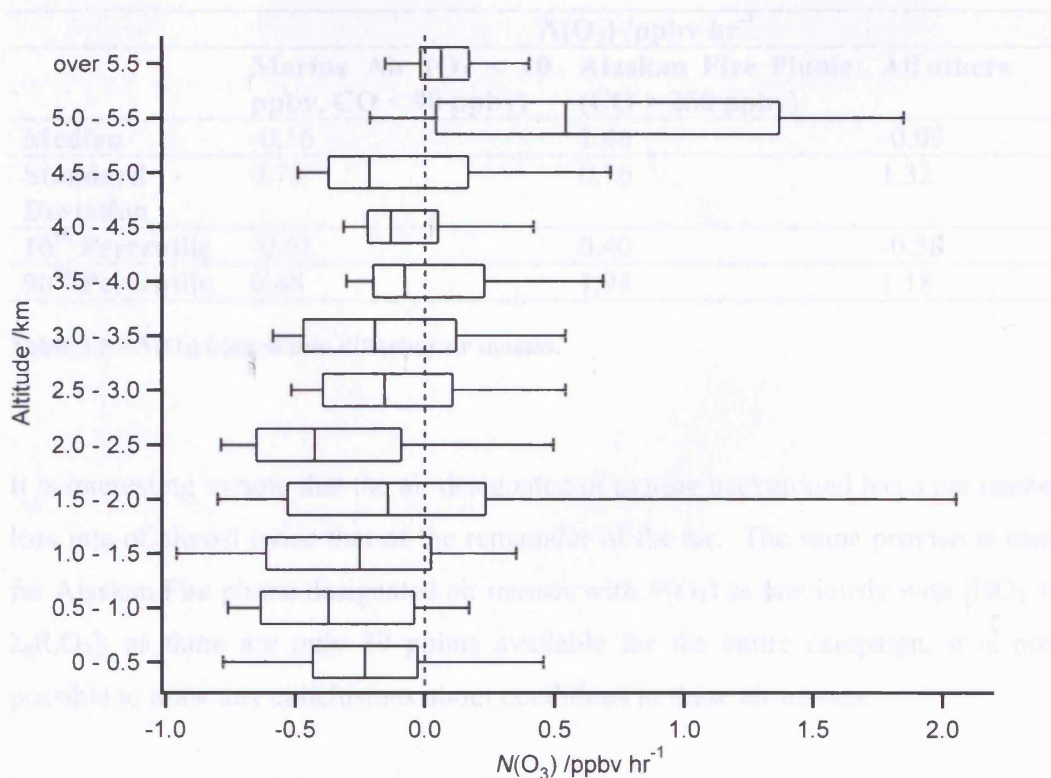


Figure 3.26 – Net ozone production rate binned with altitude. The box represents the 25<sup>th</sup>, median and 75<sup>th</sup> percentiles and the whiskers denote 10<sup>th</sup> and 90<sup>th</sup> percentiles.

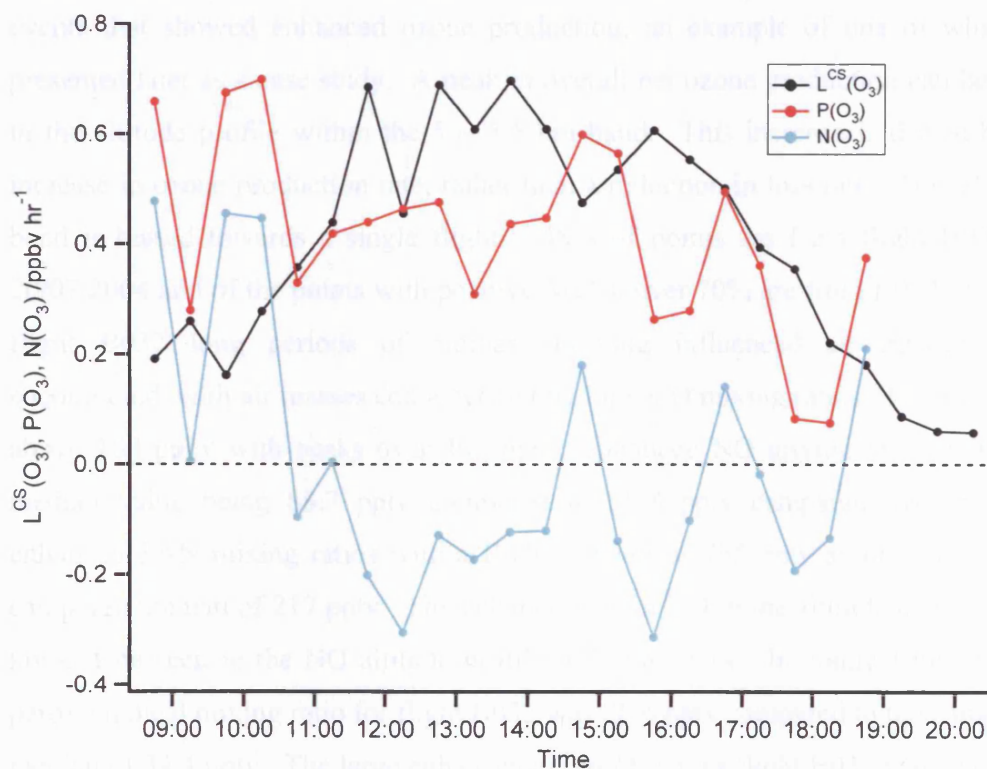


Figure 3.27 – Median ozone production, loss and net production rates for all available flights against time.

	$N(O_3) / \text{ppbv hr}^{-1}$		
	Marine Air ( $O_3 < 40$ ppbv, $CO < 90$ ppbv)	Alaskan Fire Plume ( $CO > 250$ ppbv)	All others
<b>Median</b>	-0.16	1.46	-0.09
<b>Standard Deviation</b>	0.78	0.76	1.32
<b>10<sup>th</sup> Percentile</b>	-0.61	0.40	-0.58
<b>90<sup>th</sup> Percentile</b>	0.48	1.94	1.18

Table 3.5 –  $N(O_3)$  binned into differing air masses.

It is interesting to note that the air designated of marine background has a net ozone loss rate of almost twice that of the remainder of the air. The same proviso is true for Alaskan Fire plume designated air masses with  $N(O_3)$  as previously with  $[HO_2 + \Sigma_i R_i O_2]$ ; as there are only 30 points available for the entire campaign, it is not possible to draw any conclusions about conditions in these air masses.

In general, the summertime mid-latitude Atlantic is net ozone destructive at clear sky limit. This is true of air classified as both marine background air and non-marine background air. There were however many individual long-range transport events that showed enhanced ozone production, an example of one of which is presented later as a case study. A peak in overall net ozone production can be seen in the altitude profile within the 5 – 5.5 km band. This increase is driven by an increase in ozone production rate, rather than a reduction in loss rate. This altitude band is biased towards a single flight – 48% of points are from flight B032 on 20/07/2004 and of the points with positive  $N(O_3)$ , over 70% are from B032. During flight B032 long periods of biomass burning influenced air masses were encountered, with air masses characterised by high CO mixing ratios of consistently above 100 ppbv with peaks over 400 ppbv, enhanced NO mixing ratios with the median value being 88.7 pptv compared to 20.8 pptv campaign average, and enhanced PAN mixing ratios with a flight median of 785 pptv as opposed to the campaign median of 217 pptv. The enhancement in NO in the altitude band 5 – 5.5 km can be seen in the NO altitude profile in Figure 3.14. In contrast the median peroxy radical mixing ratio for flight B032 was 36.6 pptv compared to the campaign median of 34.4 pptv. The large enhancement in  $P(O_3)$  for flight B032 is thus driven by NO rather than peroxy radicals.

The  $P(O_3)$  being driven by NO is consistent for the campaign as a whole. Ozone production rate and NO are well correlated ( $r^2 = 0.72$ ) as shown in Figure 3.28, and thus ozone production for the summer mid-Atlantic may be said to be  $NO_x$  limited.

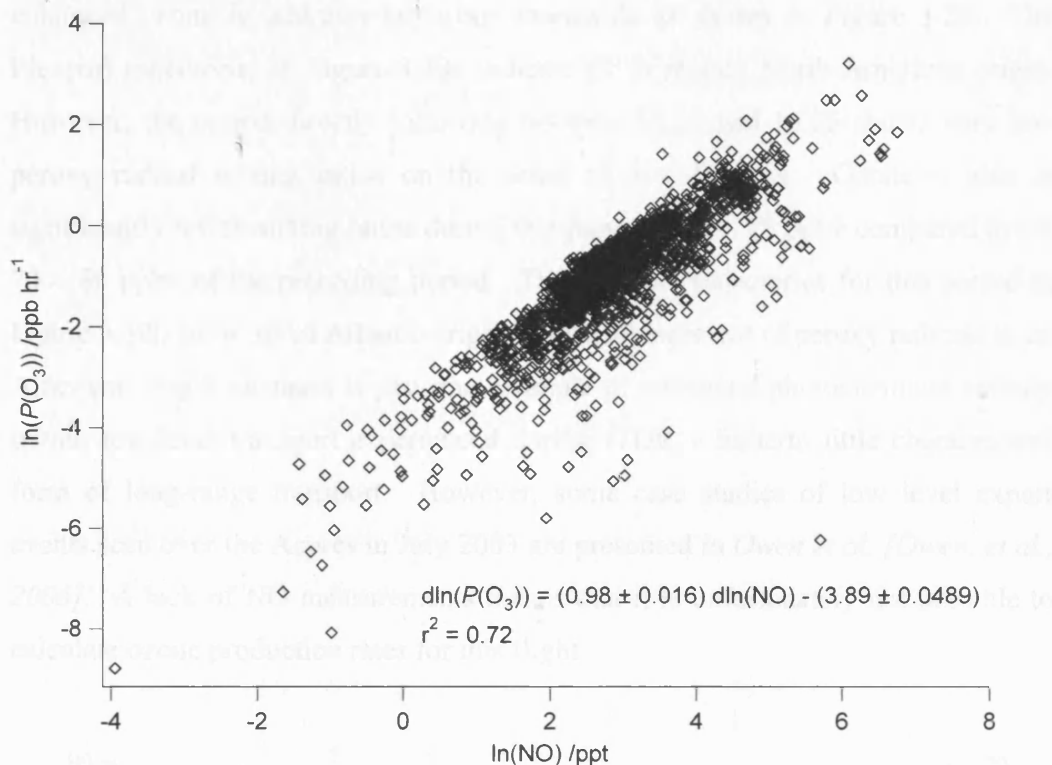


Figure 3.28 – Correlation between  $\ln(P(O_3))$  and  $\ln(NO)$

### 3.6.3 Case studies

Two case studies have been carried out to illustrate the enhancement of peroxy radicals and ozone production seen within air-masses undergoing long-range transport during ITOP.

#### 3.6.3.1 Low level (4.5km) Long-Range Transport

Flight B029 on 15/07/2004 presented a good opportunity to sample American outflow. In the period 14.45 to 15.05 a prolonged period of moderately to well aged

air of American and Asian outflow was encountered with a biomass burning CO signature. The air mass was transported at low level, staying under 4.5 km for the majority of the time, as shown by back trajectories. The period 14.45 to 15.05 during flight B029 sees peroxy radicals of 30 – 40 pptv with higher peaks and enhanced ozone in addition to carbon monoxide as shown in Figure 3.29. The Flexpart trajectories in Figure 3.30a indicate air of mainly North American origin. However, the period directly following between 15.10 and 15.25 shows very low peroxy radical mixing ratios on the order of 5 – 10 pptv. Ozone is also at significantly lower mixing ratios during this period at 15 – 25 ppbv compared to the 70 – 80 ppbv of the preceding period. The Flexpart trajectories for this period in Figure 3.30b show air of Atlantic origin. This enhancement of peroxy radicals in an American origin air-mass is just one example of enhanced photochemical activity within low-level transport experienced during ITOP, a hitherto little characterised form of long-range transport. However, some case studies of low level export events seen over the Açores in July 2003 are presented in *Owen et al. [Owen, et al., 2006]*. A lack of NO measurements means that it is unfortunately not possible to calculate ozone production rates for this flight.

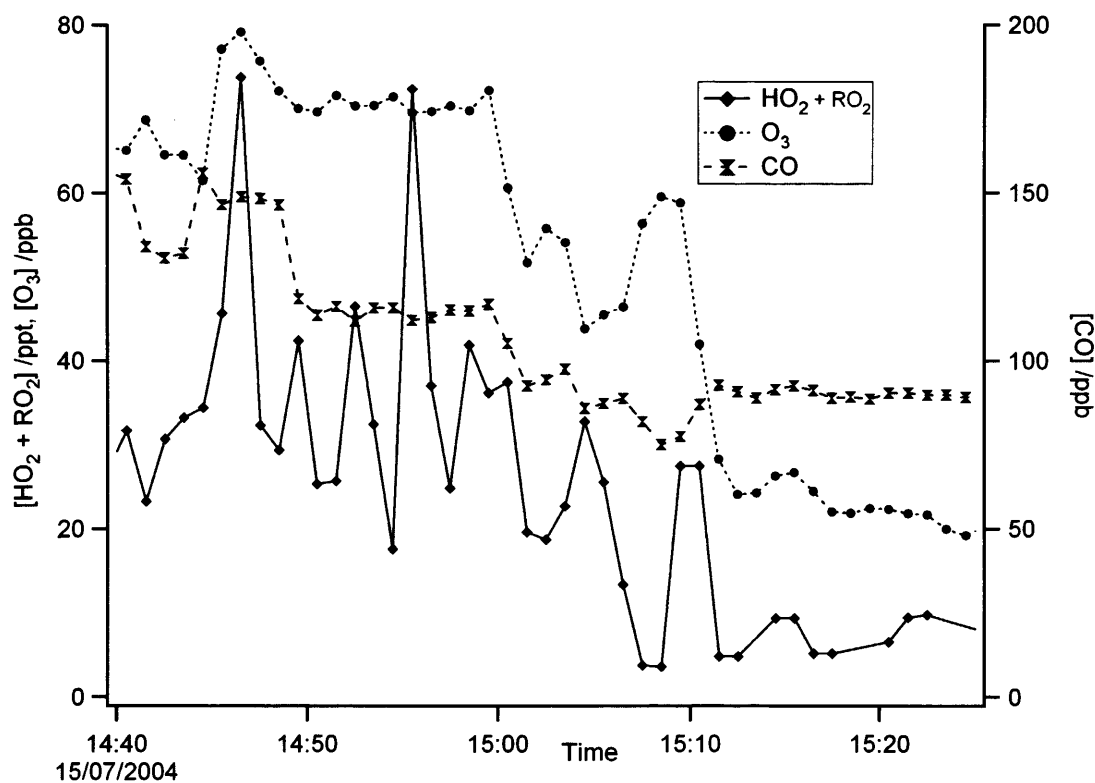


**Figure 3.29 – Peroxy radical, ozone and carbon monoxide time series for a section of flight B029 on 15/07/2004**

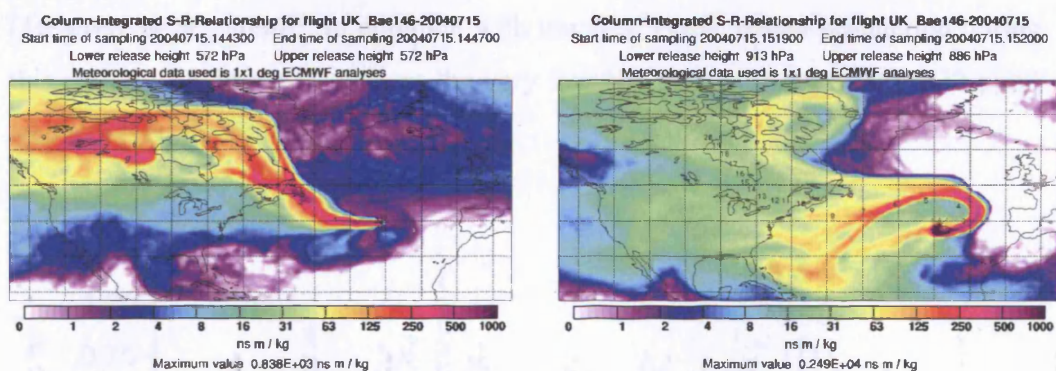
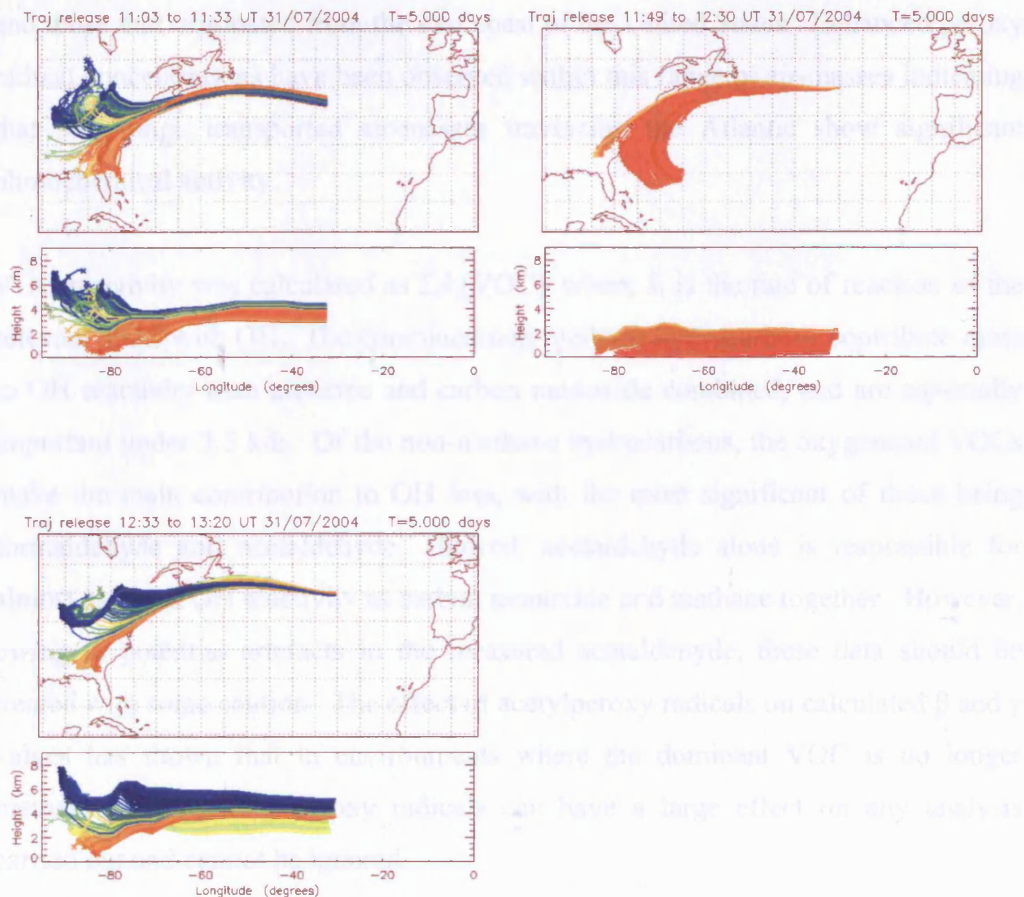


Figure 3.30 – Flexpart trajectories for a) 14.43 – 14.47 and b) 15.19 – 15.20 from flight B029 on 15/07/2004

### 3.6.3.2 Multiple interceptions of American export

Some flights allowed the opportunity to intercept long-range transported air-masses on multiple occasions. One such opportunity occurred on 31/07/2004 during flight B037. During this flight a prolonged period of US emissions of moderate age were encountered, as shown by Flexpart products. From the time series of ozone production, clear sky ozone loss and net ozone production in Figure 3.31, it can be seen that during the period 11:00 to 13:20 there were multiple interceptions of US export interspersed with a period of Atlantic origin air. The first interception was between the times of approximately 11:00 and 11:30, when a relatively young East Coast funnelled air mass was encountered showing enhanced ozone of up to 90 ppbv and CO exceeding 110 ppbv, peaking at 130 ppbv. During this period  $N(O_3)$  is enhanced to up to 0.5 ppbv  $hr^{-1}$  even at clear sky limited  $L^{CS}(O_3)$ , clearly showing photochemical ozone production within air masses undergoing long-range transport. Another interception was made between 12.30 and 13.20 again showing strong photochemically active US emissions. Peak  $N(O_3)$  is over 0.8 ppbv  $hr^{-1}$ , and is at least net neutral at clear sky limit. These two periods of ozone production are interspersed by a time of Atlantic origin air in which there is net ozone destruction, as demonstrated by the back trajectories in Figure 3.32. This is clear evidence for ozone production in long-range transported air masses and indicates the impact that long-range transported air masses can have on regions remote from the source and the consequent implications for local pollution controls. The time period covered here also includes a lagrangian matched air-mass (case 5 in *Methven et al.*





**Figure 3.32 – Back trajectories showing air-mass origins for a section of flight B037 on 31/07/2004 coloured by pressure 5 days before arrival [Methven, 2004a].**

### 3.7 Conclusions

The sum of peroxy radicals has been measured with the Peroxy Radical Chemical Amplification technique onboard the FAAM BAe Systems 146-300 aircraft during the ITOP campaign in the summer of 2004 over the mid-Atlantic. The overall peroxy radical altitude profile displays an increase with altitude, but as the aim of ITOP was to target polluted air-masses this should not be taken as a summer-time mid-tropospheric mid-Atlantic background. The peroxy radical altitude profile for air classified as of marine origin (ozone and carbon monoxide mixing ratios of less than 40 ppbv and 90 ppbv respectively) shows no discernable altitude profile. A range of air-masses were intercepted with varying source signatures, including those with aged American and Asian signatures, air-masses of biomass burning origin,

and those that originated from the east coast of the United States. Enhanced peroxy radical concentrations have been observed within this range of air-masses indicating that long-range transported air-masses traversing the Atlantic show significant photochemical activity.

VOC reactivity was calculated as  $\sum_i k_i [\text{VOC}]_i$  where  $k_i$  is the rate of reaction of the relevant VOC with OH. The combined non-methane hydrocarbons contribute more to OH reactivity than methane and carbon monoxide combined, and are especially important under 3.5 km. Of the non-methane hydrocarbons, the oxygenated VOCs make the main contribution to OH loss, with the most significant of those being formaldehyde and acetaldehyde. Indeed, acetaldehyde alone is responsible for almost as much OH reactivity as carbon monoxide and methane together. However, owing to potential artefacts in the measured acetaldehyde, these data should be treated with some caution. The effect of acetylperoxy radicals on calculated  $\beta$  and  $\gamma$  values has shown that in environments where the dominant VOC is no longer methane, fast reacting peroxy radicals can have a large effect on any analysis carried out and cannot be ignored.

Instantaneous ozone production efficiencies have been calculated for all ITOP flights for which both peroxy radical and NO data is available. The net ozone production at clear sky limit is in general negative, and as such the summer mid-Atlantic troposphere is at limit net ozone destructive. However, there is clear evidence of positive ozone production even at clear sky limit within air masses undergoing long-range transport, and during ITOP especially between 5 and 5.5 km, which in the main corresponds to a flight that extensively sampled air with a biomass burning signature. Ozone production was  $\text{NO}_x$  limited throughout ITOP, as evidenced by a good correlation ( $r^2 = 0.72$ ) between  $P(\text{O}_3)$  and NO. Strong positive net ozone production has also been seen in varying source signature air-masses undergoing long-range transport, including but not limited to low-level export events, and export from the east coast of the United States.

# Chapter 4

## Composition Control in the European Free Troposphere

### 4.1 Overview

The free troposphere (FT) is the region of the atmosphere located between the planetary boundary layer and the tropopause. The colder temperatures and lack of deposition in the free troposphere compared to the boundary layer lead to longer chemical lifetimes for many species (e.g. ozone) in the free troposphere compared to the boundary layer. As much of the transport of chemical species within the atmosphere takes place in the free troposphere, the combination of long-range transport and longer chemical lifetimes mean that the chemistry of the free troposphere is of fundamental importance in determining the chemical composition of regions remote from pollutant source regions.

Consequently, during the summer of 2005 the University of Leicester carried out a significant measurement effort at the high-altitude research station Jungfraujoch, aimed at investigating the control of composition and the effect of long-range transport (LRT) on free tropospheric chemistry.

### 4.2 Objectives

The high altitude research station Jungfraujoch is situated on a saddle point located at 7° 59' 2" E, 46° 32' 53" N and 3580 meters above sea level (asl) between two mountains, the Jungfrau to the south-west (4158 m asl) and the Mönch to the north

(4099 m asl) in the Swiss Alps. The University of Leicester instrumentation was deployed from the Sphinx laboratory. The air pressure at the Sphinx laboratory ranges from 619 mbar to 675 mbar, with a mean pressure of 653.3 mbar and air temperature ranges from  $-37^{\circ}\text{C}$  to  $+10^{\circ}\text{C}$ , with a mean temperature of  $-8.2^{\circ}\text{C}$ . The Sphinx is located in winter and very often in spring and autumn in the free troposphere [Lugauer, *et al.*, 1998; Zanis, *et al.*, 2000a]. As the Jungfrauoch is situated on a mountain saddle point, it experiences air from essentially two directions, north-west and south-east. To the north-west air arrives at the Jungfrauoch from the direction of Kleine Scheidegg and the Swiss Plateau, whilst from the south-east it arrives from the direction of Italy and travels up the glacier to the Jungfrauoch. Figure 4.1 shows the position of the Jungfrauoch in Europe, whilst Figure 4.2 shows the view from the Sphinx Laboratory to the north and south-east.

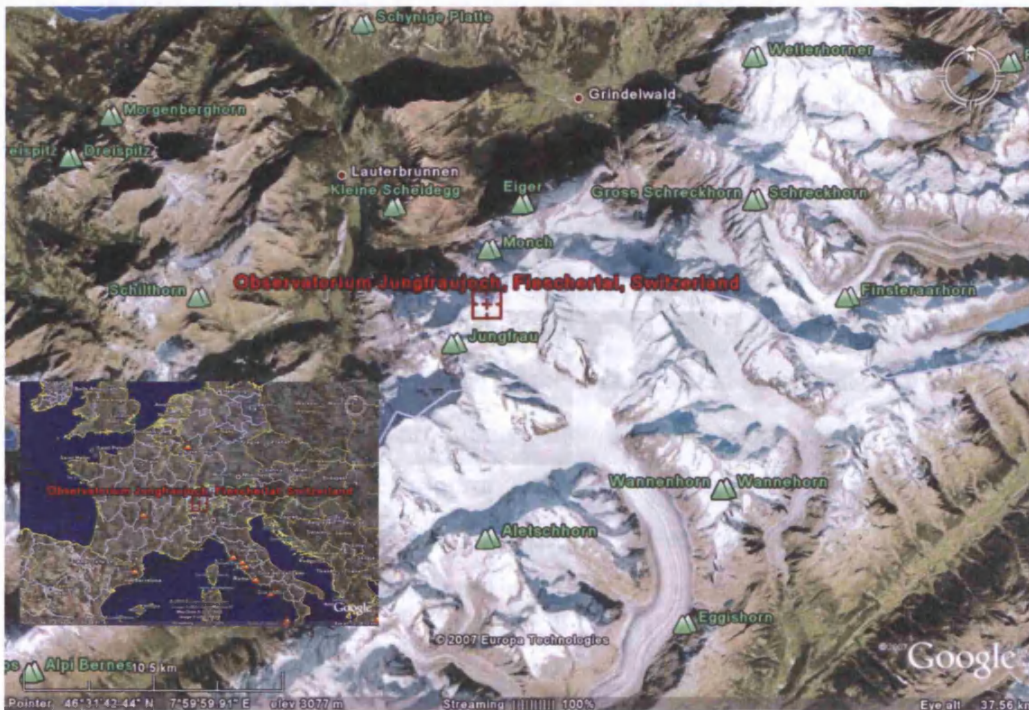


Figure 4.1 – Map showing position of Jungfrauoch observatory ©Google Earth



Figure 4.2 – Views looking a) north and b) south-west from the Sphinx laboratory.

Consequently, the site at the Jungfraujoch is ideal for the study of the European free troposphere. The work undertaken during August and September 2005 and reported in this chapter had three initial objectives: to investigate the role of *in-situ* photochemistry in the control of lower free tropospheric composition in summer; to assess European export and transatlantic import *via* long-range transport, using trajectory analysis over the Swiss Alps and to quantify transport from pollutant sources in Swiss plateau and Po valley to the lower free troposphere.

As detailed in Chapter 1, peroxy radicals are key intermediates and chain carriers in the photochemical production of ozone in the troposphere [Monks, 2005]. The presence of peroxy radicals leads to net ozone production in the presence of  $\text{NO}_x$  by allowing oxidation of NO to  $\text{NO}_2$  without the consumption of ozone. However, the relative importance of ozone production and loss processes in the background troposphere is highly sensitive to competition between reaction of peroxy radicals with NO and the cross- or self-reactions of the peroxy radicals, and therefore the local  $\text{NO}_x$  and peroxy radical concentrations.

The local ozone production  $P(\text{O}_3)$  is proportional to the product of the local NO and peroxy radical concentrations whilst hydroperoxy radicals ( $\text{HO}_2$ ) are also involved in the local destruction of ozone through the reaction between  $\text{HO}_2$  and  $\text{O}_3$ . In the very dry and cold conditions of the free troposphere this loss term can be dominant over other loss terms as direct loss by photolysis of ozone and subsequent reaction of  $\text{O}(^1\text{D})$  with water vapour is smaller. Hence, peroxy radical measurements are

essential in order to provide further insight into the fast photochemistry that controls tropospheric ozone production and loss.

## 4.3 Instrumentation

A range of instrumentation was deployed at the Jungfraujoch during the series of measurements described in this chapter, with the University of Leicester measuring peroxy radicals with the PERCA instrument and photolysis frequencies with a spectral radiometer.

### 4.3.1 Peroxy radical measurements

Peroxy radicals were measured during the campaign with the PERCA instrument as described in Chapter 2, with the exception of a different inlet system. The systems in the aircraft inlet setup (MFC tray, PICM and inlets) are contained within an inlet box, and the MFC tray and PICM components are the same for both ground and aircraft deployment. However, the inlet design varies slightly from the aircraft design as it is not constrained by having to protrude through the aircraft fuselage. Consequently the diameter of the inlet can be larger than on the aircraft, and the reagent gases are introduced *via* front and rear *tori* to aid mixing over the larger volume of the ground inlet compared to the aircraft version.

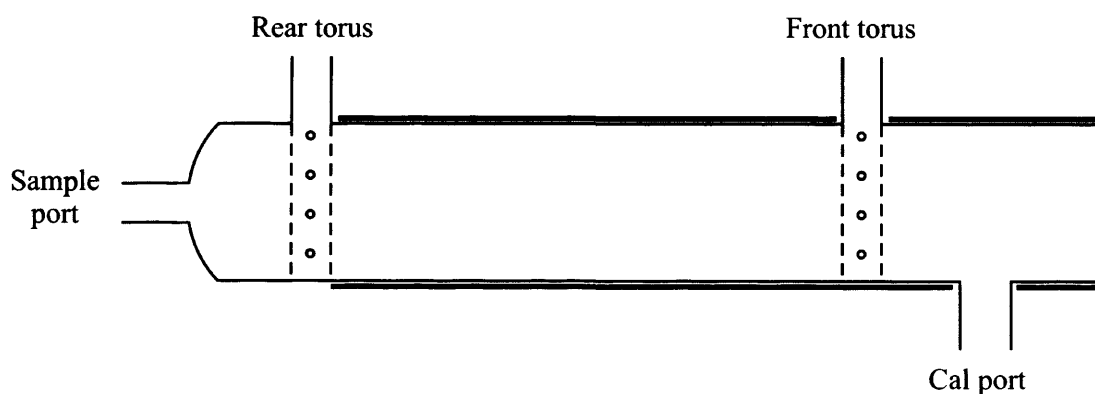


Figure 4.3 – Schematic diagram of a ground inlet. The thick black line indicates heating pads.

The calibration unit used on the ground has a larger flow tube and more powerful lamp than the aircraft version as space is not restricted on the ground, but the principle of operation is the same. Flows of varying concentrations of methyl iodide in zero air are passed past a mercury lamp at 253.7 nm. The methyl iodide is photolysed to produce methyl radicals and iodide radicals. The methyl radicals then undergo an addition reaction with oxygen in the air to produce a known quantity of methyl peroxy radicals.

### 4.3.2 Photolysis frequency measurements

As stated in section 1.3.1, the rate of photodissociation of a molecule A, denoted  $j(A)$ , is dependent on the actinic flux experienced by the molecule,  $F(\lambda)$ , the photodissociation quantum yield of the molecule,  $\phi$ , and the absorption cross-section of the molecule,  $\sigma$ .

$$j(A) = \int_{\lambda_{\min}}^{\lambda_{\max}} F(\lambda)\phi(\lambda, T)\sigma(\lambda, T)d\lambda \quad (4.1)$$

The actinic flux is the spherical flux density available to the molecules which on absorption produces photodissociation in units of quanta  $\text{cm}^{-2} \text{s}^{-1} \text{nm}^{-1}$ . The photodissociation quantum yield is the number of molecules dissociated per photon absorbed, whilst the absorption cross-section is the quantity of light absorbed with respect to wavelength.

It can be seen from equation (4.1) that if the quantum yield and absorption cross section for a given molecule at a given wavelength and temperature is known, it is possible to derive photolysis frequencies from the measurement of actinic flux. A spectral radiometer measures actinic flux over a range of wavelengths, typically of the order of  $\lambda = 280 - 450 \text{ nm}$  with a variable integration time which is typically set to 1 second.

The spectral radiometer deployed during the measurements described in this chapter was a fast, monolithic single-monochromator spectral radiometer with a

temperature-stabilized diode array detector and is a commercial instrument available from Meteorologie Consult (METCON), Glashütten, Germany. Details of the specification can be found in Table 4.1.

Characteristic	Specification
Instrument dimensions	$250 \times 150 \times 11 \text{ mm}^3$
Weight	4.1 kg
Power	115/230 V AC, 12 – 36 V DC
Detection optics	quartz actinic diffuser
Quantity measured	actinic flux
Entrance optics	round-to-slit converter ( $70 \times 2500 \mu\text{m}$ )
Grating flat field monochromator type	248 lines $\text{mm}^{-1}$ diffraction grating coupled to diode array in self-contained unit
Wavelength range	285 – 450 nm
Wavelength accuracy	> 0.1 nm
Diode wavelength separation	0.83 nm
Resolution	~ 2 nm at full width at half maximum
Detector	512-pixel diode array (Carl Zeiss)
Calibration	NIST <sup>a</sup> traceable 1000 W tungsten halogen lamp
Actinic flux detection limit	$\sim 1 \times 10^{10} \text{ photons cm}^{-2} \text{ nm}^{-1} (\pm 5\%)$
Minimal detected $j(\text{O}^1\text{D})$	$\sim 3 \times 10^{-7} \text{ s}^{-1} (\pm 13\%)$
Signal-to-noise ratio	~4:1
Temperature stability	$\sim 5 \times 10^{-4} \text{ nm K}^{-1}$
Stray light rejection ratio	$\sim 5 \times 10^4$
Dark current response	~ 200 counts $\text{s}^{-1}$ (at 303 K)
Scan time	user defined; 1 s over $\lambda = 285 - 450 \text{ nm}$ during these measurements

**Table 4.1** – Specification of METCON spectral radiometer [Edwards and Monks, 2003]; <sup>a</sup>NIST – National Institute of Standards and Technology

### 4.3.2.1 Optical collection system

Ideally all incident photons over the  $2\pi$  sr solid angle would have the same probability of detection by the diode array, in order to achieve ideal sensitivity. To try and achieve this, a  $2\pi$  sr quartz dome similar to the dome/diffuser arrangement described in [Volz-Thomas, *et al.*, 1996] is employed. Several separate domes of sand-blasted quartz are used to make up the dome/diffuser. As incident photons pass through the domes they undergo multiple reflections and refractions and they

enter and exit the domes, and thus are detected across the entire  $2\pi$  sr range. A matt black shadow ring is used to limit the collection angle of the spectral radiometer to  $2\pi$  sr. The photons then pass through a round-to-slit converter ( $70 \times 2500 \mu\text{m}$ ) which results in a spectral band pass of approximately 2 nm at full width at half maximum. Photons are then dispersed with a flat field diffraction grating (248 lines  $\text{mm}^{-1}$ ) and detected with a 512-pixel diode array (Carl Zeiss) which is capable of detecting photons in the range  $\lambda = 285 - 710$  nm. A full description of the spectral radiometer deployed during these measurements, including characterisation and calibration details is given in [Edwards and Monks, 2003].

#### 4.3.2.2 Photolysis frequencies derived

A range of photolysis frequencies were derived from the actinic flux measured with the spectral radiometer described in 4.3.2 and are shown in Table 4.2 along with the reference used for quantum yield and absorption cross-section data:

Photolysis Rate	Quantum yield, $\phi$	Absorption cross-section, $\sigma$
$j(\text{O}^1\text{D})$	[Matsumi, et al., 2002]	[Malicet, et al., 1995]
$j(\text{NO}_2)$	[Troe, 2000]	[Coquart, et al., 1995]
$j(\text{HCHO})$	[Atkinson, et al., 1999]	[Meller and Moortgat, 1999]
$j(\text{H}_2\text{O}_2)$	Unity	[Atkinson, et al., 1999]
$j(\text{HONO})$	Unity	[Bongartz, et al., 1991]
$j(\text{CH}_3\text{COOH})$	Unity	[Atkinson, et al., 1999]
$j(\text{CH}_3\text{CHO})$	[Atkinson, et al., 1999]	[Atkinson, et al., 1999]
$j(\text{CH}_3\text{COCH}_3)$	[Gierczak, et al., 1998]	[Gierczak, et al., 1998]
$j(\text{PAN})$	Unity	[Talukdar, et al., 1995]
$j(\text{HNO}_3)$	Unity	[Atkinson, et al., 2006]
$j(\text{NO}_3)$	Unity	[Yokelson, et al., 1994]
$j(\text{I}_2)$	Unity	[Saiz-Lopez, et al., 2004]

Table 4.2 – Photolysis rates measured along with reference for quantum yield and absorption cross-section reference

### 4.3.3 Other measurements

Many additional measurements were carried out during the work described in this chapter by co-workers from Eidgenössische Materialprüfungs- und Forschungsanstalt (EMPA – Swiss Federal Laboratories for Materials Testing and Research) and Eidgenössische Technische Hochschule Zürich (ETHZ - Swiss Federal Institute of Technology Zürich) and are summarized in Table 4.3.

Ozone was measured with a commercially available Thermo Environmental Instruments 49c UV absorption instrument, whilst CO was measured with another commercial instrument, a HORIBA APMA-360 which utilises the nondispersive infrared (NDIR) technique. NO, NO<sub>x</sub> and NO<sub>y</sub> were all measured with a commercially available Ecophysics CraNOx instrument equipped with two temperature controlled CLD 770 AL pptv chemiluminescence detectors. NO<sub>x</sub> was measured by conversion to NO on a PLC 760 photolytic converter, whilst NO<sub>y</sub> was converted on a gold catalyst heated to 300°C with the addition of 2% CO (Messer-Griesheim GmbH, 99.997%) to act as a reducing agent. NO<sub>2</sub> was then reported by subtraction of NO from NO<sub>x</sub> [Zellweger, *et al.*, 2000].

Peroxy acetyl nitrate (PAN) was measured with a commercially available Meteorologie Consult GmbH gas chromatograph (GC) with electron capture detection (ECD) and calibration unit. The technique is described in [Schmidt, *et al.*, 1998], and the instrument deployed at the Jungfrauoch during 2005 is described in [Balzani Lööv, *et al.*, 2007].

Formaldehyde was measured using an instrument based on the Hantzsch fluorescence technique similar to the AERO LASER CH<sub>2</sub>O analyser AL4021. The Hantzsch technique is a liquid phase technique, and as such requires the HCHO to be analysed to be transferred from the gas to liquid phase. Once in the liquid phase the HCHO is reacted with 2,4-pentadione and NH<sub>3</sub> to produce 3,5-diacetyl-1,4-dihydrolutidine (DDL). DDL fluoresces at 510 nm if excited at 412 nm and thus can be measured. The Hantzsch technique is described in [Kelly and Fortune, 1994], and the instrument deployed at the Jungfrauoch during 2005 is described in [Balzani Lööv, *et al.*, 2007].

Methane was measured *via* GC-FID and VOCs (n-pentane, iso-pentane, n-hexane, benzene, toluene, trimethylbenzene, n-butane, isobutane, butadiene, ethylbenzene, isoprene, o-xylene and m-, p-xylene) were measured with an Agilent 5793N GC-MS with a pre-concentration system after [Simmonds, *et al.*, 1995]. The system is described in detail by [Reimann, *et al.*, 2004].

There were also measurements of OVOCs (methanol, ethanol, propanol, butanol, 2-methyl-3-buten-2-ol (MBO), propanal, isopropanal, butanal, pentanal, hexanal, acetaldehyde, benzaldehyde, acrolein, methylacetate, ethylacetate, butylacetate, methyl vinyl ketone (MVK), methyl ethyl ketone (MEK), methacrolein, acetone and methyl tertiary butyl ether (MTBE)) made at the Jungfraujoch with a GC-MS system. The instrument was based on an Agilent HP 6890 – HP 5973N and constructed by EMPA.

Species	Technique	Measurement Frequency	Detection Limit	Institute
O <sub>3</sub>	UV absorption	10 minutes <sup>a</sup>	0.3 ppbv	EMPA
CO	NDIR	10 minutes <sup>a</sup>	20 ppbv	EMPA
NO	Chemiluminescence (O <sub>3</sub> reaction)	10 minutes <sup>b</sup>	20 pptv <sup>c</sup>	EMPA
NO <sub>2</sub>	Calculated from NO <sub>x</sub> – NO	10 minutes <sup>b</sup>	20 pptv <sup>c</sup>	EMPA
NO <sub>x</sub>	Photolytic conversion	10 minutes <sup>b</sup>	20 pptv <sup>c</sup>	EMPA
NO <sub>y</sub>	Au catalytic conversion	10 minutes <sup>b</sup>	20 pptv <sup>c</sup>	EMPA
PAN	GC-ECD	10 minutes	50 pptv	ETHZ
HCHO	Hantzsch fluorescence	10 minutes	22 pptv	ETHZ
CH <sub>4</sub>	GC-FID	30 minutes	100 ppbv	EMPA
VOCs	GC-MS	4 hours	1-120 pptv	EMPA
OVOCs	GC-MS	4 hours	1-120 pptv	EMPA

**Table 4.3 – Additional species measured at the Jungfraujoch during the period covered in this chapter.** <sup>a</sup>Measurements made continuously then averaged to ten minutes, <sup>b</sup>measurements made every two minutes then averaged to ten minutes, <sup>c</sup>for thirty minute averaging, 50 pptv for two minute measurements.

In addition relative humidity, temperature, pressure, wind speed and wind direction were measured by the Swiss Meteorological Service.

## 4.4 Results

### 4.4.1 Radicals and tracers observations

The campaign time series of peroxy radicals, O<sub>3</sub>, CO, NO and NO<sub>2</sub> are shown in Figure 4.4, and Figure 4.5 shows the time series of peroxy radicals with  $j(O^1D)$ . It can be seen that peroxy radicals in the period 06/09/2005 – 12/09/2005 inclusive in addition to some days after this period are suppressed relative to the period up to and including 05/09/2005. The suppression of peroxy radicals corresponds to days on which there was heavy snowfall. In order to quantify the effect of snowfall, a metric was devised by which days with mean relative humidity over 76% were considered ‘snowy’, whilst those with a mean relative humidity under 76% were considered ‘snow free’. Table 4.4 shows which days were assigned to which category.

<b>Not snowy</b>	<b>Snowy</b>
30/08/2005 – 05/09/2005 inclusive	06/09/2005 – 13/09/2005 inclusive
14/09/2005 – 16/09/2005 inclusive	17/09/2005 – 18/09/2005 inclusive

**Table 4.4 – Days of campaign considered ‘snowy’ and ‘snow free’**

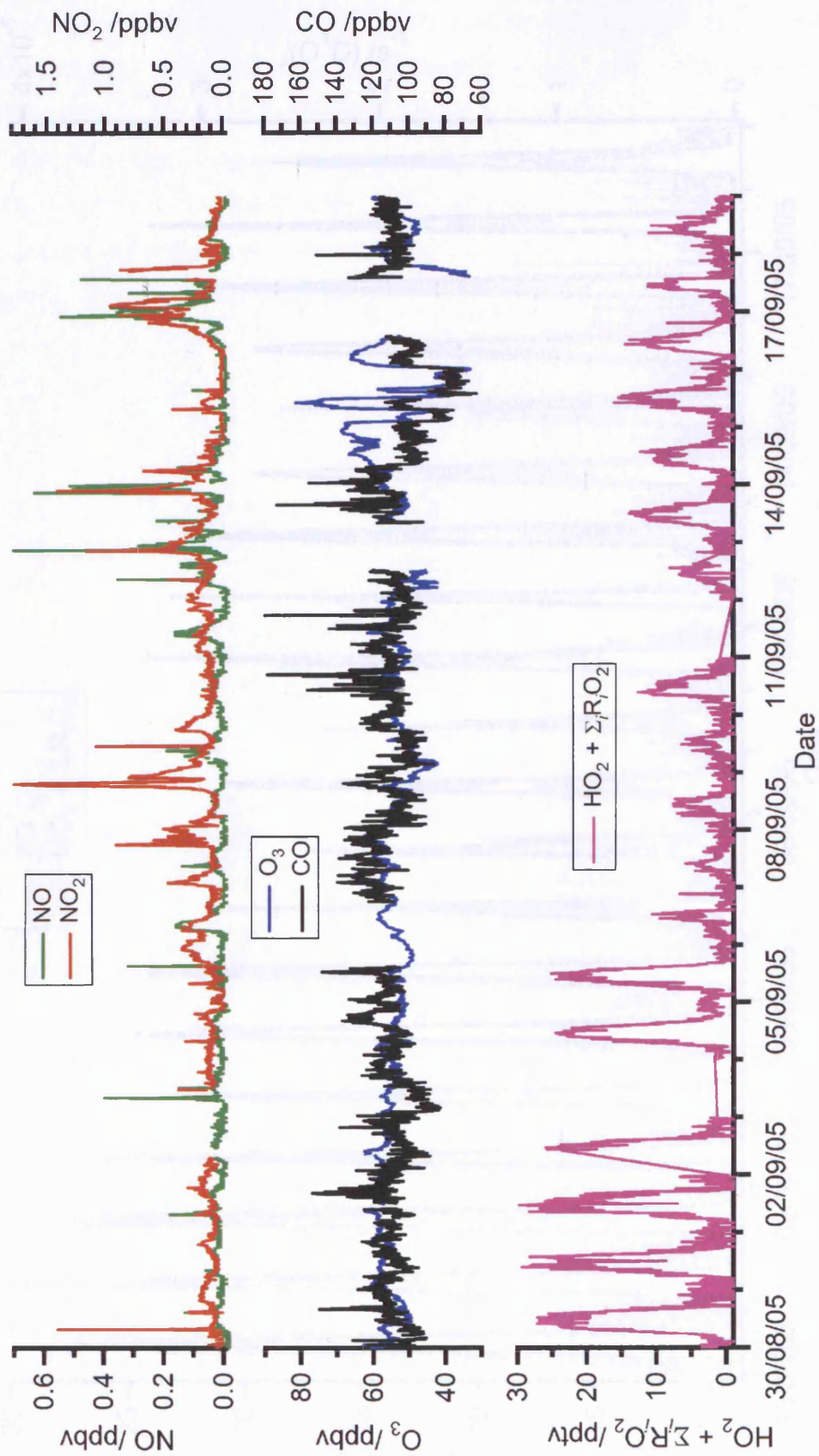
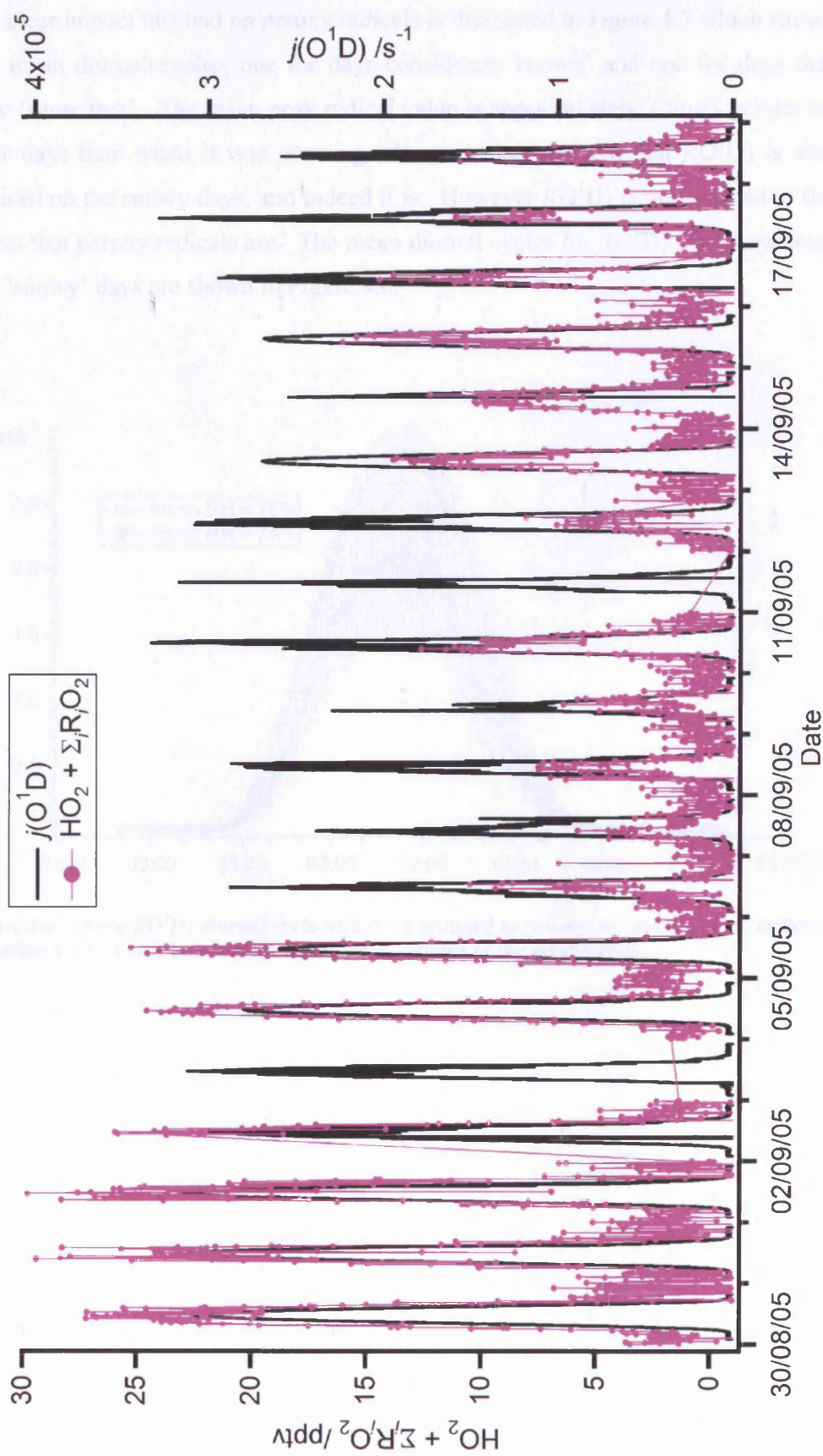


Figure 4.4 – Time series of peroxy radicals, O<sub>3</sub>, CO, NO and NO<sub>2</sub> measured at the Jungfraujoch from 30/08/05 – 18/09/05 inclusive.

Figure 4.5 – Time series of peroxy radicals and  $j(O^1D)$

The clear impact this had on peroxy radicals is illustrated in Figure 4.7 which shows two mean diurnal cycles, one for days considered ‘snowy’ and one for days that were ‘snow free’. The mean peak radical value is approximately 3 times greater on clear days than when it was snowing. It would be expected that  $j(\text{O}^1\text{D})$  is also reduced on the snowy days, and indeed it is. However  $j(\text{O}^1\text{D})$  is not reduced to the extent that peroxy radicals are. The mean diurnal cycles for  $j(\text{O}^1\text{D})$  for ‘snow free’ and ‘snowy’ days are shown in Figure 4.6.

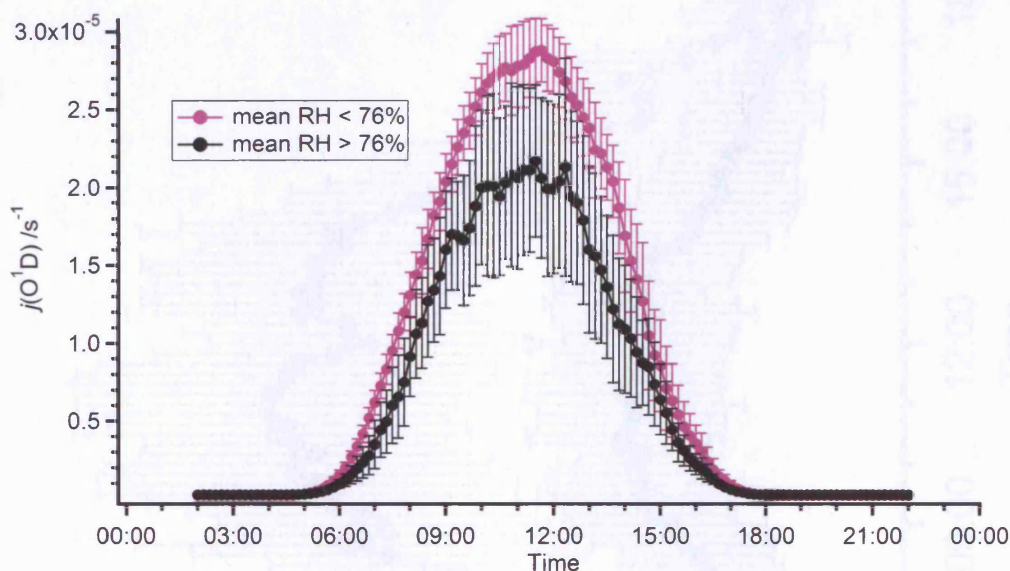


Figure 4.6 – Mean  $j(\text{O}^1\text{D})$  diurnal cycle with days assigned as ‘snowy’ or ‘snow free’ as defined in section 4.4.1. Error bars are the standard deviations of the mean values.

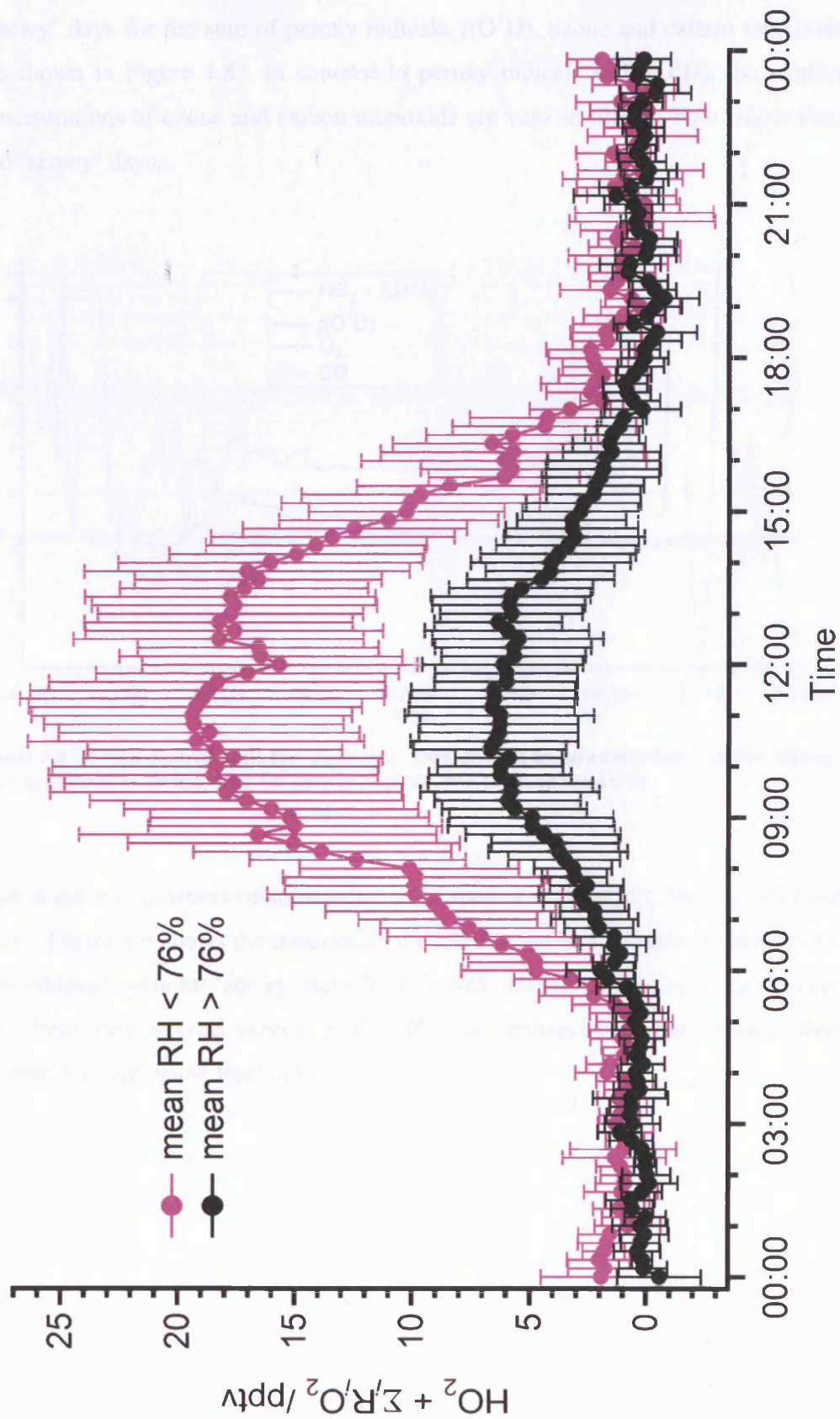


Figure 4.7 – Mean peroxy radical diurnal cycle with days assigned as ‘snowy’ or ‘snow free’ as defined in section 4.4.1. Error bars are the standard deviations of the mean values.

The mean diurnal cycle for ‘snow free’ days divided by the mean diurnal cycle for ‘snowy’ days for the sum of peroxy radicals,  $j(\text{O}^1\text{D})$ , ozone and carbon monoxide are shown in Figure 4.8. In contrast to peroxy radicals and  $j(\text{O}^1\text{D})$ , the relative concentrations of ozone and carbon monoxide are very similar on both ‘snow free’ and ‘snowy’ days.

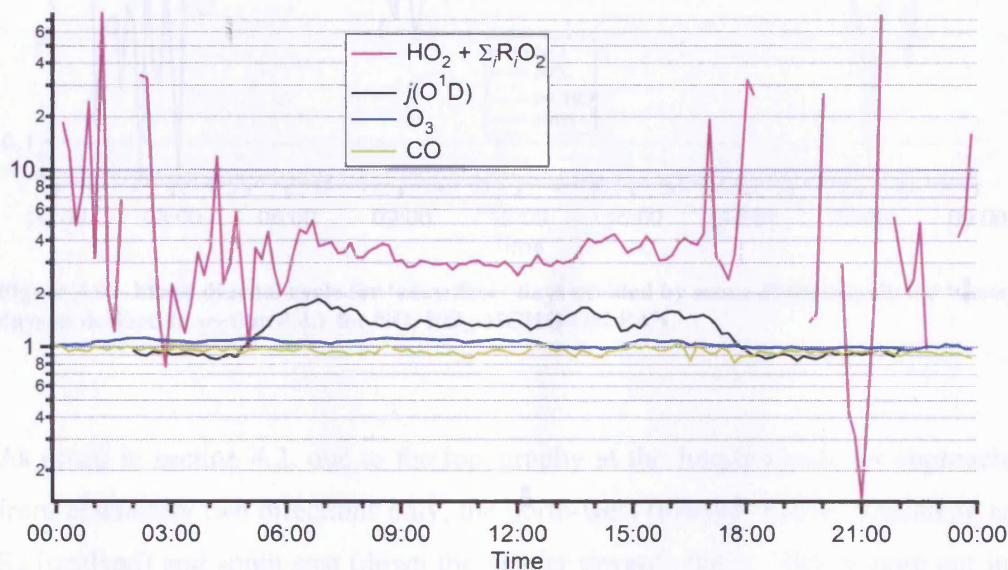


Figure 4.8 – Mean diurnal cycle for ‘snow free’ days divided by mean diurnal cycle for ‘snowy’ days as defined in section 4.4.1 for peroxy radicals,  $j(\text{O}^1\text{D})$ , ozone and CO.

This is not true however of some other trace species such as NO, NO<sub>2</sub>, HCHO and PAN. Figure 4.9 shows the mean diurnal cycle for ‘snow free’ days divided by the mean diurnal cycle for ‘snowy’ days for NO, NO<sub>2</sub>, HCHO and PAN. It can be seen that these species (and especially the NO<sub>x</sub>) are enhanced on the ‘snowy’ days compared to the ‘snow free’ days.

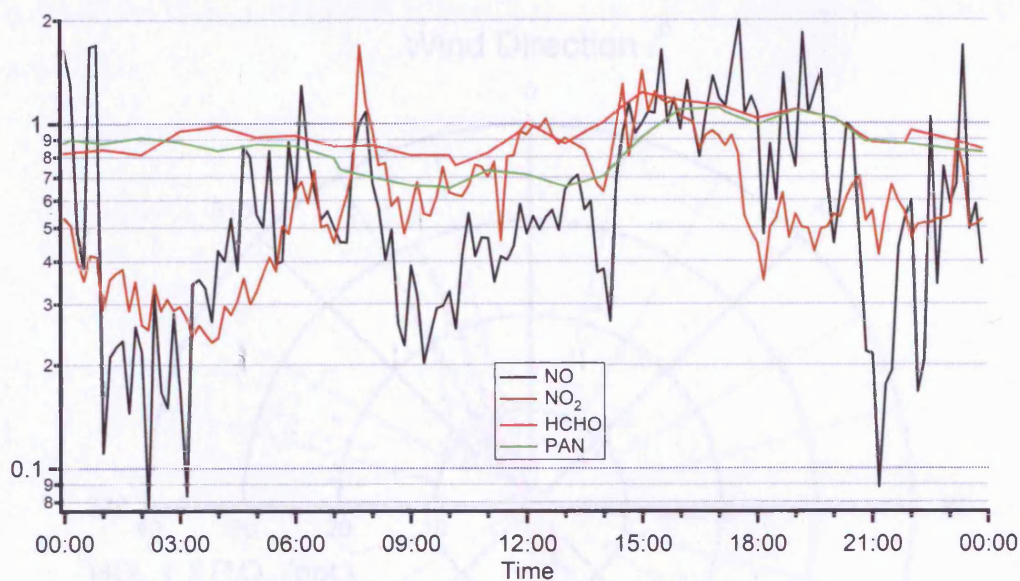


Figure 4.9 – Mean diurnal cycle for ‘snow free’ days divided by mean diurnal cycle for ‘snowy’ days as defined in section 4.4.1 for NO, NO<sub>2</sub>, HCHO and PAN.

As noted in section 4.2, due to the topography at the Jungfraujoch, air approaches from essentially two directions only, the north-west (towards Kleine Scheidegg and Switzerland) and south-east (down the glacier towards Italy). This is born out in a polar plot of peroxy radicals against wind direction as shown in Figure 4.10. Figure 4.10 is filtered by wind speed such that only those points where wind speed was greater than  $3 \text{ ms}^{-1}$  are included, and it can be seen that for the majority of points, the wind was either from the north-west or south-east.

On those days classified as ‘snowy’, the air was mostly from the south-east and on ‘snow free’ days the air was predominantly from the north-west. There is clearly then a fundamental chemical difference in air masses depending on origin, with air from the south east-arriving predominantly on ‘snowy’ days and showing suppressed peroxy radicals and enhanced NO<sub>x</sub> compared to ‘snow free’ days which are characterised by air of north-west origin. The suppression of peroxy radicals is not, however, solely due to the enhanced NO<sub>x</sub>, as shall be seen in section 4.4.3.

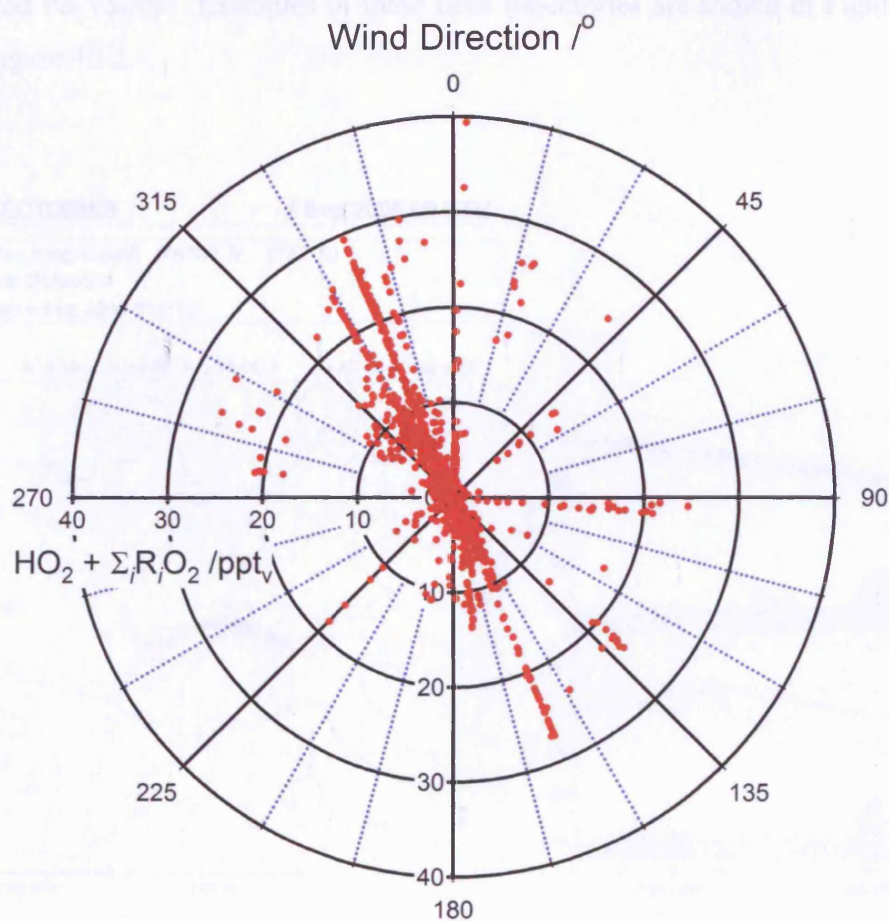


Figure 4.10 – Polar plot showing peroxy radical mixing ratio against wind direction.

#### 4.4.2 Back trajectories

Back trajectories have been run for the period of this campaign [Legreid, 2006], and have been used to investigate air mass origins for the two periods of interest, ‘snow free’ and ‘snowy’. The trajectories are available twice a day, corresponding to arrival times at Jungfraujoch of 00:00 UTC and 12:00 UTC.

The trajectories show that for days classified as ‘snow free’, the air masses arriving at the Jungfraujoch although from a wide range of starting positions, are from north of the alps and principally the Swiss plateau. However, on the days classified as ‘snowy’ the air masses are from the south over northern Italy and the heavily

polluted Po Valley. Examples of these back trajectories are shown in Figure 4.11 and Figure 4.12.

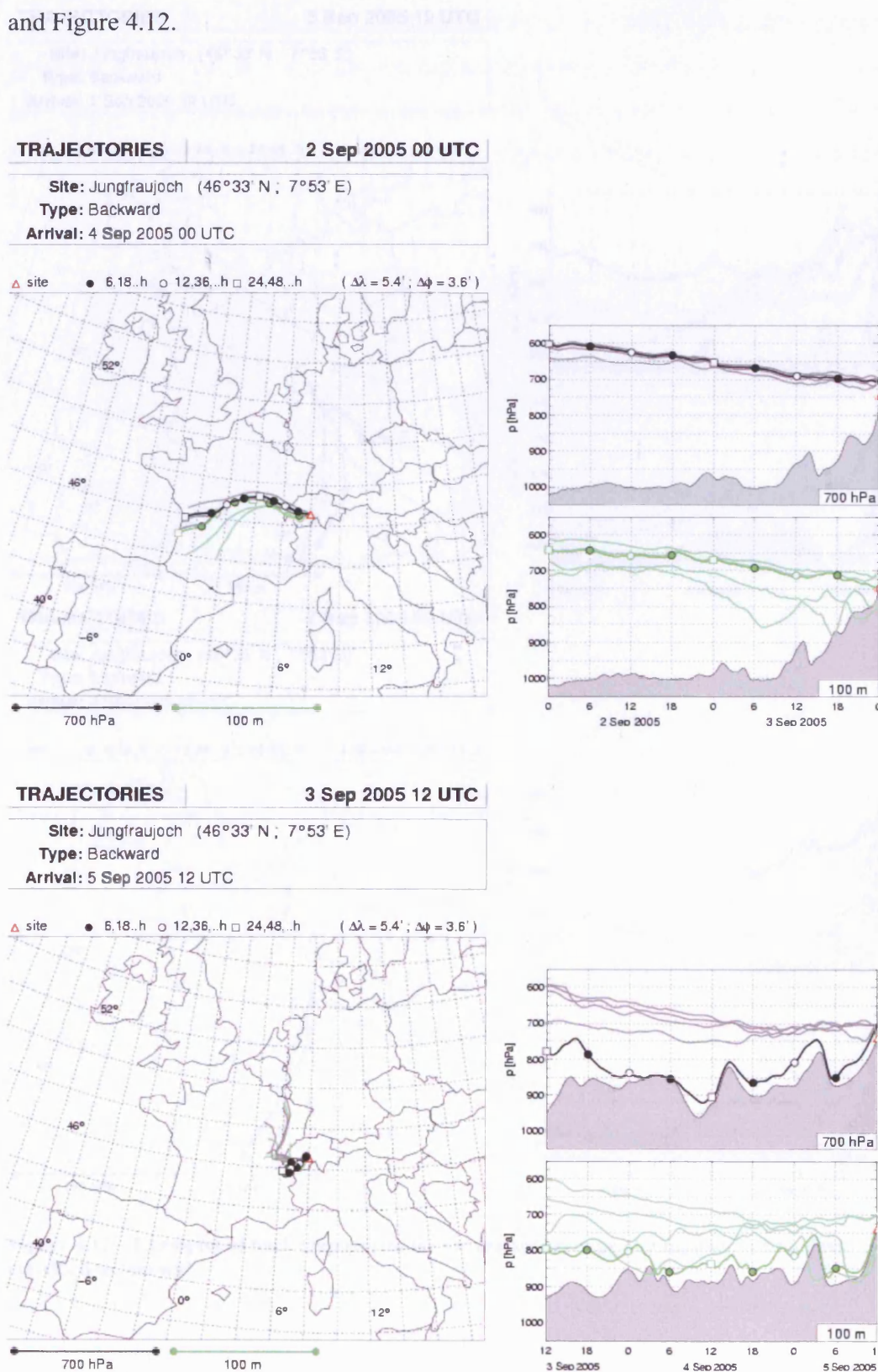


Figure 4.11 – Examples of back trajectories for air masses arriving at Jungfrauoch on days classified as ‘snow free’

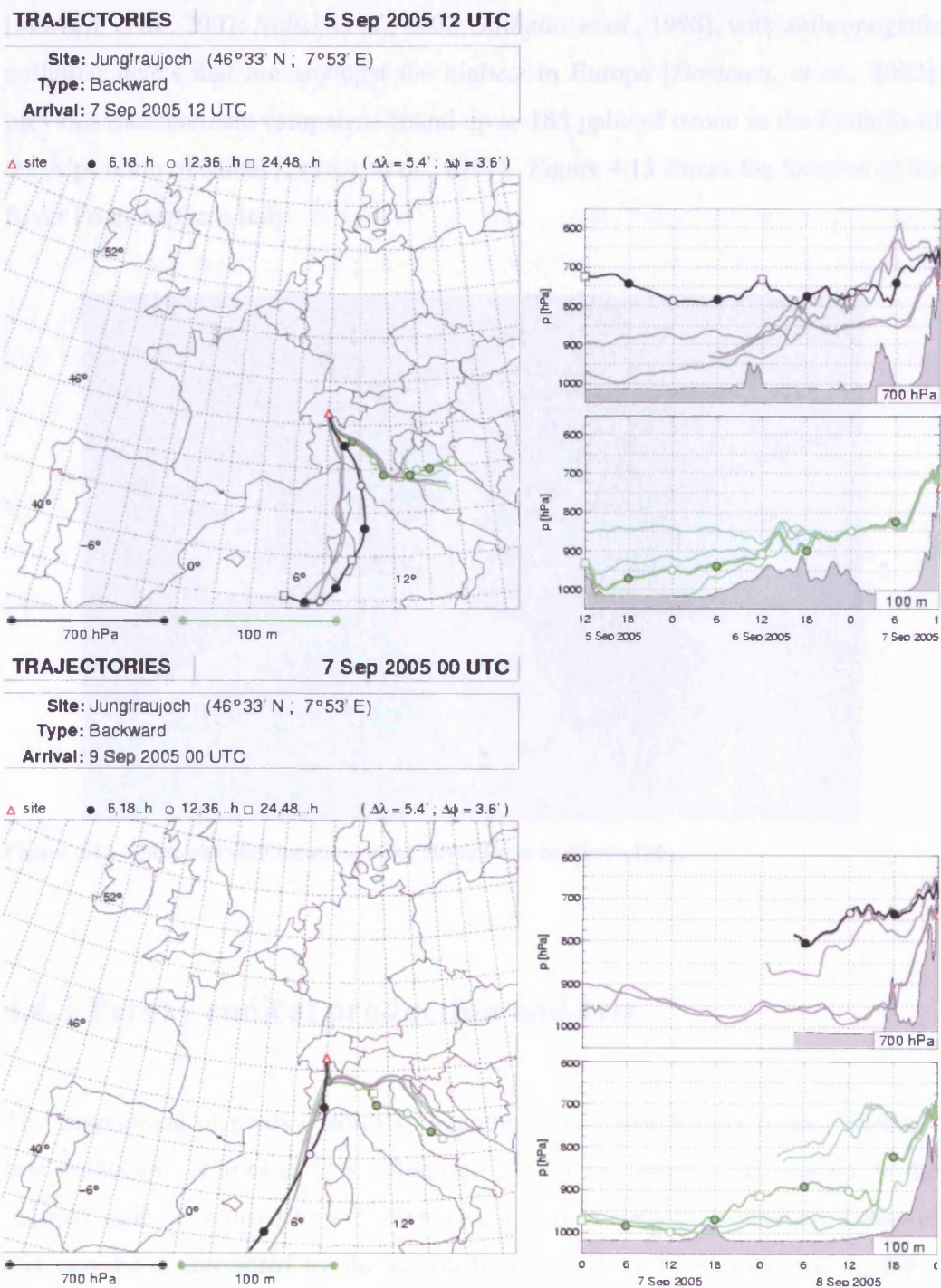


Figure 4.12 – Examples of back trajectories for air masses arriving at Jungfraujoch on days classified as ‘snowy’

The Po Valley is the river basin of the Po River in northern Italy that flows from Monviso in the Alps to the Adriatic Sea south of Venice. The Po Valley is the major industrial centre of north Italy, with cities situated within it including Turin,

Milan, Padua, Brescia and Verona. The Po Valley is a hotspot for pollution [Martilli, *et al.*, 2002; Neftel, *et al.*, 2002; Silibello, *et al.*, 1998], with anthropogenic pollution levels that are amongst the highest in Europe [Dommen, *et al.*, 2002]; previous measurement campaigns found up to 185 ppbv of ozone in the foothills of the Alps north of Milan [Prévôt, *et al.*, 1997]. Figure 4.13 shows the location of the River Po in northern Italy.

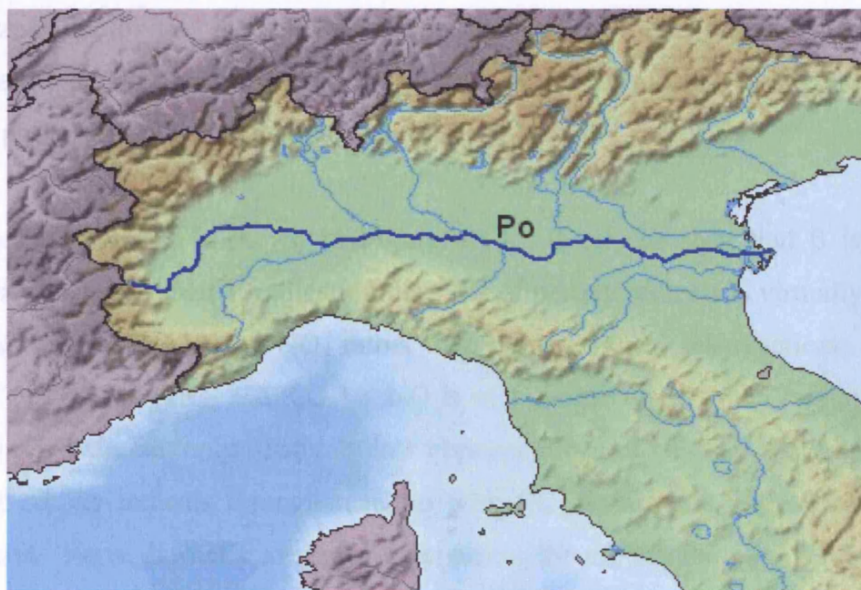


Figure 4.13 – Map showing location of the River Po in northern Italy.

#### 4.4.3 Peroxy radical production and loss

The suppression of peroxy radicals in southerly air could be due to two effects – less production or greater loss. Reduced  $j(\text{O}^1\text{D})$  on ‘snowy’ days owing to the reduced visibility caused by the snow would lead to reduced production, however this may be counteracted by the generally more humid air encountered on these days. Enhanced  $\text{NO}_x$  in the southerly air would lead to increased peroxy radical loss from the increase in reaction of peroxy radicals with  $\text{NO}_x$ . The industrialised Po Valley could be the source of this extra  $\text{NO}_x$ , and there is also the possibility of  $\text{NO}_x$  production from lightning as the moist air from the Mediterranean region rises rapidly as it reaches the Alps. There could also be another unknown peroxy radical sink other than self-reaction or reaction with  $\text{NO}_x$  causing the reduction in peroxy radical.

In order to further elucidate the reason for the suppressed peroxy radicals in the ‘snowy’ air, a steady state analysis of the production and loss of peroxy radicals during this campaign has been carried out using the method described by Mihele and Hastie [*Mihele and Hastie, 2003*] and in section 3.6.1. In this analysis,  $\beta$  is a measure of the dominant loss process for peroxy radicals. If  $\beta$  is less than one, then the dominant loss process is radical self-reaction rather than loss through reaction with  $\text{NO}_x$ .  $\gamma$  is a measure of additional peroxy radical production from sources other than ozone photolysis. A  $\gamma$  of zero indicates no excess production, whilst a  $\gamma$  of less than zero indicates that a higher concentration of peroxy radicals is calculated from ozone photolysis than is actually observed.

A time series for  $\beta$  is shown in Figure 4.14. It can be seen that  $\beta$  is almost exclusively greater than 1, indicating that loss of peroxy radicals is virtually always dominated by reaction with  $\text{NO}_x$  rather than peroxy radical self-reactions. As the rate of reaction of  $[\text{HO}_2 + \Sigma_i \text{R}_i \text{O}_2] + \text{NO}$  is of a similar order to the rate of peroxy radical self reaction, only relatively low concentrations of  $\text{NO}_x$  are required for the loss of peroxy radicals through reaction with  $\text{NO}_x$  to become important or even dominate. For a diurnally averaged time series, the mixing ratio of NO is greater than that of peroxy radicals by a minimum of 2-3 times midway through the day, and more at other times. The value of  $\beta$  reflects the suppression of peroxy radicals and enhancement of  $\text{NO}_x$  on ‘snowy’ compared to ‘snow free’ days, with median  $\beta$  four times larger on ‘snowy’ days.

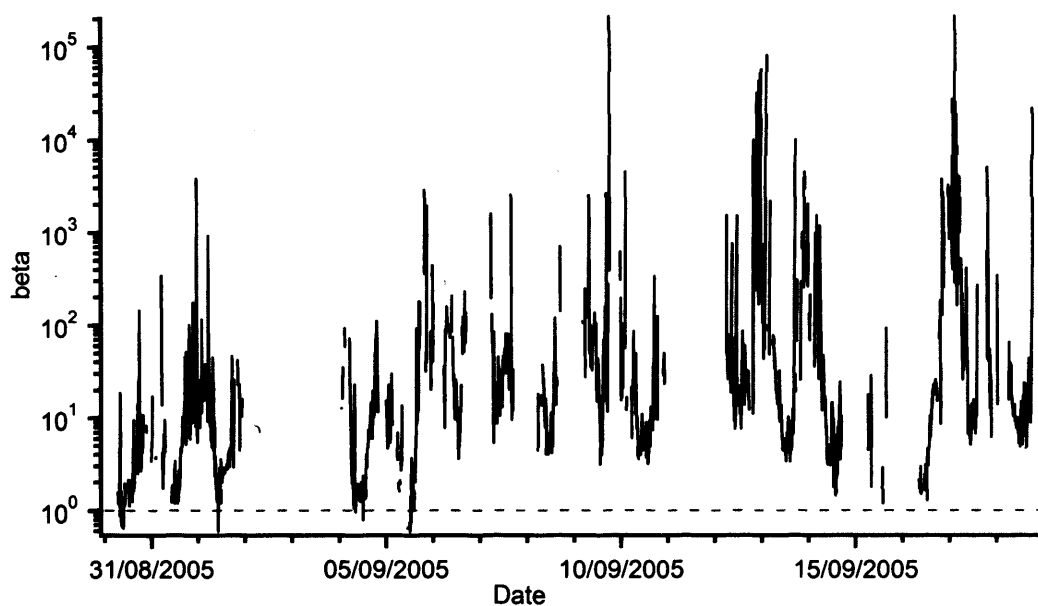


Figure 4.14 – Time series of  $\beta$

As mentioned,  $\gamma$  is a measure of additional peroxy radical production from sources other than ozone photolysis. Figure 4.15 is a plot of  $\gamma$ , from which it can be seen that on days designated ‘snowy’ there is a marked decrease in  $\gamma$  compared to days designated ‘snow free’.

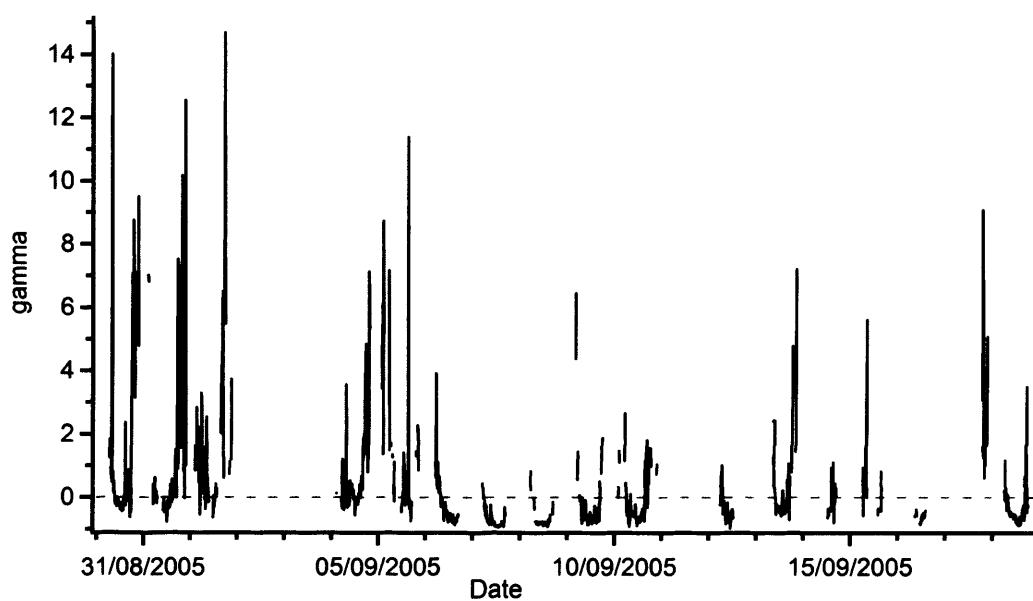


Figure 4.15 – Time series of  $\gamma$

The median  $\gamma$  for ‘snow free’ days is  $\gamma = 0.19$ , indicating that whilst the majority of peroxy radical production is from the photolysis of ozone to produce  $O(^1D)$  and

then subsequent reaction with water vapour to produce OH, followed by OH initiated oxidation of CO, CH<sub>4</sub> and other organic compounds, there is an appreciable level of peroxy radical production from other sources. This production from other sources is investigated in section 4.4.3.1.

However, for 'snowy' days the median  $\gamma$  value is  $\gamma = -0.49$ , indicating that either there is an overestimation of peroxy radical production or an underestimation of peroxy radical losses. As production *via* ozone photolysis is likely to be fairly well constrained (as  $j(\text{O}^1\text{D})$  and water vapour were both measured) and any additional production terms would lead to  $\gamma$  being even more negative, it is likely that there is an underestimation of peroxy radical losses.

In Chapter 3 the potential importance of fast reacting peroxy radicals such as acetylperoxy to an analysis of this kind was demonstrated. If we make the same assumption as in Chapter 3, that half of the organic peroxy radicals present are peroxyacetyl, there is a similar dramatic effect as seen in Chapter 3 –  $\gamma$  for 'snow free' days is increased from  $\gamma = 0.19$  to  $\gamma = 0.92$ , and for 'snowy' days  $\gamma$  is increased from  $\gamma = -0.49$  to  $\gamma = -0.24$ . Thus it can be seen that even with the questionable assumption of half of the organic peroxy radicals present being peroxyacetyl the increase in loss rate due to peroxy radical self-reaction is not enough to account for the negative  $\gamma$  observed. In fact, the atmosphere at the Jungfraujoch is relatively clean. Figure 4.16 shows the percentage loss of OH due to CO, CH<sub>4</sub>, HCHO and all other VOCs and OVOCs, as defined by the sum of the median values of  $k_{\text{OH}}[\text{VOC}]$  of interest divided by the sum of median values of  $k_{\text{OH}}[\text{VOC}]$  for all species, where  $k_{\text{OH}}$  is the rate of reaction of the VOC with OH.

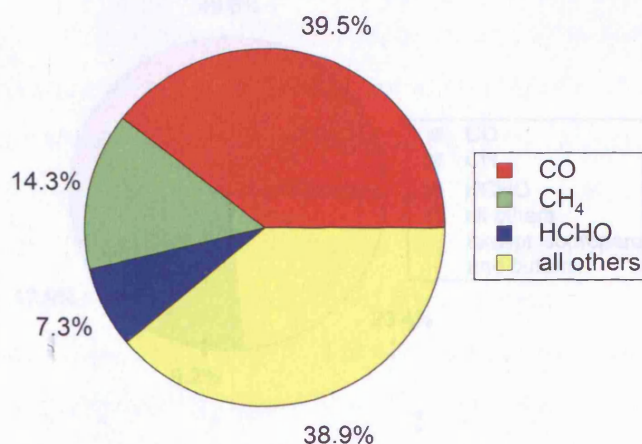


**Figure 4.16 – Relative contributions to OH loss**

Figure 4.16 shows a large contribution from species other than CO, CH<sub>4</sub> and HCHO and on further investigation over 20% of the total OH reactivity can be assigned to isopropanal and butanol. This is a surprising amount for a remote free tropospheric site and warrants further comment. Isopropanal and butanol, are both in common use at the Jungfraujoch. Butanol is used as a reagent in condensation particle counters (CPC) deployed at the site, and isopropanal is commonly used as a cleaning agent. It is therefore conceivable that some contamination has occurred, and although this raises further questions about the sampling of laboratory air by the instrument used for the OVOC measurements it is likely that the isopropanal and butanol are escaping from the lab only to be then drawn into the inlets of the OVOC instrument.

If the OH reactivity calculations are repeated whilst excluding isopropanal and butanol, the relative contributions to OH loss change markedly as shown in Figure 4.17.

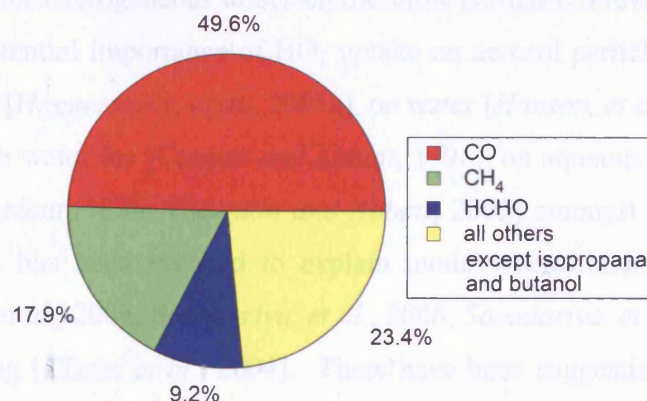


Figure 4.17 – Relative contributions to OH loss with isopropanal and butanol excluded

Nonetheless, even if there were a significant proportion of non-methyl fast reaction organic peroxy radicals present,  $\gamma$  is still significantly negative for ‘snowy’ days, indicating a missing loss term. To investigate the missing loss term, the equation for  $\gamma$  as given in Chapter 3 and repeated below:

$$\gamma = \left( \frac{[\text{HO}_2 + \sum_i \text{R}_i \text{O}_2]^2 \cdot \alpha \cdot (1 + \beta) \cdot \frac{k_{\text{self}}}{f \cdot j(\text{O}^1\text{D}) \cdot [\text{O}_3]}}{1} \right) - 1 \quad (\text{M})$$

has been expanded to include an extra loss term  $L_{\text{ex}}$ , thus

$$\gamma = \left( \frac{[\text{HO}_2 + \sum_i \text{R}_i \text{O}_2]^2 \cdot \alpha \cdot (1 + \beta) \cdot k_{\text{self}} + L_{\text{ex}}/2}{f \cdot j(\text{O}^1\text{D}) \cdot [\text{O}_3]} \right) - 1 \quad (\text{N})$$

where

$$L_{\text{ex}} = k_{\text{ex}} [\text{HO}_2 + \sum_i \text{R}_i \text{O}_2] \quad (\text{O})$$

In order to obtain  $\gamma = 0$  for ‘snowy’ days from equation (N),  $k_{\text{ex}}$  was adjusted until the median value of  $\gamma$  for ‘snowy’ days became zero. As such,  $k_{\text{ex}}$  is a pseudo first order rate constant that incorporates all extra loss processes after peroxy radical self-reaction losses and loss through reaction with  $\text{NO}_x$ . To obtain median  $\gamma = 0$  for ‘snowy’ days,  $k_{\text{ex}}$  was set so that  $k_{\text{ex}} = 0.0063 \text{ s}^{-1}$ . The question then is the origin of these extra losses.

One possibility is heterogeneous losses on the snow particles. Previous studies have outlined the potential importance of HO<sub>2</sub> uptake on aerosol particles in the marine boundary layer [Haggerstone, *et al.*, 2005a], on water [Hanson, *et al.*, 1992; Morita, *et al.*, 2004], on water ice [Cooper and Abbatt, 1996], on aqueous sulphate aerosol [Cooper and Abbatt, 1996; Thornton and Abbatt, 2005] amongst others. Aerosol uptake of HO<sub>2</sub> has been invoked to explain model overestimation of measured values [Smith, *et al.*, 2006; Sommariva, *et al.*, 2006; Sommariva, *et al.*, 2004] as has cloud processing [Olson, *et al.*, 2004]. There have been suggestions of falling ice crystals scavenging aerosols and gases absorbing onto the crystal surface or even diffusing into its bulk [Grannas, *et al.*, 2007]. However, there have been no reported studies of the loss or otherwise of HO<sub>2</sub> on snow.

#### 4.4.3.1 Additional peroxy radical production sources

It has been seen in the previous section that median  $\gamma$  is greater than zero for ‘snow free’ days, thereby signifying an additional production route over ozone photolysis. This additional production is significant with  $\gamma = 0.19$ , and could come from a variety of sources including ozonolysis of alkenes, NO<sub>3</sub> oxidation of alkenes and the photolysis of species such as HCHO and HONO. NO<sub>3</sub> oxidation of alkenes is only significant at night due to the rapid photolysis of NO<sub>3</sub> by sunlight [Monks, 2005] save for in very polluted atmospheres where daytime NO<sub>3</sub> can become important [Geyer, *et al.*, 2003]. Unfortunately HONO and NO<sub>3</sub> were not measured during this campaign, so it is not possible to determine the possible contribution they make to peroxy radical concentrations. In addition there were very sparse measurements of alkenes, so it is not possible to estimate the contribution of alkene ozonolysis to peroxy radical concentrations.

Formaldehyde and  $j(\text{HCHO})$  were measured during the campaign. The median production rate from the radical production channel of HCHO photolysis on the ‘snow free’ days where HCHO measurements are available show that formaldehyde contributes up to 13.7% as much as the median production from ozone photolysis on the same days. This corresponds to 0.14 of the total  $\gamma$  of 0.19, and as such

suggest that photolysis of formaldehyde is the most significant radical production source other than ozone photolysis.

#### 4.4.4 Seasonality

Previous peroxy radical measurements have been made at the Jungfraujoch in April and May 1996 during the Free Tropospheric Experiment 1996 (FREETEX '96) [Zanis, *et al.*, 1999; 2000b], in March and April 1998 during Free Tropospheric Experiment 1998 (FREETEX '98) [Carpenter, *et al.*, 2000; Zanis, *et al.*, 2000a] and in February and March 2001 during Free Tropospheric Experiment 2001 (FREETEX '01) [Zanis, *et al.*, 2003].

The mean daytime maximum peroxy radical concentration as reported by [Zanis, *et al.*, 2003] for FREETEX '96, '98, and '01 along with the mean daytime maximum peroxy radical concentration for all days and for 'snow free' days for this campaign are presented in Table 4.5 along with the average diurnal cycle for peroxy radicals from FREETEX '96, '98 and '01 [Zanis, *et al.*, 2003] and all days and 'snow free' days from this work in Figure 4.18.

Date	Campaign	Mean mid day peroxy radicals /pptv
mid-Feb – mid-Mar	FREETEX '01	$7 \pm 3^a$
mid-Mar – mid-Apr	FREETEX '98	$13 \pm 3^a$
mid-Apr – mid-May	FREETEX '96	$17 \pm 2^a$
end-Aug – start-Sept	This work – 'snow free' days	$19 \pm 5$
end-Aug – start-Sept	This work – all days	$13 \pm 4$

Table 4.5 – Mean daily maximum peroxy radical concentrations for FREETEX '96, '98 and '01 and this work for all days and for 'snow free' days. Errors quoted are 95% confidence limits. <sup>a</sup>[Zanis, *et al.*, 2003].

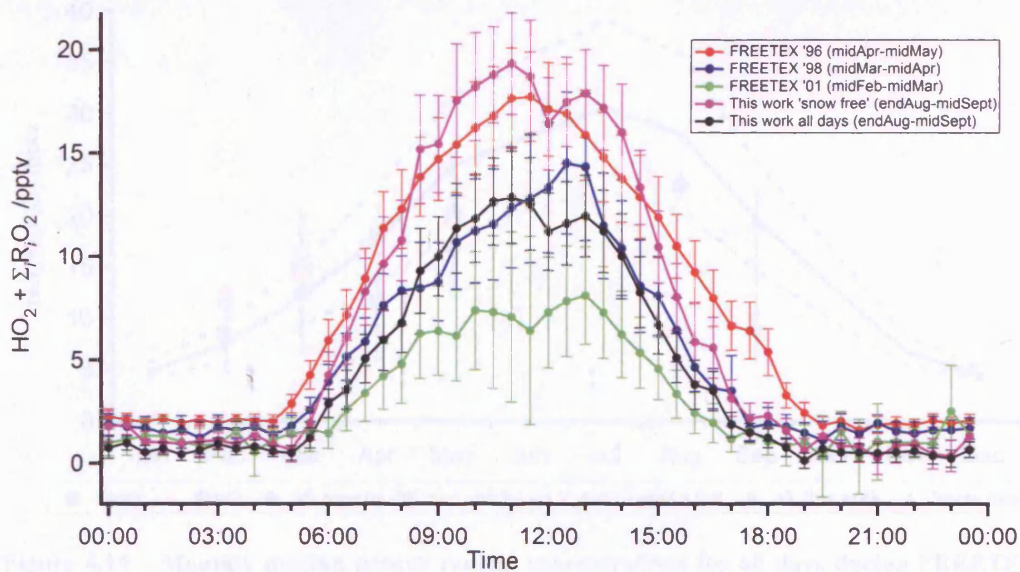


Figure 4.18 – Mean diurnal cycle for peroxy radicals from FREETEX '96, '98 and '01 [Zanis, *et al.*, 2003] and all days and 'snow free' days from this work.

It can be seen that the gradual seasonal increase in maximum mean daily peroxy radicals observed by [Zanis, *et al.*, 2003] continues through to the data taken during this work if only 'snow free' days are considered. However, if all days are considered then there is a decrease back to the maximum mean seen in mid-March to mid-April. [Zanis, *et al.*, 2000a] calculated theoretical peroxy radical concentrations for the 15<sup>th</sup> of each month using a simple CO/CH<sub>4</sub> box model constrained by climatological monthly mean values of O<sub>3</sub>, NO<sub>x</sub>, H<sub>2</sub>O, temperature and pressure measured at Jungfraujoch from 1992 – 1996. The modelled results were compared with monthly median values of measured peroxy radicals between 10:00 UTC and 13:00 UTC (a symmetric window around local noon).

Figure 4.19 shows monthly median peroxy radical concentrations as reported in [Zanis, *et al.*, 2003] for all days during FREETEX, and FREETEX data filtered by two different methods (described below), in addition to the data recorded during this work for all days and for 'snow free' days. The error bars represent the first and third quartiles. The model value on the 15<sup>th</sup> of each month as described above is shown as a solid line and the dashed lines represent the model sensitivity to 20% changes in O<sub>3</sub>, H<sub>2</sub>O, NO<sub>x</sub> and photolysis rates.

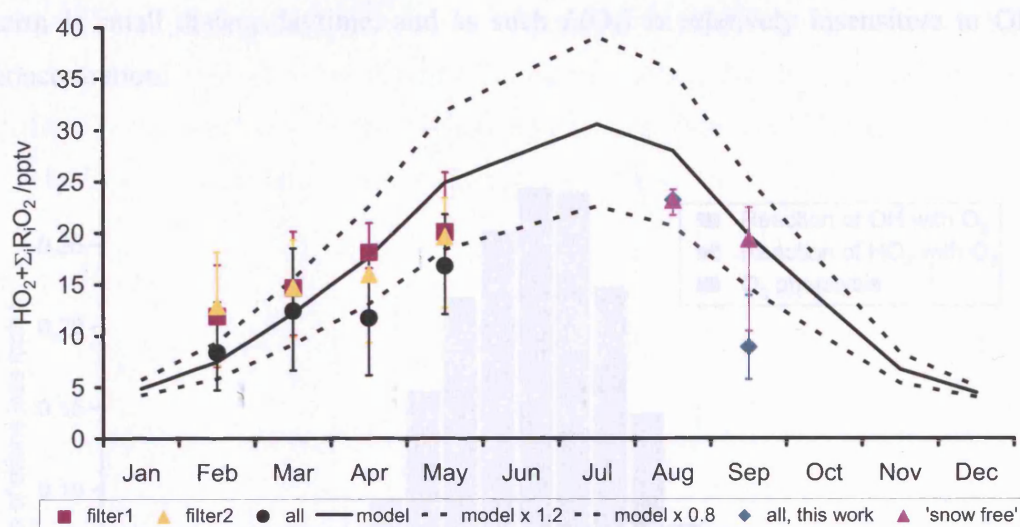


Figure 4.19 – Monthly median peroxy radical concentrations for all days during FREETEX, and filtered by two different methods (see text), with data recorded during this work for all days and for ‘snow free’ days. Error bars represent the first and third quartiles. Monthly model value on the 15<sup>th</sup> of each month is shown as a solid line, dashed lines represent model sensitivity to 20% changes in  $O_3$ ,  $H_2O$ ,  $NO_x$  and photolysis rates.

The measured values show a good agreement with the simple box model used, indicating that in the relatively clean atmosphere of the Jungfraujoch a good theoretical understanding can be achieved purely by invoking  $CO$  and  $CH_4$  chemistry, despite  $OH$  reactivity calculations indicating that up to 32.5% (discarding isopropanal and butanol) of  $OH$  reactivity is due to species other than  $CO$  and  $CH_4$ . It should be noted however that the measured monthly median peroxy radical concentrations for August only contain two days data (30/08/2005 and 31/08/2005), and thus care must be taken in extrapolating inferences too far.

#### 4.4.5 Ozone production and loss

As described in section 3.6.2 it is possible to calculate the instantaneous *in-situ* net ozone production or loss. This has been done for the period of measurements in this chapter. Similarly to chapter 3,  $OH$  and  $HO_2$  were not measured discretely, and so assumptions have to be made about their concentrations. In this chapter  $\alpha$  has been taken as 0.5 and the concentration of  $OH$  radicals has been taken at  $1 \times 10^6$  molecules  $cm^{-3}$ . It can be seen from Figure 4.20 that the relative contribution of the  $OH$  loss

term is small during daytime, and as such  $L(O_3)$  is relatively insensitive to OH concentration.

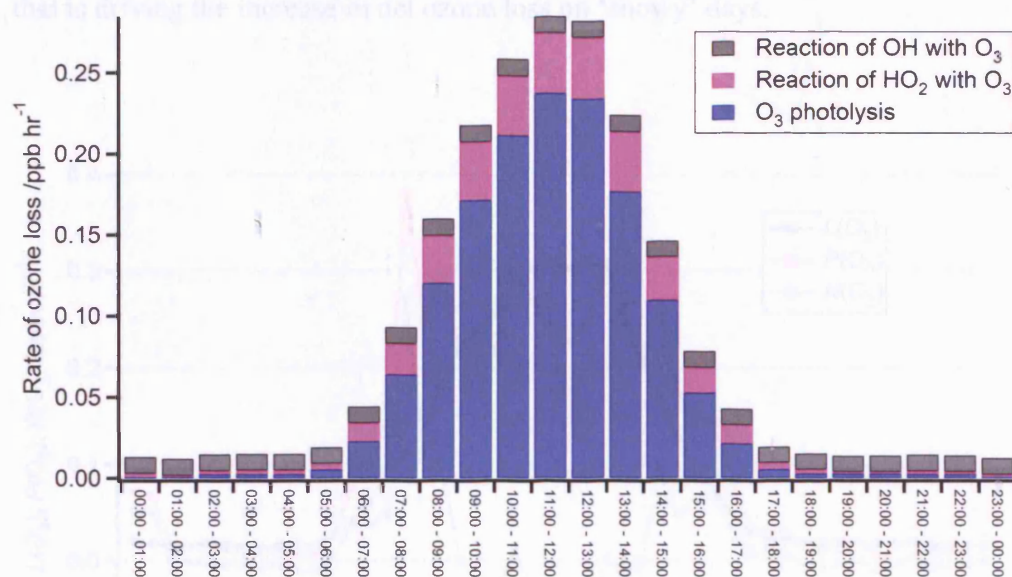


Figure 4.20 – Relative contributions of ozone loss terms to total  $L(O_3)$

This results in a time series for  $P(O_3)$ ,  $L(O_3)$  and  $N(O_3)$  as shown in Figure 4.23. It can be seen that overall the air-masses encountered during the time of this campaign were almost net neutral in terms of ozone production, with a median  $N(O_3)$  for the entire time series of  $-0.01$  ppb hr<sup>-1</sup> and a mean  $N(O_3)$  of  $0.00$  ppb hr<sup>-1</sup>.

If the days are split into ‘snow free’ and ‘snowy’ it can be seen that the ‘snowy’ days are generally more net ozone destructive. Table 4.6 details the median, mean, standard deviation and 10th and 90th percentiles for ‘snowy’ and ‘snow free’ days.

	$N(O_3)$ /ppbv hr <sup>-1</sup>	
	‘snow free’	‘snowy’
<b>Median</b>	-0.01	-0.02
<b>Mean</b>	0.02	-0.03
<b>Standard deviation</b>	0.16	0.10
<b>10<sup>th</sup> percentile</b>	-0.09	-0.14
<b>90<sup>th</sup> percentile</b>	0.11	0.03

Table 4.6 – Details of  $N(O_3)$  for ‘snow free’ and ‘snowy’ days

Mean diurnal cycles also highlight the differences between the two sets of days, as illustrated in Figure 4.21 and Figure 4.22. It can be seen that there is a much larger difference in  $P(O_3)$  between the two sets of days than there is in  $L(O_3)$ , and it is this that is driving the increase in net ozone loss on 'snowy' days.

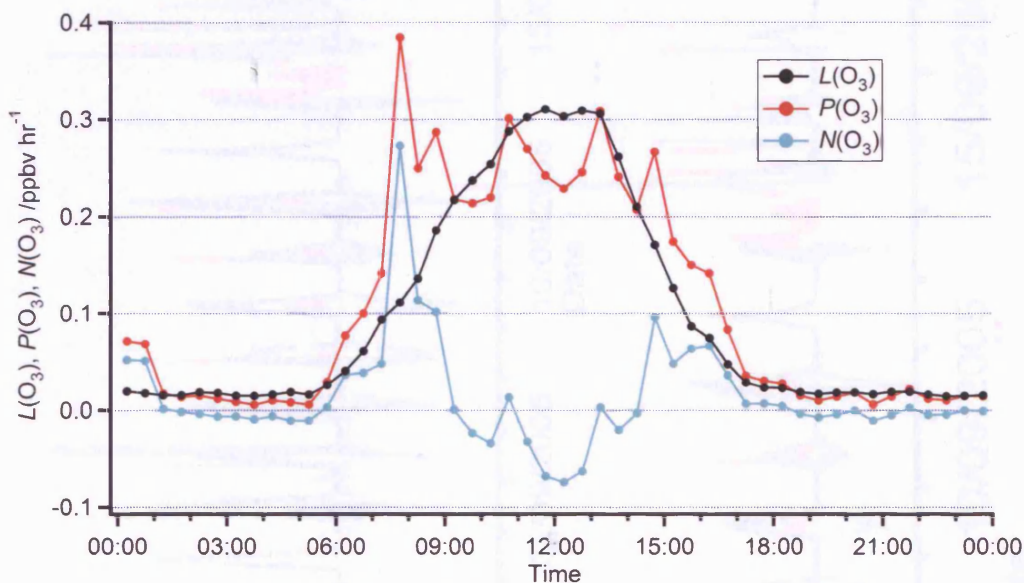


Figure 4.21 – Mean diurnal cycle for  $N(O_3)$ ,  $P(O_3)$  and  $L(O_3)$  on days classified as 'snow free'

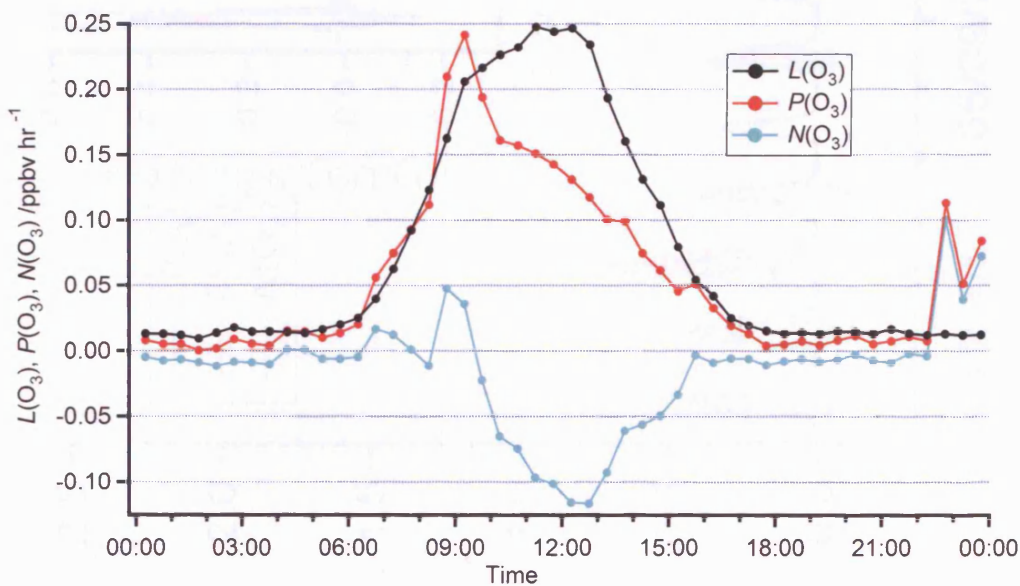
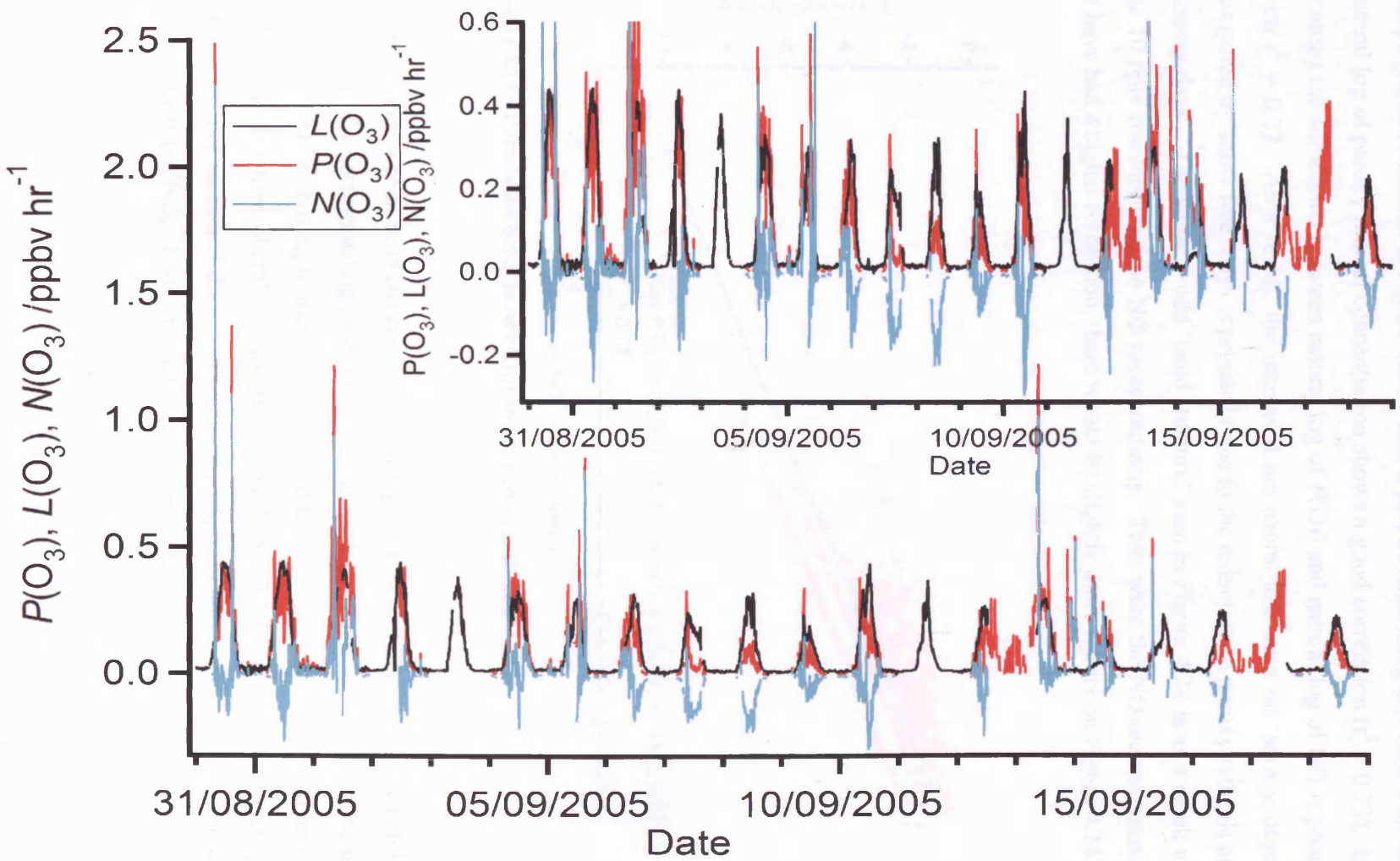


Figure 4.22 – Mean diurnal cycle for  $N(O_3)$ ,  $P(O_3)$  and  $L(O_3)$  on days classified as 'snowy'

Figure 4.23 – Time series of  $P(O_3)$ ,  $L(O_3)$  and  $N(O_3)$

The  $P(\text{O}_3)$  is itself limited by peroxy radicals throughout the measurement campaign, as evidenced in Figure 4.24 where a plot of natural log of  $P(\text{O}_3)$  with the natural log of peroxy radical concentration shows a good correlation ( $r^2 = 0.73$ ). In contrast the correlation between natural log of  $P(\text{O}_3)$  and natural log of NO is poor, with  $r^2 = 0.27$ . As a result, the increased net ozone loss seen on ‘snowy days’ compared to ‘snow free’ days is primarily due to the reduction of peroxy radicals on ‘snowy days’. The slightly odd ‘band structure’ seen in Figure 4.24 is as a result of the 10 pptv resolution of the NO measurements. Thus were the NO measurements to have had a higher resolution, there would be slightly more scatter on Figure 4.24.

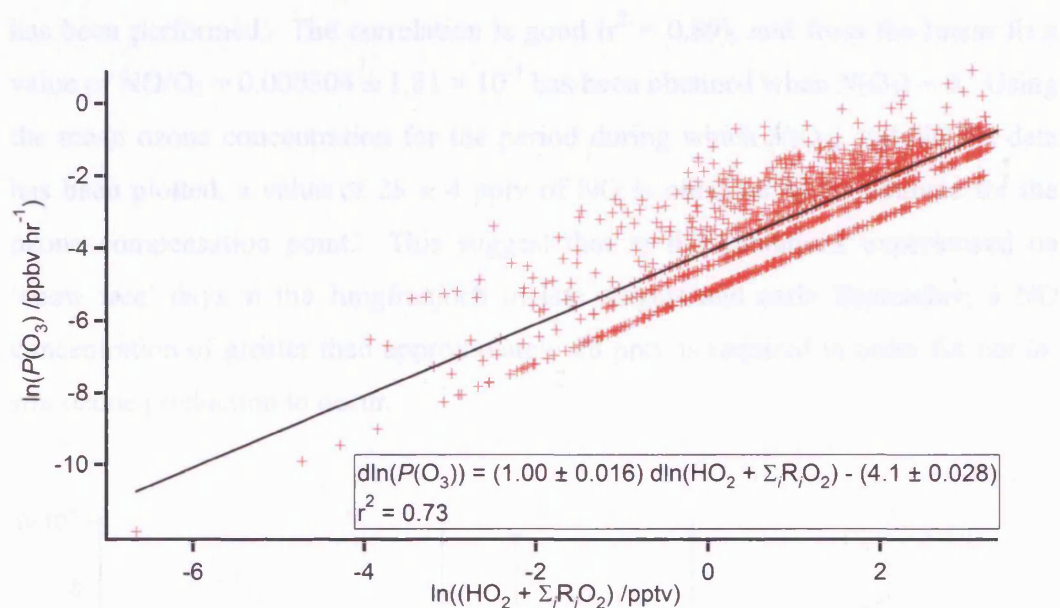


Figure 4.24 – Correlation between  $\ln(P(\text{O}_3))$  and  $\ln(\text{peroxy radicals})$

A early morning peak in  $P(\text{O}_3)$  can be seen in Figure 4.21 and Figure 4.22, which is as a result of a corresponding peak in NO. The peak in NO is at a similar time to when  $j(\text{HONO})$  is starting to increase, and could be due to an overnight build up of HONO which is then photolysed to provide the burst of NO seen. Unfortunately HONO was not measured during this campaign and therefore it is not possible to quantify the magnitude of NO production from HONO photolysis.

### 4.4.5.1 Ozone compensation point

The ozone compensation point is the concentration of NO at which  $N(\text{O}_3)$  becomes zero, *i.e.* the point at which *in-situ* ozone production matches *in-situ* loss [Zanis, *et al.*, 2000a]. To this end, Figure 4.25 is a plot of daily averaged NO/O<sub>3</sub> plotted against the respective daily mean  $N(\text{O}_3)$  during the times 06:00 UTC to 16:30 UTC for ‘snow free’ days. The times of 06:00 UTC to 16:30 UTC correspond to the period of the day where instantaneous  $j(\text{O}^1\text{D})$  is greater than 5% of the daily maximum  $j(\text{O}^1\text{D})$ . The error bars represent 95% confidence limits and a linear fit has been performed. The correlation is good ( $r^2 = 0.89$ ), and from the linear fit a value of  $\text{NO}/\text{O}_3 = 0.000504 \pm 1.81 \times 10^{-5}$  has been obtained when  $N(\text{O}_3) = 0$ . Using the mean ozone concentration for the period during which  $N(\text{O}_3)$  and NO/O<sub>3</sub> data has been plotted, a value of  $28 \pm 4$  pptv of NO is obtained as an estimate for the ozone compensation point. This suggests that in the conditions experienced on ‘snow free’ days at the Jungfrauoch in late August and early September, a NO concentration of greater than approximately 28 pptv is required in order for net *in-situ* ozone production to occur.

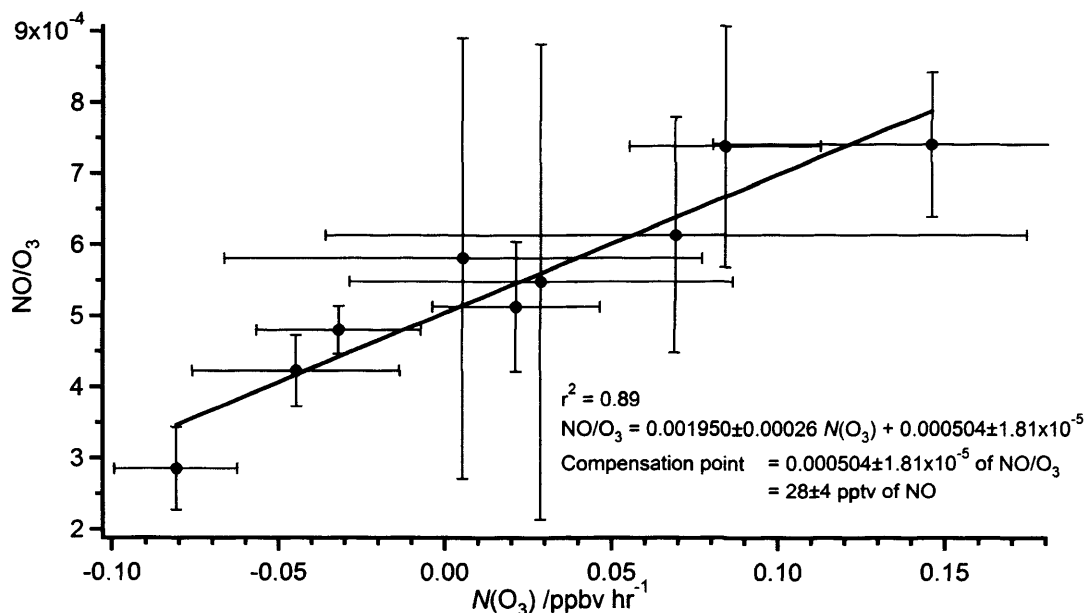


Figure 4.25 – Daily averaged NO/O<sub>3</sub> plotted against the respective daily mean  $N(\text{O}_3)$ . The error bars represent 95% confidence limits.

### 4.4.5.2 Comparison with previous results

Ozone production rates were calculated by [Zanis, *et al.*, 2003] for FREETEX '96, '98 and '01, although an estimate of NO derived from monthly median concentrations from 10:00 UTC to 13:00 UTC for 1992 – 1995 had to be used for FREETEX '96 as NO measurements were not performed. Reported values for  $N(O_3)$  range from 0.1 ppbv hr<sup>-1</sup> to 0.4 ppbv hr<sup>-1</sup> for monthly median values from 10:00 UTC to 13:00 UTC from late Winter to late Spring. For the same daily time period, the median  $N(O_3)$  measured during the work in this chapter for 'snow free' days was -0.05 ppb hr<sup>-1</sup>. The median NO concentration measured during this work for 'snow free' days between 10:00 UTC and 13:00 UTC was low at 30 pptv compared to the values quoted in [Zanis, *et al.*, 2003] of 56 pptv in February during FREETEX '01, 34 pptv in March during FREETEX '98 and '01, 67 pptv (estimated as detailed above) in April during FREETEX '96 and 65 pptv (estimated as detailed above) in May during FREETEX '96. The low concentrations of NO contribute to the reduced  $N(O_3)$  on 'snow free' days from 10:00 to 13:00 UTC as during these periods peroxy radical concentrations are relatively high and in contrast to the campaign as a whole  $P(O_3)$  is not solely peroxy radical limited but also NO limited.

The median concentration of NO on 'snow free' days between 10:00 UTC and 13:00 UTC of 30 pptv is similar to the calculated ozone compensation point for 'snow free' days of  $28 \pm 4$  pptv of NO, and helps to illustrate why  $N(O_3)$  is marginally negative during this period. In contrast, [Zanis, *et al.*, 2000a] calculated an ozone compensation point of  $24 \pm 9$  pptv of NO during FREETEX '98 when median monthly NO was 34 pptv and saw positive monthly median  $N(O_3)$  [Zanis, *et al.*, 2003].

## 4.5 Conclusions

The sum of peroxy radicals has been measured with the peroxy radical chemical amplification (PERCA) technique for a period from 30/08/2005 to 18/09/2005 inclusive along with a range of photolysis rates and supporting measurements.

During the measurement period two contrasting periods of weather were encountered – days on which heavy snowfall occurred and those on which it did not, defined herein as having a daily mean relative humidity of greater than 76%. The relative peroxy radical concentrations were very different during the two periods, with peroxy radicals significantly suppressed during ‘snowy’ days compared to ‘snow free’ days by up to a factor of 3 or more.  $j(\text{O}^1\text{D})$  was also reduced during the ‘snowy’ days, but not to the extent of peroxy radicals. In contrast ozone and CO are neither significantly suppressed nor enhanced, while NO, NO<sub>2</sub>, HCHO and PAN were all enhanced during the ‘snowy’ days.

A  $\beta$  and  $\gamma$  analysis as per [Mihele and Hastie, 2003] was carried out to investigate the origin of the suppression of peroxy radicals. The calculated median  $\gamma$  for ‘snowy’ days is -0.49, indicating that neither the increased NO<sub>x</sub> nor reduced  $j(\text{O}^1\text{D})$  can account for the suppression of peroxy radicals witnessed, and that there must be an unaccounted loss term present. A fast reacting peroxy radical (acetylperoxy) was introduced at half the total concentration of  $\Sigma_i \text{R}_i \text{O}_2$  to investigate the affect of the presence of a fast reacting peroxy radical similarly to during ITOP as detailed in chapter 3. However, the introduction of acetylperoxy resulted in  $\gamma = -0.24$ , indicating another loss term was still required to explain the discrepancy. In order to obtain median calculated  $\gamma = 0$  (with no acetylperoxy present), a pseudo first order loss rate of  $k_{\text{ex}} = 0.0063 \text{ s}^{-1}$  is required. It is speculated that this excess loss could be from heterogeneous processing on snow particles.

In contrast median  $\gamma$  for ‘snow free’ days is 0.19, indicating that on these days there is some excess radical production over that from ozone photolysis. Whilst possible sources include HONO photolysis (especially early in the morning) or oxidation of alkenes by ozone or NO<sub>3</sub> (especially at night), calculations of the photolysis of HCHO to produce radical products suggests that this route could account for up to 0.137 of the  $\gamma = 0.19$ .

The seasonal trends of peroxy radicals have been investigated in conjunction with data from the previous field campaigns FREETEX '96 [Zanis, *et al.*, 1999; 2000b], FREETEX '98 [Carpenter, *et al.*, 2000; Zanis, *et al.*, 2000a] and FREETEX '01 [Zanis, *et al.*, 2003]. The mean midday ‘snow free’ peroxy radical concentrations are marginally higher than the concentration measured during FREETEX '96 in

mid-April to mid-May, whereas if all days are considered the mean midday peroxy radical concentration recorded during this campaign is similar to that recorded during FREETEX '98 in mid-March to mid-April. The monthly median peroxy radical concentration between the hours of 10:00 to 13:00 UTC has been compared both with previous data and a simple box model as reported by [Zanis, *et al.*, 2003] and shows good agreement for 'snow free' days, but the model overestimates measured values when all days are taken into account, which could be explained by a missing loss term in the model as with the  $\gamma$  analysis.

Net ozone production rates have been calculated that show that overall the conditions encountered during this work at the Jungfraujoch were net neutral to marginally ozone destructive. Days during the snowfall period were more net ozone destructive than 'snow free' days, mainly due to reduced ozone production rather than increased ozone loss rates. Overall ozone production through the campaign was peroxy radical limited, except for a limited period around noon on 'snow free' days where low NO concentrations (median NO concentration was 30 pptv) and moderate peroxy radical concentrations (median peroxy radical concentration was 21 pptv) were experienced and ozone production was limited by both peroxy radicals and NO. The ozone compensation point was calculated for 'snow free' days during the campaign and suggests that under the conditions experienced a NO concentration of greater than approximately 28 pptv is required in order for net *in-situ* ozone production to occur.

The monthly median net ozone production on 'snow free' days between 10:00 UTC and 13:00 UTC is lower than that calculated by [Zanis, *et al.*, 2003] for , and can be explained by the lower concentrations of NO for the same time period seen in this work compared to that seen by [Zanis, *et al.*, 2003] from late Winter to late Spring. Whilst ozone production for this campaign in general is peroxy radical limited, during the times of 10:00 UTC and 13:00 UTC on 'snow free' days ozone production is limited by both peroxy radicals and NO.

# Chapter 5

## The Role of Radicals in the Formation of Secondary Organic Aerosol

This chapter describes work carried out at the atmospheric simulation chamber at the Paul Scherrer Institut, Switzerland into the role of peroxy radicals and gas-phase volatile organic compounds in the formation of Secondary Organic Aerosols (SOA).

### 5.1 Aerosols in the atmosphere

An aerosol is defined as the suspension of solid or liquid particles in a gas. The effect of aerosols on the atmosphere is well documented, and ranges from impairing visibility, climate change through perturbing the direct and indirect radiative forcing of the atmosphere [*Chung and Seinfeld, 2002; Jacobson, 2001; Lohmann, et al., 2000*], and altering atmospheric chemistry through enabling heterogeneous surface reactions [*Tie, et al., 2005*]. Fine aerosol can also have a detrimental effect on human health *via* inhalation [*Davidson, et al., 2005*], especially to susceptible portions of the population, e.g. the young and elderly. Aerosol composition is naturally dependent on the nature of the suspended particles, which can include sea salt, sulphate, nitrate, dust, ammonium, organic compounds and others, which often occur in a mixture.

Aerosols affect the direct radiative forcing of the atmosphere by scattering or absorbing solar radiation. The magnitude and direction of this effect is dependent on the both the composition and particle size of the aerosol. The net effect of black carbon aerosol is to heat the atmosphere owing to absorption then re-emission of solar radiation, whereas the net effect of most organic carbon aerosols is to cool the atmosphere as they reflect solar radiation back into space, essentially increasing the

atmospheric albedo. Aerosol particles smaller than a micrometer diameter are more efficient at scattering light than larger particles (as their diameter approaches the wavelength of light) [IPCC, 2001]. Further to this, aerosols have an indirect effect on radiative forcing *via* altering cloud properties. Aerosols can act as Cloud Condensation Nuclei (CCN) and thus alter cloud formation processes, leading to a decrease in precipitation efficiencies of warm clouds [IPCC, 2001; Novakov and Corrigan, 1996].

The impact of aerosols on atmospheric chemistry is also wide ranging. There has been much work into the importance of the reaction of  $\text{N}_2\text{O}_5$  and  $\text{NO}_3$  on the surface of aerosols and the concomitant impact on  $\text{O}_3$  and OH concentration [Dentener and Crutzen, 1993]. It has been estimated that the tropospheric global and yearly averages of  $\text{NO}_x$ ,  $\text{O}_3$  and OH are reduced by 50%, 9% and 9% respectively as a result of heterogeneous reactions of  $\text{N}_2\text{O}_5$  and  $\text{NO}_3$  on aerosols [Dentener and Crutzen, 1993]. Recent work has looked at other aerosol effects, such as the modification of photolysis rates by aerosol scattering and absorption of UV radiation and the uptake of  $\text{HO}_2$ ,  $\text{NO}_2$  and  $\text{NO}_3$  [Martin, *et al.*, 2003]. Model studies show a reduction in noontime  $j(\text{O}^1\text{D})$  at the surface throughout the Northern Hemisphere of more than 5%, mainly due to mineral dust aerosols [Martin, *et al.*, 2003] with a similar but weaker effect on  $j(\text{NO}_2)$ . The effect of mineral dust downstream of northern Africa has been estimated to reduce  $j(\text{O}^1\text{D})$  by 15–30% [Martin, *et al.*, 2002], whilst black carbon causes the majority of the 15–25% reduction over northern Europe in August [Martin, *et al.*, 2003]. Work during the Indian Ocean Experiment (INDOEX) in March 1999 found that aerosols over the northern Indian Ocean were responsible for a 40% reduction in  $j(\text{O}^1\text{D})$  at the surface [Burkert, *et al.*, 2003]

There can also be a significant aerosol contribution to atmospheric photochemistry *via* heterogeneous chemistry. It has been calculated that 10–40% of total  $\text{HO}_x$  loss in polluted continental boundary layers is down to  $\text{HO}_2$  uptake on aerosols; this rises to more than 70% over tropical biomass burning regions [Martin, *et al.*, 2003]. Further to this, uptake of  $\text{NO}_2$  and  $\text{NO}_3$  is estimated to account for 10–20% of  $\text{HNO}_3$  production (over biomass burning regions) while annual mean OH concentrations are decreased by 5–35% over the Northern Hemisphere boundary layer and 9% globally [Martin, *et al.*, 2003].

### 5.1.1 Secondary Organic Aerosol (SOA)

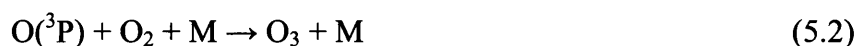
Organic aerosol, that is aerosols where the particulates are formed from organic matter, have been reported to be the main contributors to PM<sub>2.5</sub> (particulate matter with diameter less than 2.5µm) and PM<sub>10</sub> (particulate matter with diameter less than 10µm) at non-rural background sites over Western Europe [Putaud, *et al.*, 2004]. Measurements during the Cooperative LBA Airborne Regional Experiment (CLAIRE) as part of the Large Scale Biosphere-Atmosphere Experiment in Amazonia (LBA) have shown an average aerosol mass composition of 80% organics in the Amazon Basin [Roberts, *et al.*, 2001], whilst measurements during the Amazon Boundary Layer Experiment (ABLE-2) showed organic matter responsible for approximately 90% of aerosol mass [Andreae and Crutzen, 1997]. The very large potential contribution of organic matter to total aerosol and the importance of aerosols to atmospheric chemistry means it is of great importance to study the formation of organic aerosol.

Organic aerosols may be subdivided by origin into two groups – Primary Organic Aerosol (POA) and Secondary Organic Aerosol (SOA). If organic matter is released into the atmosphere directly from source (e.g. industrial combustion processes or biomass burning) then it is called POA. However, a huge variety of organic compounds are released into the atmosphere in gaseous form that can then undergo oxidative reactions to form further products that are of sufficiently low volatility to condense into the particle phase [Hoffman, *et al.*, 1997; Odum, *et al.*, 1996]. There has been much work in recent years towards identifying Volatile Organic Compounds (VOCs) that are important as SOA precursor species [Kamens, *et al.*, 1999; Larsen, *et al.*, 2001; Odum, *et al.*, 1996], with monoterpenes and aromatic compounds being particularly important.

### 5.1.2 Secondary organic aerosol formation mechanisms

Recently the importance of the formation of oligomers and polymers from VOCs to SOA formation has been recognised [Gao, *et al.*, 2004; Kalberer, *et al.*, 2004]. The

full mechanism is very complex and still not fully understood [Librando and Tringali, 2005]. However, for all of the experiments carried out in the initial part of this study and detailed in Table 5.2, there is a ‘standard’ basic experimental mechanism. Initially in the chamber is the parent VOC, NO<sub>x</sub>, and bar experiment 8, water vapour. Consequently, as the lights are switched on, NO<sub>2</sub> is photolysed to form O(<sup>3</sup>P), which can then react with oxygen to form ozone. Subsequently the ozone is photolysed to produce O(<sup>1</sup>D) which can react with water vapour to produce OH. This OH then initiates the oxidation of the parent VOC, producing RO<sub>2</sub>:



As RO<sub>2</sub> and HO<sub>2</sub> are produced, NO is oxidised to NO<sub>2</sub>, with the NO<sub>2</sub> subsequently being removed *via* production of HNO<sub>3</sub> and other organic nitrates, in addition to potentially entering the aerosol phase. As NO<sub>2</sub> is the only ozone source in the chamber, a reduction in ozone concentration follows the removal of NO<sub>x</sub> as ozone is consumed and not replaced.

Following the oxidation of the parent VOC to form primary oxidation products, these primary oxidation products can then be further oxidised, again *via* peroxy radicals. Polymerisation can then result from the carbonyls produced reacting with their hydrates [Kalberer, *et al.*, 2004]. An example of this is the formation of methyl glyoxal from oxidation of 1,3,5-trimethylbenzene and subsequent polymerisation as proposed by [Kalberer, *et al.*, 2004] and shown in Figure 5.1.

There has been much work into the role of monoterpenes, especially α- and β-pinene, which has highlighted the potential importance of multifunctional products of parent VOC oxidation such as those that contain hydroperoxide functionality in SOA formation [Kanakidou, *et al.*, 2005].

In order to fully understand the process it would be ideal to measure as many species involved in the mechanism as possible. There have been some studies into oligomerisation followed by particle phase partitioning [*Alfarra, et al.*, 2006; *Baltensperger, et al.*, 2005; *Kalberer, et al.*, 2004; *Tolocka, et al.*, 2004], with the gas phase measurements in general restricted to VOCs, O<sub>3</sub>, NO<sub>x</sub> and relative humidity. As peroxy radicals are involved at virtually all steps any proposed mechanism, it would clearly be of interest to measure peroxy radicals in addition to VOCs, O<sub>3</sub>, NO<sub>x</sub> and relative humidity during the formation processes of SOA.

Consequently, during the latter part of 2005, the University of Leicester was involved in work at the atmospheric simulation (or smog) chamber at the Paul Scherrer Institut (PSI), Switzerland in order to study the mechanisms of SOA formation.

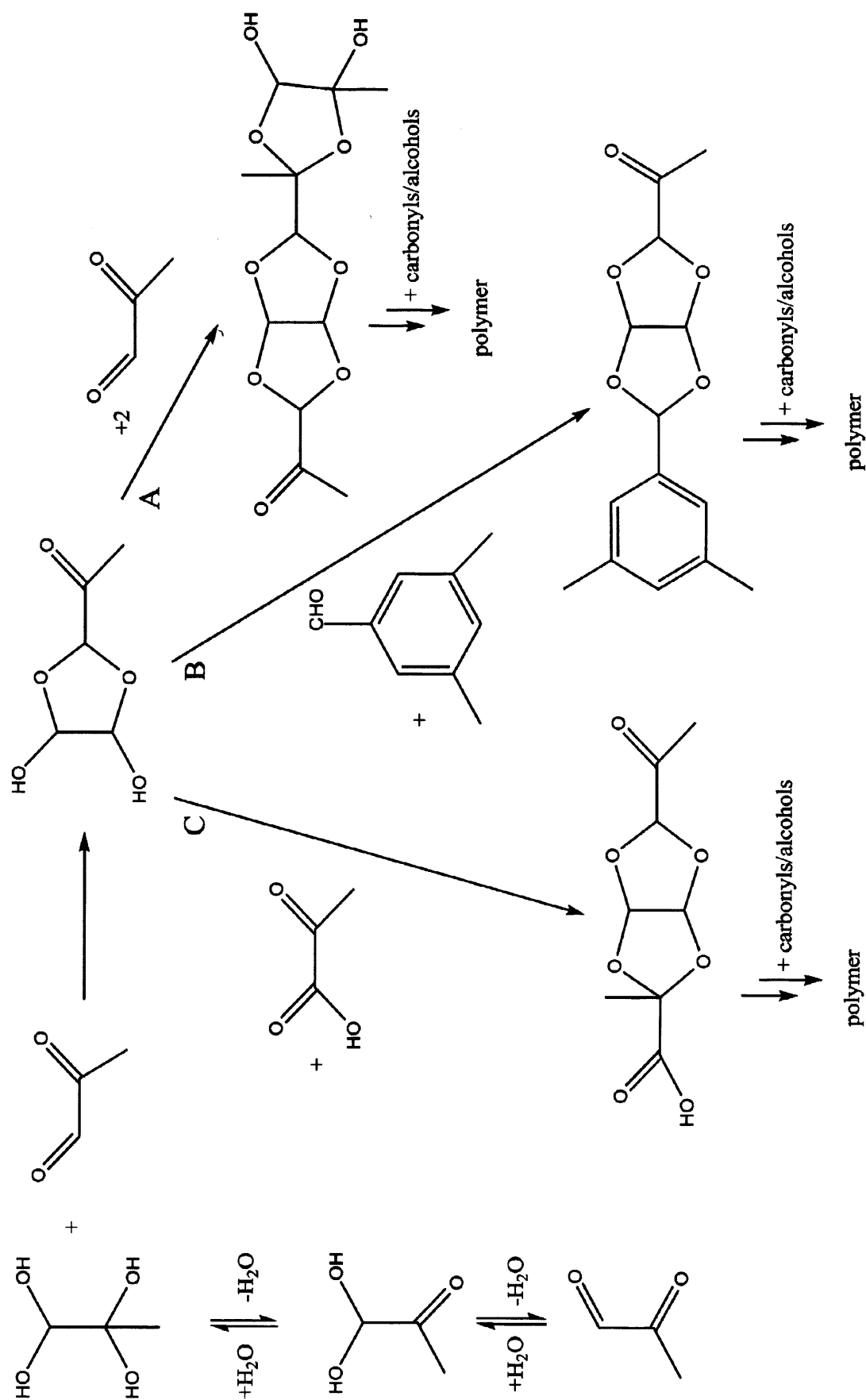


**Figure 5.1 – Proposed SOA polymerisation mechanism from methyl glyoxal [Kalberer, *et al.*, 2004]. (A) is a methyl glyoxal route only, (B) incorporates 3,5-dimethylbenzaldehyde and (C) includes pyruvic acid**

## 5.2 The PSI atmospheric simulation chamber

The atmospheric simulation chamber is described in detail by [Paulsen, *et al.*, 2005], but is described briefly here. The chamber is a 27 m<sup>3</sup> (3 × 3 × 3 m) bag constructed from *Teflon*<sup>®</sup> fluorocarbon film (fluorinated ethylene propylene – FEP) suspended within a temperature controlled (to ± 1 °C) wooden housing 4 × 5 × 4 m (w × l × h). The walls and ceiling of the wooden housing are covered in aluminium foil whilst the floor is covered with aluminium sheets in order to maximise light reflection. The solar spectrum is simulated using four xenon arc lamps at 4 kW each situated at each corner of the chamber within enclosures constructed from borosilicate glass in order to filter radiation below ~ 300 nm and thus remain representative of the solar radiation reaching the earth's surface. There are two manifolds present in the sides of the bag to allow for inlet and outlet ports, and gas generation and dilution systems make it possible to inject ozone (generated *via* UV irradiation of pure air), humidified air, NO, NO<sub>2</sub> or any other desired reagent. Hydrocarbons are injected *via* evaporation of the liquid hydrocarbon in a heated bulb. The chamber was humidified by bubbling bulk gas (nitrogen (Carbagas, 99.999%) and oxygen (Carbagas, 99.999%)) through a heated container of deionized water (15 MΩ). The chamber was then allowed to equilibrate for 30 minutes before the start of the experiment.

A plan of the chamber can be found in Figure 5.2 [Paulsen, *et al.*, 2005].

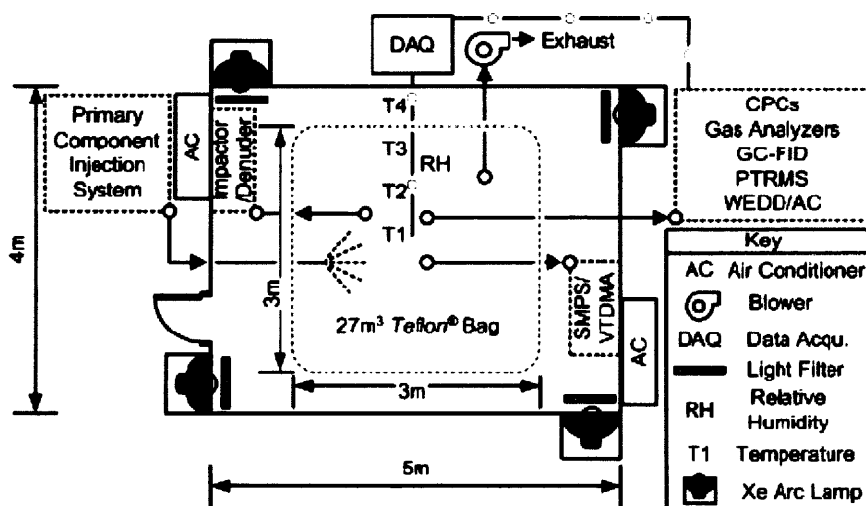


Figure 5.2 – Plan of the atmospheric simulation chamber at PSI [Paulsen, *et al.*, 2005]

## 5.3 Instrumentation

A wide range of instrumentation was deployed to monitor both the gas and particle phase during a series of experiments. The species measured are summarised in Table 5.1, with details given below.

Species measured	Technique	Institute
$\text{HO}_2 + \Sigma_i \text{R}_i \text{O}_2$	PERCA	UoL <sup>a</sup>
Gas phase organics	CIR-TOF-MS	UoL <sup>a</sup>
Gas phase organics	PTR-MS	PSI <sup>b</sup>
Ozone	UV absorption	PSI <sup>b</sup>
NO	Chemiluminescence	PSI <sup>b</sup>
NO <sub>2</sub>	Chemiluminescence	PSI <sup>b</sup>
Relative Humidity	Capacitance hygrometer	PSI <sup>b</sup>
Aerosol number concentration	Condensation particle counters	PSI <sup>b</sup>
Particle size distribution	Scanning mobility particle sizer	PSI <sup>b</sup>
Aerosol composition	Aerosol mass spectrometer	PSI <sup>b</sup>

Table 5.1 – Summary of species measured. <sup>a</sup>University of Leicester, <sup>b</sup>Paul Scherrer Institut.

### 5.3.1 Peroxy radical measurements

The sum of peroxy radicals ( $\text{HO}_2 + \Sigma_i \text{R}_i \text{O}_2$ ) was measured with a Peroxy Radical Chemical Amplifier (PERCA) instrument as described in detail in Chapter 2. In order to reduce peroxy radicals losses that sampling *via* a line would have introduced, the PERCA inlets were introduced directly to the chamber through the chamber wall *via* custom made polytetrafluoroethylene (PTFE) ports. The ports enabled the inlets to protrude into the chamber, whilst the construction from relatively chemically inert PTFE reduced any perturbation of the interior of the chamber. The inlets passed through the centre of the port and were sealed with o-rings coated in FEP (fluorinated ethylene propylene) (FEP-O-SEAL<sup>®</sup>, Angst + Pfister AG) to reduce contamination within the chamber. Consequently, the PERCA inlets were sampling from approximately 2 cm into the bag, and not from the centre of the bag as was the case for other gas phase species and aerosol measurements. This could lead to incongruities either if the bag was not well mixed

or the proximity of the PERCA inlets to the chamber wall lead to interferences from increased wall loss. Figure 5.3 is a schematic diagram showing an inlet port.

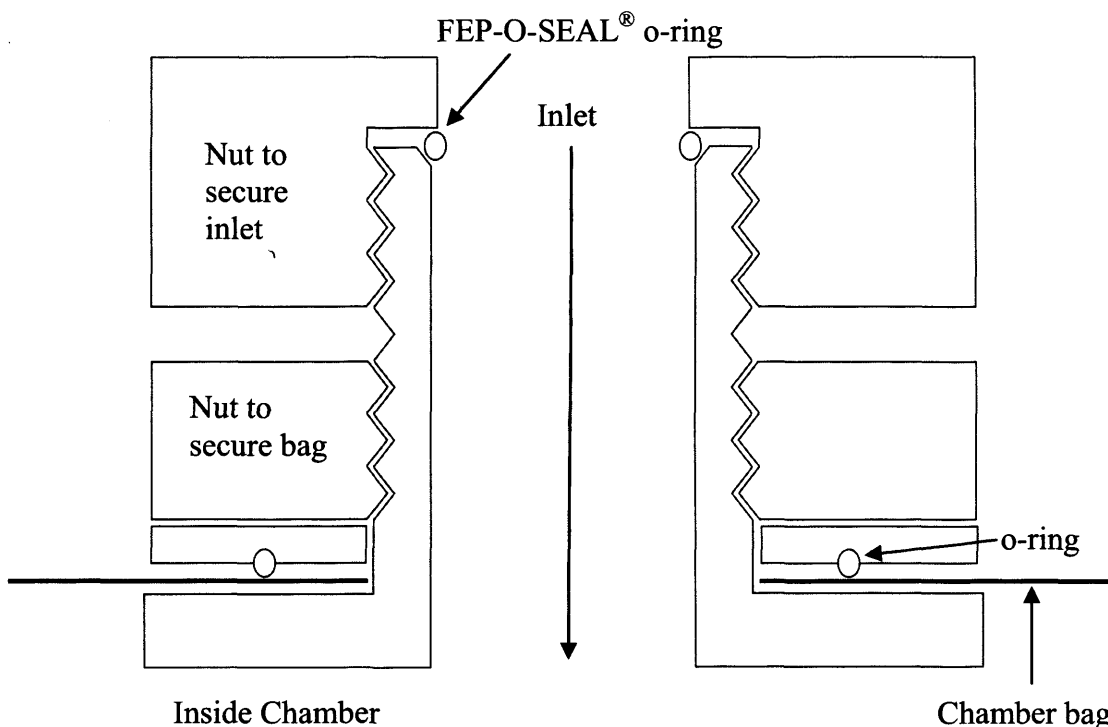


Figure 5.3 – Schematic diagram of port used to fit inlet to chamber

### 5.3.2 HO<sub>2</sub> measurements

Recently there has been work to develop a method to separate the measurements of HO<sub>2</sub> and  $\Sigma_i R_i O_2$  made by the PERCA by taking advantage of the faster wall loss rate of HO<sub>2</sub> compared to  $\Sigma_i R_i O_2$  [Jacob, 2005b]. Typically the length of the PERCA inlet before the forward reagent injection port is kept short in order to minimise radical losses. If this region is elongated and packed with a material such as PFA tubing, it is possible to greatly reduce HO<sub>2</sub> transmission without removing any RO<sub>2</sub>. Thus by denuding HO<sub>2</sub> a measurement of  $\Sigma_i R_i O_2$  becomes possible, and by subtracting the measurement of  $\Sigma_i R_i O_2$  from the denuding inlet from the measurement of HO<sub>2</sub> +  $\Sigma_i R_i O_2$  from a standard inlet, the concentration of HO<sub>2</sub> can also be found. Consequently both a standard inlet and a HO<sub>2</sub> denuding inlet were deployed during the series of experiments described in this chapter. However, a technical problem with one of the LMA-3 NO<sub>2</sub> detectors meant that the HO<sub>2</sub>

denuding inlet was unable to be operated, and thus all peroxy radical data presented in this chapter are  $\text{HO}_2 + \Sigma_i \text{R}_i \text{O}_2$ .

### 5.3.3 Additional gas phase instrumentation

A suite of other gas phase measurements were made at the chamber. The University of Leicester in addition to the PERCA also deployed a Chemical Ionisation Reaction Time-of-Flight Mass Spectrometer (CIR-TOF-MS) operating in Proton Transfer Reaction mode (PTR) as described in [Blake, *et al.*, 2004] in order to follow gas phase organic compounds. A PTR-MS (Ionicon Analytik GmbH) was also present to measure gas phase organics. Ozone was measured by UV absorption (EnviroNics S300) and NO and NO<sub>2</sub> were measured by chemiluminescence by two instruments – a Monitor Labs 9841A (for NO<sub>x</sub> concentrations: 50 - 2000 ppbv) and a Thermo Environmental Instruments Inc. 42C (for NO<sub>x</sub> concentrations: 0 - 200 ppbv). Relative humidity was measured with a Rotronic Hygro Clip SC05 humidity sensor.

### 5.3.4 Aerosol instrumentation

A suite of instrumentation was deployed to measure aerosol properties and chemical composition during the campaign. Two condensation particle counters (CPCs) (TSI Inc. 3025 and TSI Inc. 3022A) were deployed to measure the total number concentration of particles in the chamber. A Scanning Mobility Particle Sizer (SMPS) (TSI Inc. 3071 with a TSI Inc. 3010 CPC) was used to study number weighted particle size distribution. In addition an Aerosol Mass Spectrometer (AMS) (Aerodyne Research Inc.) [Alfarra, *et al.*, 2006] was present and capable of measuring the chemical composition of the aerosol, including fingerprints of organic composition.

### 5.3.5 Experiments

A total of 8 experiments were carried out over a period of 17 days in which the PERCA was operating. The parent VOCs studied were isoprene, 1,3,5-trimethylbenzene and  $\alpha$ -pinene, the structures of which are shown in Figure 5.4. All three are potentially very important in the formation of SOA, and cover VOCs with both biogenic (isoprene and  $\alpha$ -pinene) and anthropogenic (1,3,5-trimethylbenzene) origins. Biogenic sources include VOCs such as isoprene, monoterpenes and sesquiterpenes, whilst anthropogenic sources include alkanes, alkenes, carbonyls and aromatic compounds.

Isoprene is the major globally emitted biogenic VOC, accounting for approximately half of all natural VOC emissions (by mass), with estimated global emissions of between 250 and 750 Tg C y<sup>-1</sup> [Wiedinmyer, *et al.*, 2004], whilst biogenic VOC emissions are estimated to be higher than anthropogenic emissions overall [Guenther, *et al.*, 1995]. Whilst isoprene is not usually considered a major source of SOA, recent studies have suggested a small amount of isoprene can form SOA. Given the size of isoprene emissions, this could lead to significant SOA production [Kanakidou, *et al.*, 2005].

Field measurements have suggested that monoterpenes could account for 10 – 50% of biogenic VOCs emitted in an area depending on vegetation and local atmospheric conditions [Guenther, *et al.*, 1995], with  $\alpha$ -pinene contribution up to 25% of the total monoterpene load globally [Seinfeld and Pankow, 2003]. It is well known that  $\alpha$ -pinene (and monoterpenes in general) play an important role in the formation of secondary organic aerosol, even if the mechanism remains to be fully resolved [Kanakidou, *et al.*, 2005]. 1,3,5-trimethylbenzene is here representative of a larger range of aromatic compounds that have been identified as relevant to SOA formation [Odum, *et al.*, 1997], especially in urban atmospheres (along with monoterpenes) [Kamens, *et al.*, 1999; Odum, *et al.*, 1996]. An estimate of 1990 emissions puts global 1,3,5-trimethylbenzene emissions at 0.8 Tg yr<sup>-1</sup> [Tsigaridis and Kanakidou, 2003], approximately 10% of total emissions of aromatic compounds, themselves estimated to correspond to 10 – 15% of anthropogenic non-methyl VOC emissions [Kanakidou, *et al.*, 2005].

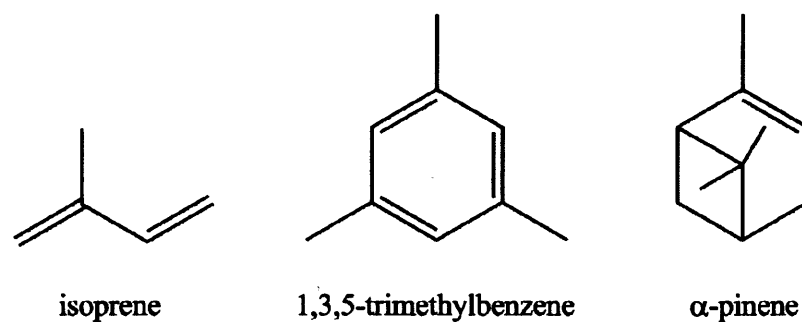


**Figure 5.4 – Structures of the three starting compounds used, isoprene, 1,3,5-trimethylbenzene and  $\alpha$ -pinene**

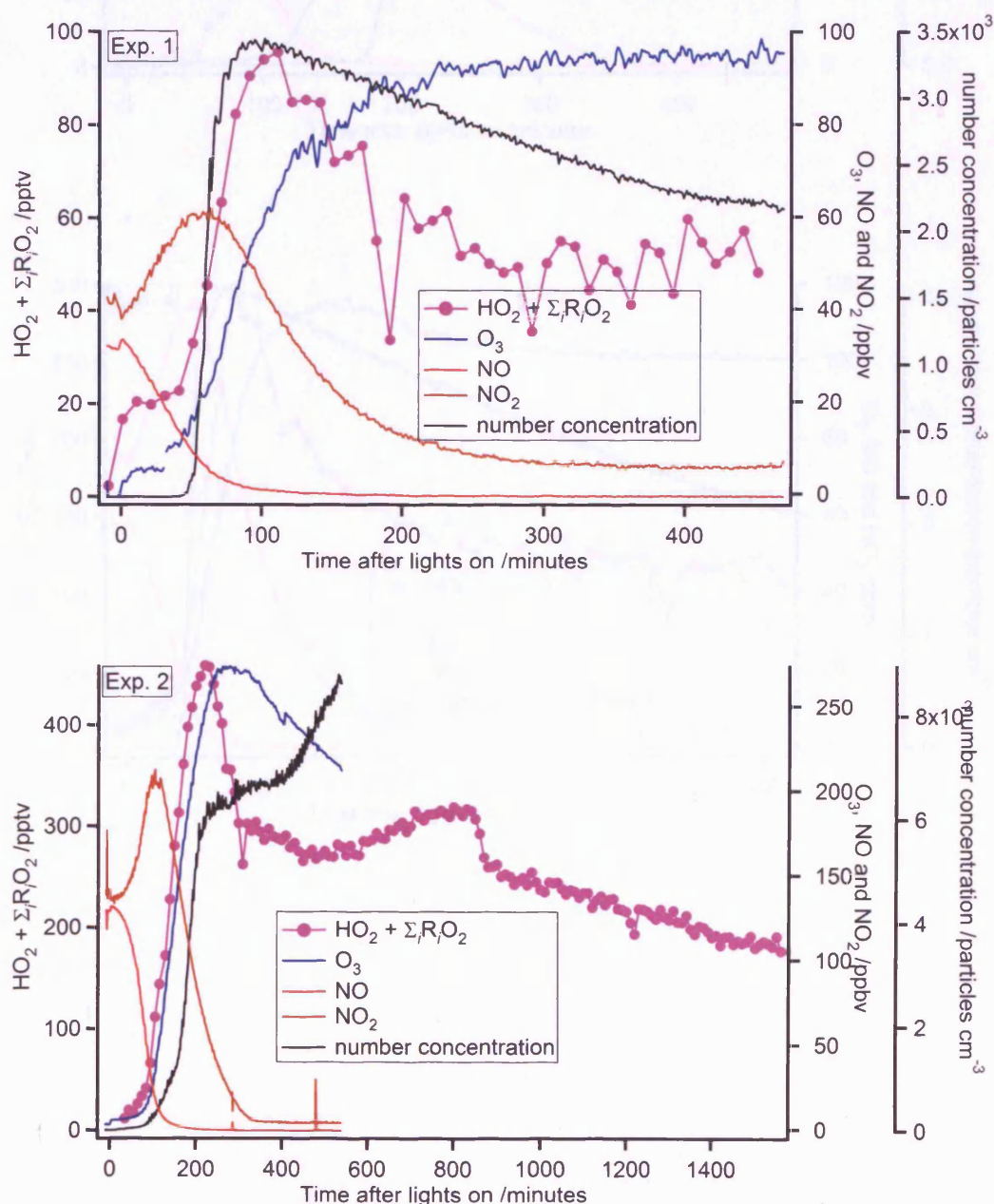
Relative humidity was a nominal 50% for all but one experiment (which was carried out dry), and temperature within the chamber was maintained at 22 °C. Owing to an unintended leak, experiment 8 also had an initial concentration of  $\sim 5$  ppmv of carbon monoxide. Details of the experiments are shown in Table 5.2

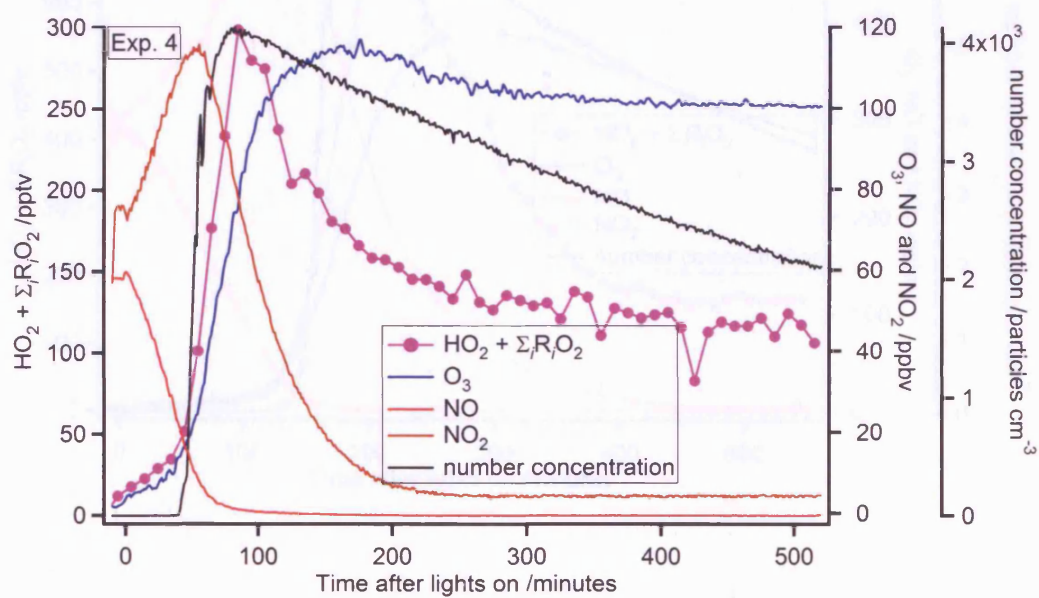
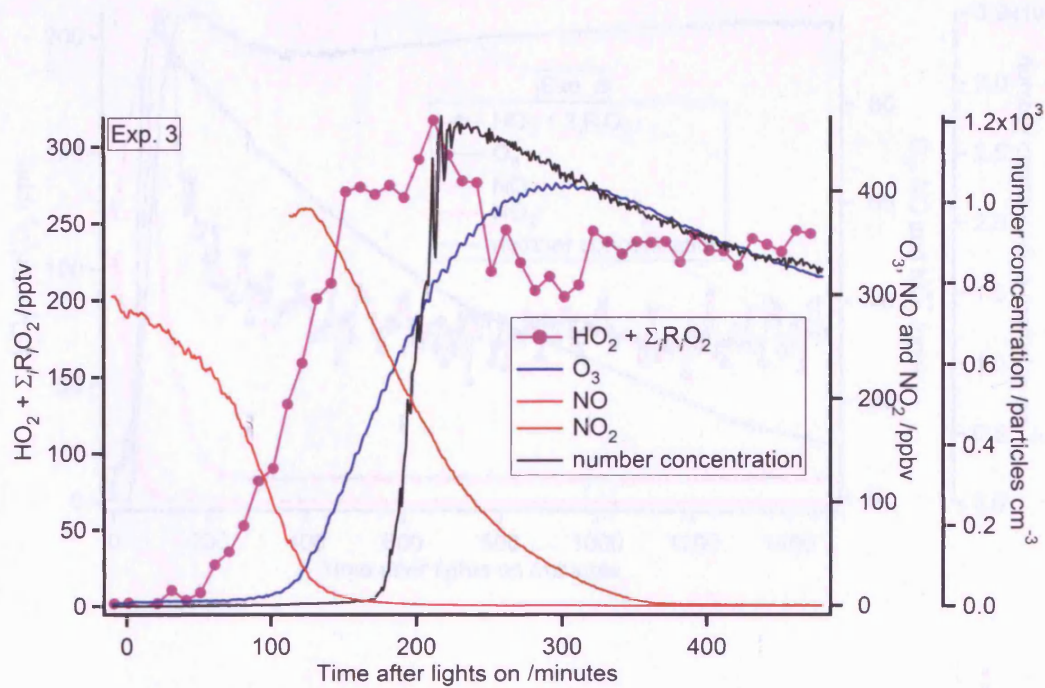
Experiment	Date	Parent VOC	Initial VOC concentration /ppbv	Initial NO concentration /ppbv	Initial NO <sub>2</sub> concentration /ppbv	Initial Relative Humidity /%	Experiment Length /h
1	26/10/2005	$\alpha$ -pinene	124	31	41	49	7.5
2	28/10/2005	1,3,5-trimethylbenzene	560	129	141	52	26
3	31/10/2005	1,3,5-trimethylbenzene	1137	300	343	46	7.9
4	02/11/2005	$\alpha$ -pinene	191	57	76	51	8.6
		1,3,5-trimethylbenzene	60				
5	04/11/2005	$\alpha$ -pinene	208	48	60	52	24.6
6	07/11/2005	isoprene	120	294	295	55	9.1
7	09/11/2005	1,3,5-trimethylbenzene	1180	535	0	49	8.4
8*	11/11/2005	$\alpha$ -pinene	205	115	110	0	6.9

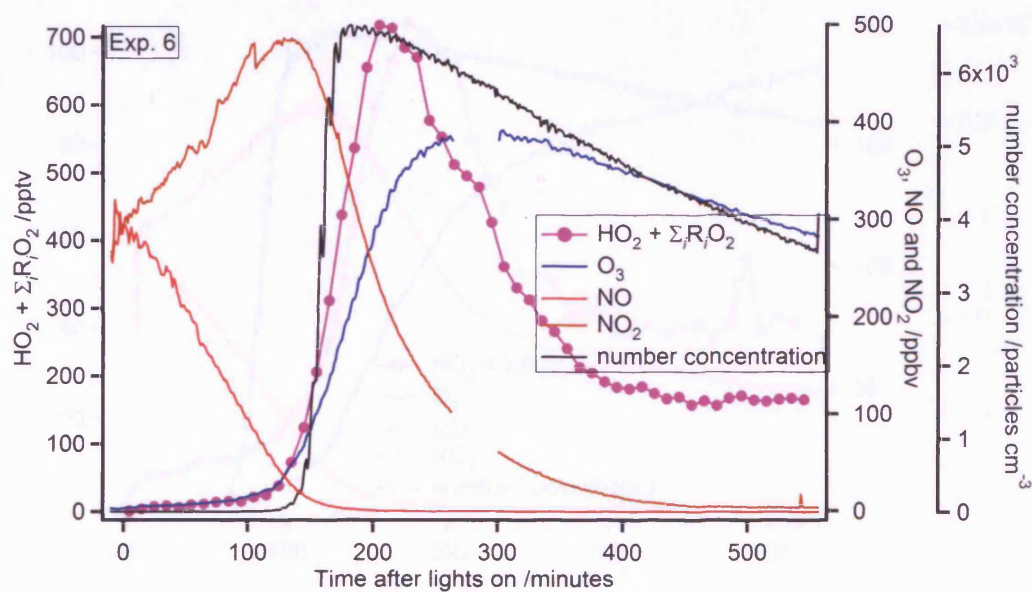
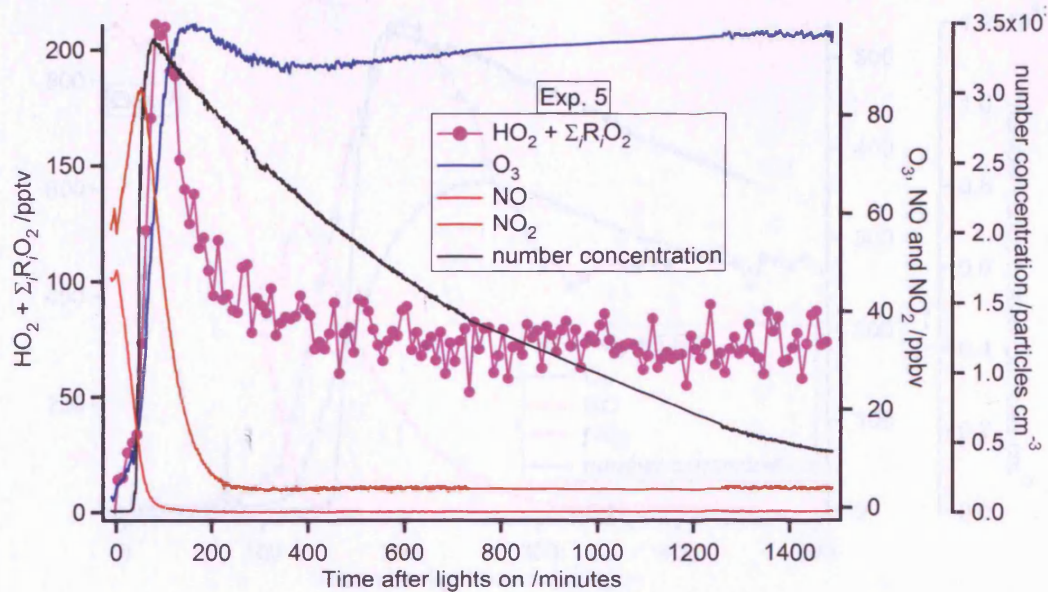
Table 5.2 – Details of the starting concentrations for PSI chamber experiment. \*Chamber also contained ~5 ppmv CO

## 5.4 Results

Peroxy radical data were recorded for all eight experiments and are shown for each experiment in Figure 5.5 along with ozone, NO, NO<sub>2</sub> and particle number concentration. The peroxy radical temporal profiles for all experiments are shown in Figure 5.6, Figure 5.7 shows the peroxy radical temporal profiles for experiments where 1,3,5-trimethylbenzene was the sole parent VOC and Figure 5.8 shows the peroxy radical temporal profiles for experiments where  $\alpha$ -pinene was the sole parent VOC.







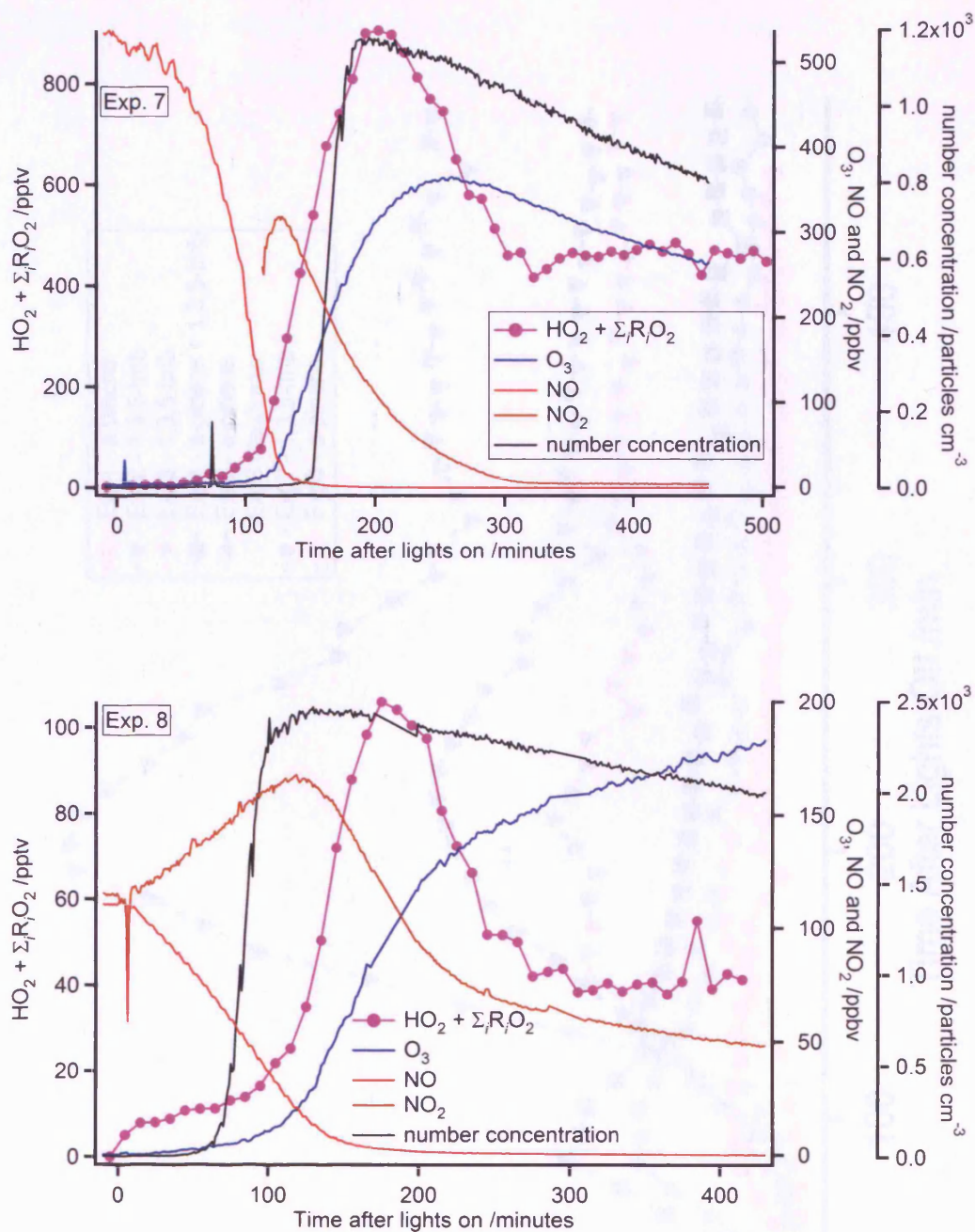


Figure 5.5 – Peroxy radicals, ozone, NO,  $\text{NO}_2$  and particle number concentration evolution with time for all eight experiments, as detailed in Table 5.2.

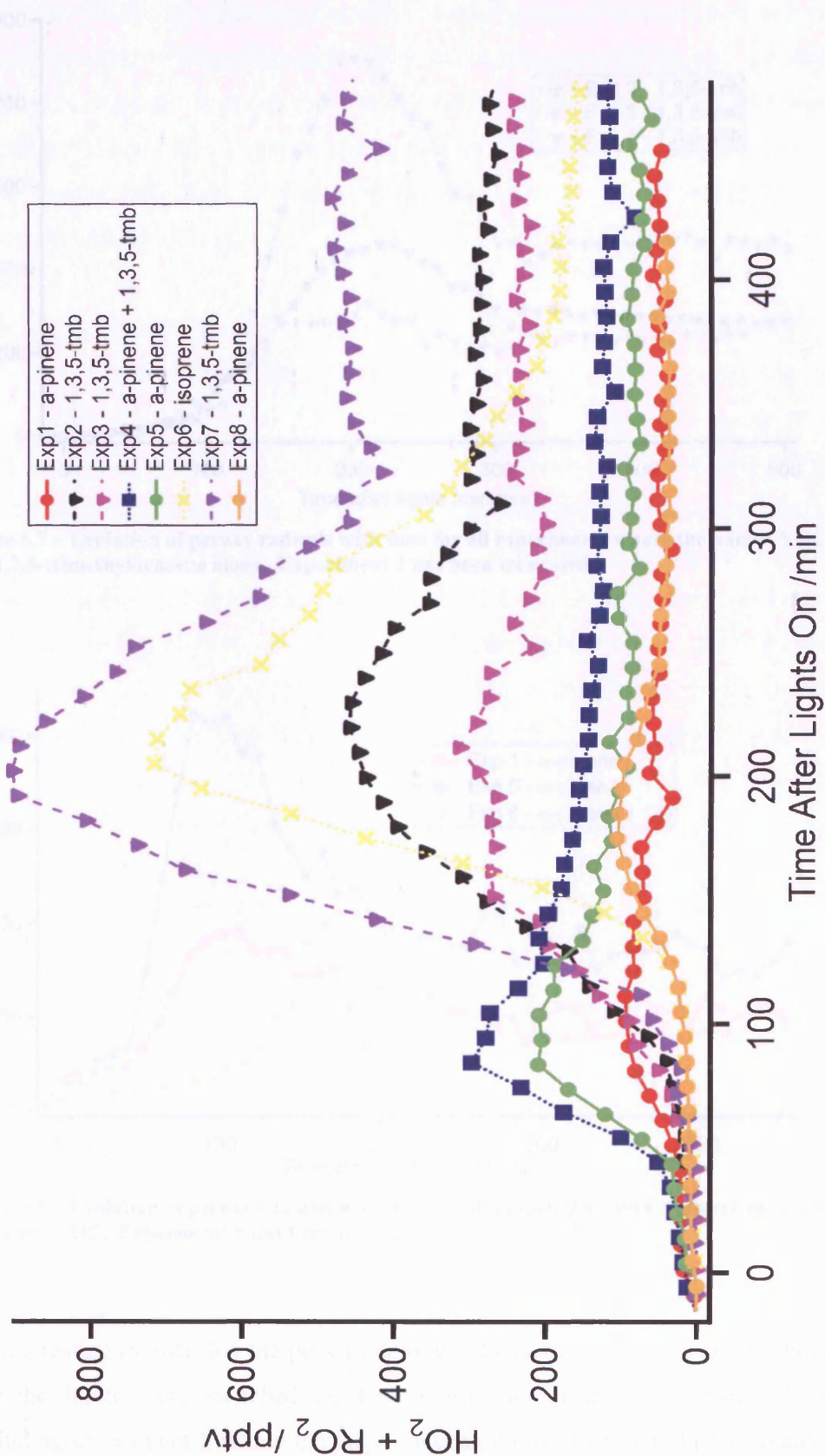


Figure 5.6 – Ten minute averaged temporal profile of peroxy radicals for all eight experiments. Time shown from fifteen minutes before lights on until eight hours after.

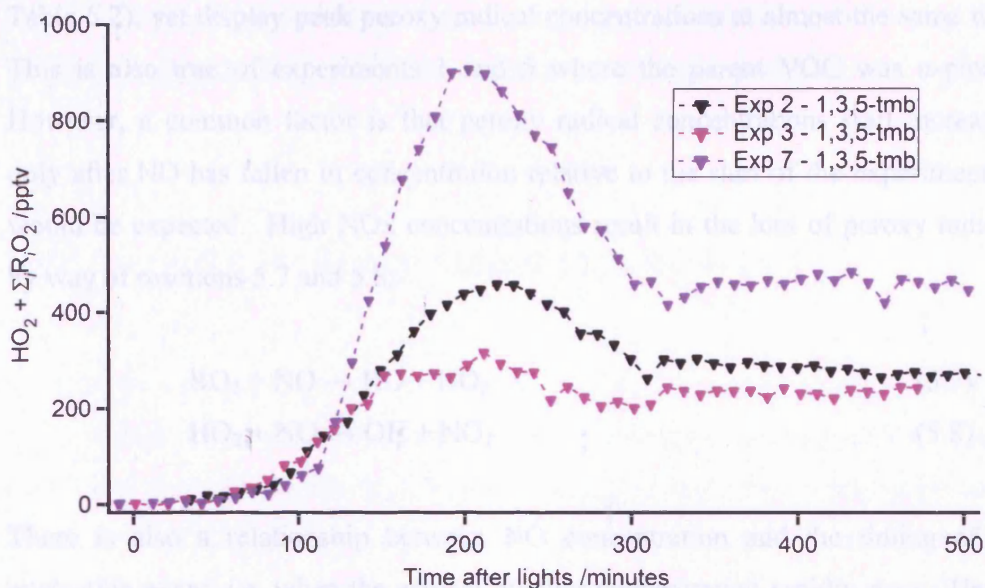


Figure 5.7 – Evolution of peroxy radicals with time for all experiments where the parent VOC was 1,3,5-trimethylbenzene alone. Experiment 2 has been truncated.

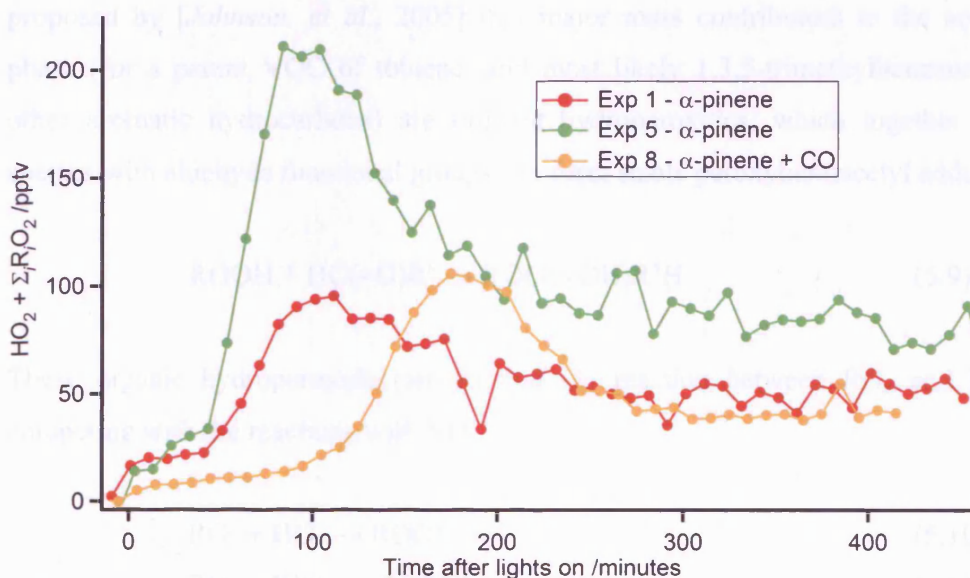
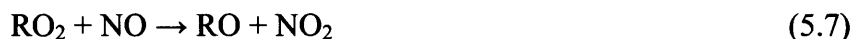


Figure 5.8 – Evolution of peroxy radicals with time for all experiments with  $\alpha$ -pinene alone as the parent VOC. Experiment 5 has been truncated.

It is interesting to note that the peak in peroxy radicals occurs at very similar times after the lights were switched on for experiments of the same parent VOC (excluding experiment 8 where the large concentrations of CO within the chamber have disrupted this). For example, experiments 2, 3 and 7 where the parent VOC was 1,3,5-trimethylbenzene have very different starting conditions (as displayed in

Table 5.2), yet display peak peroxy radical concentrations at almost the same time. This is also true of experiments 1 and 5 where the parent VOC was  $\alpha$ -pinene. However, a common factor is that peroxy radical concentrations start increasing only after NO has fallen in concentration relative to the start of the experiment, as would be expected. High NO<sub>x</sub> concentrations result in the loss of peroxy radicals by way of reactions 5.7 and 5.8:



There is also a relationship between NO concentration and the timing of the nucleation event, i.e. when the aerosol number concentration rapidly rises. Herein nucleation time is taken to be when the number concentration exceeds ten times the standard deviation of the background signal of the SMPS for five consecutive measurements (integration interval 3 minutes) after [Wyche, *et al.*, 2007b]. It is proposed by [Johnson, *et al.*, 2005] that major mass contributors to the aerosol phase (for a parent VOC of toluene, and most likely 1,3,5-trimethylbenzene and other aromatic hydrocarbons) are organic hydroperoxides, which together with species with aldehyde functional groups can form stable peroxyhemiacetyl adducts.



These organic hydroperoxides are formed *via* reaction between RO<sub>2</sub> and HO<sub>2</sub>, competing with the reactions with NO:



Consequently the formation of organic hydroperoxides is less favourable at higher concentrations of NO, and both overall aerosol yield and timing of onset of nucleation are potentially heavily affected by the formation of organic hydroperoxides. In order for significant production of organic hydroperoxides to take place, either very high concentrations of peroxy radicals or low concentrations of NO are required. Both of these requirements are met at times within the

chamber, but as shall be outlined in the next section the concentrations of NO<sub>2</sub>, ozone and peroxy radicals within the chamber present other problems.

### 5.4.1 Veracity of peroxy radical measurements

It can be seen from Figure 5.5 – Figure 5.8 that very large concentrations of peroxy radicals were observed during some of the experiments, peaking at 906 pptv in experiment 7. At these very high levels of peroxy radicals, the chemistry occurring within the PERCA inlets is likely to be perturbed from that at lower levels. Further to this, the very high concentrations of NO<sub>2</sub> and O<sub>3</sub> found in the chamber would also affect the inlet chemistry. To characterise any change, modelling of the inlet chemistry was carried out.

### 5.4.2 Inlet chemistry modelling

A simple box model was developed using the FACSIMILE computer modelling package (version 2, AEA Technology plc) as per [Hastie, *et al.*, 1991] to simulate the chain length obtained (i.e. molecules of NO<sub>2</sub> produced per peroxy radical molecule) in the inlet given the conditions within the inlet and differing ambient peroxy radical, NO<sub>2</sub> and ozone concentrations. Modelling runs were carried out for three scenarios, i) a series of differing initial peroxy radical concentrations at constant ambient NO<sub>2</sub> and ozone; ii) a series of different ambient NO<sub>2</sub> concentrations at constant peroxy radical and ambient ozone concentrations; and iii) a series of different ambient ozone concentrations at constant peroxy radical and ambient NO<sub>2</sub> concentrations. The results of the three scenarios detailed are shown in Figure 5.9, Figure 5.10, and Figure 5.11. Each set of a results has a line fitted to the data, for the effect of ambient peroxy radicals and ozone on chain length the fit is exponential, for the effect of ambient NO<sub>2</sub> on chain length the fit is a double exponential.

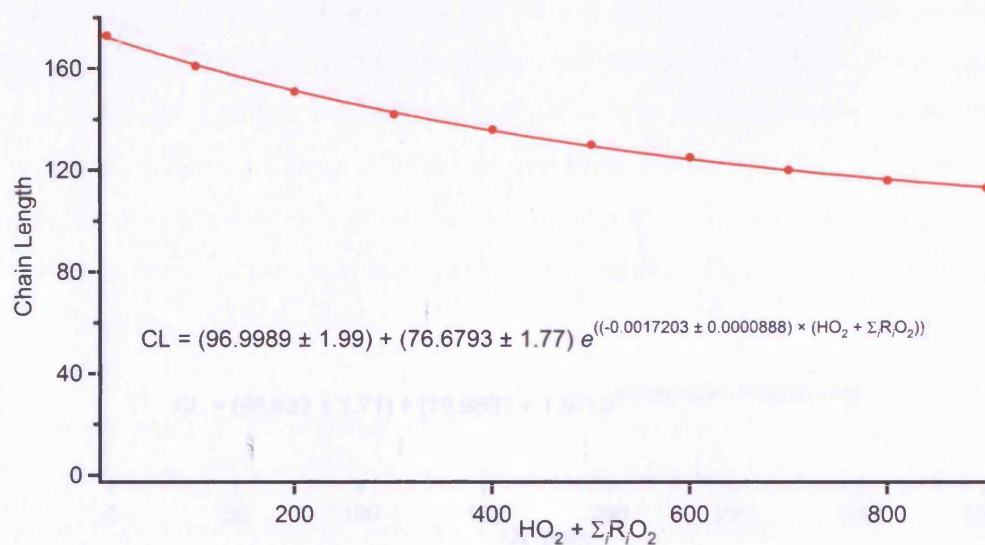


Figure 5.9 – Modelled chain length obtained from different ambient peroxy radical levels and no ambient NO<sub>2</sub> or ozone.

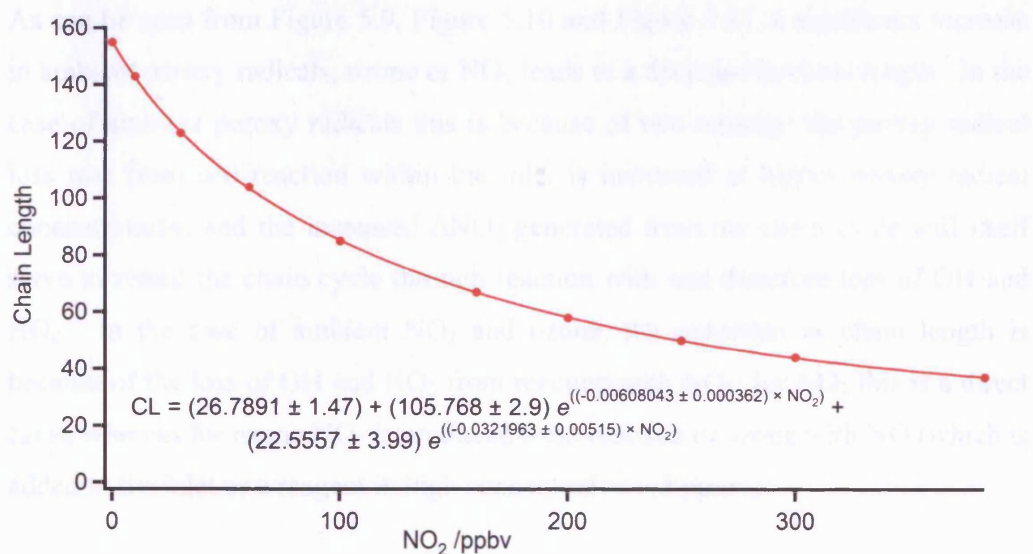
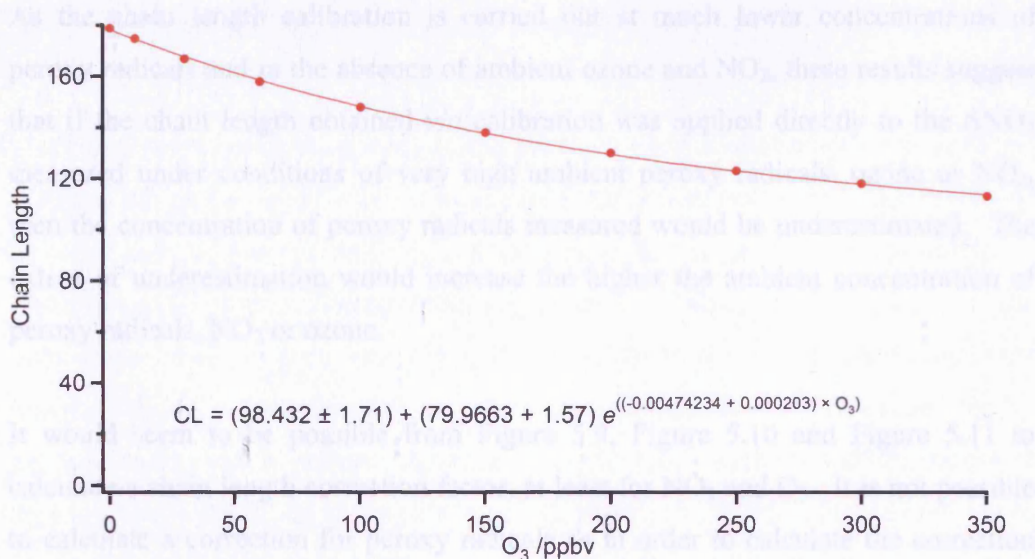


Figure 5.10 – Modelled chain length obtained from different ambient NO<sub>2</sub> concentrations, constant ambient peroxy radical concentrations and no ambient ozone.



**Figure 5.11 - Modelled chain length obtained from different ambient O<sub>3</sub> concentrations, constant ambient peroxy radical concentrations and no ambient NO<sub>2</sub>.**

As can be seen from Figure 5.9, Figure 5.10 and Figure 5.11, a significant increase in ambient peroxy radicals, ozone or NO<sub>2</sub> leads to a decrease in chain length. In the case of ambient peroxy radicals this is because of two reasons: the peroxy radical loss rate from self-reaction within the inlet is increased at higher peroxy radical concentrations; and the increased ΔNO<sub>2</sub> generated from the chain cycle will itself serve to retard the chain cycle through reaction with and therefore loss of OH and HO<sub>2</sub>. In the case of ambient NO<sub>2</sub> and ozone, the reduction in chain length is because of the loss of OH and HO<sub>2</sub> from reaction with NO<sub>2</sub>; for NO<sub>2</sub> this is a direct cause whereas for ozone NO<sub>2</sub> is produced from reaction of ozone with NO (which is added to the inlet as a reagent in high concentrations (3 ppmv)).

The effect on chain length of NO<sub>2</sub> is much more marked than the effect of ozone or peroxy radicals. NO<sub>2</sub> is present in the ambient air that is drawn into the inlet and thus can disrupt the chain cycle from the moment it begins. However, in the case of ambient ozone and peroxy radicals, the NO<sub>2</sub> that disrupts the chain cycle is produced from reactions that take place within the inlet, and thus there is a delay as NO<sub>2</sub> concentrations build up. The impact on chain length of ambient peroxy radical concentration is tempered relative to ozone and NO<sub>2</sub> as the ambient concentration being lower than that of ozone or NO<sub>2</sub>, but enhanced because of the increase of self-reaction losses.

As the chain length calibration is carried out at much lower concentrations of peroxy radicals and in the absence of ambient ozone and  $\text{NO}_2$ , these results suggest that if the chain length obtained *via* calibration was applied directly to the  $\Delta\text{NO}_2$  measured under conditions of very high ambient peroxy radicals, ozone or  $\text{NO}_2$ , then the concentration of peroxy radicals measured would be underestimated. The extent of underestimation would increase the higher the ambient concentration of peroxy radicals,  $\text{NO}_2$  or ozone.

It would seem to be possible from Figure 5.9, Figure 5.10 and Figure 5.11 to calculate a chain length correction factor, at least for  $\text{NO}_2$  and  $\text{O}_3$ . It is not possible to calculate a correction for peroxy radicals as in order to calculate the correction factor, the concentration of peroxy radicals would be required. However, in order to calculate the concentration of peroxy radicals, the correction factor would be required. It is however non-trivial to calculate a  $\text{NO}_2$  and  $\text{O}_3$  correction factor as they are interrelated; an increase in ambient  $\text{NO}_2$  from e.g. 100 ppbv to 200 ppbv produces a different relative change in chain length than an increase in ambient  $\text{NO}_2$  from e.g. 0 ppbv to 100 ppbv. Consequently, if both ambient ozone and  $\text{NO}_2$  are changing, it is not possible to disentangle the relative effects on chain length.

### 5.4.3 Effect of wall loss rate

Whilst the importance of the reactions of  $\text{HO}_2$  and  $\text{OH}$  with  $\text{NO}_2$  to chain termination has been noted above, the most significant chain termination reaction as suggested by modelling is likely that of radical loss to the walls of the inlet. The chain length was modelled with the same  $\text{NO}_2$ , ozone and peroxy radical concentrations as are present during a chain length calibration, which resulted in a modelled chain length of approximately 160. However, when the calibration was carried out the measured chain length was approximately 110. Consequently, the wall loss rate within the model was increased from the initial value of  $2.5 \text{ s}^{-1}$  to  $4.75 \text{ s}^{-1}$  in order to fit the measured chain length. However this resulted in very little difference to the relative effects of increased ambient  $\text{NO}_2$ , ozone or peroxy radicals.

### 5.4.4 Impact on atmospheric measurements

The chain length modelling study in the previous section raises the question of the extent to which the chain length is affected by the typical ambient concentrations of peroxy radicals, ozone and  $\text{NO}_2$  experienced when performing atmospheric measurements. At typical concentrations of peroxy radicals and  $\text{NO}_2$  present in the troposphere, it can be seen from Figure 5.9 and Figure 5.10 that the impact on chain length is small. However, the impact on chain length of ambient ozone has the potential to be more important. A similar study on chain length to the one presented here has been carried out in the literature [*Hastie, et al.*, 1991], where in addition to the modelling study ozone in varying concentrations was introduced to the inlet to determine any measurable effect. It was discovered that the impact of ozone on chain length was considerably smaller than that suggested by modelling. Consequently, whilst there is an effect on chain length of ozone, at typical atmospheric concentrations the effect is small.

It is therefore possible to amend the error analysis performed in Chapter 2 to include an estimated additional error in chain length calculation as a result of chain length calibrations being performed in the absence of ozone and  $\text{NO}_2$ . Chain length calibrations are performed with peroxy radical concentrations of  $\sim 40$  pptv to  $\sim 140$  pptv and as such are similar to ambient concentrations. From Figure 5.10 and Figure 5.11 an estimate of an additional error in chain length calibration has been made; measurements made at an ambient ozone concentration of 70 ppbv and an ambient  $\text{NO}_2$  concentration of 5 ppbv result in the error for a single-inlet PERCA as calculated in Chapter 2 increasing from 36% to 38%.

## 5.5 HONO experiments

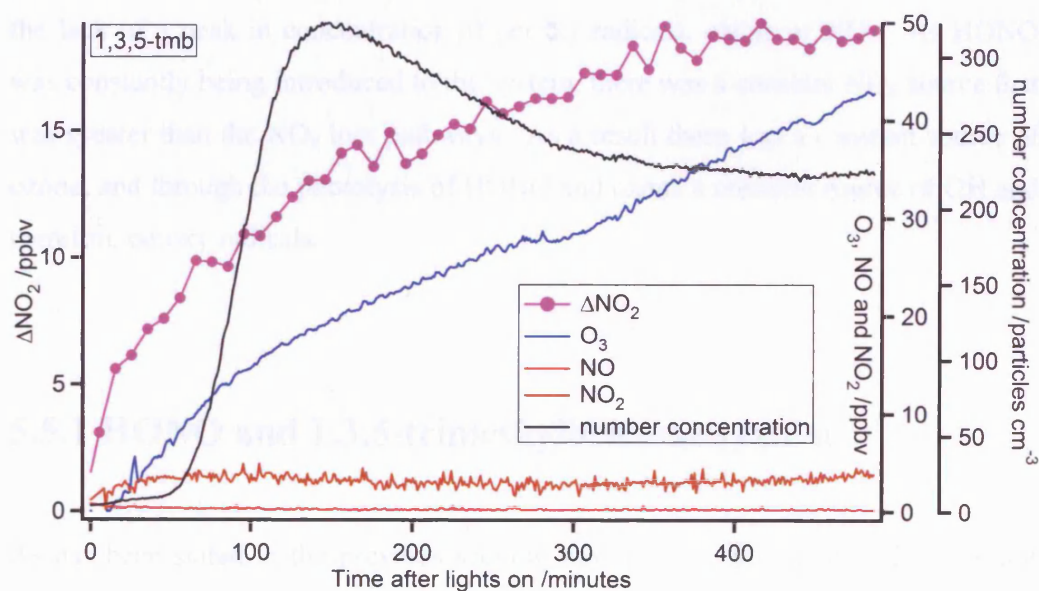
As has been seen in the previous section, the use of very high concentrations of  $\text{NO}_x$  and precursor VOCs lead to problems with measuring peroxy radicals *via* the PERCA technique, and as such it is difficult to perform an in-depth analysis of SOA formation mechanisms on the basis of the measurements made. Following on from

the experiments described thus far, a second set of experiments were carried out at PSI in November 2006. During the second series of experiments, two experiments were carried out at low concentrations of parent VOC and no initial  $\text{NO}_x$ , but with a constant 10 ppbv of HONO present in the chamber throughout as detailed in Table 5.3.

Parent VOC	Initial VOC /ppbv	Initial NO /ppbv	Initial $\text{NO}_2$ /ppbv	Initial HONO /ppbv
1,3,5-trimethylbenzene	151	0	0	10
Isoprene	500	0	0	10

Table 5.3 – Details of HONO experiments carried out at PSI during November 2006.

The temporal profiles for peroxy radicals, ozone, NO,  $\text{NO}_2$  and particle number concentration for the two experiments detailed in Table 5.3 are shown in Figure 5.12. Unfortunately as a result of the chain length calibration unit failing, peroxy radicals are reported as  $\Delta\text{NO}_2$ .



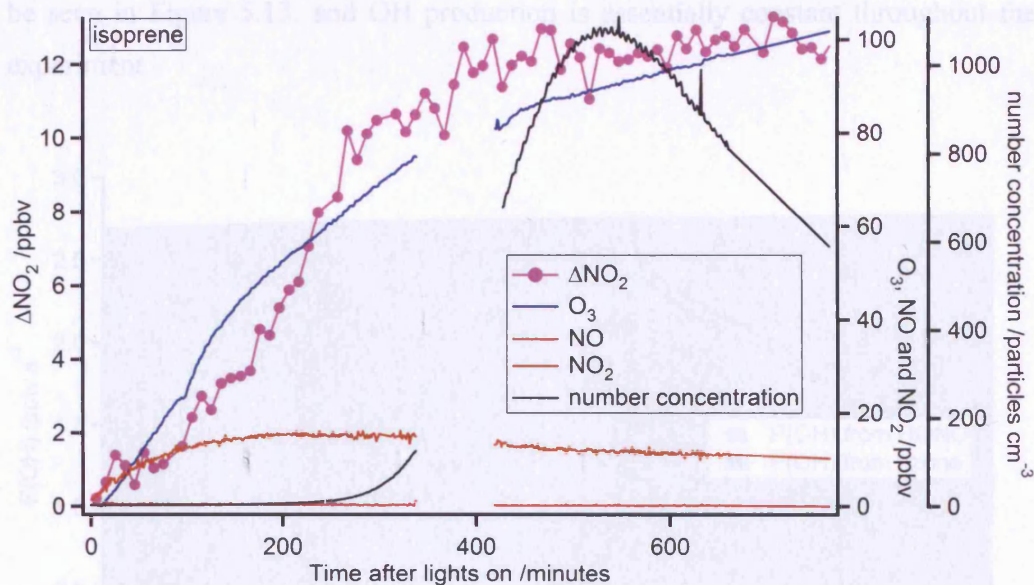


Figure 5.12 – Temporal profiles of peroxy radicals (in  $\Delta\text{NO}_2$ ), ozone, NO,  $\text{NO}_2$  and particle number concentration for HONO experiments.

As can be seen, a very obvious difference between these experiments and those previously carried out under high  $\text{NO}_x$  conditions and in the absence of HONO, is the lack of a peak in concentration of peroxy radicals, ozone or  $\text{NO}_2$ . As HONO was constantly being introduced to the system, there was a constant  $\text{NO}_x$  source that was greater than the  $\text{NO}_x$  loss pathways. As a result there was a constant source of ozone, and through the photolysis of HONO and ozone a constant source of OH and therefore peroxy radicals.

### 5.5.1 HONO and 1,3,5-trimethylbenzene system

As has been stated in the previous section, through the introduction of a constant concentration of HONO within the chamber, there was a constant supply of OH from HONO photolysis within the chamber.  $j(\text{HONO})$  and  $j(\text{O}^1\text{D})$  have been measured for the chamber [Metzger, 2007], and thus it is possible to calculate a nominal OH production rate from HONO as well as from ozone. The production of OH from HONO photolysis is significantly larger than that from ozone photolysis, even at the end of the experiment when ozone is at its highest concentration, as can

be seen in Figure 5.13, and OH production is essentially constant throughout the experiment.

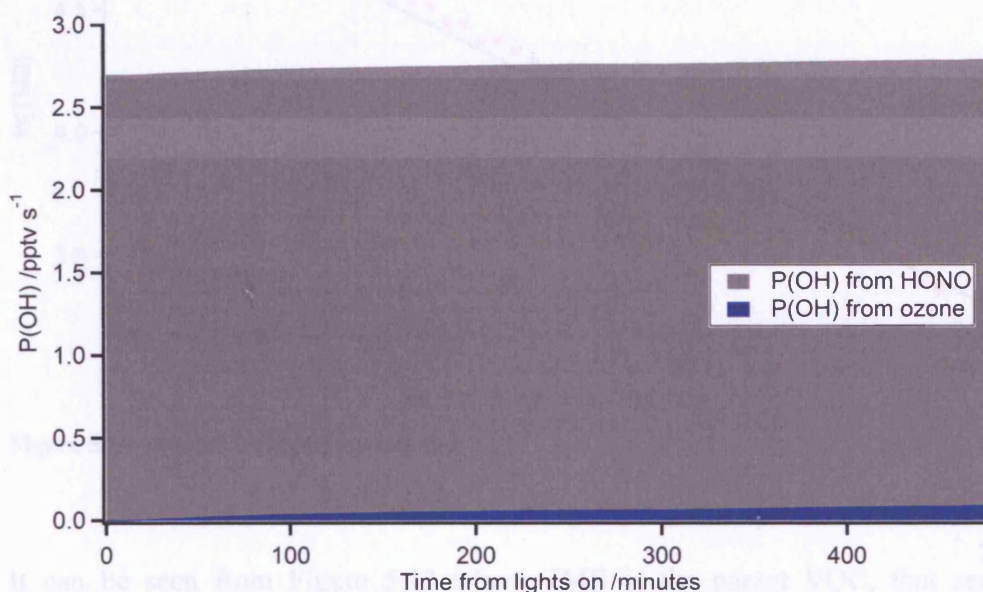


Figure 5.13 – Contribution of HONO and ozone photolysis to OH production.

If the assumption is made that OH is constant throughout the experiment and the loss of 1,3,5-trimethylbenzene (referred to hereafter as TMB) is solely owing to reaction with OH, it is possible to treat the loss of TMB as a pseudo first order process, and thus obtain an estimate of OH concentration. Where  $k_{5.12}$  is the rate of reaction 5.12 and  $k'_{5.12} = k_{5.12}[\text{OH}]$ , the gradient of a plot of  $\ln[\text{TMB}]$  against time is equal to  $-k'_{5.12}$ , from which OH can be calculated.



As can be seen from Figure 5.14,  $k'_{5.12} = 6.0378 \times 10^{-5} (\pm 9.68 \times 10^{-7}) \text{ s}^{-1}$ . At 296K (the chamber was held at 293K),  $k_{5.12} = 5.75 \times 10^{-11} \text{ cm}^3 \text{ molecule}^{-1} \text{ s}^{-1}$  [Atkinson and Aschmann, 1989], which results in an OH concentration within the chamber of  $1.05 \times 10^6 (\pm 1.68 \times 10^4) \text{ molecules cm}^{-3}$ .

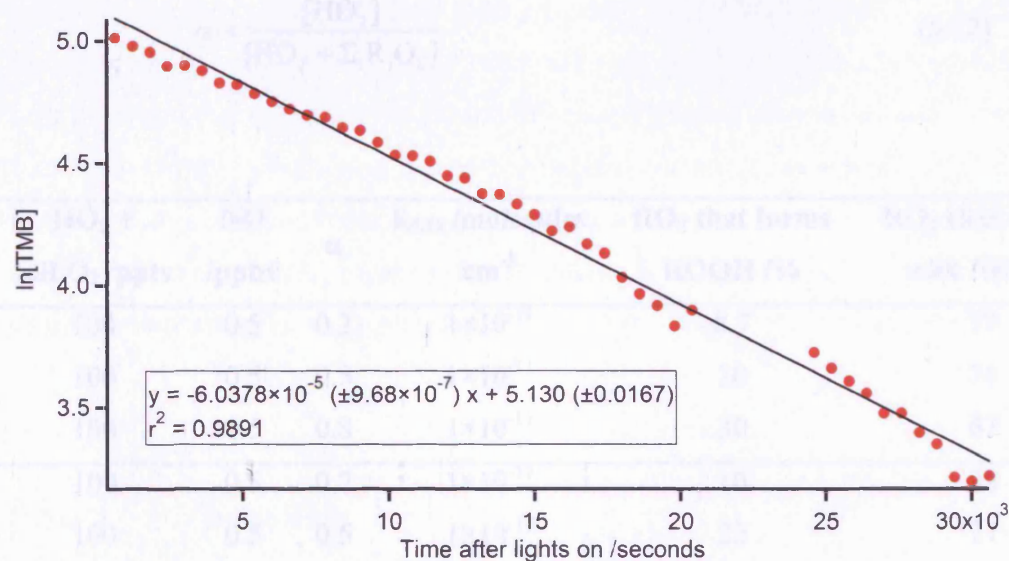


Figure 5.14 – Plot of  $\ln[\text{TMB}]$  against time.

It can be seen from Figure 5.12 where TMB is the parent VOC, that aerosol nucleation commences much more quickly after lights on compared to any of the previous experiments with TMB as the parent VOC but with high initial  $\text{NO}_x$  concentrations. As  $\text{NO}$  is relatively low (in the range 0.2 – 0.5 ppbv), peroxy radical concentration begins to rise immediately that the lights are switched on. Following from the hypothesis of [Johnson, *et al.*, 2005] that the formation of organic hydroperoxides is important to the formation of secondary organic aerosol, it can be postulated that as the relative ratio of peroxy radicals to  $\text{NO}$  is greater than in the high initial  $\text{NO}_x$  experiments, the production of organic hydroperoxides is more efficient, leading to earlier aerosol nucleation in the HONO experiment. At sample concentrations of 100 pptv peroxy radicals (estimated by taking the chain length to be  $\sim 100 - 150$ ) and 0.5 ppbv  $\text{NO}$ , and taking a range of values for  $\alpha$  (where  $\alpha$  is a metric for the partitioning between  $\text{HO}_2$  and  $\Sigma_i \text{R}_i \text{O}_2$ ), the fate of organic peroxy radicals can be estimated and compared to their fate under sample high  $\text{NO}_x$  conditions. The rate constants for Reactions 5.7 (reaction of generic  $\text{RO}_2$  and  $\text{NO}$ ) and 5.10 (generic  $\text{RO}_2$  with  $\text{HO}_2$ ) have been taken from the Master Chemical Mechanism (v3.1, [Jenkin, *et al.*, 1997]), whilst the rate constant for Reaction 5.11 has been varied (as can be seen in Table 5.4) as no generic  $\text{RO}_2$  self-reaction rate constant for aromatic  $\text{RO}_2$  is available.

$$\alpha = \frac{[\text{HO}_2]}{[\text{HO}_2 + \sum_i \text{R}_i\text{O}_2]} \quad (5.12)$$

$\text{HO}_2 + \sum_i \text{R}_i\text{O}_2$ /pptv	NO /ppbv	$\alpha$	$k_{5.11}$ /molecules $\text{cm}^{-3}$	RO <sub>2</sub> that forms ROOH /%	RO <sub>2</sub> that reacts with NO /%
100	0.5	0.2	$1 \times 10^{-11}$	8.7	77
100	0.5	0.5	$1 \times 10^{-11}$	20	71
100	0.5	0.8	$1 \times 10^{-11}$	30	67
100	0.5	0.2	$1 \times 10^{-12}$	10	88
100	0.5	0.5	$1 \times 10^{-12}$	22	77
100	0.5	0.8	$1 \times 10^{-12}$	31	69
50	170	0.2	$1 \times 10^{-11}$	0.017	~100
50	170	0.5	$1 \times 10^{-11}$	0.042	~100
50	170	0.8	$1 \times 10^{-11}$	0.067	~100
50	170	0.2	$1 \times 10^{-12}$	0.017	~100
50	170	0.5	$1 \times 10^{-12}$	0.042	~100
50	170	0.8	$1 \times 10^{-12}$	0.067	~100

**Table 5.4 – Fate of RO<sub>2</sub> under different chamber conditions.**

The production of ROOH has been calculated by

$$\% \text{ROOH production} = \frac{k_{5.10} [\text{HO}_2] [\text{RO}_2]}{[\text{RO}_2] (k_{5.10} [\text{HO}_2] + k_{5.11} [\text{RO}_2] + k_{5.7} [\text{NO}])} \quad (5.13)$$

and similarly for the proportion of RO<sub>2</sub> that reacts with NO. The concentrations of peroxy radicals and NO used in Table 5.4 for the high NO scenario, whilst taken from experiment 3 of the first set of experiments, are largely arbitrary. However, they serve to demonstrate the point that the significant production of organic hydroperoxides requires either low NO concentrations or high peroxy radical concentrations, and as such can only occur in the experiments performed at high initial NO<sub>x</sub> and absence of HONO after the NO has been removed from the system and the concentration of peroxy radicals begins to increase.

It can be seen that in the first set of TMB experiments with high initial  $\text{NO}_x$  that the aerosol nucleation event only takes place after the peroxy radical concentrations have increased to a significant level, and NO concentrations are close to zero. This, combined with the situation in the HONO experiment where, as mentioned above, peroxy radicals are also already present in reasonable concentrations relative to NO when nucleation occurs, supports the postulate of [Johnson, *et al.*, 2005] that organic hydroperoxides are potentially an important contributor to SOA formation.

### 5.5.1.1 Modelling

Preliminary work on the modelling the TMB – HONO system using the MCM (v3.1, [Jenkin, *et al.*, 1997]) has been undertaken, and the results of a first analysis are presented. Dr. Andrew Rickard at the University of Leeds has performed the MCM runs in order to try to recreate the conditions encountered within the chamber during this experiment. A comparison between various VOC concentrations measured and modelled is out of the scope of this thesis and shall be presented elsewhere [Wyche, *et al.*, 2007b], but peroxy radicals have also been modelled and shall be examined here.

Figure 5.15 shows measured peroxy radicals plotted against time after lights on along with various combinations of modelled peroxy radicals. TM135BPRO2 is the MCM name for the peroxy radical formed by OH oxidation of TMB and is shown in Figure 5.16.

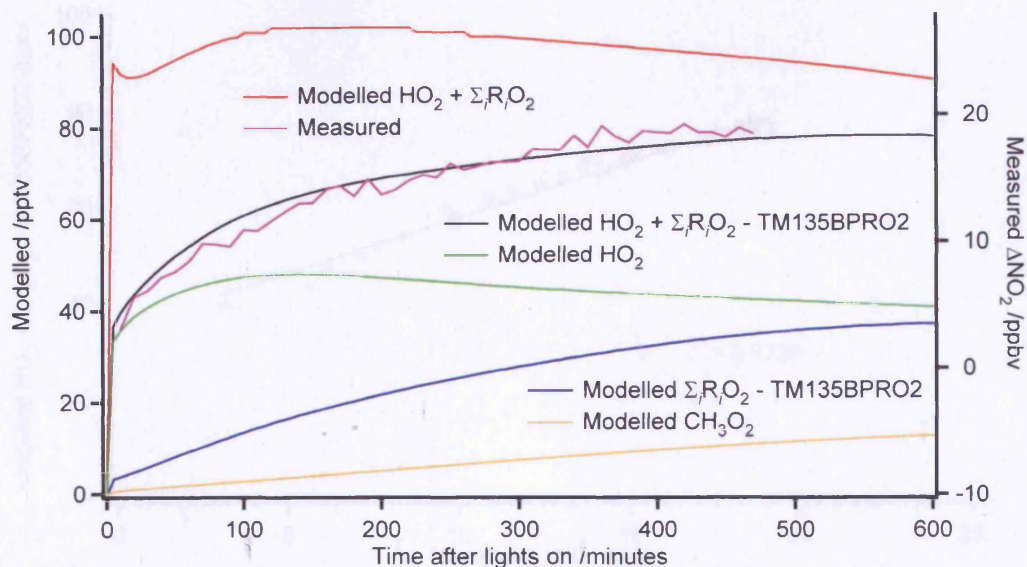


Figure 5.15 – Measured and modelled peroxy radicals plotted against time since lights on.

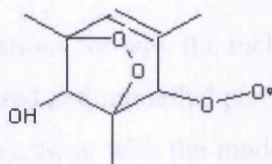
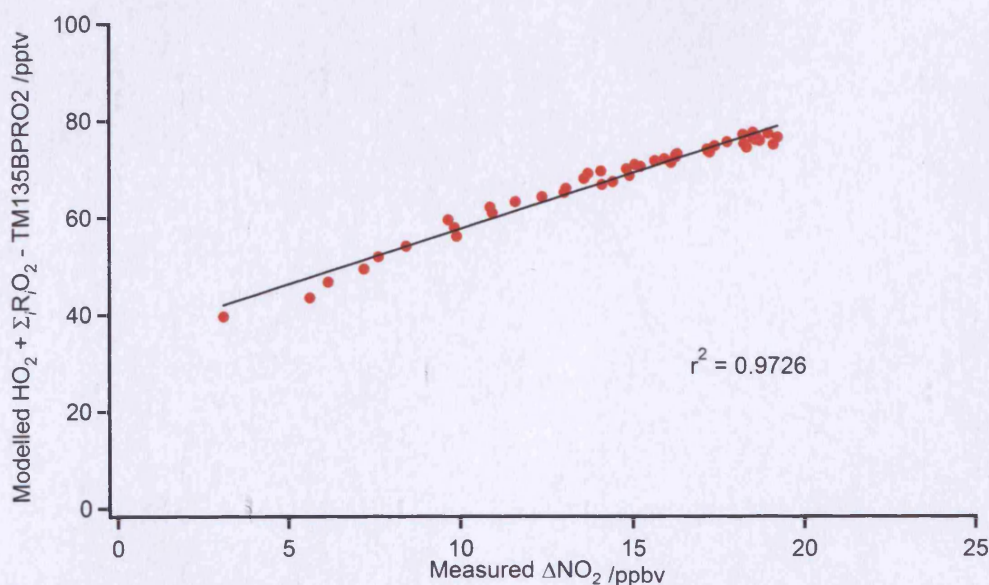


Figure 5.16 – Structure of compound referred to as TM135BPRO2 in the MCM

Whilst it is not possible to directly compare concentrations as measured peroxy radicals are reported in terms of  $\Delta\text{NO}_2$  for reasons outlined in section 5.5, it is possible to compare trends. It can be seen that the largest individual contributors to total modelled  $\text{HO}_2 + \Sigma \text{R}_i\text{O}_2$  are  $\text{HO}_2$ , TM135BPRO2 and  $\text{CH}_3\text{O}_2$ . The profiles of measured and modelled total peroxy radicals look distinctly different, yet if the contribution of TM135BPRO2 is removed, the measured and modelled profiles become much closer, as is evidenced by the very good correlation between the two as shown in Figure 5.17.



**Figure 5.17 – Correlation between modelled and measured peroxy radicals with the contribution of TM135BPRO2 to modelled data removed.**

There are two possible explanations for why the inclusion of TM135BPRO2 makes the correlation between measured and modelled peroxy radicals worse; that there is a problem either with the measured or with the modelled data. It is known that the conversion efficiency of RO<sub>2</sub> to HO<sub>2</sub> within the PERCA inlets drops with large, complex RO<sub>2</sub> owing to increasing branching reactions competing with the production of HO<sub>2</sub> from the reaction of O<sub>2</sub> with RO [Ashbourn, *et al.*, 1998]. It is therefore possible that the measurement efficiency of the PERCA towards TM135BPRO2 is very low, to the extent that the majority is not detected. If this were the case however, it would be expected that there would be a number of additional peroxy radicals that would also not be detected, rendering the observed correlation between measured total peroxy radicals and modelled peroxy radicals without TM135BPRO2 surprising. However, most other peroxy radicals simulated in the modelling study have similar profiles to that of CH<sub>3</sub>O<sub>2</sub> shown in Figure 5.15, so the inclusion of these or otherwise would have a smaller impact on the overall correlation.

The other possibility is that the modelled peroxy radical values from the MCM simulation are erroneous. If TM135BPRO2 as predicted by the MCM did not form under the conditions encountered within the chamber, this would explain the discrepancy. Further, it can be seen from Figure 5.17 that there is an offset in the

correlation between measured peroxy radicals and modelled without TM135BPRO2. From Figure 5.15 it can be seen this is because modelled HO<sub>2</sub> immediately jumps to a high concentration. If this initial surge is removed, the offset in Figure 5.17 is also removed. The initial surge in the modelled HO<sub>2</sub> is as a result of the reaction of TM135BPRO2 with both other RO<sub>2</sub> and NO to form the associated alkoxy radical, which then decomposes to give methyl glyoxal, 3,5-dimethyl-2(5H)-furanone, 2-methyl-4-oxo-pent-2-enal and HO<sub>2</sub>. As a result, were TM135BPRO2 not to be present, nor would the initial HO<sub>2</sub> surge. There is some supporting evidence for this as some of the corresponding oxidised VOCs that would be expected to be formed from TM135BPRO2 are not detected in the VOC data measured by the CIR-TOF-MS.

In order to distinguish between these two possibilities further work is required. Additional experiments to measure other oxidation products unique to a particular pathway within the MCM would help evaluate the production and loss routes of peroxy radicals within the MCM, in order to further reconcile measured and modelled peroxy radicals. Given the very large proportion of  $\Sigma_i R_i O_2 + HO_2$  that is HO<sub>2</sub>, it would also be of interest for future measurements to discriminate between HO<sub>2</sub> and  $\Sigma_i R_i O_2$ , either by way of the HO<sub>2</sub> discrimination method outlined in section 5.3.2 (after further characterisation experiments) or by way of an additional technique such as PerCIMS or FAGE (should sampling considerations allow).

### 5.5.2 HONO and isoprene system

In common with the 1,3,5-trimethylbenzene system, the initial oxidation of isoprene by OH (produced from the photolysis of HONO) results in the production of organic peroxy radicals, as evidenced by the following extract from the Master Chemical Mechanism (v3.1, [Jenkin, *et al.*, 1997]).

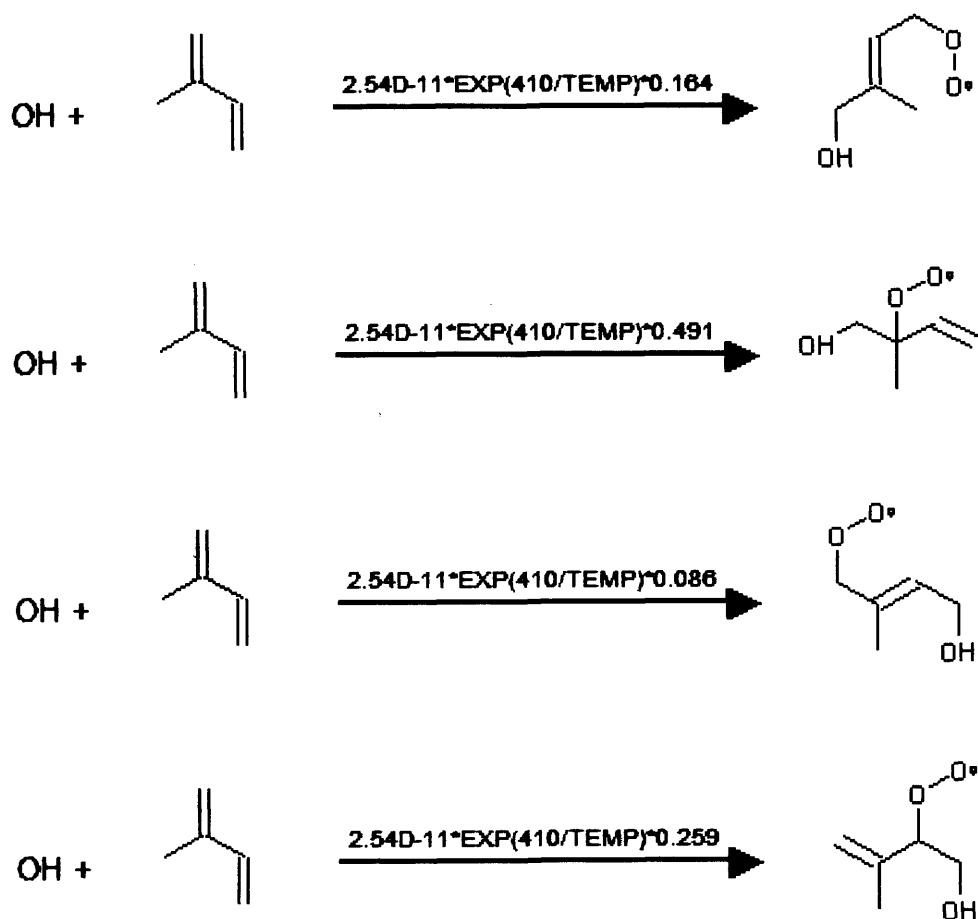


**Figure 5.18 – Extract from the Master Chemical Mechanism showing the initial oxidation of isoprene by OH.**

There are many theories as to how secondary organic aerosol is formed from isoprene including but not exclusively the gas phase formation of condensable products, oxidation reactions of isoprene products leading to SOA formation, the reaction of isoprene and methacrolein with  $\text{H}_2\text{O}_2$  in acidic particles, and with the involvement of organic peroxides ([*Pun and Seigneur, 2007*] and references therein).

The importance of organic peroxides in the formation of SOA from isoprene was postulated by [*Kroll, et al., 2006*], with supporting evidence provided by [*Surratt, et al., 2006*]. If organic peroxides are an important component of SOA formation from isoprene, it could be expected that as in the case of the TMB system, peroxy radicals would be present prior to the nucleation event occurring. This is certainly true of the experiment carried out in the presence of HONO and the absence of initial  $\text{NO}_x$  (as evidenced by Figure 5.12), but is less clear cut for the situation of

high initial  $\text{NO}_x$  (experiment 6, Figure 5.5). In the high initial  $\text{NO}_x$  experiment, whilst peroxy radical concentration does indeed begin to increase before the nucleation event occurs, the peak in peroxy radical concentration occurs after the peak in aerosol number concentration. However, this is one experiment only, and as has been discussed above the peroxy radical measurements for the high  $\text{NO}_x$  experiments are not without problems, and thus no firm conclusions should be drawn on this basis.

## 5.6 Conclusions

Organic aerosol within the atmosphere is an important contributor to overall atmospheric aerosol [Andreae and Crutzen, 1997; Putaud, *et al.*, 2004; Roberts, *et al.*, 2001], which itself has many wide-ranging impacts on atmospheric chemistry and climate (see section 5.1). The formation mechanism of secondary organic aerosol is not well known [Librando and Tringali, 2005; Pun and Seigneur, 2007], and so a series of chamber studies were carried out at the atmospheric simulation chamber at the Paul Scherrer Institut, Switzerland with the aim of improving understanding. To this end, the sum of peroxy radicals was measured along with a large range of VOCs and inorganic compounds in order to investigate the role of peroxy radicals in secondary organic aerosol formation.

The starting conditions employed in the initial set of experiments carried out resulted in very high initial  $\text{NO}_x$  concentrations and subsequent very high ozone and peroxy radical concentrations within the chamber, which caused problems with the measurement of peroxy radicals due to interfering with the PERCA inlet chain chemistry. As a result a modelling study was carried out to characterise the effect of high  $\text{NO}_2$ , ozone and peroxy radical concentrations on chain length. The modelling study showed that whilst the peroxy radical measurements made at the very high  $\text{NO}_2$ , ozone and peroxy radical concentrations found within the chamber are significantly affected by the conditions, the effect on measurements at atmospheric conditions (70 ppbv ozone and 5 ppbv  $\text{NO}_2$ ) are only impacted to a

negligible extent, with the overall single-channel PERCA error increasing from 36% to 38%.

As a result, two additional experiments were carried out in the absence of initial  $\text{NO}_x$  and the presence of a constant 10 ppbv of HONO. From the loss rate of 1,3,5-trimethylbenzene in the first HONO experiment an estimate of OH concentration can be calculated, resulting in an OH concentration of  $1.05 \times 10^6$  ( $\pm 1.68 \times 10^4$ ) molecules  $\text{cm}^{-3}$ . Hypotheses has been put forward that for both 1,3,5-trimethylbenzene [Johnson, *et al.*, 2005] and isoprene [Kroll, *et al.*, 2006] organic hydroperoxides are important contributors to secondary organic aerosol formation. This is supported by the peroxy radical measurements here reported, as aerosol nucleation only occurs after peroxy radical concentrations have started to build up, with the exception of the high initial  $\text{NO}_x$  isoprene experiment.

Whilst the work reported herein supports the idea of peroxy radicals reacting to form organic hydroperoxides potentially being important in the formation of secondary organic aerosol, more work is required to confirm this. Work is ongoing at the University of Leicester to characterise and analyse VOC data recorded during these experiments by the CIR-TOF-MS, and further experiments carried out both at levels of  $\text{NO}_x$ , ozone and peroxy radicals so that peroxy radical data can be reliably recorded, and with the concurrent measurement of additional species such as peroxides has the potential to greatly increase our understanding of the formation mechanisms of secondary organic aerosols.

Initial modelled peroxy radicals from the Master Chemical Mechanism have been compared to the measured peroxy radicals. Whilst the initial correlation between measured and modelled is not ideal, if TM135BPRO2 is removed then the correlation becomes excellent ( $r^2 = 0.9726$ ). This could either be as a result of an error in the measurements or the model result, and explanations for both being the case have been suggested. Further work is required to investigate the origin of peroxy radicals predicted by the MCM, but the initial results presented are promising and go some way to showing the importance of peroxy radicals in understanding secondary organic aerosol formation process.

## Chapter 6

# Conclusions and Proposals for Future Work

This chapter draws together the work described in the preceding chapters, and makes suggestions for potentially “fruitful” areas of future research.

Three different field campaigns have been described within this thesis, the Intercontinental Transport of Ozone and Precursors (ITOP) campaign (Chapter 3), a campaign focusing on composition control in the European free troposphere (Chapter 4), and a chamber study into the formation of secondary organic aerosol (Chapter 5). Whilst specific conclusions on the work undertaken may be found within the relevant chapter, here it may be useful to address some more general conclusions.

### 6.1 Peroxy radical measurements

A range of techniques exist for measuring peroxy radicals within the atmosphere, as detailed in Chapter 2. These techniques rely on differing underlying techniques, e.g. PERCA is based on chemical amplification and chemiluminescence, PerCIMS is based on a different chemical amplification scheme and mass spectrometry, and FAGE is based on (for HO<sub>2</sub> measurements) chemical conversion then laser induced fluorescence. This is beneficial for testing the veracity of peroxy radical measurements, as if there were to be a common systematic bias in a particular measurement technique, only that technique should suffer from it, making it easier to identify. However in order for any biases to be identified, controlled

intercomparisons should be carried out. At the moment owing to time and financial constraints this perhaps does not happen as often as would be ideal.

A common disadvantage to all of the techniques mentioned above is that they are indirect, i.e. the peroxy radicals must be converted into another species before being measured. The only current direct technique, MIESR, is impractical for most field applications for reasons outlined in Chapter 2. A direct technique has the potential to remove inaccuracies inherent in an indirect technique, and would be a very interesting area of research.

Whilst all current measurement techniques have their advantages and disadvantages, what none can yet achieve is the speciation of organic peroxy radicals, with the exception of the limited speciation of MIESR, whose other drawbacks render it an unwieldy technique. The speciation of organic peroxy radicals is in many ways the 'holy grail' of peroxy radical measurements.

## 6.2 Atmospheric field measurements

The importance of trans-continental transport of pollutants and precursors means that pollution is an international problem. It is not sufficient to think of pollution as a purely local issue. The production of ozone within air-masses undergoing long-range transport across the Atlantic as described in Chapter 3 demonstrates the necessity of looking at atmospheric chemistry in global terms. This is of special importance in political and legislative terms – in order to have successful pollution and air quality controls in place, atmospheric chemistry can play a vital and leading role in identifying the most effective areas to focus on. A (relatively) simple example of this can be seen from the ozone isopleth in Figure 1.6 – the most efficient way of reducing pollutants may not always be the most intuitive owing to the highly complex and non-linear chemical systems within the atmosphere.

It is only by testing the current status of our knowledge by carrying out field measurement campaigns that we can identify potential new areas of research. This

is clearly evidenced by the missing peroxy radical loss term identified in Chapter 4 and the possibility that it could be due to heterogeneous reactions on snow. This also illustrates the need to further integrate gas and particle phase atmospheric chemistry (and physics), as there is the temptation to treat the two separately where in reality a unification is required.

### **6.3 Aerosol chamber studies**

As stated in Chapter 5, the mechanism for the formation of secondary organic aerosol (SOA) is currently uncertain. Recent studies including that in Chapter 5 have outlined the potential importance of organic hydroperoxides and by extension peroxy radicals in SOA formation, and future measurement studies to build on this can be envisaged with a wider suite of measurements than has been utilised in the past including, but not limited to peroxy radicals, peroxides, VOCs as well as other inorganic species and aerosol parameters.

It would also be ideal in the future to perform such chamber studies under more atmospherically representative conditions; not only would it better simulate the real atmosphere but would furthermore help with the problems encountered with the PERCA chain chemistry as a result of the extremely high concentrations of NO<sub>2</sub>, ozone and peroxy radicals within the chamber. However, performing such experiments under atmospheric conditions is currently not always trivial, as in order to produce quantities of aerosol that can be measured by current aerosol instrumentation within a chamber starting concentrations must by necessity be high. Aerosols are of huge interest to atmospheric chemistry and as such their formation mechanisms should be of primary interest.

In conclusion, whilst there is much we do know, there is much more that remains to be discovered, and atmospheric science shall remain the immensely exciting research area it currently is for a long time to come.

# Appendix A

## IGOR Data Workup Routines

This appendix contains the data workup routines written in Wavemetrics<sup>®</sup> IGOR Pro v6 software.

### A.1 Main.ipf

```
#pragma rtGlobals=1      // Use modern global access method.
#include "C:PERCA:Procedures:WAOWEX_Cals_ITOP"
#include "C:PERCA:Procedures:Work-up2"

Menu "ToolBox AEP"
  Submenu "Data Workup"
    "Initial Data Workup", Initial_WAOWEX_Data_reduction()
    "Calculate Sensitivities", Calculate_sensitivities()
    "Final Data Workup", Final_WAOWEX_data_reduction()
    "Compare single and dual channel data", compare_single_dual()
  end
end
```

### A.2 WAOWEX\_Cals\_ITOP.ipf

```
Function declare_globals()
  variable/G pointnumber = 0
  variable/G NO2_cal_perm_rate = 0
end

Function Find_za_flow(ctrlName) : ButtonControl
  String ctrlName
  Execute"find_za_flow_for_cals()"
End

Function Accept_values_1(ctrlName) : ButtonControl
```

```

    String ctrlName
    Execute"Accept_cal_values_1()"
End

Function Accept_values_2(ctrlName) : ButtonControl
    String ctrlName
    Execute"Accept_cal_values_2()"
End

Function reset_pnt_num(ctrlName) : ButtonControl
    String ctrlName
    Execute"reset_point_number()"
End

Function int_zero1(ctrlName) : ButtonControl
    String ctrlName
    Execute"interpolate_zero_1()"
End

Function int_zero2(ctrlName) : ButtonControl
    String ctrlName
    Execute"interpolate_zero_2()"
End

Macro Do_WAOWEX_NO2_cal(pointnumber)
variable pointnumber
pointnumber = 0
make/N = 10/o no2_sens1_ZA_flow, no2_sig1, no2_sens2_ZA_flow, no2_sig2
Display raw_signal_1,raw_signal_2 vs timewave; AppendToGraph/R
ZA_flow_NO2cal vs timewave; delayupdate
Showinfo;delayupdate
DoWindow/C/T NO2_Cals,"Put cursors on signal & press 'accept' "; delayupdate
ModifyGraph lsize(ZA_flow_NO2cal)=2,rgb(ZA_flow_NO2cal)=(52224,52224,0);
delayupdate
ModifyGraph rgb(raw_signal_2)=(0,13050,100);delayupdate
ControlBar 50
Button find_cal_region proc=find_ZA_flow,title="Find Cals"
Button Accept_cal_values_1 proc=Accept_values_1,title="Accept Values
#1",size={90, 20}
Button Accept_cal_values_2 proc=Accept_values_2,title="Accept Values
#2",size={90, 20}
Setvariable cal_pnt_no size={110,20},title="Cal pnt
no.",value=pointnumber,limits={0,9,1};DelayUpdate
Button reset_pointnumber proc = reset_pnt_num,title="Rest pnt no.",size={80,20}
Button int_zero_1 proc = int_zero1, size={100,20},title="Interpolate zero #1",
pos={0,25}, help={"Ensure cursors are on the two sections of zero"}
SetVariable zero_point1 size={155,20},pos = {106,25}, value=
pointnumber,title="and insert at point",limits={0,9,1};DelayUpdate
Button int_zero_2 proc= int_zero2, size={100,20},title="Interpolate zero #2",
pos={280,25} , help={"Ensure cursors are on the two sections of zero"}
SetVariable zero_point2 size={155,20},pos = {388,25}, value= pointnumber,
title="and insert at point",limits={0,9,1};DelayUpdate

```

end macro

```
macro find_za_flow_for_cals()
  variable i = 0
  variable first_cal_point = nan
  variable last_cal_point = nan
  variable no2_cal_state = 0
  do
    if((ZA_flow_NO2cal[i] > 0.5)%&(no2_cal_state ==0))
      first_cal_point = i
      no2_cal_state = 1
    endif
    if((ZA_flow_NO2cal[i] < 0.5)%&((no2_cal_state) ==1))
      last_cal_point = i
      no2_cal_state = 0
    endif
    i+=1
    if(i == 1000 | i == 5000 | i == 10000 | i == 20000)
      print i
    endif
  while(i<(numpts(ZA_flow_NO2cal)))
  //valdisplay valdisp0 value = (first_cal_point)
  Cursor A raw_signal_1 first_cal_point;Cursor B raw_signal_1 last_cal_point
  SetAxis bottom timewave[first_cal_point-100],timewave[last_cal_point]
  Edit no2_sens1_ZA_flow, no2_sig1, no2_sens2_ZA_flow, no2_sig2
end macro
```

```
macro Accept_cal_values_1()
  variable first_i = xcsr(A)
  variable last_i = xcsr(B)
  WaveStats/Q/R=[first_i,last_i] raw_signal_1
  NO2_sig1[pointnumber] = V_avg
  WaveStats/Q/R=[first_i,last_i] ZA_flow_NO2cal
  NO2_sens1_ZA_flow[pointnumber] = V_avg
  pointnumber+=1
end macro
```

```
macro Accept_cal_values_2()
  variable first_i = xcsr(A)
  variable last_i = xcsr(B)
  WaveStats/Q/R=[first_i,last_i] raw_signal_2
  NO2_sig2[pointnumber] = V_avg
  WaveStats/Q/R=[first_i,last_i] ZA_flow_NO2cal
  NO2_sens2_ZA_flow[pointnumber] = V_avg
  pointnumber+=1
end macro
```

```
macro reset_point_number()
  //variable pointnumber
  pointnumber = 0
end macro
```

```
macro interpolate_zero_1()
  variable first_i = vcsr(A)
  variable last_i = vcsr(B)
  NO2_sig1[pointnumber] = (first_i+last_i)/2
  NO2_sens1_ZA_flow[pointnumber] = nan
  pointnumber+=1
end macro
```

```
macro interpolate_zero_2()
  variable first_i = vcsr(A)
  variable last_i = vcsr(B)
  NO2_sig2[pointnumber] = (first_i+last_i)/2
  NO2_sens2_ZA_flow[pointnumber] = nan
  pointnumber+=1
end macro
```

```
Function calc_cal_sens(ctrlName) : ButtonControl
  String ctrlName
  Execute"calculate_calibration_sens()"
End
```

```
Function graph_cal_sens(ctrlName) : ButtonControl
  String ctrlName
  Execute"graph_calibration_sens()"
End
```

```
Macro Calculate_sensitivities()
  NewPanel
  DrawText 50,20,"NO2 Calibration Panel"
  SetVariable no2_cal_perm_rate size={240,20},title="NO2 Cal perm rate /
ng.min-1:",value=no2_cal_perm_rate;DelayUpdate
  Button Calc_cal_sens pos={0,25},
size={80,20},proc=calc_cal_sens,title="Calc. cal sens"
  Button graph_sens pos={100,25},size={80,20},
proc=graph_cal_sens,title="Graph Sens"
end macro
```

```
Macro calculate_calibration_sens()
  duplicate/o no2_sig1 no2_sig1_cal_mr, no2_sig2_cal_mr
  variable/G no2_cal_mr = (((no2_cal_perm_rate *1e-9)/46)*22400)/42
  variable i = 0
  ////Put in Freetex 2001 ZA calcs done on 19.11.2001 (in lab book)
  ////Put in WAOWEX 'guessed ZA calcs
  no2_sig1_cal_mr = no2_cal_mr *(42 / ((no2_sens1_za_flow*1000) + (42)))
  no2_sig2_cal_mr = (no2_cal_mr *42) / ((no2_sens2_za_flow*1000) + (42))
  do
    if(numtype(no2_sig1_cal_mr[i]) ==2)
      no2_sig1_cal_mr[i] = 0
    endif
    if(numtype(no2_sig2_cal_mr[i]) ==2)
      no2_sig2_cal_mr[i] = 0
    endif
  enddo
```

```

        endif
        i+=1
    while(i<100)
endmacro

Macro graph_calibration_sens()
    Display no2_sig1 vs no2_sig1_cal_mr ; AppendToGraph no2_sig2 vs
no2_sig2_cal_mr
    ModifyGraph mode=3,rgb(no2_sig2)=(13056,8704,0)
    Label left "NO\B2\M calibration signal / Volts";DelayUpdate
    Label bottom "Calculated NO\B2\M mixing ratio / parts";delayupdate
    Legend/N=text0/M/A=MC
    CurveFit/Q line no2_sig1 /X=no2_sig1_cal_mr /D
    variable/G final_no2_sens1 = W_coef[1]
    variable/G final_no2_sens1_err = (V_sigB/W_coef[1]*100)
    variable/G final_no2_sens_sd
    CurveFit/Q line no2_sig2 /X=no2_sig2_cal_mr /D
    variable/G final_no2_sens2 = W_coef[1]
    variable/G final_no2_sens2_err = (V_sigB/W_coef[1]*100)
    print ">> final_no2_sens1 = ",final_no2_sens1,"+/-",final_no2_sens1_err,"%"
    print ">> final_no2_sens2 = ",final_no2_sens2,"+/-",final_no2_sens2_err,"%"
endmacro

macro use_average_of_both_channels()
    duplicate/o raw_signal_1 COSMAS_amp_no2_ppb, COSMAS_ro2
    COSMAS_amp_no2_ppb = COSMAS_bkgd_avg_i_modulus /
((final_no2_sens1+final_no2_sens2)/2)
    //amp_no2_ppb1/=final_no2_sens1
    //amp_no2_ppb2/=final_no2_sens2
    //amp_no2_ppb2*=-1 ////use if out of phase with inlet1
    //amp_no2_1and2avg = (amp_no2_ppb1+amp_no2_ppb2)/2
    //amp_no2_1and2avg*=mx_key
    Display COSMAS_amp_no2_ppb vs timewave;delayupdate
    //ModifyGraph gaps(amp_no2_ppb1)=0;delayupdate
    //ModifyGraph mode
=0,gaps=0,rgb(amp_no2_ppb2)=(0,13056,0);delayupdate
    //ModifyGraph mode(amp_no2_ppb2)=2;delayupdate
    //AppendToGraph amp_no2_1and2avg vs timewave;delayupdate
    //ModifyGraph
gaps=0,ls(amp_no2_1and2avg)=3,rgb(amp_no2_1and2avg)=(0,52224,0);delayu
pdate
    COSMAS_ro2 = cosmas_amp_no2_ppb/150
    display cosmas_ro2 vs timewave
end macro

```

### A.3 Work-up2.ipf

```

Macro Initial_WAOWEX_Data_reduction()
    declare_globals()

```

```

switching()

Display
raw_signal_1,raw_signal_2,bkgd_avg2,amp_avg2,bkgd_avg1,amp_avg1,amp_avg2
_i,amp_avg1_i,bkgd_avg2_i,bkgd_avg1_i vs timewave
ModifyGraph
rgb(raw_signal_2)=(0,0,0),mode(bkgd_avg2)=3,marker(bkgd_avg2)=5;DelayUpdate
e
ModifyGraph
rgb(bkgd_avg2)=(65280,0,0),mode(amp_avg2)=3,marker(amp_avg2)=5;DelayUpdate
te
ModifyGraph
rgb(amp_avg2)=(0,39168,19712),mode(bkgd_avg1)=3,marker(bkgd_avg1)=6;DelayUpdate
yUpdate
ModifyGraph
mode(amp_avg1)=3,marker(amp_avg1)=6,rgb(amp_avg1)=(0,39168,19712);DelayUpdate
Update
ModifyGraph
rgb(amp_avg2_i)=(0,39168,19712),rgb(amp_avg1_i)=(0,39168,19712)
Legend/N=text0/A=MC

do_WAOWEX_NO2_cals(0)
end Macro

```

```

Function switching()
variable/G amp_sw_time = 5
variable/G bkgd_sw_time = 5
variable i = 0
variable k=0
variable j =0
variable loop_variable = 0
variable amp_sum1 = 0
variable bkgd_sum1 = 0
variable amp_sum2 = 0
variable bkgd_sum2 = 0
variable modacq = 1
variable bkgdacq = 0
variable test = 0
variable test2
wave modmode
wave timewave
wave raw_signal_1
wave raw_signal_2

duplicate/o raw_signal_2, amp_avg1, bkgd_avg1, amp_avg2, bkgd_avg2,
cosmas_perca

amp_avg1=nan
amp_avg2 = nan
bkgd_avg1 = nan

```

```

bkgd_avg2 = nan

do
    loop_variable = modmode[i]
    //print loop_variable
    test = modmode[i-amp_sw_time]
    test2 = timewave[i]
    if(modmode[i-amp_sw_time] ==0)

        if(modacq ==1)
            amp_sum1+= raw_signal_1[i]
            amp_sum2+= raw_signal_2[i]
            j+=1
            //print amp_sum1, amp_sum2, j, test, modacq,
bkgdacq, test2
        endif

        if(modmode[i+1]==1 | j == 55)
            bkgd_avg1[i-round(j/2)] = amp_sum1 / (j)
            amp_avg2[i-round(j/2)] = amp_sum2 / (j)
            //print k
            j = 0
            amp_sum1 = 0
            amp_sum2 = 0
            bkgdacq = 1
            modacq = 0
        endif
    endif

    if(modmode[i-bkgd_sw_time] ==1)

        if (bkgdacq == 1)
            bkgd_sum1+= raw_signal_1[i]
            bkgd_sum2+= raw_signal_2[i]
            j+=1
            //print bkgd_sum1, bkgd_sum2, j, test, modacq,
bkgdacq, test2
        endif

        if(modmode[i+1] == 0 | j == 55)
            amp_avg1[i-round(j/2)] = bkgd_sum1 / (j)
            bkgd_avg2[i-round(j/2)] = bkgd_sum2 / (j)
            //print amp_avg1[i-5], amp_sum1,i-5
            j = 0
            bkgd_sum1 = 0
            bkgd_sum2 = 0
            bkgdacq = 0
            modacq = 1
        endif
    endif
endif

```

```

        i+=1
        //      if((modmode[i] >0)%&(modmode[i] <1)) //this doesn't work!
Just Nan them out by hand!!
        //      amp_avg[i] = nan
        //      bkgd_avg[i] = nan
        //      endif
while(i<=(numpts(timewave)))

duplicate/o raw_signal_1 bkgd_avg1_i, bkgd_avg2_i, amp_avg1_i,
amp_avg2_i, amp_no2_volts1, amp_no2_volts2, COSMAS_perca

interpolatewave(bkgd_avg1_i, bkgd_avg1)
interpolatewave(bkgd_avg2_i, bkgd_avg2)
interpolatewave(amp_avg1_i, amp_avg1)
interpolatewave(amp_avg2_i, amp_avg2)

duplicate/o raw_signal_1 midmod1, midmod2

midmod1 = (amp_avg1_i + bkgd_avg1_i) / 2
midmod2 = (amp_avg2_i + bkgd_avg2_i) / 2
amp_no2_volts1 = raw_signal_1 - midmod1 //// taken out for Freetex01 data
amp_no2_volts2 = raw_signal_2 - midmod2

////using 'modulus' saves extracting the amp and background segments
COSMAS_perca, but biases all
////the data to positive values. So I'm not convinced about its validity...!
//alex// duplicate/o COSMAS_perca COSMAS_perca_mod
//alex// modulus(COSMAS_perca, COSMAS_perca_mod)
end function

```

Function Interpolatewave(w\_int, w) //This function performs a linear interpolation on wave w.

Wave /D w\_int, w //The interpolation built into igor can change wave scaling, so be careful if you use that.

```

duplicate/o w w_i, w_2i
variable x=0, y=0, n=numpts(w)
string cmd
WaveStats /Q w_2i
if (V_numNans!=n)
    x=FindFirst(w_2i,0)
    y=FindLast(w_2i,n)
    w_2i[0]=w_2i[x]
    w_2i[n-1]=w_2i[y]
    cmd="interpolate /T=1/y=w_i, w_2i"
    Execute cmd
    w_int=w_i
else
    print "interpolation is a problem"
endif
killwaves w_i,w_2i

```

end

Function FindFirst(w1, beginpoint) // FindFirst() finds the first non-nan value after (not including) beginpoint in a wave.

Wave w1 // If all values after beginpoint is nans, Findfirst will return number of points -1.

Variable beginpoint

Variable x, n=numpts(w1)

x=beginpoint+1

if (numtype(w1[x])!=2)

return(x)

else

do

x+=1

while ( (numtype(w1[x])==2)\*(x<(n-1)) )

return (x)

endif

End

/\*\*/

// FindLast() finds the last non-nan value before (or including) endpoint in a wave.

// If the entire wave is nans FindLast will return 0.

Function FindLast(w1, endpoint)

Wave w1

Variable endpoint

Variable x=endpoint-1

if (numtype(w1[x])!=2)

return(x)

else

do

x-=1

while ((numtype(w1[x])==2)\*(x>0)) )

return (x)

endif

End

Macro Final\_WAOWEX\_data\_reduction()

Get\_CL()

COSMAS\_perca = (amp\_no2\_volts1/final\_no2\_sens1)/CL1 -  
(amp\_no2\_volts2/final\_no2\_sens2)/CL2

extract\_data\_from\_COSMAS\_perca()

make\_mx\_key()

COSMAS\_ro2\_min\*=mx\_key

display cosmas\_ro2\_min vs timewave

ModifyGraph mode=2, lsize=3, rgb=(16384,28160,65280)

AppendToGraph/R ZA\_flow\_NO2cal,raw\_signal\_1,raw\_signal\_2,mx\_key  
vs timewave

```

    ModifyGraph
    rgb(ZA_flow_NO2cal)=(40960,65280,16384),rgb(mx_key)=(65280,65280,16384),r
    gb(raw_signal_2)=(0,0,0)
    ShowInfo
end macro()

```

```

Function extract_data_from_COSMAS_perca()

```

```

    variable i = 0
    variable k=0
    variable j =0
    variable loop_variable = 0
    variable amp_sum = 0
    variable bkgd_sum = 0
    wave modmode
    nvar amp_sw_time
    nvar bkgd_sw_time
    wave cosmas_perca
    wave ZA_flow_NO2cal
    duplicate/o raw_signal_2, COSMAS_amp_avg, COSMAS_bkgd_avg,
COSMAS_ro2_min
    COSMAS_amp_avg=nan
    COSMAS_bkgd_avg = nan
    COSMAS_ro2_min = nan
    loop_variable = 0
    variable modacq = 1
    variable bkgdacq = 0
    do
        loop_variable = modmode[i]
        //print loop_variable
        if(modmode[i-amp_sw_time] ==1)
            if(modacq ==1)
                amp_sum+= cosmas_perca[i]
                j+=1
                //print amp_sum, j, timewave[i]
            endif
            if(modmode[i+1] == 0 | j == 55)
                COSMAS_ro2_min[i-round(j/2)] = amp_sum / (j)
                //print k
                j = 0
                amp_sum = 0
                bkgdacq = 1
                modacq = 0
            endif
        endif
        if(modmode[i-bkgd_sw_time] ==0)
            if (bkgdacq == 1)
                bkgd_sum+= COSMAS_perca[i]
                j+=1
                //print bkgd_sum, j, timewave[i]
            endif
            if(modmode[i+1] == 1 | j == 55)
                COSMAS_ro2_min[i-round(j/2)] = -bkgd_sum / (j)

```

```
                j = 0
                bkgd_sum = 0
                bkgdacq = 0
                modacq = 1
            endif
        endif
        i+=1
    while(i<=(numpts(timewave)))
end macro
```

```
Function Make_mx_key()
    wave ZA_flow_NO2cal
    duplicate/o ZA_flow_NO2cal mx_key
    mx_key=1
    variable i = 0
    do
        if(ZA_flow_NO2cal[i] > 0.1)
            mx_key[i] = nan
        endif
        i+=1
    while(i<numpts(ZA_flow_NO2cal))
end
```

```
Function Get_CL()
    variable/G CL1
    variable/G CL2
    variable CLL1 = 100
    variable CLL2 = 100
    prompt CLL1, "Inlet 1"
    prompt CLL2, "Inlet 2"
    doprompt "Enter chainlengths", CLL1, CLL2
    CL1 = CLL1
    CL2 = CLL2
end
```

# Appendix B

## Postgraduate Record

### **B.1 Induction/Training Sessions Attended**

Departmental Induction

Graduate School Induction

Cross Faculty Induction

Introduction to Techniques

Advanced Departmental Safety Procedures and Fire Safety

Demonstrating/Small Group Teaching

An Introduction to PowerPoint

Personal Skills Portfolio

Writing Skills

Applications of Endnote

Advanced Scientific Writing for Chemists

### **B.2 Undergraduate Lecture Courses Attended**

Earth Observation Science

Life in the Universe

Photochemistry

## B.3 Departmental Seminars

08/10/03 – NMR and Proteins – Prof. Iain Campbell (University of Oxford)

28/10/03 – Climate Change, Fact or Fiction – Dr. S. P. Lawrence (Space Research Centre, University of Leicester)

03/11/03 – Controlling Electrons and Molecules Using Light – Prof. Helen Fielding (University College London)

14/11/03 – Green Solvents for Catalysis – From Molecular Understanding to Process Design – Prof. Walter Leitner (Max Planck Institute, Mulheim)

17/11/03 – Building High-Performance Magnetic Materials By Assembling Nanoclusters – Prof. Chris Binns (University of Leicester)

18/11/03 – UK Space Science Policy – Dr. David Hall (British National Space Centre)

20/11/03 – Richard Anschutz, Archibald Scott Couper and Josef Loschmidt: A Detective at Work – Dr Alfred Bader (Sigma-Aldrich)

02/12/03 – The Public Face of Space – Gareth James (National Space Centre)

08/12/03 – Bird Navigation: A Photochemical Magnetic Compass? – Prof. Peter Hore (University of Oxford)

12/12/03 – Scalable Parallel Quantum Chemistry: The Coarse Grained Approach – Prof. P. Taylor (University of Warwick, MMC Colloquium)

13/01/04 – Preparing for IASI Using Airborne Infrared Remote Sensing – Dr. J. Taylor (UK Meteorological Office)

20/01/04 – Habitability of Mars Subsurface: Evidence from the Meteorites – Dr. Everett Gibson (NASA – JSC)

28/01/04 – The Impact Crater as a Habitat: Life in the Aftermath of a Catastrophe – Charles Cockell (British Antarctic Survey)

10/02/04 – Clouds – The Big Unknown in Future Global Warming – Can Cloud RADAR and LIDAR Help? – Prof Anthony Illingworth (University of Reading)

16/02/04 – Accelerated Discovery of Electrochemical Materials – Dr. John Owen (University of Southampton)

08/03/04 – Applications of ESR Spectroscopy to Biological Problems – Dr. Chris Kay (Free University, Berlin)

09/03/04 – Radiative and Climate Impact of Aerosols – Dr. Eleanor Highwood (University of Reading)

15/03/04 – Connectivity of Functionalised Nanoparticles and Their Arrays – Prof. David Schiffrin (University of Liverpool)

11/05/04 – Traceable Radiometric Calibration of Detectors and Detector Matrices – Dr. E Thecharous (National Physical Laboratory)

25/05/04 – Auroral Imaging: A Novel Approach – Fraser Hamilton (Space Research Centre, University of Leicester)

29/09/04 – Adventures with Neutrons – Prof. John Watterson (Schonland Research Institute, University of Witwatersrand)

15/10/04 – The Chemistry of Interstellar Space – Prof. Eric Herbert (Ohio State University)

01/11/04 – Chemistry Of, Within and On Atomic and Molecular Clusters – Dr Stuart MacKenzie (University of Warwick)

17/11/04 – Meteors – What Impact Do They Have On The Atmosphere – Prof. John Plane (University of East Anglia)

23/11/04 – Some Aspects of Ion-Molecule and Electron Attachment Processes: Fundamentals and Applications – Dr Chris Mayhew (University of Birmingham)

11/01/05 – Remote Sensing the Earth's Atmosphere – Dr Don Grainger (University of Oxford)

11/01/06 – The Atmosphere-Space Interactions Monitor (ASIM) – Dr Torsten Neubert (Danish National Space Centre)

30/01/2006 - Density Functional Based Molecular Dynamics Simulation of Redox Reactions in Solution – Prof. Michiel Sprik (University of Cambridge)

01/02/2006 – What Can We Learn From Current and Future Satellite Observations of Tropospheric Composition – Dr Paul Palmer (University of Leeds)

03/02/2006 – Explosives and Explosive Detection – Dr Dan Wood (Home Office Scientific Development Branch)

20/02/2006 – Ion Mobility Spectrometry: Shaping up for Structural and Trace Analysis – Prof Colin Creaser (Nottingham Trent University)

08/03/2006 – Soft Ionization Mass Spectrometry for Quantitative Studies of non-Covalent Interactions – Prof Renato Zenobi (ETHZ)

08/05/2006 – Origin and Evolution of the Atmosphere – Prof Richard Wayne (University of Oxford)

07/02/2007 – The Atmospheric Chemistry Experiment (ACE): Spectroscopy from orbit – Prof Peter Bernath (University of York)

07/03/2007 – Chemistry and Giant Thunderstorms – Prof Geraint Vaughan  
(University of Manchester)

16/05/2007 – The Earth's Upper Atmosphere as a Natural Plasma Laboratory – Prof  
Terry Robinson (University of Leicester)

16/05/2007 – Skating on Thin Ice – What's In the Universe's Freezers? – Dr Helen  
Fraser – University of Strathclyde

16/05/2007 – RSC Tilden Lecture – Meteors and their Impact on the Atmosphere –  
Prof John Plane – University of Leeds

## **B.4 Conferences/Meetings Attended**

20/10/03 – Royal Society of Chemistry Symposium / Centenary Lecture –  
University of Leeds

30/10/03 – 31/10/03 – ITOP Planning Meeting – University of York

16/12/03 – 17/12/03 – IGAC Lagrangian Planning Meeting – University of East  
Anglia

27/01/04 – DIAC Launch Meeting – University of London

01/04/04 – Atmospheric Chemistry Special Interest Group of the Royal  
Meteorological Society Annual Meeting – University of Leicester

27/10/04 – 28/10/04 – ACCENT Experts Symposium: Interfacing Science with  
Policy and Public – Gothenburg, Sweden

10/11/04 – ITOP Preliminary Results Meeting – University of Leeds

11/04/05 – 13/04/05 – Faraday Discussions 130: Atmospheric Chemistry – University of Leeds

13/04/05 – 15/04/05 – ACCENT Experts Meeting on Atmospheric Free Radicals

24/04/05 – 29/04/05 – European Geophysical Union General Assembly – Vienna, Austria

05/12/05 – 09/12/05 – American Geophysical Union Fall Meeting Conference – San Francisco, United States

17/02/06 – AMMA Planning Meeting – University of Cambridge

03/05/06 – Atmospheric Chemistry Special Interest Group of the Royal Meteorological Society Conference – University of Leicester

19-21/06/06 – EUFAR Expert Working Group: Gas-Phase Chemistry Workshop – DFL, Munich

04/07/06 – AMMA Health and Safety Planning Meeting – Cranfield University

04/10/06 – Midlands Gas-phase Research Symposium – University of Warwick

08/12/06 – OP3 Meeting on Ground Based Measurements – CEH Lancaster

14/12/06 – NCAS Conference 2006 – University of Cambridge

20/02/07 – OP3 Meeting on Ground Based Measurements – University of Manchester

05-06/03/07 – AMMA UK Conference – CEH Wallingford

19/03/07 – OP3 aircraft meeting – University of Leicester

03/04/07 – Atmospheric Chemistry Special Interest Group of the Royal Meteorological Society Conference – University of Leicester

## B.5 Presentations Given at Conferences

10/11/04 – ITOP Preliminary Results Meeting – University of Leeds: Talk entitled ***“PERCA -  $\Sigma RO_2 + HO_2$ ”***

11/04/05 – Faraday Discussions 130: Atmospheric Chemistry – University of Leeds: Poster entitled ***“Measurements of peroxy radicals in air masses undergoing long-range transport during ITOP with a new dual-channel PERCA”***

13/04/05 – ACCENT Experts Meeting on Atmospheric Free Radicals – University of Leeds: Poster entitled ***“Ground and airborne measurements of peroxy radicals using the PERCA technique”***

28/04/05 – European Geophysical Union General Assembly – Vienna, Austria: Poster ***“Deployment of a Dual-Channel Peroxy Radical Chemical Amplifier (PERCA) on an airborne platform during ITOP”***

28/04/05 – European Geophysical Union General Assembly – Vienna, Austria: Poster ***“Measurements of peroxy radicals in air masses undergoing long range transport during ITOP”***

07/12/05 – American Geophysical Union Fall Meeting – San Francisco, United States: Talk ***“Measurements of peroxy radicals in air masses undergoing long range transport during ITOP”***

16/03/06 - Brocks Hill Environment Centre - Leicester: Public Lecture ***“Environmental Monitoring”***

04/10/06 – Midlands Gas-phase Research Symposium – University of Warwick:  
Talk “*Peroxy radicals, chemistry and transport*”

10/10/06 – Talk to Pupils – Warwick School: Talk “*The Changing Atmosphere*”

14/11/06 – Talk to Pupils – John Cleveland College: Talk “*Ozone Holes: Fact or Fiction?*”

14/12/06 – NCAS Conference 2006 – University of Cambridge: Talk “*Airborne measurements of peroxy radicals ( $HO_2 + RO_2$ ) and the photolysis rates of ozone and  $NO_2$  during AMMA: initial results and insights*”

## **B.6 Departmental Presentations**

14/11/03 – Talk “*Peroxy Radical Chemical Ionisation Mass Spectrometer (PerCIMS)*”

05/02/04 – First Year Talk “*Measurements of Peroxy Radicals in the Free Troposphere: Long-range Transport and Chemical Processing*”

26/03/04 – Talk “*Iodine in the Marine Boundary Layer*”

12/11/04 – Talk “*Long Range Transport: Ways and Means*”

25/02/05 – Talk “*The Photochemistry Experiment during BERLIOZ (PHOEBE)*”

04/07/05 – Second Year Talk: “*Aircraft measurements of peroxy radicals during long-range transport*”

25/11/05 – Talk “*Transport and Chemical Evolution over the Pacific (TRACE-P)*”

15/06/06 – Third Year Talk: *“Measurements of peroxy radicals in air masses undergoing long range transport during ITOP and at the Jungfraujoch  
The role of peroxy radicals in secondary organic aerosol formation”*

## B.7 Papers

Parker, A. E., P. S. Monks, M. J. Jacob, S. A. Penkett, A. C. Lewis, D. Stewart, L. Whalley, J. Methven, and A. Stohl (2007), Peroxy radicals and ozone photochemistry in air masses undergoing long-range transport, *Journal of Geophysical Research*, *submitted*.

Lewis, A. C., M. J. Evans, J. Methven, N. Watson, J. D. Lee, J. R. Hopkins, R. M. Purvis, S. R. Arnold, J. B. McQuaid, L. K. Whalley, M. J. Pilling, D. E. Heard, P. S. Monks, A. E. Parker, C. E. Reeves, D. E. Oram, G. Mills, B. J. Bandy, D. Stewart, H. Coe, P. Williams, and J. Crozier (2007), Chemical composition observed over the mid-Atlantic and the detection of pollution signatures far from source regions, *Journal of Geophysical Research*, [*Atmospheres*], 112.

Cook, P. A., N. H. Savage, S. Turquety, G. D. Carver, F. M. O'Connor, A. Heckel, D. Stewart, L. Whalley, A. E. Parker, H. Schlager, H. B. Singh, M. A. Avery, G. W. Sachse, W. Brune, A. Richter, J. P. Burrows, R. Purvis, A. C. Lewis, C. Reeves, P. S. Monks, J. G. Levine, and J. A. Pyle (2007), Forest fire plumes over the North Atlantic: p-TOMCAT model simulations with aircraft and satellite measurements from the ITOP/ICARTT campaign, *Journal of Geophysical Research*, *in press*.

Wyche, K. P., R. L. Cordell, A. M. Ellis, A. E. Parker, C. Whyte, P. S. Monks, J. Dommen, A. Metzger, J. Duplissy, A. S. H. Prévôt, U. Baltensperger, and A. R. Rickard (2007), Potential Gas-Phase Precursors in the Photooxidation of 1,3,5-trimethylbenzene, *In preparation*.

## B.8 Other

Wyche, K.P., Parker, A.E., Ellis, A.M. and Monks, P.S. – Process Studies of Trace Gases and Aerosols in Simulation Chambers – EGU 2006

Paul Monks, Zoë Flemming, Mark Jacob, Alex Parker, and Tim Green & Stuart Penkett – Ground and airborne measurements of peroxy radicals using the PERCA technique – Leeds Expert Meeting

Kevin Wyche, Christopher Whyte, Alex Parker, Rebecca Cordell, Andrew Ellis, Paul Monks, Axel Metzger, Jonathan Duplissy, Josef Dommen, André Prévôt, Urs Baltensperger – Formation & Evolution of Potential Gas Phase Precursors to Secondary Organic Aerosol – NCAS Meeting, University of York, 4-5th April 2007

Sommariva, R., S. S. Brown, J. M. Roberts, A. E. Parker, P. S. Monks, D. M. Brookes, H. D. Osthoff, B. M. Lerner, E. J. Williams, F. C. Fehsenfeld, A. R. Ravishankara and M. Trainer – Peroxy Radical Measurements from R/V Brown during TEXAQS 2006 – TEXAQS Campaign Data Workshop.

# References

- Alfarra, M. R., D. Paulsen, M. Gysel, A. A. Garforth, J. Dommen, A. S. H. Prévôt, D. R. Worsnop, U. Baltensperger, and H. Coe (2006), A mass spectrometric study of secondary organic aerosols formed from the photooxidation of anthropogenic and biogenic precursors in a reaction chamber, *Atmospheric Chemistry and Physics*, *6*, 5279-5293.
- Andreae, M. O., and P. J. Crutzen (1997), Atmospheric Aerosols: Biogeochemical Sources and Role in Atmospheric Chemistry, *Science*, *276*, 1052-1058.
- Andrés Hernández, M. D., J. Burkert, L. Reichert, D. Stöbener, J. Meyer-Arnek, J. P. Burrows, R. R. Dickerson, and B. G. Doddridge (2001), Marine boundary layer peroxy radical chemistry during the AEROSOLS99 campaign: Measurements and analysis, *Journal of Geophysical Research*, *106*, 20,833-820,846.
- Apel, E. C., A. J. Hills, R. Lueb, S. Zindel, S. Eisele, and D. D. Riemer (2003), A fast-GC/MS system to measure C<sub>2</sub> to C<sub>4</sub> carbonyls and methanol aboard aircraft, *Journal of Geophysical Research*, *108*.
- Ashbourn, S. F. M., M. E. Jenkin, and K. C. Clemitshaw (1998), Laboratory studies of the response of a peroxy radical chemical amplifier to HO<sub>2</sub> and a series of organic peroxy radicals, *J. Atmos. Chem.*, *29*, 233-266.
- Atkinson, R. (1986), Kinetics and mechanisms of the gas-phase reactions of the hydroxyl radical with organic compounds under atmospheric conditions, *Chemical Reviews*, *86*.
- Atkinson, R. (2003), Kinetics of the gas-phase reactions of OH radicals with alkanes and cycloalkanes, *Atmospheric Chemistry and Physics*, *3*, 2233-2307.
- Atkinson, R., and S. M. Aschmann (1989), Rate constants for the gas-phase reactions of the OH radical with a series of aromatic hydrocarbons at 296 ± 2 K, *Int. J. Chem. Kinet.*, *21*.
- Atkinson, R., D. L. Baulch, R. A. Cox, J. N. Crowley, R. F. Hampson Jr, R. G. Hynes, M. E. Jenkin, J. A. Kerr, M. J. Rossi, and J. Troe (2004), Summary of Evaluated Kinetic and Photochemical Data for Atmospheric Chemistry, *Web Version July 2004*.
- Atkinson, R., D. L. Baulch, R. A. Cox, J. N. Crowley, R. F. Hampson Jr, R. G. Hynes, M. E. Jenkin, J. A. Kerr, M. J. Rossi, and J. Troe (2005), Summary of Evaluated Kinetic and Photochemical Data for Atmospheric Chemistry, *Web Version March 2005*.
- Atkinson, R., D. L. Baulch, R. A. Cox, J. N. Crowley, R. F. Hampson Jr, R. G. Hynes, M. E. Jenkin, J. A. Kerr, M. J. Rossi, and J. Troe (2006), Summary of Evaluated Kinetic and Photochemical Data for Atmospheric Chemistry, *Web Version February 2006*.

Atkinson, R., D. L. Baulch, R. A. Cox, R. F. Hampson, J. A. Kerr, M. J. Rossi, and J. Troe (1999), Evaluated kinetic and photochemical data for atmospheric chemistry, organic species: Supplement VII, *Journal of Physical and Chemical Reference Data*, 28, 191-393.

Atkinson, R., D. L. Baulch, R. A. Cox, R. F. Hampson, J. A. Kerr, and J. Troe (1992), Evaluated Kinetic and Photochemical Data for Atmospheric Chemistry Supplement-IV - Iupac Subcommittee on Gas Kinetic Data Evaluation for Atmospheric Chemistry, *Journal of Physical and Chemical Reference Data*, 21, 1125-1568.

Auvray, M., and I. Bey (2005), Long-Range Transport to Europe: Seasonal Variations and Implications for the European Ozone Budget, *Journal of Geophysical Research*, 110.

Baltensperger, U., M. Kalberer, J. Dommen, D. Paulsen, M. R. Alfarra, H. Coe, R. Fisseha, A. Gascho, M. Gysel, S. Nyeki, M. Sax, M. Steinbacher, A. S. H. Prévôt, S. Sjögren, E. Weingartner, and R. Zenobi (2005), Secondary organic aerosols from anthropogenic and biogenic precursors, *Faraday Discussions*, 130, 265-278.

Balzani Lööv, J. M., G. Legreid, J. Staehelin, S. Reimann, A. S. H. Prévôt, S. Henne, and M. Steinbacher (2007), Seasonal background concentration variations of selected trace gases at the Swiss high Alpine station Jungfraujoch during 2005, *unpublished manuscript*.

Bey, I. (2004), edited, Presentation to ACCENT T&TP start-up meeting October 2004.

Blake, R. S., C. Whyte, C. O. Hughes, A. M. Ellis, and P. S. Monks (2004), Demonstration of Proton-Transfer Reaction Time-of-Flight Mass Spectrometry for Real-Time Analysis of Trace Volatile Organic Compounds, *Anal. Chem.*, 76, 3841-3845.

Bloss, W. J., J. D. Lee, D. E. Heard, R. A. Salmon, S. J.-B. Baugitte, H. K. Roscoe, and A. E. Jones (2007), Observations of OH and HO<sub>2</sub> radicals in coastal Antarctica, *Atmospheric Chemistry and Physics Discussions*, 7, 2893-2935.

Bloss, W. J., J. D. Lee, G. P. Johnson, R. Sommariva, D. E. Heard, A. Saiz-Lopez, J. M. C. Plane, G. McFiggans, H. Coe, M. Flynn, P. Williams, A. R. Rickard, and Z. L. Fleming (2005), Impact of halogen monoxide chemistry upon boundary layer OH and HO<sub>2</sub> concentrations at a coastal site, *Geophys. Res. Lett.*, 32.

Bongartz, A., J. Kames, F. Welter, and U. Schurath (1991), Near-UV absorption cross-sections and trans cis equilibrium of nitrous acid, *Journal of Physical Chemistry*, 95, 1076-1082.

Boodaghians, R. B., I. W. Hall, F. S. Toby, and R. P. Wayne (1987), Absolute determinations of the kinetics and temperature dependences of the reactions of OH with a series of alkynes, *Journal of the Chemical Society Faraday Transactions 2*, 83.

Brune, W. H., I. Faloon, D. Tan, A. Weinheimer, T. Campos, B. A. Ridley, S. Vay, J. E. Collins, G. W. Sachse, L. Jaeglé, and D. J. Jacob (1998), Airborne in-situ OH

and HO<sub>2</sub> observations in the cloud-free troposphere and lower stratosphere during SUCCESS, *Geophys. Res. Lett.*, *25*, 1701-1704.

Brune, W. H., D. Tan, I. Faloon, L. Jaégle, D. J. Jacob, B. G. Heikes, J. Snow, Y. Kondo, R. Shetter, G. W. Sachse, B. Anderson, G. L. Gregory, S. Vay, H. B. Singh, D. D. Davis, J. H. Crawford, and D. R. Blake (1999), OH and HO<sub>2</sub> chemistry in the North Atlantic free troposphere, *Geophys. Res. Lett.*, *26*, 3077-3080.

Burkert, J., M. D. Andrés-Hernández, L. Reichert, J. Meyer-Arneke, B. Doddridge, R. R. Dickerson, J. Mühle, A. Zahn, T. Carsey, and J. P. Burrows (2003), Trace gas and radical diurnal behaviour in the marine boundary layer during INDOEX 1999, *Journal of Geophysical Research*, *108*.

Burkert, J., M. D. Andrés Hernández, D. Stobener, J. P. Burrows, M. Weissenmayer, and A. Kraus (2001), Peroxy radical and related trace gas measurements in the boundary layer above the Atlantic Ocean, *Journal of Geophysical Research*, *106*, 5457-5477.

Cantrell, C. A., G. D. Edwards, S. Stephens, L. Mauldin, E. Kosciuch, M. Zondlo, and F. Eisele (2003a), Peroxy radical observations using chemical ionization mass spectrometry during TOPSE, *J. Geophys. Res.-Atmos.*, *108*, art. no.-8371.

Cantrell, C. A., G. D. Edwards, S. Stephens, R. L. Mauldin, M. A. Zondlo, E. Kosciuch, F. L. Eisele, R. E. Shetter, B. L. Lefer, S. Hall, F. Flocke, A. Weinheimer, A. Fried, E. Apel, Y. Kondo, D. R. Blake, N. J. Blake, I. J. Simpson, A. R. Bandy, D. C. Thornton, B. G. Heikes, H. B. Singh, W. H. Brune, H. Harder, M. Martinez, D. J. Jacob, M. A. Avery, J. D. Barrick, G. W. Sachse, J. R. Olson, J. H. Crawford, and A. D. Clarke (2003b), Peroxy radical behavior during the Transport and Chemical Evolution over the Pacific (TRACE-P) campaign as measured aboard the NASA P-3B aircraft, *J. Geophys. Res.-Atmos.*, *108*.

Cantrell, C. A., L. Mauldin, M. Zondlo, F. Eisele, E. Kosciuch, R. Shetter, B. Lefer, S. Hall, T. Campos, B. Ridley, J. Walega, A. Fried, B. Wert, F. Flocke, A. Weinheimer, J. Hannigan, M. Coffey, E. Atlas, S. Stephens, B. Heikes, J. Snow, D. Blake, N. Blake, A. Katzenstein, J. Lopez, E. V. Browell, J. Dibb, E. Scheuer, G. Seid, and R. Talbot (2003c), Steady state free radical budgets and ozone photochemistry during TOPSE, *J. Geophys. Res.-Atmos.*, *108*, art. no.-8361.

Cantrell, C. A., R. E. Shetter, and J. Calvert (1996a), Peroxy radical chemistry during FIELDVOC 1993 in Brittany, France, *Atmos. Environ.*, *30*, 3947-3957.

Cantrell, C. A., R. E. Shetter, and J. G. Calvert (1996b), Dual-inlet chemical amplifier for atmospheric peroxy radical measurements, *Anal. Chem.*, *68*, 4194-4199.

Cantrell, C. A., R. E. Shetter, J. G. Calvert, F. L. Eisele, and D. J. Tanner (1997a), Some considerations of the origin of nighttime peroxy radicals observed in MLOPEX 2c, *J. Geophys. Res.-Atmos.*, *102*, 15899-15913.

Cantrell, C. A., R. E. Shetter, J. G. Calvert, F. L. Eisele, E. Williams, K. Baumann, W. H. Brune, P. S. Stevens, and J. H. Mather (1997b), Peroxy radicals from photostationary state deviations and steady state calculations during the

- Tropospheric OH Photochemistry Experiment at Idaho Hill, Colorado, 1993, *J. Geophys. Res.-Atmos.*, *102*, 6369-6378.
- Cantrell, C. A., R. E. Shetter, J. G. Calvert, D. D. Parrish, F. C. Fehsenfeld, P. D. Goldan, W. Kuster, E. J. Williams, H. H. Westberg, G. Allwine, and R. Martin (1993a), Peroxy-Radicals as Measured in Rose and Estimated from Photostationary State Deviations, *J. Geophys. Res.-Atmos.*, *98*, 18355-18366.
- Cantrell, C. A., R. E. Shetter, T. M. Gilpin, and J. G. Calvert (1996c), Peroxy radicals measured during Mauna Loa observatory photochemistry experiment 2: The data and first analysis, *J. Geophys. Res.-Atmos.*, *101*, 14643-14652.
- Cantrell, C. A., R. E. Shetter, J. A. Lind, A. H. McDaniel, J. G. Calvert, D. D. Parrish, F. C. Fehsenfeld, M. P. Buhr, and M. Trainer (1993b), An Improved Chemical Amplifier Technique for Peroxy Radical Measurements, *J. Geophys. Res.-Atmos.*, *98*, 2897-2909.
- Cantrell, C. A., and D. H. Stedman (1982), A Possible Technique for the Measurement of Atmospheric Peroxy-Radicals, *Geophys. Res. Lett.*, *9*, 846-849.
- Cantrell, C. A., D. H. Stedman, and G. J. Wendel (1984), Measurement of Atmospheric Peroxy-Radicals by Chemical Amplification, *Anal. Chem.*, *56*, 1496-1502.
- Carpenter, L. J. (1996), Measurements of peroxy radicals in clean and polluted atmospheres, *Ph.D. Thesis, University of East Anglia*.
- Carpenter, L. J., K. C. Clemitshaw, R. A. Burgess, S. A. Penkett, J. N. Cape, and G. C. McFadyen (1998), Investigation and evaluation of the NO<sub>x</sub>/O<sub>3</sub> photochemical steady state, *Atmos. Environ.*, *32*, 3353-3365.
- Carpenter, L. J., T. J. Green, G. P. Mills, S. Baugitte, S. A. Penkett, P. Zanis, E. Schuepbach, N. Schmidbauer, P. S. Monks, and C. Zellweger (2000), Oxidized nitrogen and ozone production efficiencies in the springtime free troposphere over the Alps, *Journal of Geophysical Research*, *105*, 14,547-514,559.
- Carpenter, L. J., P. S. Monks, B. J. Bandy, S. A. Penkett, I. E. Galbally, and C. P. Meyer (1997), A study of peroxy radicals and ozone photochemistry at coastal sites in the northern and southern hemispheres, *J. Geophys. Res.-Atmos.*, *102*, 25417-25427.
- Carslaw, N., L. J. Carpenter, J. M. C. Plane, B. J. Allan, R. A. Burgess, K. C. Clemitshaw, H. Coe, and S. A. Penkett (1997), Simultaneous observations of nitrate and peroxy radicals in the marine boundary layer, *J. Geophys. Res.-Atmos.*, *102*, 18917-18933.
- Carslaw, N., D. J. Creasey, D. E. Heard, P. J. Jacobs, J. D. Lee, A. C. Lewis, J. B. McQuaid, M. J. Pilling, S. Baugitte, S. A. Penkett, P. S. Monks, and G. Salisbury (2002), Eastern Atlantic Spring Experiment 1997 (EASE97) - 2. Comparisons of model concentrations of OH, HO<sub>2</sub>, and RO<sub>2</sub> with measurements, *J. Geophys. Res.-Atmos.*, *107*, art. no.-4190.

- Carslaw, N., D. J. Creasey, D. E. Heard, A. C. Lewis, J. B. McQuaid, M. J. Pilling, P. S. Monks, B. J. Bandy, and S. A. Penkett (1999), Modeling OH, HO<sub>2</sub>, and RO<sub>2</sub> radicals in the marine boundary layer - 1. Model construction and comparison with field measurements, *J. Geophys. Res.-Atmos.*, *104*, 30241-30255.
- Chung, S. H., and J. H. Seinfeld (2002), Global distribution and climate forcing of carbonaceous aerosols, *Journal of Geophysical Research*, *107*.
- Clemmshaw, K. C. (2004), A review of instrumentation and measurement techniques for ground-based and airborne field studies of gas-phase tropospheric chemistry, *Critical Reviews in Environmental Science and Technology*, *34*, 1-108.
- Clemmshaw, K. C., L. J. Carpenter, S. A. Penkett, and M. E. Jenkin (1997), A calibrated peroxy radical chemical amplifier for ground-based tropospheric measurements, *J. Geophys. Res.-Atmos.*, *102*, 25405-25416.
- Cooper, O., A. Stohl, R. Doherty, P. Hess, and P. Grennfelt (2007), Draft TF HTAP Interim Report Chapter 2 - Conceptual Overview of Hemispheric or Intercontinental Transport Processes.
- Cooper, P., and J. P. D. Abbatt (1996), Heterogeneous Interactions of OH and HO<sub>2</sub> Radicals with Surfaces Characteristic of Atmospheric Particulate Matter, *Journal of Physical Chemistry*, *100*, 2249-2254.
- Coquart, B., A. Jenouvrier, and M. F. Merienne (1995), The NO<sub>2</sub> absorption spectrum. II. Absorption cross-sections at low temperatures in the 400-500 nm region, *J. Atmos. Chem.*, *21*, 251-261.
- Creasey, D. J., P. A. Halford-Maw, D. E. Heard, J. E. Spence, and B. J. Whitaker (1998), Fast photomultiplier tube gating system for photon counting applications, *Review of Scientific Instruments*, *69*, 4068-4073.
- Creasey, D. J., P. A. Halford-Maw, D. E. Heard, M. J. Pilling, and B. J. Whitaker (1997), Implementation and initial deployment of a field instrument for measurement of OH and HO<sub>2</sub> in the troposphere by laser-induced fluorescence, *J. Chem. Soc.-Faraday Trans.*, *93*, 2907-2913.
- Davidson, C. I., R. F. Phalen, and P. A. Solomon (2005), Airborne Particulate Matter and Human Health: A Review, *Aerosol Science and Technology*, *39*, 737-749.
- de Gouw, J., and C. Warneke (2007), Measurements of volatile organic compounds in the Earth's atmosphere using Proton-Transfer-Reaction Mass Spectrometry, *Mass Spectrometry Reviews*, *26*, 223-257.
- Dentener, F. J., and P. J. Crutzen (1993), Reaction of N<sub>2</sub>O<sub>5</sub> on Tropospheric Aerosols: Impact on the Global Distributions of NO<sub>x</sub>, O<sub>3</sub> and OH, *Journal of Geophysical Research*, *98*, 7149-7163.
- Derwent, R. G., P. G. Simmonds, S. Seuring, and C. Dimmer (1998), Observation and interpretation of the seasonal cycles in the surface concentrations of ozone and carbon monoxide at Mace Head, Ireland from 1990 to 1994, *Atmos. Environ.*, *32*, 145-157.

- Derwent, R. G., D. S. Stevenson, W. J. Collins, and C. E. Johnson (2004), Intercontinental transport and the origins of the ozone observed at surface sites in Europe, *Atmos. Environ.*, *38*, 1891-1901.
- Dlugokencky, E. J., S. Houweling, L. Bruhwiler, K. A. Masarie, P. M. Lang, J. B. Miller, and P. P. Tans (2003), Atmospheric methane levels off: Temporary pause or a new steady-state?, *Geophys. Res. Lett.*, *30*.
- Dommen, J., A. S. H. Prévôt, B. Neininger, and M. Bäumle (2002), Characterization of the photooxidant formation in the metropolitan area of Milan from aircraft measurements, *Journal of Geophysical Research*, *107*.
- Duncan, B. N., and I. Bey (2004), A modelling study of the export pathways of pollution from Europe: Seasonal and interannual variations (1987-1997), *J. Geophys. Res.-Atmos.*, *109*, art. no.-D08301.
- Eckhardt, S., A. Stohl, H. Wernli, P. James, C. Forster, and N. Spichtinger (2004), A 15-Year Climatology of Warm Conveyor Belts, *Journal of Climate*, *17*, 218-237.
- Edwards, G. D., C. A. Cantrell, S. Stephens, B. Hill, O. Goyea, R. E. Shetter, R. L. Mauldin, III, E. Kosciuch, D. J. Tanner, and F. L. Eisele (2003), Chemical Ionization Mass Spectrometer Instrument for the Measurement of Tropospheric HO<sub>2</sub> and RO<sub>2</sub>, *Analytical Chemistry*, *75*, 5317-5327.
- Edwards, G. D., and P. S. Monks (2003), Performance of a single-monochromator diode array spectroradiometer for the determination of actinic flux and atmospheric photolysis frequencies, *Journal of Geophysical Research*, *108*.
- Eisele, F. L., and D. J. Tanner (1993), Measurement of the Gas-Phase Concentration of H<sub>2</sub>SO<sub>4</sub> and Methane Sulfonic-Acid and Estimates of H<sub>2</sub>SO<sub>4</sub> Production and Loss in the Atmosphere, *Journal of Geophysical Research-Atmospheres*, *98*, 9001-9010.
- Emmerson, K. M., N. Carslaw, D. C. Carslaw, J. D. Lee, G. McFiggans, W. J. Bloss, T. Gravesstock, D. E. Heard, J. R. Hopkins, T. Ingham, M. J. Pilling, S. C. Smith, M. J. Jacob, and P. S. Monks (2007), Free radical modelling studies during the UK TORCH Campaign in Summer 2003, *Atmospheric Chemistry and Physics*, *7*, 161-181.
- Evans, M. (2004), ICARTT flight tracks, edited.
- Evans, M. J., D. E. Shallcross, K. S. Law, J. O. F. Wild, P. G. Simmonds, T. G. Spain, P. Berrisford, J. Methven, A. C. Lewis, J. B. McQuaid, M. J. Pilling, B. J. Bandy, S. A. Penkett, and J. A. Pyle (2000), Evaluation of a Lagrangian box model using field measurements from EASE (Eastern Atlantic Summer Experiment) 1996, *Atmos. Environ.*, *34*, 3843-3863.
- Faloona, I., D. Tan, W. H. Brune, L. Jaeglé, D. J. Jacob, Y. Kondo, M. Koike, R. Chatfield, R. Pueschel, G. Ferry, G. Sachse, S. Vay, B. Anderson, J. Hannon, and H. Fuelberg (2000), Observations of HO<sub>x</sub> and its relationship with NO<sub>x</sub> in the upper troposphere during SONEX, *Journal of Geophysical Research*, *105*, 3771-3783.

- Farman, J. C., B. G. Gardiner, and J. D. Shanklin (1985), Large losses of total ozone in Antarctica reveal seasonal ClO<sub>x</sub>/NO<sub>x</sub> interaction, *Nature (London, United Kingdom)*, *315*, 207-210.
- Fehsenfeld, F. C., G. Ancellet, T. S. Bates, A. H. Goldstein, R. M. Hardesty, R. Honrath, K. S. Law, A. C. Lewis, R. Leatch, S. McKeen, J. Meagher, D. D. Parrish, A. A. P. Pszenny, R. P. B., H. Schlager, J. Seinfeld, R. Talbot, and R. Zbinden (2006), International Consortium for Atmospheric Research on Transport and Transformation (ICARTT): North America to Europe - Overview of the 2004 summer field study, *Journal of Geophysical Research, [Atmospheres]*, *111*.
- Finlayson-Pitts, B. J., and J. N. Pitts, Jr. (1993), Atmospheric chemistry of tropospheric ozone formation: scientific and regulatory implications, *Air & Waste*, *43*, 1091-1100.
- Finlayson-Pitts, B. J., and J. N. Pitts Jr. (2000), Chemistry of the Upper and Lower Atmosphere.
- Fiore, A. M., D. J. Jacob, J. A. Logan, and J. H. Yin (1998), Long-term trends in ground level ozone over the contiguous United States, 1980-1995, *Journal of Geophysical Research*, *103*.
- Fleming, Z. L. (2005), The measurement of peroxy radicals in the marine boundary layer using the PERCA technique, Ph.D. thesis, University of Leicester, Leicester.
- Fleming, Z. L., P. S. Monks, A. R. Rickard, B. J. Bandy, N. Brough, T. J. Green, C. E. Reeves, and S. A. Penkett (2006a), Seasonal dependence of peroxy radical concentrations at a Northern hemisphere marine boundary layer site during summer and winter: evidence for radical activity in winter, *Atmospheric Chemistry and Physics*, *6*, 5415-5433.
- Fleming, Z. L., P. S. Monks, A. R. Rickard, D. E. Heard, W. J. Bloss, P. W. Seakins, T. J. Still, R. Sommariva, M. J. Pilling, R. Morgan, T. J. Green, N. Brough, G. P. Mills, S. A. Penkett, A. C. Lewis, J. D. Lee, A. Saiz-Lopez, and J. M. C. Plane (2006b), Peroxy radical chemistry and the control of ozone photochemistry at Mace Head, Ireland during the summer of 2002, *Atmospheric Chemistry and Physics*, *6*, 2193-2214.
- Forster, C., U. Wandinger, G. Wotawa, P. James, I. Mattis, D. Althausen, P. G. Simmonds, S. O'Doherty, S. G. Jennings, C. Kleefeld, J. Schneider, T. Trickl, S. Kreipl, H. Jager, and A. Stohl (2001), Transport of boreal forest fire emissions from Canada to Europe, *Journal of Geophysical Research*, *106*, 22,887-822,906.
- Frost, G. J., M. Trainer, G. Allwine, M. P. Buhr, J. G. Calvert, C. A. Cantrell, F. C. Fehsenfeld, P. D. Goldan, J. Herwehe, G. Hubler, W. C. Kuster, R. Martin, R. T. McMillen, S. A. Montzka, R. B. Norton, D. D. Parrish, B. A. Ridley, R. E. Shetter, J. G. Walega, B. A. Watkins, H. H. Westberg, and E. J. Williams (1998), Photochemical ozone production in the rural southeastern United States during the 1990 Rural Oxidants in the Southern Environment (ROSE) program, *J. Geophys. Res.-Atmos.*, *103*, 22491-22508.

- Fuchs, H. (2006), Measurement of peroxy radicals using laser-induced fluorescence technique, *Schriften des Forschungszentrums Juelich, Reihe Umwelt/Environment*, 72.
- Gao, S., N. L. Ng, M. Keywood, V. Varutbangkul, R. Bahreini, A. Nenes, J. He, K. Y. Yoo, J. L. Beauchamp, R. P. Hodyss, R. C. Flagan, and J. H. Seinfeld (2004), Particle Phase Acidity and Oligomer Formation in Secondary Organic Aerosol, *Environmental Science & Technology*, 38, 6582-6589.
- Gerbig, C., S. Schmitgen, D. Kley, A. Volz-Thomas, K. Dewey, and D. Haaks (1999), An improved fast-response vacuum-UV resonance fluorescence CO instrument, *Journal of Geophysical Research, [Atmospheres]*, 104, 1699-1704.
- Geyer, A., B. Alicke, R. Ackermann, M. Martinez, H. Harder, W. H. Brune, P. di Carlo, E. Williams, T. Jobson, S. Hall, R. Shetter, and J. Stutz (2003), Direct observations of daytime NO<sub>3</sub>: Implications for urban boundary layer chemistry, *Journal of Geophysical Research*, 108.
- Gierczak, T., J. B. Burkholder, S. Bauerle, and A. R. Ravishankara (1998), Photochemistry of acetone under tropospheric conditions, *Chemical Physics*, 231, 229-244.
- Grannas, A. M., A. E. Jones, J. Dibb, M. Ammann, C. Anastasio, H. J. Beine, M. Bergin, J. Bottenheim, C. S. Boxe, G. Carver, G. Chen, J. H. Crawford, F. Dominé, M. M. Frey, M. I. Guzmán, D. E. Heard, D. Helmig, M. R. Hoffmann, R. E. Honrath, L. G. Huey, M. Hutterli, H. W. Jacobi, P. Klán, B. Lefer, J. McConnell, J. Plane, R. Sander, J. Savarino, P. B. Shepson, W. R. Simpson, J. R. Sodeau, R. von Glasow, R. Weller, E. W. Wolff, and T. Zhu (2007), An overview of snow photochemistry: evidence, mechanisms and impacts, *Atmospheric Chemistry and Physics Discussions*, 7, 4165-4283.
- Green, T. J. (2003), PERCA Technical Specification of Scientific Equipment.
- Green, T. J., C. E. Reeves, N. Brough, G. D. Edwards, P. S. Monks, and S. A. Penkett (2003), Airborne measurements of peroxy radicals using the PERCA technique, *J. Environ. Monit.*, 5, 75-83.
- Green, T. J., C. E. Reeves, Z. L. Flemming, N. Brough, A. R. Rickard, B. J. Bandy, P. S. Monks, and S. A. Penkett (2006), An improved dual channel PERCA instrument for atmospheric measurements of peroxy radicals, *J. Environ. Monit.*, 8, 530-536.
- Guenther, A., C. N. Hewitt, D. Erickson, R. Fall, C. Geron, T. Graedel, P. Harley, L. Klinger, M. Lerdau, and et al. (1995), A global model of natural volatile organic compound emissions, *Journal of Geophysical Research, [Atmospheres]*, 100, 8873-8892.
- Guerova, G., I. Bey, J.-L. Attie, and R. V. Martin (2005), Case studies of ozone transport between North America and Europe in summer 2000, *Atmospheric Chemistry and Physics Discussions*, 5, 6127-6184.
- Haggerstone, A.-L., L. J. Carpenter, N. Carslaw, and G. McFiggans (2005a), Improved model predictions of HO<sub>2</sub> with gas to particle mass transfer rates

calculated using aerosol number size distribution, *Journal of Geophysical Research*, **110**.

Haggerstone, A. L., L. J. Carpenter, N. Carslaw, and G. McFiggans (2005b), Improved model predictions of HO<sub>2</sub> with gas to particle mass transfer rates calculated using aerosol number size distributions, *J. Geophys. Res.-Atmos.*, **110**.

Handisides, G. M., X. Plass-Dolmer, Σ. Γιλγε, Η. Βινγεμερ, and Η. Βερρεσηειμ (2003), Hohenpeissenberg Photochemical Experiment (HOPE 2000): Measurements and photostationary state calculations of OH and peroxy radicals, *Atmospheric Chemistry and Physics*, **3**, 1565-1588.

Hanke, M., J. Uecker, T. Reiner, and F. Arnold (2002), Atmospheric peroxy radicals: ROXMAS, a new mass-spectrometric methodology for speciated measurements of HO<sub>2</sub> and Sigma RO<sub>2</sub> and first results, *International Journal of Mass Spectrometry*, **213**, 91-99.

Hanson, D., J. Orlando, B. Noziere, and E. Kosciuch (2004), Proton transfer mass spectrometry studies of peroxy radicals, *Int. J. Mass Spectrom.*, **239**, 147-159.

Hanson, D. R., J. B. Burkholder, C. J. Howard, and A. R. Ravishankara (1992), Measurement of hydroxyl and hydroperoxy radical uptake coefficients on water and sulfuric acid surfaces, *Journal of Physical Chemistry*, **96**, 4979-4985.

Hard, T. M., R. J. O'Brien, C. Y. Chan, and A. A. Mehrabzadeh (1984), Tropospheric Free-Radical Determination by Fage, *Environmental Science & Technology*, **18**, 768-777.

Hastie, D. R., M. Weissenmayer, J. P. Burrows, and G. W. Harris (1991), Calibrated Chemical Amplifier for Atmospheric RO<sub>x</sub> Measurements, *Anal. Chem.*, **63**, 2048-2057.

Heard, D. E., L. J. Carpenter, D. J. Creasey, J. R. Hopkins, J. D. Lee, A. C. Lewis, M. J. Pilling, and P. W. Seakins (2004), High levels of the hydroxyl radical in the winter urban troposphere, *Geophys. Res. Lett.*, **31**.

Heard, D. E., and M. J. Pilling (2003), Measurement of OH and HO<sub>2</sub> in the Troposphere, *Chemical Reviews*, **103**, 5163-5198.

Heard, D. E., K. A. Read, J. Methven, S. Al-Haider, W. J. Bloss, G. P. Johnson, M. J. Pilling, P. W. Seakins, S. C. Smith, R. Sommariva, J. C. Stanton, T. J. Still, T. Ingham, B. Brooks, G. De Leeuw, A. V. Jackson, J. B. McQuaid, R. Morgan, M. H. Smith, L. J. Carpenter, N. Carslaw, J. F. Hamilton, J. R. Hopkins, J. D. Lee, A. C. Lewis, R. M. Purvis, D. J. Wevill, N. Brough, T. J. Green, G. Mills, S. A. Penkett, J. M. C. Plane, A. Saiz-Lopez, D. Worton, P. S. Monks, Z. Fleming, A. R. Rickard, M. R. Alfarra, J. D. Allan, K. Bower, H. Coe, M. Cubison, M. Flynn, G. McFiggans, M. Gallagher, E. G. Norton, C. D. O'Dowd, J. Shillito, D. Topping, G. Vaughan, P. Williams, M. Bitter, S. M. Ball, R. L. Jones, I. M. Povey, S. O'Doherty, P. G. Simmonds, A. Allen, R. P. Kinnersley, D. C. S. Beddows, M. Dall'Osto, R. M. Harrison, R. J. Donovan, M. R. Heal, S. G. Jennings, C. Noone, and G. Spain (2006), The North Atlantic Marine Boundary Layer Experiment (NAMBLEX). Overview of the campaign held at Mace HEad, Ireland, in summer 2002, *Atmospheric Chemistry and Physics*, **6**, 2241-2272.

- Hoffman, T., J. R. Odum, F. Bowman, D. Collins, D. Klockow, R. C. Flagan, and J. Seinfeld (1997), Formation of Organic Aerosols from the Oxidation of Biogenic Hydrocarbons, *J. Atmos. Chem.*, *26*, 189-222.
- Holland, F., A. Hofzumahaus, J. Schäfer, A. Kraus, and H.-W. Pätz (2003), Measurements of OH and HO<sub>2</sub> radical concentrations and photolysis frequencies during BERLIOZ, *Journal of Geophysical Research*, *108*.
- IPCC (2001), *Climate Change: The Scientific Basis*, Cambridge University Press, U.K.
- Jacob, M. J. (2005a), Inlet Gas Delivery, *personal communication*.
- Jacob, M. J. (2005b), *personal communication*.
- Jacobson, M. Z. (2001), Global direct radiative forcing due to multicomponent anthropogenic and natural aerosols, *Journal of Geophysical Research*, *106*, 1551-1568.
- Jaegle, L., D. J. Jacob, W. H. Brune, I. Faloona, D. Tan, B. G. Heikes, Y. Kondo, G. W. Sachse, B. Anderson, G. L. Gregory, H. B. Singh, R. Poeschel, G. Ferry, D. R. Blake, and R. E. Shetter (2000), Photochemistry of HO<sub>x</sub> in the upper troposphere at northern midlatitudes, *Journal of Geophysical Research, [Atmospheres]*, *105*, 3877-3892.
- Jaeglé, L., D. J. Jacob, W. H. Brune, I. Faloona, D. Tan, B. G. Heikes, Y. Kondo, G. W. Sachse, B. Anderson, G. L. Gregory, H. B. Singh, R. Poeschel, G. Ferry, D. R. Blake, and R. E. Shetter (2000), Photochemistry of HO<sub>x</sub> in the upper troposphere at northern midlatitudes, *Journal of Geophysical Research, [Atmospheres]*, *105*, 3877-3892.
- Jaeglé, L., D. J. Jacob, W. H. Brune, I. Faloona, D. Tan, Y. Kondo, G. W. Sachse, B. Anderson, G. L. Gregory, S. Vay, H. Singh, D. R. Blake, and R. Shetter (1999), Ozone production in the upper troposphere and the influence of aircraft during SONEX: Approach of NO<sub>x</sub>-saturated conditions, *Geophys. Res. Lett.*, *26*, 3081-3084.
- Jaeglé, L., D. J. Jacob, W. H. Brune, D. Tan, I. Faloona, A. Weinheimer, B. A. Ridley, T. Campos, and G. W. Sachse (1998), Sources of HO<sub>x</sub> and production of ozone in the upper troposphere over the United States, *Geophys. Res. Lett.*, *25*, 1709-1712.
- Jenkin, M. E., S. M. Saunders, and M. J. Pilling (1997), The tropospheric degradation of volatile organic compounds: a protocol for mechanism development, *Atmos. Environ.*, *31*, 81-104.
- Johnson, D., M. E. Jenkin, K. Wirtz, and M. Martin-Reviejo (2005), Simulating the Formation of Secondary Organic Aerosol from the Photooxidation of Aromatic Hydrocarbons, *Environmental Chemistry*, *2*, 35-48.
- Junkerman, W., U. Platt, and A. Volz-Thomas (1989), A Photoelectric Detector for the Measurement of Photolysis Frequencies of Ozone and other Atmospheric Molecules, *Journal of Atmospheric Chemistry*, *8*, 203-227.

- Kalberer, M., D. Paulsen, M. Sax, M. Steinbacher, J. Dommen, A. S. H. Prévôt, R. Fisseha, E. Weingartner, V. Frankevich, R. Zenobi, and U. Baltensperger (2004), Identification of Polymers as Major Components of Atmospheric Organic Aerosols, *Science*, *303*, 1659-1662.
- Kamens, R., M. Jang, C.-J. Chien, and K. Leach (1999), Aerosol Formation from the Reaction of  $\alpha$ -Pinene and Ozone Using a Gas-Phase Kinetics-Aerosol Partitioning Model, *Environmental Science & Technology*, *33*, 1430-1438.
- Kanakidou, M., J. H. Seinfeld, S. N. Pandis, I. Barnes, F. J. Dentener, M.-C. Facchini, R. van Dingenen, B. Ervens, A. Nenes, C. J. Nielsen, E. Swietlicki, J.-P. Putaud, Y. Balkanski, S. Fuzzi, J. Horth, G. K. Moortgat, R. Winterhalter, C. E. L. Myhre, K. Tsigaridis, E. Vignati, E. G. Stephanou, and J. Wilson (2005), Organic aerosol and global climate modelling: a review, *Atmospheric Chemistry and Physics*, *5*, 1053-1123.
- Kelly, T. J., and C. R. Fortune (1994), Continuous monitoring of formaldehyde using an improved fluorescence approach, *International Journal of Environmental Analytical Chemistry*, *54*, 249-263.
- Kelly, T. J., C. W. Spicer, and G. F. Ward (1990), An Assessment of the Luminol Chemiluminescence Technique for Measurement of NO<sub>2</sub> in Ambient Air, *Atmospheric Environment Part a-General Topics*, *24*, 2397-2403.
- Kiley, C. M., and H. E. Fuelberg (2006), An examination of summertime cyclone transport processes during intercontinental chemical transport experiment (INTEX-A), *Journal of Geophysical Research*, *111*.
- Kraus, A., and A. Hofzumahaus (1998), Field measurements of atmospheric photolysis frequencies for O<sub>3</sub>, NO<sub>2</sub>, HCHO, CH<sub>3</sub>CHO, H<sub>2</sub>O<sub>2</sub> and HONO by UV spectroradiometry, *J. Atmos. Chem.*, *31*, 161-180.
- Kroll, J. H., N. L. Ng, S. M. Murphy, R. C. Flagan, and J. H. Seinfeld (2006), Secondary organic aerosol formation from isoprene photooxidation, *Environmental Science & Technology*, *40*, 1869 - 1877.
- Larsen, B. R., D. Di Bella, M. Glasius, R. Winterhalter, N. R. Jensen, and J. Hjorth (2001), Gas-Phase OH Oxidation of Monoterpenes: Gaseous and Particulate Products, *J. Atmos. Chem.*, *38*, 231-276.
- Lee, J. D., A. C. Lewis, P. S. Monks, M. Jacob, J. F. Hamilton, J. R. Hopkins, N. M. Watson, J. E. Saxton, C. Ennis, L. J. Carpenter, N. Carslaw, Z. Fleming, B. J. Bandy, D. E. Oram, S. A. Penkett, J. Slemr, E. Norton, A. R. Rickard, L. K. Whalley, D. E. Heard, W. J. Bloss, T. Gravesstock, S. C. Smith, J. Stanton, M. J. Pilling, and M. E. Jenkin (2006), Ozone photochemistry and elevated isoprene during the UK heatwave of August 2003, *Atmos. Environ.*, *40*, 7598-7613.
- Legreid, G. (2006), personal communication.
- Lewis, A. C., M. J. Evans, J. Methven, N. Watson, J. D. Lee, J. R. Hopkins, R. M. Purvis, S. R. Arnold, J. B. McQuaid, L. K. Whalley, M. J. Pilling, D. E. Heard, P. S. Monks, A. E. Parker, C. E. Reeves, D. E. Oram, G. Mills, B. J. Bandy, D. Stewart, H. Coe, P. Williams, and J. Crozier (2007), Chemical composition observed over

the mid-Atlantic and the detection of pollution signatures far from source regions, *Journal of Geophysical Research, [Atmospheres]*, 112.

Lewis, A. C., N. Watson, M. J. Evans, J. Methven, J. D. Lee, J. R. Hopkins, R. M. Purvis, S. R. Arnold, J. B. McQuaid, L. K. Whalley, M. J. Pilling, D. E. Heard, P. S. Monks, A. E. Parker, C. E. Reeves, D. E. Oram, G. Mills, B. J. Bandy, D. Stewart, H. Coe, P. Williams, and J. Crozier (2006), Chemical composition observed over the mid-Atlantic and the detection of pollution signatures far from source regions, *Journal of Geophysical Research, [Atmospheres]*.

Li, Q., D. J. Jacob, R. J. Park, Y. Wang, C. L. Heald, R. M. Hudman, R. M. Yantosca, V. Martin, and M. Evans (2005), North American pollution outflow and the trapping of convectively lifted pollution by upper-level anticyclone, *Journal of Geophysical Research*, 110.

Liang, Q., L. Jaegle, D. A. Jaffe, P. Weiss-Penzias, A. Heckman, and J. A. Snow (2004), Long-range transport of Asian pollution to the northeast Pacific: Seasonal variations and transport pathways of carbon monoxide, *Journal of Geophysical Research*, 109.

Librando, V., and G. Tringali (2005), Atmospheric fate of OH initiated oxidation of terpenes. Reaction mechanism of  $\alpha$ -pinene degradation and secondary organic aerosol formation, *Journal of Environmental Management*, 75, 275-282.

Lippmann, M. (1993), Health effects of tropospheric ozone: review of recent research findings and their implications to ambient air quality standards, *Journal of Exposure Analysis and Environmental Epidemiology*, 3, 103-128.

Liu, H., D. J. Jacob, I. Bey, R. M. Yantosca, B. N. Duncan, and G. W. Sachse (2006), Transport pathways for Asian pollution outflow over the Pacific: Interannual and seasonal variations, *Journal of Geophysical Research*, 108.

Liu, S. C., M. Trainer, F. C. Fehsenfeld, D. D. Parrish, E. J. Williams, D. W. Fahey, G. Hubler, and P. C. Murphy (1987), Ozone Production in the Rural Troposphere and the Implications for Regional and Global Ozone Distributions, *J. Geophys. Res.-Atmos.*, 92, 4191-4207.

Lohmann, U., J. Feichter, J. Penner, and R. Leaitch (2000), Indirect effect of sulfate and carbonaceous aerosols: A mechanistic treatment, *Journal of Geophysical Research*, 105, 12,193-112,206.

Lugauer, M., U. Baltensperger, M. Furger, H. W. Gäggeler, D. T. Jost, M. Schwikowski, and H. Wanner (1998), Aerosol transport to the high Alpine sites Jungfraujoch (3454 m asl) and Colle Gnifetti (4452 m asl), *Tellus*, 50B, 76-92.

Madronich, S., and S. Flocke (1998), in *Handbook of Environmental Chemistry*, edited by P. Boule, pp. 1-26, Springer-Verlag, Heidelberg.

Malicet, J., D. Daumont, J. Charbonnier, C. Parisse, A. Chakir, and J. Brion (1995), Ozone UV spectroscopy. 2. Absorption cross-sections and temperature-dependence, *J. Atmos. Chem.*, 21, 263-273.

- Martilli, A., A. Neftel, G. Favaro, F. Kirchner, S. Sillman, and A. Clappier (2002), Simulation of the ozone formation in the northern part of the Po Valley, *Journal of Geophysical Research*, 107.
- Martin, R. V., D. J. Jacob, J. A. Logan, I. Bey, R. M. Yantosca, A. C. Staudt, Q. Li, A. M. Fiore, B. N. Duncan, H. Liu, P. Ginoux, and V. Thouret (2002), Interpretation of TOMS observations of tropical tropospheric ozone with a global model and in situ observations, *Journal of Geophysical Research*, 107.
- Martin, R. V., D. J. Jacob, R. M. Yantosca, M. Chin, and P. Ginoux (2003), Global and regional decreases in tropospheric oxidants from photochemical effects of aerosols, *Journal of Geophysical Research*, 108.
- Mather, J. H., P. S. Stevens, and W. H. Brune (1997), OH and HO<sub>2</sub> measurements using laser-induced fluorescence, *Journal of Geophysical Research*, 102, 6427-6436.
- Matsumi, Y., F. J. Comes, G. Hancock, A. Hofzumahaus, A. J. Hynes, M. Kawasaki, and A. R. Ravishankara (2002), Quantum yields for production of O(<sup>1</sup>D) in the ultraviolet photolysis of ozone: Recommendation based on evaluation of laboratory data, *Journal of Geophysical Research*, 107.
- Mauldin III, R. L., E. Kosciuch, B. Henry, F. Eisele, R. Shetter, B. Lefer, G. Chen, D. Davis, G. Huey, and D. Tanner (2004), Measurements of OH, HO<sub>2</sub> + RO<sub>2</sub>, H<sub>2</sub>SO<sub>4</sub>, and MSA at the South Pole during ISCAT 2000, *Atmos. Environ.*, 38, 5423-5437.
- McIntosh, D. (2004), ARA Air-to-Air Photo (courtesy of BAE Systems), edited, <http://www.faam.ac.uk>.
- Meller, R., and G. K. Moortgat (1999), Temperature dependence of the absorption cross sections of formaldehyde between 223 and 323 K in the wavelength range 225-375 nm, *Journal of Geophysical Research*, 105.
- Methven, J. (2004a), *personal communication*.
- Methven, J. (2004b), ICARTT Lagrangian Opportunities, *personal communication*.
- Methven, J. (2004c), ITOP Flight Summaries, paper presented at ITOP meeting 10/11/2004.
- Methven, J., S. R. Arnold, A. Stohl, M. J. Evans, M. Avery, K. Law, A. C. Lewis, P. S. Monks, D. D. Parrish, C. E. Reeves, H. Schlager, E. Atlas, D. R. Blake, H. Coe, J. Crosier, F. M. Flocke, J. S. Holloway, J. R. Hopkins, J. McQuaid, R. Purvis, B. Rappenglück, H. B. Singh, N. M. Watson, L. K. Whalley, and P. I. Williams (2006), Establishing Lagrangian connections between observations within air masses crossing the Atlantic during the International Consortium for Atmospheric Research on Transport and Transformation experiment, *Journal of Geophysical Research*, [Atmospheres], 111.
- Methven, J., M. Evans, P. G. Simmonds, and G. Spain (2001), Estimating relationships between air mass origin and chemical composition, *Journal of Geophysical Research*, 106, 5005-5019.

- Metzger, A. (2007), personal communication.
- Mihelcic, D., D. H. Ehhalt, G. F. Kulesa, J. Klomfass, M. Trainer, U. Schmidt, and H. Roers (1978), Measurements of free radicals in the atmosphere by matrix isolation and electron paramagnetic resonance, *Pure Applied Geophysics*, *116*, 530.
- Mihelcic, D., F. Holland, A. Hofzumahaus, L. Hoppe, S. Konrad, P. Musgen, H. W. Patz, H. J. Schafer, T. Schmitz, A. Volz-Thomas, K. Bachmann, S. Schlomski, U. Platt, A. Geyer, B. Alicke, and G. K. Moortgat (2003), Peroxy radicals during BERLIOZ at Pabstthum: Measurements, radical budgets and ozone production, *J. Geophys. Res.-Atmos.*, *108*.
- Mihelcic, D., D. Klemp, P. Musgen, H. W. Patz, and A. Volzthomas (1993), Simultaneous Measurements of Peroxy and Nitrate Radicals at Schauinsland, *J. Atmos. Chem.*, *16*, 313-335.
- Mihelcic, D., P. Musgen, and D. H. Ehhalt (1985), An Improved Method of Measuring Tropospheric NO<sub>2</sub> and RO<sub>2</sub> by Matrix-Isolation and Electron-Spin-Resonance, *Journal of Atmospheric Chemistry*, *3*, 341-361.
- Mihele, C. M., and D. R. Hastie (1998), The sensitivity of the radical amplifier to ambient water vapour, *Geophys. Res. Lett.*, *25*, 1911-1913.
- Mihele, C. M., and D. R. Hastie (2003), Radical chemistry at a forested continental site: Results from the PROPHET 1997 campaign, *J. Geophys. Res.-Atmos.*, *108*, art. no.-4450.
- Mihele, C. M., M. Mozurkewich, and D. R. Hastie (1999), Radical loss in a chain reaction of CO and NO in the presence of water: Implications for the radical amplifier and atmospheric chemistry, *Int. J. Chem. Kinet.*, *31*, 145-152.
- Molina, M. J., and F. S. Rowland (1974), Stratospheric sink for chlorofluoromethanes. Chlorine atom-catalyzed destruction of ozone, *Nature (London, United Kingdom)*, *249*, 810-812.
- Monks, P. S. (2005), Gas-phase radical chemistry in the troposphere, *Chemical Society Reviews*, *34*, 376-395.
- Monks, P. S. (2007), personal communication.
- Monks, P. S., L. J. Carpenter, S. A. Penkett, and G. P. Ayers (1996), Night-time peroxy radical chemistry in the remote marine boundary layer over the Southern ocean, *Geophys. Res. Lett.*, *23*, 535-538.
- Monks, P. S., L. J. Carpenter, S. A. Penkett, G. P. Ayers, R. W. Gillett, I. E. Galbally, and C. P. Meyer (1998), Fundamental ozone photochemistry in the remote marine boundary layer: The SOAPEX experiment, measurement and theory, *Atmos. Environ.*, *32*, 3647-3664.
- Monks, P. S., G. Salisbury, G. Holland, S. A. Penkett, and G. P. Ayers (2000), A seasonal comparison of ozone photochemistry in the remote marine boundary layer, *Atmos. Environ.*, *34*, 2547-2561.

Morita, A., Y. Kanaya, and J. S. Francisco (2004), Uptake of the HO<sub>2</sub> radical by water: molecular dynamics calculations and their implications for atmospheric modeling, *Journal of Geophysical Research, [Atmospheres]*, 109, D09201/09201-D09201/09210.

Neftel, A., C. Spirig, A. S. H. Prévôt, M. Furger, J. Stutz, B. Vogel, and J. Hjorth (2002), Sensitivity of photooxidant production in the Milan Basin: An overview of results from a EUROTRAC-2 Limitation of Oxidant Production field experiment, *Journal of Geophysical Research*, 107.

NOAA (2004), ICARTT Implementation Plan, edited.

Northway, M. J., J. A. d. Gouw, D. W. Fahey, R. S. Gao, C. Warneke, J. M. Roberts, and F. Flocke (2004), Evaluation of the role of heterogenous oxidation of alkenes in the detection of atmospheric acetaldehyde, *Atmos. Environ.*, 38, 6017 - 6028.

Novakov, T., and C. E. Corrigan (1996), Cloud condensation nucleus activity of the organic component of biomass smoke particles, *Geophys. Res. Lett.*, 23, 2141-2144.

Odum, J. R., T. Hoffman, F. Bowman, D. Collins, R. C. Flagan, and J. H. Seinfeld (1996), Gas/Particle Partitioning and Secondary Organic Aerosol Yields, *Environmental Science & Technology*, 30, 2580-2585.

Odum, J. R., T. P. W. Jungkamp, R. J. Griffin, R. C. Flagan, and J. H. Seinfeld (1997), The atmospheric aerosol forming potential of whole gasoline vapor, *Science*, 276, 96.

Olson, J. R., J. H. Crawford, G. Chen, A. Fried, M. J. Evans, C. E. Jordan, S. T. Sandholm, D. D. Davis, B. E. Anderson, M. A. Avery, J. D. Barrick, D. R. Blake, W. H. Brune, F. L. Eisele, F. Flocke, H. Harder, D. J. Jacob, Y. Kondo, B. L. Lefer, M. Martinez, R. L. Mauldin, G. W. Sachse, R. E. Shetter, H. B. Singh, R. W. Talbot, and D. Tan (2004), Testing fast photochemical theory during TRACE-P based on measurements of OH, HO<sub>2</sub>, and CH<sub>2</sub>O, *Journal of Geophysical Research, [Atmospheres]*, 109, D15S10/11-D15S10/16.

Oshima, N., M. Koike, H. Nakamura, Y. Kondo, N. Takegawa, Y. Miyazaki, D. R. Blake, T. Shirai, K. Kita, S. Kawakami, and T. Ogawa (2004), Asian chemical outflow to the Pacific in late spring observed during the PEACE-B aircraft mission, *J. Geophys. Res.-Atmos.*, 109, art. no.-D23S05.

Owen, R. C., O. R. Cooper, A. Stohl, and R. E. Honrath (2006), An analysis of the mechanisms of North American pollutant transport to the central North Atlantic lower free troposphere, *J. Geophys. Res.-Atmos.*, 111.

Parker, A. E., P. S. Monks, M. J. Jacob, S. A. Penkett, A. C. Lewis, D. Stewart, L. Whalley, J. Methven, and A. Stohl (2007), Peroxy radicals and ozone photochemistry in air masses undergoing long-range transport, *Journal of Geophysical Research, submitted*.

Paulsen, D., J. Dommen, M. Kalberer, A. S. H. Prévôt, R. Richter, M. Sax, M. Steinbacher, E. Weingartner, and U. Baltensperger (2005), Secondary Organic Aerosol Formation by Irradiation of 1,3,5-Trimethylbenzene-NO<sub>x</sub>-H<sub>2</sub>O in a New

Reaction Chamber for Atmospheric Chemistry and Physics, *Environmental Science & Technology*, 39, 2668-2678.

Penkett, S. A., K. C. Clemitshaw, N. H. Savage, R. A. Burgess, L. M. Cardenas, L. J. Carpenter, G. C. McFadyen, and J. N. Cape (1999), Studies of Oxidant Production at the Weybourne Atmospheric Observatory in Summer and Winter Conditions, *J. Atmos. Chem.*, 33, 111-128.

Penkett, S. A., M. J. Evans, C. E. Reeves, K. S. Law, P. S. Monks, S. J.-B. Baugitte, J. A. Pyle, T. J. Green, B. J. Bandy, G. Mills, L. M. Cardenas, H. Barjat, D. Kley, S. Schmitgen, J. M. Kent, K. Dewey, and J. Methven (2004), Long-range transport of ozone and related pollutants over the North Atlantic in spring and summer, *Atmospheric Chemistry and Physics Discussions*, 4, 4407-4454.

Penkett, S. A., P. S. Monks, L. J. Carpenter, K. C. Clemitshaw, G. P. Ayers, R. W. Gillett, I. E. Galbally, and C. P. Meyer (1997), Relationships between ozone photolysis rates and peroxy radical concentrations in clean marine air over the Southern Ocean, *J. Geophys. Res.-Atmos.*, 102, 12805-12817.

Phillips, G. J. (2002), Studies of Atmospheric Photochemistry in the European Troposphere, *Ph.D. Thesis, University of Leicester*.

Platt, U., B. Alicke, R. Dubois, A. Geyer, A. Hofzumahaus, F. Holland, M. Martinez, D. Mihelcic, T. Klüpfel, B. Lohrmann, W. Pätz, D. Perner, F. Rohrer, H. J. Schäfer, and J. Stutz (2002), Free Radicals and Fast Photochemistry during BERLIOZ, *J. Atmos. Chem.*, 42, 359-394.

Prather, M. J., and D. J. Jacob (1997), A persistent imbalance in HO<sub>x</sub> and NO<sub>x</sub> photochemistry of the upper troposphere driven by deep tropical convection, *Geophys. Res. Lett.*, 24, 3189-3192.

Prévôt, A. S. H., J. Staehelin, G. L. Kok, R. D. Schillawski, B. Neining, T. Staffelbach, A. Neftel, H. Wernli, and J. Dommen (1997), The Milan photooxidant plume, *Journal of Geophysical Research*, 102, 3375-3388.

Pun, B. K., and C. Seigneur (2007), Investigative modeling of new pathways for secondary organic aerosol formation, *Atmospheric Chemistry and Physics*, 7, 2199 - 2216.

Putaud, J.-P., F. Raes, R. Van Dingenen, E. Brüggemann, M.-C. Facchini, S. Decesari, S. Fuzzi, R. Gehrig, C. Hüglin, P. Laj, G. Lorbeer, W. Maenhaut, N. Mihalopoulos, K. Müller, X. Querol, S. Rodriguez, J. Schneider, G. Spindler, H. ten Brink, K. Tørseth, and A. Wiedensohler (2004), A European aerosol phenomenology—2: chemical characteristics of particulate matter at kerbside, urban, rural and background sites in Europe, *Atmos. Environ.*, 38, 2579-2595.

Ravetta, F., D. J. Jacob, W. H. Brune, B. G. Heikes, B. E. Anderson, D. R. Blake, G. L. Gregory, G. W. Sachse, S. T. Sandholm, R. E. Shetter, H. B. Singh, and R. W. Talbot (2001), Experimental evidence for the importance of convected methylhydroperoxide as a source of hydrogen oxide (HO<sub>x</sub>) radicals in the tropical upper troposphere, *Journal of Geophysical Research*, 106, 709-732, 716.

- Reichert, L., M. D. A. Hernandez, D. Stobener, J. Burkert, and J. P. Burrows (2003), Investigation of the effect of water complexes in the determination of peroxy radical ambient concentrations: Implications for the atmosphere, *J. Geophys. Res.-Atmos.*, *108*, art. no.-4017.
- Reimann, S., D. Schaub, K. Stemmler, D. Folini, M. Hill, P. Hofer, B. Buchmann, P. G. Simmonds, B. R. Grealley, and S. O'Doherty (2004), Halogenated greenhouse gases at the Swiss high Alpine site of Jungfraujoch (3580 m asl): Continuous measurements and their use for regional European source allocation, *Journal of Geophysical Research*, *109*.
- Reiner, T., M. Hanke, and F. Arnold (1997), Atmospheric peroxy radical measurements by ion molecule reaction mass spectrometry: A novel analytical method using amplifying chemical conversion to sulfuric acid, *J. Geophys. Res.-Atmos.*, *102*, 1311-1326.
- Reiner, T., M. Hanke, F. Arnold, H. Ziereis, H. Schlager, and W. Junkermann (1999), Aircraft-borne measurements of peroxy radicals by chemical conversion/ion molecule reaction mass spectrometry: Calibration, diagnostics, and results, *Journal of Geophysical Research*, *104*, 18,647-618,659.
- Ren, X. R., G. D. Edwards, C. A. Cantrell, R. L. Leshner, A. R. Metcalf, T. Shirley, and W. H. Brune (2003), Intercomparison of peroxy radical measurements at a rural site using laser-induced fluorescence and Peroxy Radical Chemical Ionization Mass Spectrometer (PerCIMS) techniques, *J. Geophys. Res.-Atmos.*, *108*, art. no.-4605.
- Rickard, A. R., D. Johnson, C. D. McGill, and G. Marston (1999), OH Yields in the Gas-Phase Reactions of Ozone with Alkenes, *Journal of Physical Chemistry A*, *103*, 7656-7664.
- Roberts, G. C., M. O. Andreae, J. Zhou, and P. Artaxo (2001), Cloud condensation nuclei in the Amazon Basin: "Marine" conditions over a continent?, *Geophys. Res. Lett.*, *28*, 2807-2810.
- Sadanaga, Y., J. Matsumoto, K. Sakurai, R. Isozaki, S. Kato, T. Nomaguchi, H. Bandow, and Y. Kajii (2004), Development of a measurement system of peroxy radicals using a chemical amplification/laser-induced fluorescence technique, *Rev. Sci. Instrum.*, *75*, 864-872.
- Saiz-Lopez, A., R. W. Saunders, D. M. Joseph, S. H. Ashworth, and J. M. C. Plane (2004), Absolute absorption cross-section and photolysis rate of I<sub>2</sub>, *Atmospheric Chemistry and Physics*, *4*, 1443-1450.
- Salisbury, G. (2001), Measurements of peroxy radicals in the marine boundary layer, Ph.D. thesis, University of Leicester, Leicester.
- Salisbury, G., P. S. Monks, S. Bauguitte, B. J. Bandy, and S. A. Penkett (2002), A seasonal comparison of the ozone photochemistry in clean and polluted air masses at Mace Head, Ireland, *J. Atmos. Chem.*, *41*, 163-187.
- Salisbury, G., A. R. Rickard, P. S. Monks, B. J. Allan, S. Bauguitte, S. A. Penkett, N. Carslaw, A. C. Lewis, D. J. Creasey, D. E. Heard, P. J. Jacobs, and J. D. Lee

- (2001), Production of peroxy radicals at night via reactions of ozone and the nitrate radical in the marine boundary layer, *J. Geophys. Res.-Atmos.*, *106*, 12669-12687.
- Savage, N. H., K. S. Law, J. A. Pyle, A. Richter, H. Nüß, and J. P. Burrows (2004), Using GOME NO<sub>2</sub> satellite data to examine regional differences in TOMCAT model performance, *Atmospheric Chemistry and Physics*, *4*, 1895-1912.
- Schmidt, R. W. H., F. Slemr, and U. Schurath (1998), Airborne peroxyacetyl nitrate (PAN) measurements and peroxypropionyl nitrate (PPN) measurements during TRACT 1992, *Atmos. Environ.*, *32*, 1203-1227.
- Seinfeld, J. H., and J. F. Pankow (2003), Organic atmospheric particulate material, *Annual Reviews of Physical Chemistry*, *54*, 121-140.
- Short Sr., N. M. (2004), NASA Remote Sensing Tutorial, edited.
- Silibello, C., G. Calori, G. Brusasca, G. Catenacci, and G. Finzi (1998), Application of a photochemical grid model to Milan metropolitan area, *Atmos. Environ.*, *32*, 2025-2038.
- Simmonds, P. G., R. G. Derwent, A. L. Manning, and G. Spain (2004), Significant growth in surface ozone at Mace Head, Ireland, 1987-2003, *Atmos. Environ.*, *38*, 4769-4778.
- Simmonds, P. G., S. O'Doherty, G. Nickless, G. A. Sturrock, R. Swaby, P. Knight, J. Ricketts, G. Woffendin, and R. Smith (1995), Automated Gas Chromatograph/Mass Spectrometer for Routine Atmospheric Field Measurements of the CFC Replacement Compounds, the Hydrofluorocarbons and Hydrochlorofluorocarbons, *Anal. Chem.*, *67*, 717-723.
- Smith, S. C., J. D. Lee, W. J. Bloss, G. P. Johnson, T. Ingham, and D. E. Heard (2006), Concentrations of OH and HO<sub>2</sub> radicals during NAMBLEX: measurements and steady state analysis, *Atmospheric Chemistry and Physics*, *6*, 1435-1453.
- Sommariva, R., W. J. Bloss, N. Brough, N. Carslaw, M. Flynn, A.-L. Haggerstone, D. E. Heard, J. R. Hopkins, J. D. Lee, A. C. Lewis, G. McFiggans, P. S. Monks, S. A. Penkett, M. J. Pilling, J. M. C. Plane, K. A. Read, A. Saiz-Lopez, A. R. Rickard, and P. I. Williams (2006), OH and HO<sub>2</sub> chemistry during NAMBLEX: roles of oxygenates, halogen oxides and heterogeneous uptake, *Atmospheric Chemistry and Physics*, *6*, 1135-1153.
- Sommariva, R., A. L. Haggerstone, L. J. Carpenter, N. Carslaw, D. J. Creasey, D. E. Heard, J. D. Lee, A. C. Lewis, M. J. Pilling, and J. Zador (2004), OH and HO<sub>2</sub> chemistry in clean marine air during SOAPEX-2, *Atmospheric Chemistry and Physics*, *4*, 839-856.
- Stedman, J. R. (2004), The predicted number of air pollution related deaths in the UK during the August 2003 heatwave, *Atmos. Environ.*, *38*, 1087-1090.
- Stohl, A. (2001), A 1-year Lagrangian "climatology" of airstreams in the Northern Hemisphere troposphere and lowermost stratosphere, *J. Geophys. Res.-Atmos.*, *106*, 7263-7279.

- Stohl, A., S. Eckhardt, C. Forster, P. James, and N. Spichtinger (2002), On the pathways and timescales of intercontinental air pollution transport, *J. Geophys. Res.-Atmos.*, *107*, art. no.-4684.
- Stohl, A., C. Forster, S. Eckhardt, N. Spichtinger, H. Huntrieser, J. Heland, H. Schlager, S. Wilhelm, F. Arnold, and O. Cooper (2003), A backward modelling study of intercontinental pollution transport using aircraft measurements, *Journal of Geophysical Research*, *108*.
- Stohl, A., C. Forster, A. Frank, P. Seibert, and G. Wotawa (2005), Technical Note: The Lagrangian particle dispersion model FLEXPART version 6.2, *Atmospheric Chemistry and Physics*, *5*, 2461-2474.
- Stohl, A., and T. Trickl (1999), A textbook example of long-range transport: Simultaneous observation of ozone maxima of stratospheric and North American origin in the free troposphere over Europe, *J. Geophys. Res.-Atmos.*, *104*, 30445-30462.
- Stroud, C., S. Madronich, E. Atlas, C. A. Cantrell, A. Fried, B. Wert, B. Ridley, F. Eisele, L. Mauldin, R. Shetter, B. Lefer, F. Flocke, A. Weinheimer, M. Coffey, B. Heikes, R. Talbot, and D. Blake (2004), Photochemistry in the Arctic Free Troposphere: Ozone Budget and Its Dependence on Nitrogen Oxides and the Production Rate of Free Radicals, *J. Atmos. Chem.*, *47*, 107-138.
- Surratt, J. D., S. M. Murphy, J. H. Kroll, N. L. Ng, L. Hilderbrandt, A. Sorooshian, R. Szmigielski, R. Vermeylen, W. Maenhaut, M. Claeys, R. Flagan, and J. H. Seinfeld (2006), Chemical composition of secondary organic aerosol formed from the photooxidation of isoprene, *Journal of Physical Chemistry A*, *110*, 9665 - 9690.
- Talukdar, R. K., J. B. Burkholder, A.-M. Schmoltner, J. M. Roberts, R. W. Wilson, and A. R. Ravishankara (1995), Investigation of the loss processes for peroxyacetyl nitrate in the atmosphere: UV photolysis and reaction with OH, *Journal of Geophysical Research*, *100*, 14163-14174.
- Tan, D., I. Faloon, J. B. Simpas, W. Brune, J. Olson, J. Crawford, M. Avery, G. Sachse, S. Vay, S. Sandholm, H.-W. Guan, T. Vaughn, J. Mastromarino, B. Heikes, J. Snow, J. Podolske, and H. Singh (2001a), OH and HO<sub>2</sub> in the tropical Pacific: Results from PEM-Tropics B, *Journal of Geophysical Research*, *106*, 32,667-632,681.
- Tan, D., I. Faloon, J. B. Simpas, W. Brune, P. B. Shepson, T. L. Couch, A. L. Sumner, M. A. Carroll, T. Thornberry, E. Apel, D. Riemer, and W. Stockwell (2001b), HO<sub>x</sub> budgets in a deciduous forest: Results from the PROPHET summer 1998 campaign, *Journal of Geophysical Research*, *106*, 24,407-424,427.
- Thornton, J., and J. P. D. Abbatt (2005), Measurements of HO<sub>2</sub> uptake to aqueous aerosol: mass accommodation coefficients and net reactive loss, *Journal of Geophysical Research*, [Atmospheres], *110*, D08309/08301-D08309/08312.
- Tie, X., S. Madronich, S. Walters, D. P. Edwards, P. Ginoux, N. Mahowald, R. Y. Zhang, C. Lou, and G. Brasseur (2005), Assessment of the global impact of aerosols on tropospheric oxidants, *Journal of Geophysical Research*, *110*.

- Tolocka, M. P., M. Jang, J. M. Ginter, F. J. Cox, R. M. Kamens, and M. V. Johnston (2004), Formation of Oligomers in Secondary Organic Aerosol, *Environmental Science & Technology*, *38*, 1428-1434.
- Troe, J. (2000), Are primary quantum yields of NO<sub>2</sub> photolysis at  $\lambda \leq 398$  nm smaller than unity?, *Zeitschrift Fur Physikalische Chemie - International Journal of Research in Physical Chemistry & Chemical Physics*, *214*, 573-581.
- Tsigaridis, K., and M. Kanakidou (2003), Global modelling of secondary organic aerosol in the troposphere: a sensitivity analysis, *Atmospheric Chemistry and Physics*, *3*, 1849-1869.
- Tulet, P., K. Suhre, C. Mari, F. Solmon, and R. Rosset (2002), Mixing of boundary layer and upper tropospheric ozone during a deep convective event over Western Europe, *Atmos. Environ.*, *36*, 4491-4501.
- van Aardenne, J. A., G. R. Carmichael, H. Levy, D. Streets, and L. Hordijk (1999), Anthropogenic NO<sub>x</sub> emissions in Asia in the period 1990-2020, *Atmos. Environ.*, *33*, 633-646.
- Volz-Thomas, A., A. Lerner, H. S. Patz, M. Schultz, D. McKenna, R. Schmitt, S. Madronich, and E. Roth (1996), Airborne Measurements of the Photolysis of NO<sub>2</sub>, *Journal of Geophysical Research, [Atmospheres]*, *101*, 18613-18627.
- Volz-Thomas, A., H.-W. Pätz, N. Houban, S. Konrad, and D. Mihelcic (2003), Inorganic trace gases and peroxy radicals during BERLIOZ at Pabstthum: An investigation of the photostationary state of NO<sub>x</sub> and O<sub>3</sub>, *Journal of Geophysical Research*, *108*.
- Wayne, R. P. (2000), *Chemistry of Atmospheres*, Third Edition ed., Oxford University Press.
- Wayne, R. P., I. Barnes, P. Biggs, J. P. Burrows, C. E. Canosa-Mas, J. Hjorth, G. Lebras, G. K. Moortgat, D. Perner, G. Poulet, G. Restelli, and H. Sidebottom (1991), The nitrate radical - physics, chemistry and the atmosphere, *Atmos. Environ.*, *25*, 1-203.
- Wiedinmyer, C., A. Guenther, P. Harley, N. Hewitt, C. Geron, P. Artaxo, R. Steinbrecher, and R. Rasmussen (2004), Global Organic Emissions from Vegetation, in *Emissions of Atmospheric Trace Compounds*, edited by C. Granier, et al., pp. 115-170, Kluwer Academic Publishers, Dordrecht, The Netherlands.
- Wild, O., and H. Akimoto (2001), Intercontinental transport of ozone and its precursors in a three-dimensional global CTM, *J. Geophys. Res.-Atmos.*, *106*, 27729-27744.
- Wyche, K. P., R. S. Blake, A. M. Ellis, P. S. Monks, T. Brauers, R. Koppmann, and E. C. Apel (2007a), Technical Note: Performance of Chemical Ionization Reaction Time-of-Flight Mass Spectrometry (CIR-TOF-MS) for the measurement of atmospherically significant oxygenated volatile organic compounds, *Atmospheric Chemistry and Physics*, *7*, 609-620.

- Wyche, K. P., R. L. Cordell, A. M. Ellis, A. E. Parker, C. Whyte, P. S. Monks, J. Dommen, A. Metzger, J. Duplissy, A. S. H. Prévôt, U. Baltensperger, and A. R. Rickard (2007b), Potential Gas-Phase Precursors in the Photooxidation of 1,3,5-trimethylbenzene, *In preparation*.
- Yokelson, R. J., J. B. Burkholder, R. W. Fox, R. K. Talukdar, and A. R. Ravishankara (1994), Temperature-dependence of the NO<sub>3</sub> absorption spectrum, *Journal of Physical Chemistry*, *98*, 13144-13150.
- Zanis, P., P. S. Monks, T. J. Green, E. Schuepbach, L. J. Carpenter, G. P. Mills, A. R. Rickard, N. Brough, and S. A. Penkett (2003), Seasonal variation of peroxy radicals in the lower free troposphere based on observations from the FREE Tropospheric EXperiments in the Swiss Alps, *Geophys. Res. Lett.*, *30*, art. no.-1497.
- Zanis, P., P. S. Monks, E. Schuepbach, L. J. Carpenter, T. J. Green, G. P. Mills, S. Bauguitte, and S. A. Penkett (2000a), In situ ozone production under free tropospheric conditions during FREETEX '98 in the Swiss Alps, *J. Geophys. Res.-Atmos.*, *105*, 24223-24234.
- Zanis, P., P. S. Monks, E. Schuepbach, and S. A. Penkett (1999), On the relationship of HO<sub>2</sub>+RO<sub>2</sub> with j(O<sup>1</sup>D) during the Free Tropospheric Experiment (FREETEX '96) at the Jungfraujoch Observatory (3580 m above sea level) in the Swiss Alps, *J. Geophys. Res.-Atmos.*, *104*, 26913-26925.
- Zanis, P., P. S. Monks, E. Schuepbach, and S. A. Penkett (2000b), The role of *In Situ* Photochemistry in the Control of Ozone during Spring at the Jungfraujoch (3,580 m asl) - Comparison of Model Results with Measurements, *J. Atmos. Chem.*, *37*, 1-27.
- Zellweger, C., M. Ammann, B. Buchmann, P. Hofer, M. Lugauer, R. Ruttimann, N. Streit, E. Weingartner, and U. Baltensperger (2000), Summertime NO<sub>y</sub> speciation at the Jungfraujoch, 3580 m above sea level, Switzerland, *Journal of Geophysical Research*, *105*, 6655-6667.